High resolution coherent spectroscopy of a polariton fluid : Bogoliubov modes, non equilibrium phase transitions and turbulence

Ferdinand Claude

THÈSE DE DOCTORAT
DE SORBONNE UNIVERSITÉ

Spécialité : Physique

École doctorale n°564: Physique en Île-de-France

réalisée

au Laboratoire Kastler Brossel

sous la direction de Alberto BRAMATI et Quentin GLORIEUX

présentée par

Ferdinand CLAUDE

pour obtenir le grade de :

DOCTEUR DE SORBONNE UNIVERSITÉ

Sujet de la thèse :

High resolution coherent spectroscopy of a polariton fluid: Bogoliubov modes, non equilibrium phase transitions and turbulence

soutenue le 28/11/2022

devant le jury composé de :

Mme.	Anna MINGUZZI	Rapporteuse
M.	Atac IMAMOGLU	Rapporteur
Mme.	Jacqueline BLOCH	Examinatrice
M.	David CLÉMENT	Examinateur
Mme.	Agnès MAÎTRE	Examinatrice
M.	Alberto BRAMATI	Directeur de thèse

Contents

Chapter 1

Introduction

The concept of wave-particle duality was definitively settled by L. de Broglie in 1924, stating that every particle has an associated wave [49]. One year later, A. Einstein, building on de Broglie's theory and S. N. Bose's work on photon statistics, envisioned that an atomic (matter) gas should undergo a phase transition to a condensed state of lowest possible energy [55]. He stipulated as a prerequisite for the achievement of such a phenomenon that the de Broglie thermal wavelength of particles has to be at least equal to the interatomic spacing. These ideas are today unanimously embraced, following the first observation of superfluidity by P. Kapitsa in helium in 1938 [82], linked to the Bose Einstein condensation by F. London [105]. Most of the work of the last few decades has been carried out in matter particle systems, among which the dilute gases of cold atoms are the paradigmatic representative, after the first experimental demonstrations of their condensation in 1995 in the W. Ketterle [12] and E. Cornell [48] groups with sodium and rubidium atoms respectively.

Besides matter particles, the same investigations have been carried out for photons, as bosonic quanta of the electromagnetic field. However, the possibility to observe collective phenomena seems less straightforward, as they lack a crucial ingredient compared to their matter equivalent: interactions, mediating collisions between particles and responsible for the collective hydrodynamic-like behavior of quantum fluids. To solve this issue, the field originating from the propagation of light through an optical nonlinear medium can be used to engineer an effective photon-photon interaction. For a Kerr-type nonlinear medium, the paraxial propagation of a laser field is described by the nonlinear Schrödinger equation (NLSE), which is tightly related to the Gross-Pitaevskii equation (GPE) governing the mean field dynamics of quantum fluids.

In the hydrodynamic picture provided by the GPE, the laser field is equivalent to a quantum fluid of light, whose density and flow velocity are defined from the local intensity and phase gradient, respectively. The self-focusing and self-defocusing effects of the nonlinearity simulate attractive and repulsive interactions between photons.

In order to achieve large nonlinear interactions to ensure collective behavior, the mixing

mechanisms of the photons with the nonlinear medium can be enhanced via the so-called strong light-matter coupling regime. This gives rise to the generation of a new quasiparticle, the polariton, equivalent to a photon dressed by matter excitations. These can be created in a wide diversity of material systems, however in this manuscript we will only be interested in those originating from semiconductors, in which photons mix with bound electron-hole pairs (excitons). The rapid development in the late twentieth century of heterostructure growth techniques reaching sub-Bohr radius accuracy, allowed the design of planar quantum wells embedded in optical cavities, which, by confining the motion of photons and excitons in the same plane, strengthen the light-matter exchange. In this way, the strong coupling regime in semiconductor cavities was first observed by C. Weisbuch in 1992 [172]. This led to the creation of massive bosonic quasiparticles in interaction with each other, called exciton-polaritons. Here, the interactions are mediated by the optical nonlinearity arising from the exchange interactions between excitons; the mass from the spatial confinement of photons operated by the optical cavity. Regarding the bosonic nature, it is directly inherited from the photon and the exciton, considered as a composite boson following the rules of composition of two fermions (electron and hole).

Remarkably, the space-time evolution of the mean-field wave function of polaritons is very similar to that of atomic Bose-Einstein condensates. It is described by a driven-dissipative GPE, taking into account the losses and the driving of the system. Thanks to a dispersion curve acting as a trap in the momentum space and a low effective mass, four orders of magnitude below that of the electron, polaritons can in principle undergo a BEC transition at room temperatures. After a first theoretical proposal by A. Imamoglu [75], the first experimental demonstration of exciton-polariton condensation was performed in 2006 by J. Kasprzak and M. Richard [84]. Following these observations, the hydrodynamics aspect of quantum fluids in semiconductor microcavities has gained a great interest, mainly because of the experimental opportunities offered by the all-optical control and detection of exciton-polariton dynamics. Thus, a whole series of works on superfluidity have experimentally demonstrated the dispersionless flow of exciton-polaritons [9, 10], the nucleation of quantized vortex-antivortex pairs [145, 124] and the generation of dark and bright solitons [8, 153].

Thanks to the light-matter nature of polaritons, a wide range of potential geometries can be designed to modify the behavior of the quantum fluid [151]. For instance, the tailoring of the refractive index by etching a planar microcavity provides a way to tightly confine polaritons in different geometries, in order to simulate different Hamiltonians. In this way, the fabrication of microwires has led to the generation of one-dimensional polariton fluids to investigate condensation phenomena [95, 173], create solitons [62], or implement logic circuits [126]. The dimensionality can be further reduced by etching micropillars, to study for example condensation [160] and squeezing [28] of polaritons in zero-dimension. Furthermore, these pillars can be combined with each other, one by one to study polariton molecules [113] or in lattices [115, 88, 77], typically used for topological experiments.

In this manuscript, the fluid dynamics is controlled by structuring the excitation laser profile

using phase and intensity modulation techniques [7] in a planar semiconductor microcavity. They can be described in the framework of the Bogoliubov theory, demonstrating that the superfluidity stems from the peculiar behavior of elementary excitations spreading on top of quantum fluids [24]. The characterization of such excitations is therefore crucial to master the dynamics at stake in exciton-polariton systems. This is the guiding line followed throughout this thesis work: each experiment presented here is related to the measurement and control of exciton-polariton elementary excitations.

The **second chapter** is dedicated to the description of the semiconductor microcavity. After the presentations of the cavity photons and the quantum well excitons, we will show how exciton-polaritons arise from the strong light-matter coupling. We will then focus on the all-optical excitation and detection of the system, in our case in a continuous and quasi-resonant regime, and how this influence the behavior of the quantum fluid.

In the **third chapter**, we will detail the high-resolution coherent pump-probe spectroscopy method that we have implemented in order to measure the spectrum of elementary excitations of the exciton-polariton fluid. Its use will allow us to demonstrate how the dynamics of an out-of-equilibrium quantum fluid deviates from its in-equilibrium counterpart, through the study of the close relationship between the properties of elementary excitations and the driving field parameters. In doing so, we will reveal the sonic, gapped and instability modes of superfluid, forced and turbulent regimes respectively.

Operating in an optical parametric oscillation regime, implying the scattering of two pump polaritons into an idler and a signal one via the strong nonlinearity of quantum wells, we will present in the **fourth chapter** the measurement of another type of elementary excitation, the Goldstone mode, resulting from the spontaneous breaking of the U(1) phase symmetry of the system. The high resolution achieved with our spectroscopy setup will allow us to highlight the charecteristic spectral narrowing, expected for such a mode in the long wavelength limit, and its diffusive character, specific to out-of-equilibrium systems. Finally, we will prove that the Goldstone mode indeed originates from a spontaneous symmetry breaking by explicitly destroying it via the pinning of the polariton phase with the injection of an additional laser.

The **fifth chapter** concerns the implementation of a new technique to reshape the driving field intensity profile, in order to promote the development of modulational instability elementary excitations. In the excitation scheme that we will present in a first step, the polariton fluid exhibits a low density channel between two high density domain walls, embedding a pair of dark solitons. Then, we will show in a second step that the respective control of the densities inside and outside the channel provides a control knob on the transverse instability modes, called snake instabilities, leading to the decay of solitons into streets of vortex-antivortex pairs with different patterns. Moreover, the confining potential induced by the channel walls freezes the motion of the vortices, allowing their direct observation with low temporal resolution devices.

In the **sixth chapter**, we will focus on another type of dependence of the exciton-polaritons on the driving field by studying a first-order phase transition whose existence depends on the

dimensionality of the fluid. This study will lead us to deviate from the mean field description of polaritons, in order to include quantum fluctuations in the dynamics of our system. These have a strength that depends on the shape of the driving field profile. Therefore, we will show that they lead to a first-order dissipative phase transition between the exciton-polariton density and the driving field strength, which arises only when the fluid density profile is bidimensional.

Chapter 2

Exciton-polaritons quantum fluids

Light-matter interactions occurs when a set of material oscillators are in near resonance with an electromagnetic field. In such situation, which is usually achieved placing the material system in an optical resonator, light couples with matter and if the strength of this coupling exceeds the individual losses of photons and matter excitations, then the system enter in the so-called regime of strong light-matter coupling. As a textbook definition, polaritons are the quasi-particle originating from such a strong coupling. They result from the splitting of the energy levels of the material oscillator and the photon, giving rise to two new hybrid eigenstates: the upper (UP) and lower polaritons (LP), inheriting both light and matter properties.

Polaritons are the particles of a quantum fluid of light. Their study thus relies on the possibility of implementing a strong coupling regime. In this manuscript, this is achieved in a planar semiconductor microcavity by confining two-dimensional quantum wells at the antinodes of the electromagnetic field of a high quality factor optical cavity, in order to enhance the light-matter exchange rate. In such a device, polaritons result from the coherent superposition of cavity photons with quantum well excitons.

In this chapter we will first study independently the design of these two components. We will focus on the dynamics of excitons confined in a two-dimensional semiconductor quantum well and of photons in a planar optical cavity. Then, we will describe the strong coupling of these components giving rise to exciton-polaritons. In the second part, we will present the collective dynamics of exciton-polaritons. In particular, we will see how the driven-dissipative nature of the system modifies the properties of the microcavity quantum fluid with respect to those in equilibrium.

2.1 Quantum well excitons

2.1.1 Excitons in a bulk semiconductor

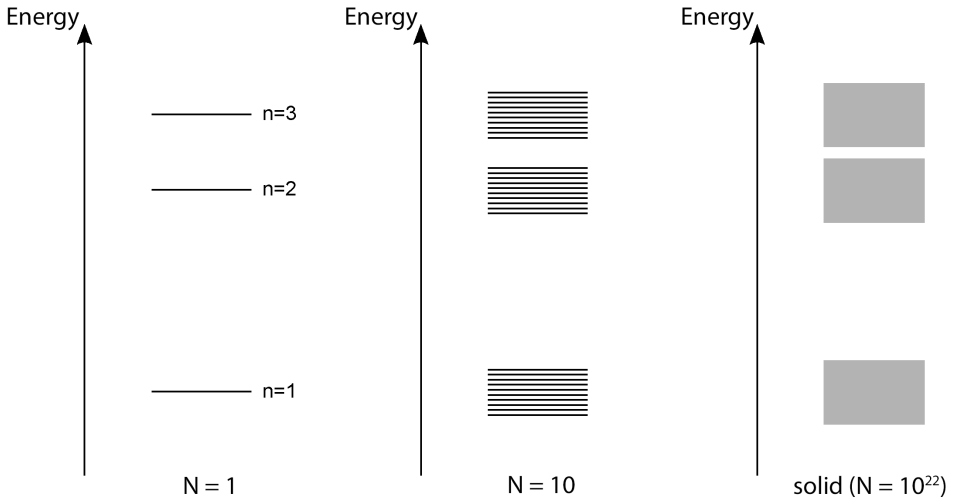

Figure 2.1: **Emergence of band structure in solid state physics.** Energy levels of a chain of N atoms. For the single atom N=1, the system has a number n of atomic orbitals, of discrete energy levels according to the Bohr model. For N=10 atoms, the system has $10n$ orbitals at different energy levels centered around the orbitals of the single atom. For N=10^{22} atoms, the typical population of a solid, the density of orbitals around each level of the single atom becomes so large that a structure of n bands associated with a finite energy continuum appears. Adapted from [108].

In the Bohr model of the atom, the electron of an isolated single atom occupies discrete energy levels associated to different atomic orbitals. In this regard, its behavior differs from that of the free electron, evolving in a continuum of energies. In the framework of solid-state physics, the description of electrons dynamics along a matrix of bound atoms lies in between these two extreme situations.

Band structure. First, if we consider two atoms placed in the vicinity of each other, at a distance of the order of their Bohr radius a_0, an overlap of their wave function occurs: the electrons are no longer localized on a single atom. The resulting coupling induces an energy splitting of the atomic orbitals of the same level. Thus, the two-atom system features two new discrete states, of non-degenerate energies different from that of the single atom. For a solid, with a large number N $\simeq 10^{22}$ of atoms packed in a crystalline matrix, the electrons are delocalized on a macroscopic scale all along the atomic chains: they start acting like free particles. Similarly to the two-atom system, the atomic orbitals split on N new different levels spaced from each other by a very small energy, of the order of 10^{-22} eV. Consequently, their state density becomes so large that they can be considered as a continuum along a finite energy band, described via the so-called *band theory* of solid-state physics [13, 89].

Since a solid encloses a very large number of electrons in a small volume, the Fermi exclusion principle applies and the electrons follow the Fermi-Dirac statistical distribution:

$$f(E) = \frac{1}{1 + e^{(E-E_F)/k_B T}}, \tag{2.1}$$

where k_B is the Boltzmann constant and temperature T. The law $f(E)$ gives the probability to find an electron at the energy E, equal to $1/2$ at the Fermi energy E_F.

Bulk semiconductors. A large part of the conductive properties of a solid can be inferred from the value of E_F, as it governs the distribution of electrons that are in the bands just below and above its level, called the valence and conduction bands respectively. For a conductive material, E_F lies in the conduction band, which is therefore partially filled with electrons able to move freely under application of an external electric field. On the contrary, for an insulator, E_F lies in a gap, below the conduction band and above the valence band, which are, as a result, completely empty and filled respectively: under application of an external electric field, there is no possibility to set the electrons in motion.

The semiconductor material exhibits an intermediate behavior. The gap between its conduction and valence bands is small enough that at sufficiently high temperature the number of electrons in the conduction band is no longer negligible, accordingly to the Fermi-Dirac distribution, and it behaves as a conductor; while at low-temperature it behaves again as an insulator.

Direct gap semiconductor. The dynamics of electrons in the conduction and valence bands are studied using the Bloch model [13]. By considering the translational invariance and the periodicity inherent to the solid, the eigenmodes of the system are expressed as a product of plane waves of wavevector $\mathbf{k}$ and of the same periodicity as the crystal potential. Within the bands, they behave as free particles, with effective masses $m^*_{c,v}$ and energies:

$$E_c(\mathbf{k}) = E_G + \frac{\hbar^2 \mathbf{k}^2}{2m^*_c}, \tag{2.2}$$

$$E_v(\mathbf{k}) = -\frac{\hbar^2 \mathbf{k}^2}{2m^*_v}, \tag{2.3}$$

for the electron of the conduction (c) and valence (v) bands respectively. E_G denotes the gap energy between the valence and conduction bands. These dispersion relations have the typical parabolic shape of single particles, as shown in Fig. 2.2. Here, we have considered a direct gap semiconductor: the extrema of the valence and conduction bands are at the same $\mathbf{k}$. This feature has the advantage of increasing the probability of radiative excitation and relaxation of electrons, occurring without change of momentum and therefore compatible with photon exchanges typically near zero momentum compared to the spatial frequencies involved in solids when working with optical wavelength.

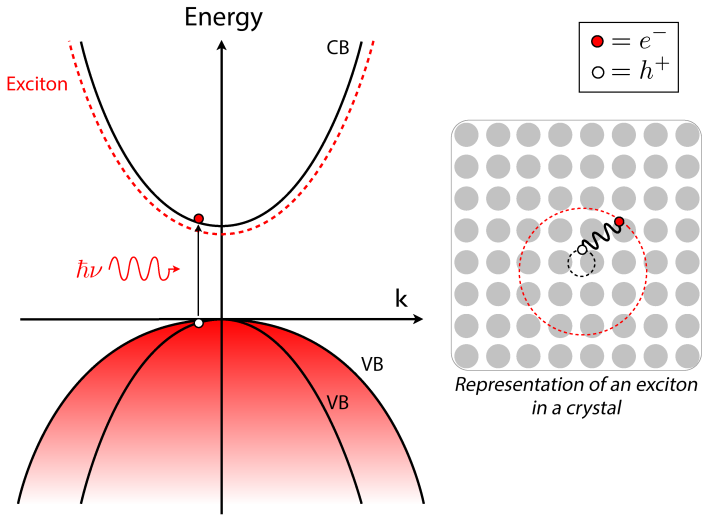

Figure 2.2: **Dispersion relations of a direct gap semiconductor.** The inverted lower parabola in red corresponds to the valence band (VB) filled with electrons, while the upper parabola corresponds to the empty conduction band (CB). Since their extrema are aligned at the same wave vector, the VB and CB are associated to a direct-gap semiconductor, allowing the absorption of a photon of almost zero wavevector at the optical frequency ν associated with the gap energy $h\nu$. This results in the promotion of an electron from VB to CB, with an energy plotted in dashed red, slightly lower than the energy of CB due to its interaction with the hole left free in VB. The bound electron-hole pair forms an exciton state, depicted on the right-hand side, over the crystal structure, with a red-dashed Bohr radius larger than the the black-dashed lattice cell radius. Adapted from [108].

Excitons. For such materials, an electron can be transferred from the valence to the conduction band via an optical or an electrical excitation. In doing so, it leaves a vacant site in the valence band, called a *hole* of positive effective charge $+e$, inducing an attraction potential due to Coulombian interactions. The Hamiltonian of the composite electron-hole system reads:

$$\mathcal{H} = E_G + \frac{p_e^2}{2m_e^*} + \frac{p_h^2}{2m_h^*} - \frac{e^2}{\epsilon|r_e - r_h|}, \tag{2.4}$$

where $p_{e,h}^2$ and $r_{e,h}^2$ are respectively the momentum and position operators of the electron (e) and hole (h), $m_{e,h}^*$ the effective masses, -e the charge of the electron, E_G the gap energy and ϵ the static dielectric permittivity of the semiconductor medium, responsible for the screening of the electron-hole attraction by the lower-band electrons.

The associated Schrödinger equation is solved by dissociating the free motion of the center-of-mass of coordinate $R = (m_e^* r_e - m_h^* r_h)/M$ and mass $M = m_e^* + m_h^*$, from the relative motion of the electron and the hole. The solution of this problem is well known: the eigenstates are hydrogen-like bound electron-holes quasiparticles, called *excitons*, of energy:

$$E_X(\mathbf{k}_X) = \frac{\hbar^2 \mathbf{k}_X^2}{2M} - \frac{R_X}{n^2} + E_G. \tag{2.5}$$

The first term is the kinetic energy of the center-of-mass of the electron-hole pair, behaving like a free particle of wavevector $\mathbf{k}_X$. The second term corresponds to the exciton binding energy, involving $R_X = \hbar^2/2\mu a_X^2$, the Rydberg constant for excitons, with $\mu = m_e^* m_h^*/M$ the electron-hole reduced mass, $a_X = \hbar^2\kappa^2/\mu e^2$ the exciton Bohr radius and n the conduction band principal quantum number. R_X is directly related to the Rydberg constant R_y of the hydrogen atom via $R_X = R_y \times \mu/m_0\epsilon_r^2$, where m_0 is the mass of the free electron in vacuum and $\epsilon_r = \epsilon/\epsilon_0$ the relative dielectric permittivity. The last term, E_G, is the gap energy.

GaAs band structure. Beyond the Bloch model, the GaAs material we use in our experiments has a band structure shown in Fig. 2.3(b), whose distribution of the different energy levels is explained by looking at the origin of the electrons involved in the formation of the covalent bonds between Gallium and Arsenic [178]. Both Ga $3d^{10}4s^24p^1$ and As $3d^{10}4s^24p^3$ exhibit incomplete outer shells on a p-type orbital (l=1), resulting in a GaAs hybrid covalent bonds of sp^3-type for the valence band, with a dominant p character, and in a s-type covalent bonds for the conduction band as the electrons originate only from s-orbitals. In the valence band, the spin-orbit interaction generates a degeneracy lifting between the states with total angular momentum $J = 1/2$ and $J = 3/2$. The former, called the split-off band, has a lower energy than the latter, which is divided into two sub-bands of total angular momentum projection $J_z = \pm\, 3/2$ and $J_z = \pm\, 1/2$ on the growth axis, with the same energy at $k = 0$ but with different dispersion relations corresponding to different effective masses. The heavier band, $J_z = \pm\, 3/2$,

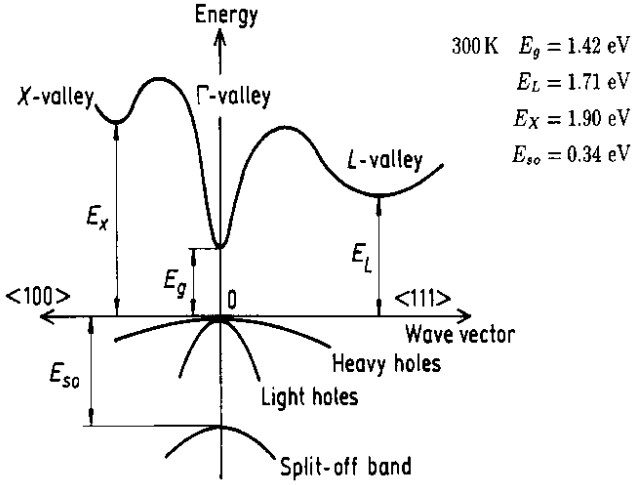

Figure 2.3: **Band structure of GaAs in the first Brillouin zone.** The valence band includes three p subbands, two of which are energy degenerate at k=0, corresponding to heavy and light holes. The conduction band of s-type includes only one subband. The parabolic approximation seen in Fig. 2.2 only holds at low-k. Adapted from [2]

is associated with heavy holes, while the lighter band $J_z = \pm\, 1/2$ is associated with light holes. The s-type conduction band has a total angular momentum $J = 1/2$, $J_z = \pm\, 1/2$.

Optical excitation. The electron-photon coupling is described in the electric dipole approximation with the Hamiltonian:

$$\mathcal{H}_{dip} = -e\frac{\mathbf{p_e} \cdot \mathbf{A}}{m_e^*}, \tag{2.6}$$

with $\mathbf{p_e}$ the momentum operator of the electron of charge -e and $\mathbf{A}$ the potential vector of the electromagnetic field. Such a coupling operates according to selection rules involving:

- the conservation of the total momentum: one exciton of wavevector $\mathbf{K}$ couples only with one photon of same wavevector $\mathbf{k} = \mathbf{K}$.
- the conservation of the total angular momentum.

The latter restricts the number of optically active excitons. From the rules of composition of the angular momentum applied to the electron-hole pair system, the excitons have a total angular momentum calculated to be J = 0,1,2. Thus, from the semiconductor ground-state J=0, only the J=1 states are addressed by a circularly polarized wave of angular momentum J=1 (the direction of propagation of the plane wave coinciding with the quantization axis of J since $\mathbf{k}$=$\mathbf{K}$). These states correspond to "bright" excitons, which are in a σ^+ or in a σ^- spin state depending on the projection of J along the quantization axis, whereas the other states, such as the J=2 heavy hole and the J=0 light hole, correspond to "dark" excitons.

From (Eq.) 2.5, we now calculate the energy that a photon must have in order to generate

an exciton from the heavy band. Due to the GaAs high relative permittivity $\epsilon/\epsilon_0 = 12.4$ and the low effective masses of the electron and hole compared to the mass of the free electron in vacuum, the binding energy of the electron-hole pair is several orders of magnitude below that of hydrogen $E_b = 4.96$ meV $\simeq 3.6{\times}10^{-4} R_y$. The exciton is therefore a weakly bound state. Importantly, by considering the value of the thermal energy at room temperature of the order of $k_B T = 25$ meV, it can thus only be observed at cryogenic temperatures, below a few tens of kelvin in our experiments. In addition, its Bohr radius $a_X = 11.6$ nm $\simeq 100$Å is larger than that of the hydrogen atom and larger than the GaAs crystalline lattice cell size $a_0 = 5.65$Å: it is delocalised over the semiconductor structure. In the literature, such a weakly bound exciton is generally referred to as a Mott-Wannier exciton, as opposed to the Frenkel exciton, which is a localised state due to the much smaller dielectric constant of the material [13]. In the end, by considering a gap energy $E_G = 1.519$ eV, the photons energy has to be equal to 1.514 eV (818 nm) in order to be at resonance with the GaAs excitons.

Bulk GaAs parameters						
Material	E_G (eV)	m_c^*/m_0	m_{hh}^*/m_0	ϵ/ϵ_0	E_b (meV)	a_X (nm)
GaAs	1.519	0.063	0.51	12.4	4.96	11.6

2.1.2 Bidimensional confinement in a quantum well

We now consider a planar layer of GaAs, of width comparable to the Bohr radius of the exciton a_X. It is doped with InAs, another direct gap semiconductor material. As a result, its gap energy E_G is lowered, proportionally to the p-fraction in the final $\mathrm{In}_p\mathrm{Ga}_{1-p}\mathrm{As}$ semiconductor. Then, it is sandwiched between two planar GaAs layers, of same gap energy as the bulk material. According to Eq. (2.5), the decrease of E_G in $\mathrm{In}_p\mathrm{Ga}_{1-p}\mathrm{As}$ leads to a reduction of the energy of excitons with respect to the pure GaAs: the semiconductor heterostructure behaves as a quantum well (QW), confining electrons and holes to the plane of the lowest energy semiconductor material, as depicted in Fig. 2.4(a), which illustrates the distribution of the valence and conduction bands maxima and minima across the three superimposed layers along the z-growth axis.

Confined excitons. The energy of the excitons in the trap induced by the gap difference is derived from the Hamiltonian:

$$\mathcal{H} = E_G^{QW} + \frac{p_e^2}{2m_e^*} + \frac{p_h^2}{2m_h^*} - \frac{e^2}{\epsilon|r_e - r_h|} + V_e(z_e) + V_h(z_h), \tag{2.7}$$

with V_e and V_h the QW potential barriers felt by the electrons and the holes respectively and E_G^{QW} the gap energy in the $\mathrm{In}p\mathrm{Ga}_{1-p}\mathrm{As}$. Assuming the geometry shown in Fig. 2.4(a), the electrons and holes are free to move in the QW plane (x, y), while they are confined in the transverse direction z. Accordingly, their wave function, eigenstates of the Hamiltonian, can be simplified as follows:

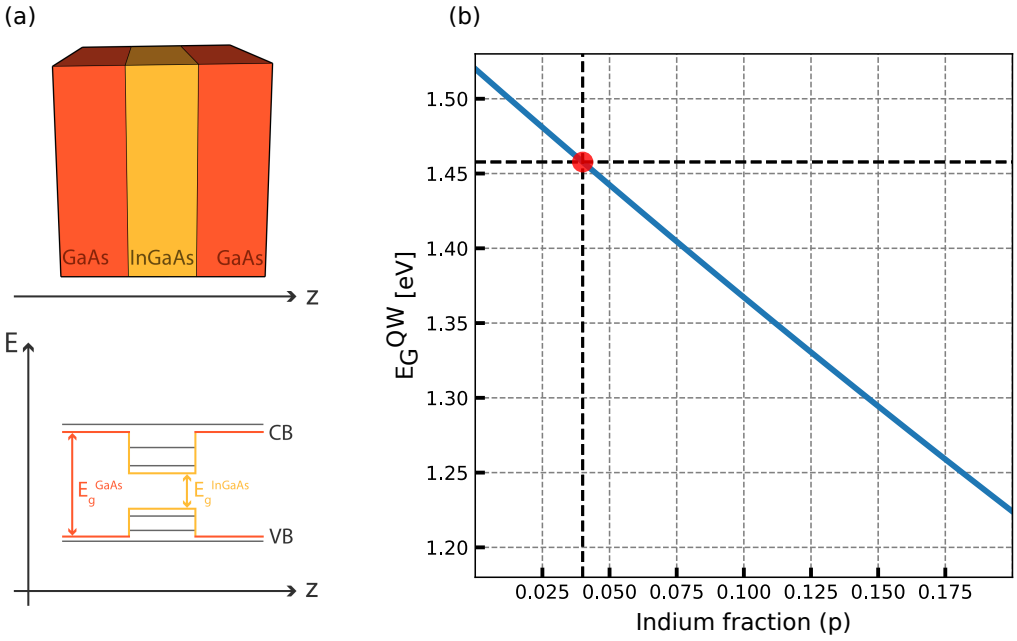

Figure 2.4: **Quantum well in InGaAs/GaAs. (a)** Upper line: spatial structure of the semiconductor heterostructure. An In_pGa_{1-p} layer is placed between two GaAs layers. Lower line: corresponding energy structure of the valence (VB) and conduction (CB) bands. The doping with a low In fraction p lowers the gap energy E_G^{InGaAs} of In_pGa_{1-p} with respect to the gap energy E_G^{GaAs} of GaAs. As a consequence, the energy profile of the heterostructure along the growth z-axis exhibits a dip (a bump) for the VB (CB), forming a localized quantum well in the In_pGa_{1-p} layer. The energy of the excitons confined therein is discretized along the gray lines. **(b)** Tuning of the In_pGa_{1-p} gap energy E_G^{QW} as a function of the fraction of injected Indium p, calculated from [129] at T=4K. For the material of our experiments, $p = 0.04$, highlighted by the red dot. Adapted from [108].

$$\Psi(x, y, z) = \psi(x, y)\phi(z), \tag{2.8}$$

allowing to solve separately the Schrödinger equation for $\psi(x, y)$ and $\phi(z)$. The eigenvalues for the confinement wave function $\phi(z)$ are easily inferred from the textbook model of the quantum box, leading to a quantization of the energies of electrons and holes:

$$E_n^{e,h} = \frac{\hbar^2 \pi^1}{2m_{e,h}^* L^2}, \tag{2.9}$$

which are inversely proportional to the effective mass $m_{e,h}^*$ and the box width L. This results in a splitting of each of the sub-bands of the valence band. As a consequence, light and heavy-holes at $\mathbf{k}$=0 are no longer degenerate. Then, we will consider in the following only the lowest

energy excitations of the quantum wells, i.e. the excitons generated from the heavy-holes, and we will exclude from our analysis those generated from the light-holes, as they will not be optically addressed.

The planar wave function $\psi(x, y)$ is again expressed with the standard hydrogen model and involves the definition of a new Rydberg constant R_X^{QW} for the QW. From these considerations, the dispersion relation of the exciton reads:

$$E_X(\mathbf{k}_{||}) = E_G^{QW} + E_n^e + E_n^h + \frac{\hbar^2 \mathbf{k}_{||}^2}{2M} - \frac{R_X^{QW}}{n^2}. \tag{2.10}$$

The design of our $In_{0.04}Ga_{0.96}As$ system is such that the $n = 1$ state, called the two-dimensional $1s$ exciton in reference to the hydrogen atom, is significantly lower in energy than the higher order states $n > 1$. This will be the only excited state in our experiments and so every mention to excitons in what follows refers to it.

As an interesting difference from the bulk semiconductor to be noted, the Bohr radius of the QW exciton is twice as smaller than the GaAs exciton in the bulk $a_X^{QW} = a_X/2$, and therefore the binding energy derived from the Rydberg constant is four times larger $E_b^{QW} = 4E_b$. This results from the enhanced overlap between the electron and hole wave functions induced by the confinement potential of the heterostructure.

Optical selection rules. Most importantly, by breaking the translational invariance along the z-direction, the confinement changes the coupling properties of excitons with light. Now, the conservation of momentum law only applies to the (x, y) plane of the semiconductor structure, as the momentum in the z direction is fixed by the QW spacing. Correspondingly, The relaxation/excitation of an exciton of wavevector $\mathbf{k}_X = (\mathbf{k}_X^{||}, k_X^z)$ conserves the in-plane wavevector $\mathbf{k}_\gamma^{||}$ of the emitted/absorbed photon. This means that the selection rules no longer operate on the component k_γ^z of the electromagnetic field, which can thus take any value: in contrast to the bulk semiconductor in which one exciton mode is only coupled to one photon mode, the geometry of the quantum well allows one exciton mode to be coupled to a continuum of photon modes.

The law of conservation of energy must still be fulfilled

$$E_X^{2D} + \frac{(\hbar \mathbf{k}_X^{||})^2}{2M} = \frac{\hbar c}{n_{QW}} \sqrt{(\mathbf{k}_\gamma^{||})^2 + (\mathbf{k}_\gamma^z)^2}. \tag{2.11}$$

Here, on the left-hand side of the equality, the kinetic energy of excitons in the plane of the QW is dissociated from the energy in the z direction governed by Eq. (2.9). On the right-hand side, n_{QW} denotes the refractive index felt by the photons in the QW medium. Under the condition of momentum-conservation, it follows that

$$\left|\mathbf{k}_X^{||}\right| \leqslant \frac{n_{QW} E_X^{2D}}{\hbar c}. \tag{2.12}$$

Consequently, the reservoir of photon modes to which excitons couple is not infinite: only excitons with wavevectors verifying the above condition exchange photons with the electromagnetic field. For higher $\mathbf{k}_X^{||}$, they are no longer radiative. From the resonance energy value of $E_X^{2D} \simeq 1.485$ meV in our system, the radiative mode range is about $\mathbf{k}_X^{||} \leqslant 30\ \mu\text{m}^{-1}$. Accordingly, the coupling occurs on large length scales with respect to the exciton Bohr radius, i.e. $2\pi/\mathbf{k}_X^{||} \gg a_X^{QW}$.

In addition, the conservation of angular momentum remains valid. The QW sets the quantization axis of J along the growth axis z, collinear with the photon propagation at $\mathbf{k}_\gamma^{||} = 0$. For large wavevectors, the circularly polarized field no longer excites pure spin states, but a mixture of σ^+ and σ^- states [38].

Bosonic nature of excitons. Since electrons and holes are fermions, the exciton has an integer pseudo-spin. Its ground state creation and annihilation ($\hat{b}^\dagger$,$\hat{b}$) operators verify the bosonic commutation relation [47, 67]

$$\left\langle \left[\hat{b}, \hat{b}^\dagger\right] \right\rangle \simeq 1. \tag{2.13}$$

The assimilation of excitons to composite bosons is maintained only if the Coulombian attraction binding the electron to its hole is dominant over the electron-electron and hole-hole repulsive interactions. Such a condition can be reasonably satisfied when the spacing between excitons is much larger than their Bohr radius a_X^{QW}. By estimating that the number of exciton states follows the same scale as a_X^{QW}, one must verify $n_X(a_X^{QW})^2 \ll 1$, with n_X the exciton density per unit area. For a_X^{QW} of the order of 6 nm in the QW InGaAs systems, the maximum density is equal to 4×10^4 paticles per μm^2, well above the densities at stake in our experiments. We can therefore safely assume that the excitons studied here are indeed bosons.

Exciton-exciton nonlinear interactions. So far we have omitted in the motion of excitons the interactions between their holes and electrons. We need now take them into consideration, as they are at the heart of the dynamics of our quantum fluid. In addition to the Hamiltonian corresponding to the free motion of the QW exciton, expressed from Eq. (2.7) into the exciton basis, of creation and annihilation operators ($\hat{b}_\mathbf{k}^\dagger$, $\hat{b}_\mathbf{k}$) [141, 37]

$$\mathcal{H}_X = \sum_\mathbf{k} \frac{d^2\mathbf{k}}{(2\pi)^2} E_X(\mathbf{k}) \hat{b}_\mathbf{k}^\dagger \hat{b}_\mathbf{k}, \tag{2.14}$$

with $E_X(\mathbf{k})$ the QW exciton dispersion relation for the in-plane wavevector $\mathbf{k}$ given by Eq. (2.10), we introduce a second Hamiltonian of interaction

$$\mathcal{H}_{XX} = \sum_{\mathbf{k},\mathbf{k}',\mathbf{q}} M_{X,X}(\mathbf{k},\mathbf{k}',\mathbf{q}) \hat{b}^\dagger_{\mathbf{k}+\mathbf{q}} \hat{b}^\dagger_{\mathbf{k}'-\mathbf{q}} \hat{b}_{\mathbf{k}} \hat{b}_{\mathbf{k}'}. \tag{2.15}$$

$M_{XX}(\mathbf{k},\mathbf{k}',\mathbf{q})$ is the element of the exciton-exciton interaction matrix [141], composed of the energies of exchange and Coulomb interactions between electrons and holes. In our QW system, direct Coulomb interactions are dominant at scales smaller than the Bohr radius of excitons, while exchange interactions are dominant at larger scale. Therefore, by considering only radiative modes, i.e. dynamics occuring on scales much larger than the Bohr radius of excitons $\mathbf{k}a_X \ll 1$, Coulomb interactions can be neglected. It allows us to express $\mathcal{H}_{XX}$ as a simple two-body contact interaction term, weighted by an energy potential derived from only the exchange potential of excitons and labelled $V_{XX}(\mathbf{k})$ in the reciprocal space

$$\mathcal{H}_{XX} = \frac{1}{2} \sum_{\mathbf{k},\mathbf{k}',\mathbf{q}} V_{XX}(\mathbf{q}) \hat{b}^\dagger_{\mathbf{k}+\mathbf{q}} \hat{b}^\dagger_{\mathbf{k}'-\mathbf{q}} \hat{b}_{\mathbf{k}} \hat{b}_{\mathbf{k}'}. \tag{2.16}$$

Here, we don't account for the spin degree of freedom J_z for the sake of simplification; its contribution is important as it modifies the strength of interactions: between parallel spin excitons, the interactions are the strongest and repulsive ($V_{XX} > 0$), whereas between opposite spins interactions are weaker and attractive ($V_{XX} < 0$) [170]. For the first case, one calculates [141, 163]

$$V_{XX} = \frac{e^2 a_X^{QW}}{\epsilon A}, \tag{2.17}$$

with A the quantification area equal to the quantum well surface. This expression remains valid in the limit of low wavevectors (verified for radiative modes), where the energy of excitons varies only slightly with $\mathbf{k}$ (in contrast to the energy of photons that excite them) and therefore where V_{XX} can be assumed constant. The numerical calculation gives $A \times V_{XX} \simeq 3$ μeV$\cdot\mu$m^2 for our InGaAs system.

Exciton lifetime. Exciton linewidth broadening is pricipally determined by:

- The coupling of excitons to phonons, which becomes weaker the lower the temperature is. In the material of our system, the decay rate of excitons into phonons is of the order of 1.5 μeV (440 ps) at $T = 10$K.
- The exciton-exciton coupling. The broadening due to the collisions between excitons increases with the density of excitons in the system. For a typical density of a few tens of excitons per μm^2, it induces a decay rate of about 80 μeV (8 ps).

2.2 Photons in planar microcavity

Let us come back to our initial objective: to couple light with matter. Now that the type and the geometry of the matter medium are well defined, i.e. a set of quantum wells source planar excitons, we have to find a tool operating the coupling of photons with excitons. As a historical and paradigmatic example of the implementation of such a light-matter coupling, one can consider atoms trapped in optical cavity, exhibiting an enhancement of their exchange with photons thanks to the modification of their spontaneous emission rate. As for a laser, the optical cavity performs both the key roles of selecting and strengthening the photon oscillations across the atoms. This is the device that has also been chosen to couple the excitons with light. Its particular structure and geometry that we will discuss in this section, reduces to one mode the reservoir of photons compatible with the exciton modes, resulting in a enhancement of the light-matter coupling.

Fabry-Perot microcavity. More specifically, the standard cavity used for exciton-polariton systems is a Fabry-Perot interferometer, made of two flat mirrors parallel to each other. Its optical length selects the wavelengths of the electromagnetic field that can interfere constructively within it. As with any type of resonator, the decay rate of the field oscillation is characterized by a quality factor Q, defined as

$$Q = \frac{\omega_\gamma}{\delta\omega_\gamma}, \tag{2.18}$$

with ω_γ the cavity resonance frequency and $\delta\omega_\gamma$ its linewidth, taken equal to the full width at half mamixmum (FWHM) of the cavity transmission peak at ω_γ and fixed by the lifetime of photons in the cavity $\tau_\gamma = 1/\delta\omega_\gamma$, which is typically determined by the transmission, reflection and absorption coefficients of the two mirrors. Another relevant parameter to consider is the spectral resolution of the cavity, i.e. its ability to separate two adjacent resonance peaks. It is derived from the from cavity finenesse $\mathcal{F}$, related two the free spectral range (FSR) $\Delta\omega_\gamma$

$$\mathcal{F} = \frac{\Delta\omega_\gamma}{\delta\omega_\gamma} = \pi\frac{\sqrt{R}}{1-R}, \tag{2.19}$$

where $R = \sqrt{R_1 R_2}$ is the total reflectivity of the cavity, whose two mirrors have a reflectivity R_1 and R_2 respectively.

To design our coupling system, we first need to match the resonance of the cavity with that of the quantum wells. Consequently, the optical distance between the two mirrors must be proportionnal to a half-integer number $m/2$ of the exciton resonance wavelength $L_{\text{cav}} = m\lambda_0/2n_{\text{cav}}$, with λ_0 the wavelength of the electromagnetic field in vacuum and n_{cav} the refractive index of the cavity medium. Then, we want the system to undergo as much as possible photon/exciton exchange cycles: the photons must be kept inside the cavity on time scales typically of the same order of magnitude as the exciton lifetime. Therefore, the linewidth $\delta\omega_\gamma$ of the Fabry-Perot

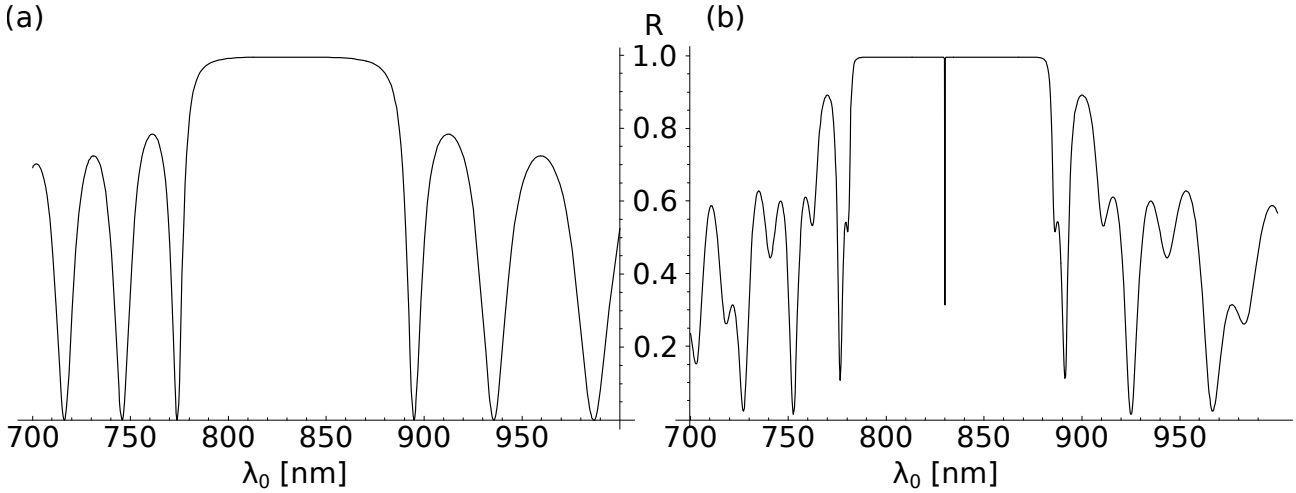

Figure 2.5: **DBR and Fabry-Perot cavity reflectivity. (a)** Reflectivity R of a Bragg mirror of 20 pairs of $Ga_{0.9}Al_{0.1}As$/AlAs, illuminated at normal incidence for different wavelengths λ. The DBR has a reflectivity close to 1 over a large range of wavelengths called the stop-band, which is designed to be centered on $\lambda_0 = 836$ nm by tuning the thickness of each of the mirror layers. **(b)** Corresponding reflectivity of the optical cavity built from the facing of two DBRs mirrors identical to that in (a) and separated by a distance $L_{\text{cav}} = 2\lambda_0/n_{\text{cav}}$, leading to the appearance of a very narrow resonance at λ_0. Adapted from [83].

cavity has to be as narrow as possible, limiting our choice to cavities of large Q, corresponding to mirrors with a very high reflectivity.

Distributed Bragg Reflectors. Cavities built with Distributed Bragg Reflectors (DBR) are typically adequate to meet this last criterion. Their mirrors are made of an alternating stack of N layers of two materials of different refractive indices $n_1 < n_2$, which induce a partial reflection of the electromagnetic field at each of the N interfaces. It leads to a very high total reflection coefficient R, given by the following expression [146]

$$R = \left[\frac{(n_2/n_1)^{2N} - n_f/n_0}{(n_2/n_1)^{2N} + n_f/n_0}\right]^2, \tag{2.20}$$

with n_0 and n_f the refactive indices of the media before and after the mirrors. Fig. 2.5(a) shows the evolution of R with respect to the wavelength of the electromagnetic field for one DBR mirror used in our system, built with 20 pairs of $Ga_{0.9}Al_{0.1}As$/AlAs layers, with respective refractive indices $n_2 = 3.48$ and n_1=2.95. R is equal to 0.9985 over a wide range of wavelength, called the stop-band, of central wavelenght close to $\lambda_0 = 836$ nm, which has been tuned by setting the thickness of the different layers equal to $d_{1,2} = \lambda_0/4n_{1,2}$.

The Fabry-Perot cavity of our system is built by placing two of these mirrors in front of each other, spaced by $L_{cav} = 2\lambda_0/n_{\text{cav}}$, suitable for the establishment of three antinodes of the electromagnetic field at λ_0. Its resonance corresponds to the appearance of a very narrow dip

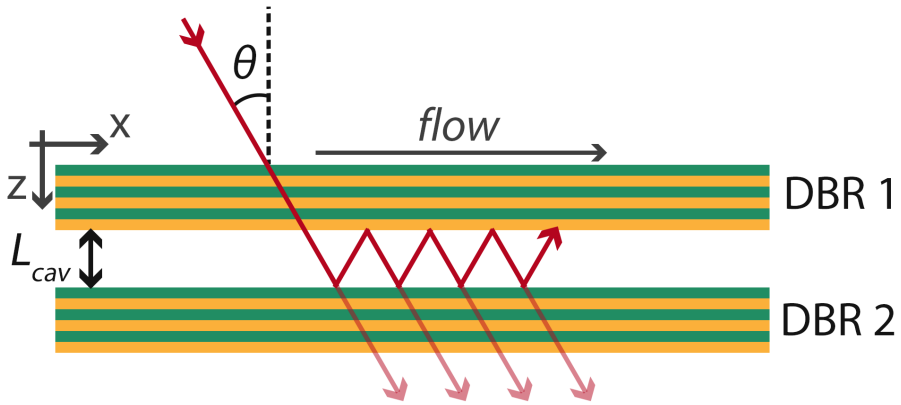

Figure 2.6: **Geometry of the optical cavity.** Depending on their incidence angle θ, photons experience a different optical cavity thickness $L_\theta = L_{\text{cav}}/\cos\theta$, corresponding to a different resonance energy. Provided that the transverse wavevector k_z fixed by the space between the two mirrors is conserved, such θ dependence leads to the parabolic dispersion relation (2.25). Adapted from [108].

in the reflectivity of the cavity as shown in Fig. 2.5(b), at λ_0, such that the wavelength in the cavity spacer medium $\lambda_{\text{cav}} = \lambda_0/n_{\text{cav}}$ matches the resonance of QW excitons.

Fabry-Perot cavity parameters					
R_1	R_2	n_1	n_2	n_{cav}	λ_0 (nm)
0.9992	0.9985	2.95	3.48	3.54	836

Photon lifetime The linewidth of the cavity can be calculated simply from the finesse $\mathcal{F}$ and the free spectral range $\Delta\omega_\gamma$:

$$\delta\omega_\gamma = \frac{\Delta\omega_\gamma}{\mathcal{F}} = \frac{c}{n_{\text{cav}} L_{eff}} \frac{1-R}{\sqrt{R}}. \tag{2.21}$$

$L_{eff} = L_{cav} + L_{\text{Bragg}}$ is the effective length of the cavity, which includes the length of penetration of the in-cavity electromagnetic field through the various layers of Bragg mirrors [146]:

$$L_{\text{Bragg}} = \frac{\lambda_0}{2} \frac{n_1 n_2}{n_{\text{cav}}(n_2 - n_1)} \tag{2.22}$$

The numerical calculation performed with the cavity parameters given in the table 2.2 leads to a finesse $\mathcal{F} = 2850$ and a linewidth of the resonance $\hbar\delta\omega_\gamma = 140$ μeV, corresponding to a photon lifetime $\tau_\gamma = 5$ ps.

Dynamics of cavity photons. In free space, the energy of photons is given by

$$E_\gamma = \frac{\hbar c}{n}\sqrt{k_x^2 + k_y^2 + k_z^2}. \tag{2.23}$$

However, between the two DBRs, the confinement plane imposes a quantification of the transverse component k_z of the photon wavevector, which must coincide with one of the resonances of the cavity. In our case, the free spectral range is large enough to consider a single cavity mode, corresponding to the one at the centre of the stop-band

$$k_z = \frac{2\pi n_{\text{cav}}}{\lambda_0}. \tag{2.24}$$

By assuming small incident angles with respect to the cavity plane, i.e. $k_x, k_y \ll k_z$, one can rewrite Eq. (2.23) with a Taylor expansion

$$E_\gamma = \frac{\hbar c}{n_{\text{cav}}}\sqrt{\mathbf{k}^2 + k_z^2} \simeq \frac{hc}{\lambda_0}\left[1 + \frac{1}{2}\left(\frac{\lambda_0 \mathbf{k}^2}{2\pi n_{\text{cav}}}\right)\right], \tag{2.25}$$

where $\mathbf{k} = \sqrt{k_x^2 + k_y^2}$ is the wavevector of photons lying in the cavity plane (x, y). This is the dispersion relation of cavity photons, exhibiting the parabolic shape of single particles, for which one can define an effective mass from the relation

$$\frac{1}{m_\gamma^*} = \frac{1}{\hbar^2}\frac{\partial^2 E_\gamma}{\partial k^2}, \tag{2.26}$$

leading to

$$m_\gamma^* = \frac{n_{\text{cav}}^2 \hbar}{\lambda_0 c}, \tag{2.27}$$

which is of the order of 10^{-4} times the mass of the exciton.

2.3 Semiconductor microcavity

We have just described in the previous sections the two components of our system: the optical cavity and the quantum well, which share the common feature of breaking the translational invariance in one direction of space, chosen here along z. The semiconductor microcavity originates from the combination of the structures, by inserting the quantum wells between the two mirrors of the optical cavity.

Exciton-photon coupling. By neglecting the losses of the two components which would lead to a broadening of the linewidth of the resonances, such a configuration reduces to one mode $\mathbf{k}_\gamma$ the photon reservoir able to excite an exciton mode $\mathbf{k}_X$. Thus, an exciton of in-plane wavevector $\mathbf{k}_X^{||} = (k_X^x, k_X^y)$ can be excited only by a photon of in-plane momentum $\mathbf{k}_\gamma^{||} = (k_\gamma^x, k_\gamma^y)$, with an incidence angle $\theta_\gamma = (\theta_\gamma^x, \theta_\gamma^y)$ that fulfills the relations

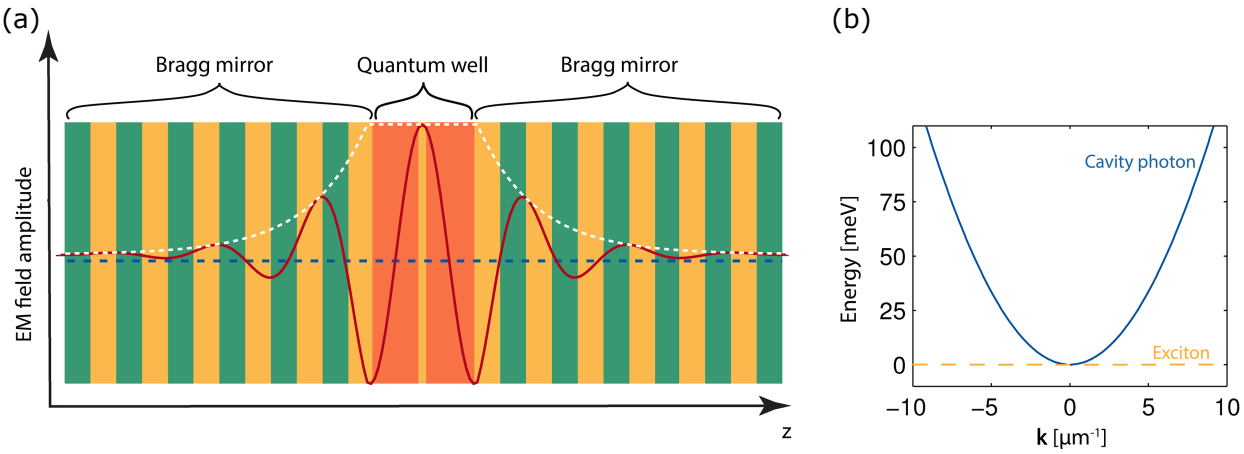

Figure 2.7: **Quantum well embedded in a Fabry-Perot cavity.** **(a)** Geometry of the semiconductor microcavity. The quantum well is inserted in the optical cavity such as the confinement planes $(x,\ y)$ are overlapped. Its location on an antinode of the electromagnetic field, indicated by the red line, enhances its coupling with the cavity photons. **(b)** Dispersion relations of photons and excitons. Since their mass is four orders of magnitude above that of photons, excitons have a near-flat dispersion relation at the wavevector scale considered here. At $\mathbf{k}$=0, the energy of excitons and photons coincide to increase their coupling. Adapted from [108].

$$k_X^x = k_{\gamma,\mathrm{cav}}^x = |\mathbf{k}_{\gamma,\mathrm{cav}}|\sin\theta_{\gamma,\mathrm{cav}}^{\mathrm{x}} = \frac{\mathrm{En}_{\mathrm{cav}}}{\hbar \mathrm{c}}\sin\theta_{\gamma,\mathrm{cav}}^{\mathrm{x}} = \frac{\mathrm{E}}{\hbar \mathrm{c}}\sin\theta_{\gamma}^{\mathrm{x}}, \tag{2.28}$$

$$k_X^y = k_{\gamma,\mathrm{cav}}^y = abs\mathbf{k}_{\gamma,\mathrm{cav}}\sin\theta_{\gamma,\mathrm{cav}}^{\mathrm{y}} = \frac{\mathrm{En}_{\mathrm{cav}}}{\hbar \mathrm{c}}\sin\theta_{\gamma,\mathrm{cav}}^{\mathrm{y}} = \frac{\mathrm{E}}{\hbar \mathrm{c}}\sin\theta_{\gamma}^{\mathrm{y}}, \tag{2.29}$$

where $\mathbf{k}_{\gamma,\mathrm{cav}}^{||} = (k_{\gamma,\mathrm{cav}}^x, k_{\gamma,\mathrm{cav}}^y)$ is the wavevector of the photon in the medium of index n_{cav} and $\theta_{\gamma,\mathrm{cav}} = (\theta_{\gamma,\mathrm{cav}}^x, \theta_{\gamma,\mathrm{cav}}^y)$ is the corresponding angle, obtained from the Snell-Descartes law. This means that the choice of the incidence angle of photons, provided that their energy is equal to $E_\gamma(\mathbf{k}_\gamma^{||})$, enables to select the wavevector of excitons created in the QWs. Reciprocally, the photons issued from the relaxation of the excitons and leaking from the optical cavity have an emission angle imposed by the conservation of the transverse momentum. The design of the system thus allows an all-optical control of the modes flowing within it.

Spontaneous emission. Another consequence of the narrowing of the reservoir of photon modes concerns the relaxation rate of an exciton from its excited state to its ground state. It can be deduced from the Fermi golden rule [66], giving the spontaneous emission of an exciton when a two-level system goes from an initial i state to a final f state

$$\Gamma_{i\to f} = \frac{2\pi}{\hbar}|\langle f|\, V\, |i\rangle|^2 \delta(E_f - E_i)\rho(E_f), \tag{2.30}$$

where $\Gamma_{i\to f}$ is the transition rate from i to f per time unit, weighted by the number of final states $\rho(E_f)$ available at the energy E_f and by the squared coupling matrix element of $|\langle f|\,V\,|i\rangle|^2$ giving the probability of this transition. $\delta(E_f - E_i)$ ensures the respect of the conservation of energy. Therefore, with our system, by selecting with the cavity a single photon mode compatible with a single exciton mode, the number of final states accessible is reduced to one and the exciton spontaneous photon emission is drastically lowered, occurring at a characteristic frequency, $|\langle f|\,V\,|i\rangle|^2$, also denoted Ω_R and called the vacuum Rabi frequency.

Coupling regimes. By taking into account the finite lifetimes of excitons and photons, different coupling regimes are defined according to the values of the loss rates γ_{cav} and γ_X with respect to the Rabi frequency Ω_R. When $\Omega_R \ll \gamma_{cav}, \gamma_X$, the oscillator strength is not sufficient to reabsorb a spontaneously emitted photon, which is then lost outside the cavity. The conversion of an exciton into a photon and vice versa is irreversible: it is the weak coupling regime. On the contrary, when $\Omega_R \gg \gamma_{cav}, \gamma_X$, the particles lifetimes are long enough to allow the reabsorption of a photon emitted by an exciton. The conversion process is reversible: it is the so-called strong coupling regime, leading to several coherent energy exchanges between photons and excitons, called Rabi oscillations.

2.3.1 Excitons polaritons

It is from such a strong coupling regime that excitons polaritons emerge. These are the eigenmodes of semiconductor microcavities, first observed in 1992 by C. Weisbuch [172].

Linear Hamiltonian. Let us write the Hamiltonian of the coupled system from the Hamiltonians of photons and excitons expressed in the basis of creation and annihilation operators, $(\hat{a}^\dagger_{\mathbf{k}}, \hat{a}_{\mathbf{k}})$ and $(\hat{b}^\dagger_{\mathbf{k}}, \hat{b}_{\mathbf{k}})$ respectively, for the in-plane wavevector $\mathbf{k}$. We consider at first a regime of weak optical excitation, which allows us to neglect the interactions between excitons as their density remains low. The Hamiltonian reads

$$\mathcal{H}_{lin} = \sum_{\mathbf{k}} \left[E_X(\mathbf{k}) \hat{b}^\dagger_{\mathbf{k}} \hat{b}_{\mathbf{k}} + E_\gamma(\mathbf{k}) \hat{a}^\dagger_{\mathbf{k}} \hat{a}_{\mathbf{k}} + \frac{\hbar\Omega_R}{2} (\hat{a}^\dagger_{\mathbf{k}} \hat{b}_{\mathbf{k}} + \hat{b}^\dagger_{\mathbf{k}} \hat{a}_{\mathbf{k}}) \right], \tag{2.31}$$

where $E_X(\mathbf{k})$ and $E_\gamma(\mathbf{k})$ are respectively the dispersion relation of excitons and photons written in Eq. (2.10) and (2.25) respectively. The last term describes the linear exciton-photon coupling, driving the emission of a photon by relaxation of an exciton $\hat{a}^\dagger_{\mathbf{k}} \hat{b}_{\mathbf{k}}$, and, vice versa, the excitation of an exciton by absorption of a photon $\hat{b}^\dagger_{\mathbf{k}} \hat{a}_{\mathbf{k}}$. From these exchanges, the system acquires an energy determined by its Rabi frequency Ω_R, equal to the exciton-photon conversion rate. This Hamiltonian is linear in the sense that only terms with same wavevectors are mixed. This is of course a first convenient approximation, we will deviate from it when accounting for the interactions between excitons.

Polariton basis. The linear hamiltonian is diagonalized into a basis of two new eigenstates, the exciton-polaritons, that we will call in the following polaritons for simplicity. It yields

$$\mathcal{H}_{lin} = \sum_{\mathbf{k}} \left[\hbar\omega_{LP}(\mathbf{k}) \hat{p}^\dagger_{\mathbf{k}} \hat{p}_{\mathbf{k}} + \hbar\omega_{UP}(\mathbf{k}) \hat{u}^\dagger_{\mathbf{k}} \hat{u}_{\mathbf{k}} \right], \tag{2.32}$$

with ($\hat{u}^\dagger$, $\hat{u}$) and ($\hat{p}^\dagger$, $\hat{p}$) the creation/annihilation operators for the upper (UP) and lower (LP) polaritons, of respective energies $\hbar\omega_{LP}$ and $\hbar\omega_{UP}$. These eigen-operators are derived from the sum of the photon $\hat{a}$ and exciton $\hat{b}$ operators, which obey the commutation rule of bosons. Consequently, polaritons are also bosons satisfying their own bosonic commutation rules: $[\hat{u}^\dagger, \hat{u}] = \delta_{\mathbf{k}'}$ and $[\hat{p}^\dagger, \hat{p}] = \delta_{\mathbf{k}'}$. ($\hat{u}$, $\hat{p}$) are given by the transformation

$$\begin{bmatrix} \hat{p}_{\mathbf{k}} \\ \hat{u}_{\mathbf{k}} \end{bmatrix} = \begin{bmatrix} C_{\mathbf{k}} & X_{\mathbf{k}} \\ X_{\mathbf{k}} & -C_{\mathbf{k}} \end{bmatrix} \begin{bmatrix} \hat{a}_{\mathbf{k}} \\ \hat{b}_{\mathbf{k}} \end{bmatrix}, \tag{2.33}$$

where $X_{\mathbf{k}}$ and $C_{\mathbf{k}}$ are the Hopfield coefficients of excitons and photons respectively [72]. Since $X^2_{\mathbf{k}} + C^2_{\mathbf{k}} = 1$ because the transformation is unitary, $X^2_{\mathbf{k}}$ and $C^2_{\mathbf{k}}$ quantify the weigth of the respective contribution of excitons and photons to the polariton states. We often refer to them as the exciton and photon fraction of polaritons, equal to

$$X^2_{\mathbf{k}} = \frac{\sqrt{\Delta E^2_{X-\gamma} + \hbar^2\Omega^2_R} + \Delta E_{X-\gamma}}{2\sqrt{\Delta E^2_{X-\gamma} + \hbar^2\Omega^2_R}}, \tag{2.34}$$

$$C^2_{\mathbf{k}} = \frac{\sqrt{\Delta E^2_{X-\gamma} + \hbar^2\Omega^2_R} - \Delta E_{X-\gamma}}{2\sqrt{\Delta E^2_{X-\gamma} + \hbar^2\Omega^2_R}}. \tag{2.35}$$

These relations depend on the detuning between the photon and exciton resonances $\Delta E_{X-\gamma}(\mathbf{k}) = E_\gamma(\mathbf{k}) - E_X(\mathbf{k})$. Therefore, the Hopfield coefficients can be tuned by modifying the resonance energy of excitons or photons. In our case, a wedge between the two mirrors of the optical cavity introduces a small gradient in the energy of photons, along one direction of the (x, y) plane, measured to be about 0.7 μeV/μm.

Dispersion relations. The analytical calculation of the eigenenergies of the upper and lower polaritons leads to the following dispersion relations

$$\hbar\omega_{UP,LP}(\mathbf{k}) = \frac{E_\gamma(\mathbf{k}) + E_X(\mathbf{k})}{2} \pm \frac{1}{2}\sqrt{(\hbar\Omega_R)^2 + \Delta E^2_{X-\gamma}}, \tag{2.36}$$

with $\omega_{UP} > \omega_{LP}$ for all $\mathbf{k}$. These are plotted for different values of the exciton-photon detuning $\Delta E_{X-\gamma}$ at $\mathbf{k} = 0$ μm^{-1} in Fig. 2.8, where one can see the exciton and photon energies splitting, signature of the strong coupling regime that results in the emergence of the UP and LP branches.

For positive detuning, $\Delta E_{X-\gamma} > \hbar\Omega_R$, the UP and LP branches almost follows the shapes of the exciton and photons branches. At $\Delta E_{X-\gamma} = 0$, the plot of the Hopfield fractions $X^2_{\mathbf{k}}$ and $C^2_{\mathbf{k}}$ shows that the polaritons at $\mathbf{k} = 0$ μm^{-1} originate from the perfect balanced mixture of

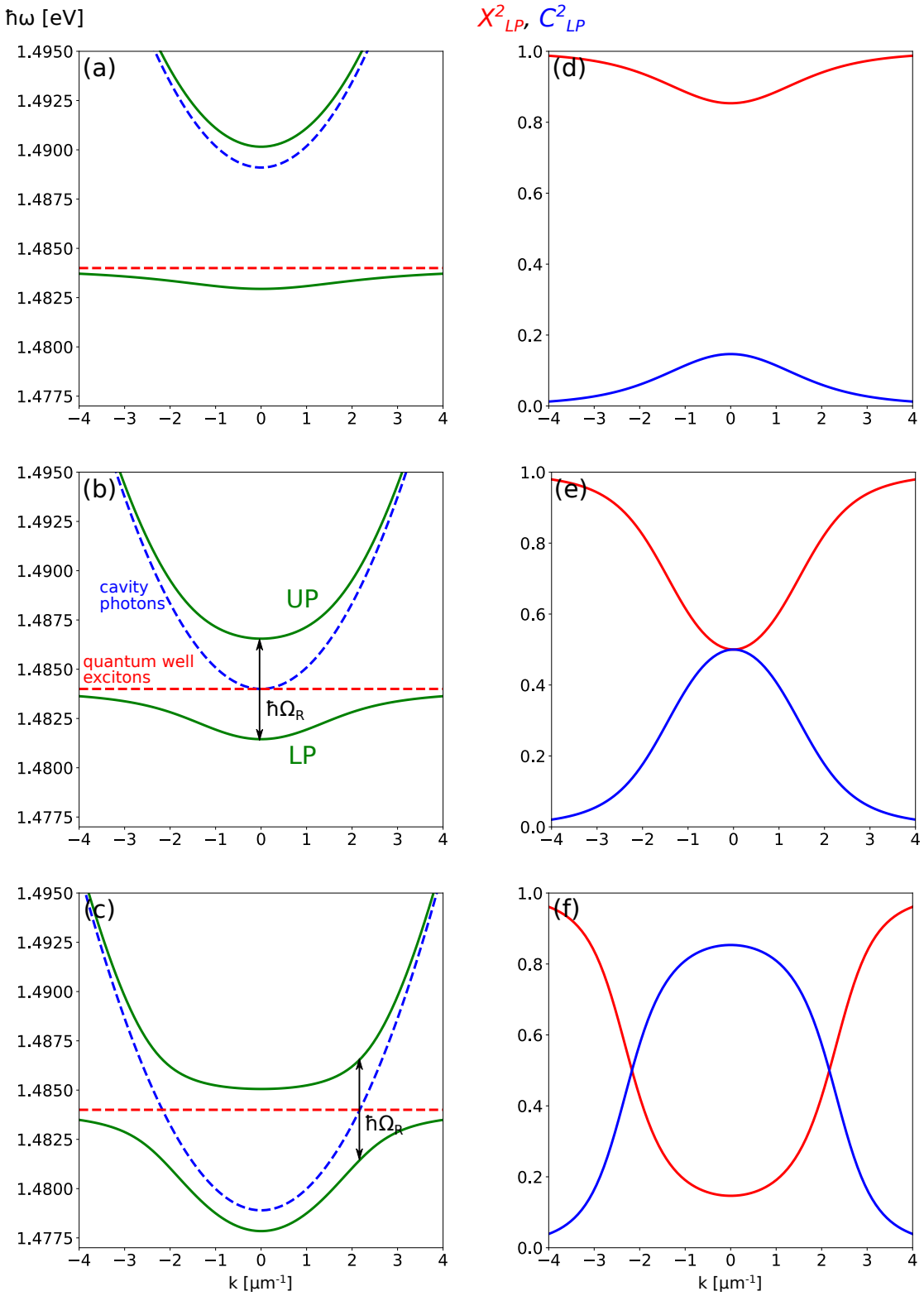

Figure 2.8: **Polariton dispersion relations and Hopfield coefficients. (a, b, c)**. Dispersion relations of the upper (UP) and lower (LP) polaritons in the strong coupling regime, calculated from (Eq.) 2.36 for different values of the exciton-photon detuning $\Delta E_{X-\gamma} = -\hbar\Omega_R, 0, \hbar\Omega_R$ at k=0. At the crossing points of the exciton and photon branches, respectively in red and blue dashed lines, the UP and LP branches are spaced by the coupling energy $\hbar\Omega_R$. **(d, e, f)** Corresponding Hopfield fractions of exciton X^2_{LP} and photons C^2_{LP}, in red and blue lines, calculated from (Eq.) 2.34 for the LP. Changing $\Delta E_{X-\gamma}$ modifies the photonic and excitonic character of polaritons.

excitons and photons. At large-k, as the detuning becomes larger, the UP and LP recovers an exciton and photon shape respectively. At negative detuning, $\Delta E_{X-\gamma} < \hbar\Omega_R$, the anticrossing is clearly visible where the exciton and photon branches cross each other. In contrast to the positive detuning case, the UP branch is now mostly made of excitons at low-k, while the LP branch is mostly made of photons.

The exciton-photon detuning range suitable for the strong coupling regime is summarised in Fig. 2.9, where the energy of the upper and lower polariton branches at $\mathbf{k}$=0 is plotted as a function of the exciton-photon detuning. The splitting at $\Delta E_{X-\gamma} = 0$ meV is fixed by the Rabi frequency Ω_R, whereas, for significantly higher $\Delta E_{X-\gamma} > \hbar\Omega_R$, its value tends to $\Delta E_{X-\gamma}$.

Effective mass. Consequence of the modification of the shape of the dispersion relations, the change in exciton-photon detuning $\Delta E_{X-\gamma}$ results into a change in the mass of polaritons m^* defined from the curvature of the parabolic regions of the dispersion curves at $\mathbf{k} = 0$ μm^{-1}. The second derivative of Eq. (2.36) leads to

$$\frac{1}{m^*} = \frac{X_0^2}{m_X^*} + \frac{C_0^2}{m_\gamma^*} \simeq \frac{C_0^2}{m_\gamma^*}, \tag{2.37}$$

in which the first term is neglected because the mass of excitons m_X^* is much larger than the mass of photons m_γ^*. To conclude, with a typical mass $m^* = C_0^2/m_\gamma^* \simeq 5 \times 10^{-35}$ kg, four orders of magnitude below the mass of electrons, polaritons are very light quasiparticles. Consequently, their de Broglie thermal wavelength is much larger than that of bosons commonly used in quantum fluid experiments, such as cold atoms, which would allow in principle Bose-Einstein condensation at the high cryogenic temperatures used to generate excitons.

Dissipation. Until now, the finite lifetimes of excitons and photons have been neglected in the description of polaritons. Their consideration is however essential as it determines whether it is possible to reach the strong coupling regime in our system and thus whether polaritons can be generated. Their inclusion to the dynamics of the system is done directly by adding the corresponding decay rates γ_X and γ_{cav} to the imaginary part of the Hamiltonian (2.32). The decomposition in the polaritons basis yields

$$\begin{bmatrix} \gamma_{LP}(\mathbf{k}) \\ \gamma_{UP}(\mathbf{k}) \end{bmatrix} = \begin{bmatrix} X_\mathbf{k}^2 & C_\mathbf{k}^2 \\ C_\mathbf{k}^2 & X_\mathbf{k}^2 \end{bmatrix} \begin{bmatrix} \gamma_X \\ \gamma_{cav} \end{bmatrix}. \tag{2.38}$$

Therefore, in addition to altering the mass, the exciton and photon fractions values also impact the lifetime of polaritons. The lower polariton decay rate γ_{LP} is measured equal to 70 μeV in our system, at an exciton-photon detuning $\Delta E_{X-\gamma} = 0$ meV ($\tau = 10$s).

The transformation (Eq.) 2.38 implies the following dispersion relation

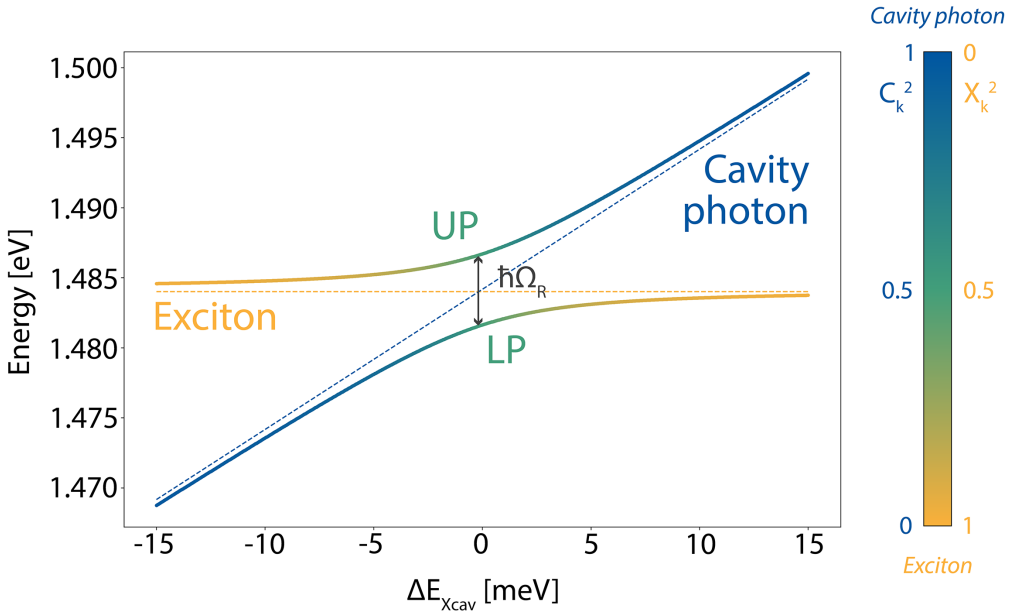

Figure 2.9: **Anticrossing of energy levels.** Energies of the upper (UP) and lower (LP) polaritons branches at $\mathbf{k} = 0\ \mu\text{m}^{-1}$, with respect to the exciton-photon detuning ΔE_{Xcav} and the color-coded squared modulus of the Hopfield coefficient X^2 (exciton) and C^2 (photon). The yellow and blue dashed lines are respectively the bare exciton and photon energies. At $\Delta E_{\text{Xcav}} = 0$ meV, the energy splitting is equal to the Rabi energy $\hbar\Omega_R$. Adapted from [108].

$$\hbar\omega_{UP,LP}(\mathbf{k}) = \frac{E_\gamma(\mathbf{k}) + E_X(\mathbf{k})}{2} - \mathrm{i}\hbar\frac{\gamma_{cav} + \gamma_X}{2} \pm \frac{1}{2}\sqrt{[\hbar\Omega_R]^2 + [\Delta E_{X-\gamma} - \mathrm{i}\hbar(\gamma_{cav} - \gamma_X)]^2}. \tag{2.39}$$

From this, still at $\Delta E_{X-\gamma} = 0$ meV around $\mathbf{k} = 0\ \mu\text{m}^{-1}$, one recovers the conditions of strong coupling expressed above. If $|\gamma_{cav} - \gamma_X| > \Omega_R$, the square root term in Eq. (2.39) is purely imaginary. As a result, the real part of the energies of the UP and LP branches matches that of photons and excitons, thus there is no splitting and the system is in a regime of weak coupling. On the other hand, if $|\gamma_{cav} - \gamma_X| < \Omega_R$, the square root term contribute to the real part of the energy: the UP and LP are split and different from photons and excitons. The system is in a regime of strong coupling. Now, if one wants to resolve the energy splitting from the spectral broadening of excitons and photons, the coupling energy must be much larger than the decay rates of the system, hence the ideal strong coupling condition expressed as $\Omega_R \gg \gamma_X, \gamma_{cav}$.

2.3.2 Polariton interactions

The low-density regime assumption we made was sufficient to demonstrate the creation of polaritons when excitons couple with photons. Now, the richness of the phenomena described

in this manuscript stems from the nonlinear dynamics of excitons, whose nature as a pair of interacting charged particles reappears for densities that are no longer close to zero. Before explaining how polaritons inherit these exciton-exciton interactions, some preliminary observations must be made.

Coupling saturation. First, for high densities, the Pauli exclusion principle applies again for electrons and holes, prohibiting the creation of an exciton in the Bohr radius of a neighboring exciton. Under optical excitation, this leads to an additional interaction term in the Hamiltonian of excitons, expressed as an exciton exchange mediated by photons [42, 43]

$$\mathcal{H}_{sat} = \frac{1}{2}\sum_{\mathbf{k},\mathbf{k}',\mathbf{q}} V_{sat}\left[\hat{a}^{\dagger}_{\mathbf{k}+\mathbf{q}}\hat{b}^{\dagger}_{\mathbf{k}'-\mathbf{q}}\hat{b}_{\mathbf{k}}\hat{b}_{\mathbf{k}'} + h.c.\right], \tag{2.40}$$

with a saturation potential $V_{sat} = \hbar\Omega_R/An_{sat}$ defined from the saturation density $n_{sat} \propto 1/(a_X^{QW})^2$ and assumed constant for the scale of wavevectors considered. With such a Hamiltonian, we express that the interaction leading to the annihilation of two excitons results in the creation of only one new exciton with a partner photon, thus reduces the population of excitons in the saturated QW, in contrast to the process depicted by the standard exciton exchange Hamiltonian $\mathcal{H}_{XX}$. For our system, one calculates $n_{sat} \simeq 10^4\mu\text{m}^{-2}$, hence $A \times V_{sat}$ about 0.1 μeV$\cdot\mu$m^2, one order of magnitude below $A \times V_{XX}$.

Truncation of the polariton basis. Secondly, in order to consider that the spectrum always exhibits two distinct UP and LP branches, the interactions between excitons must remain significantly weaker than the splitting energy $\hbar\Omega_R$. In this way, the polariton basis can be truncated to the LP eigenstate without loss of generality. By rewritting the interactions Hamiltonian (2.16) and (2.40) as a function of polariton operators ($\hat{b} = X\hat{p} - C\hat{u}$), the terms depending on $\hat{p}$ are isolated to derive an effective interaction potential felt by lower polaritons

$$V_{pp} = |X_{\mathbf{k}}|^4 V_{XX} + 2|X_{\mathbf{k}}|^2 X_{\mathbf{k}} C_{\mathbf{k}} V_{sat}. \tag{2.41}$$

Its strength can be tuned with the exciton-photon detuning $\Delta E_{X-\gamma}$, via the Hopfield coefficients X and C. When $\Delta E_{X-\gamma} = 0$ meV, $A \times V_{pp}$ is about 1 μeV$\cdot\mu$m^2 for our system

LP nonlinear hamiltonian. Finally, these considerations lead to the following expression for the LP Hamiltonian

$$\mathcal{H}_{LP} = \sum_{\mathbf{k}} \hbar\omega_{LP}(\mathbf{k})\hat{p}^{\dagger}_{\mathbf{k}}\hat{p}_{\mathbf{k}} + \frac{1}{2}\sum_{\mathbf{k},\mathbf{k}',\mathbf{q}} V_{pp}\left[\hat{p}^{\dagger}_{\mathbf{k}+\mathbf{q}}\hat{p}^{\dagger}_{\mathbf{k}'-\mathbf{q}}\hat{p}_{\mathbf{k}}\hat{p}_{\mathbf{k}'}\right]. \tag{2.42}$$

The second term corresponds to the interaction Hamiltonian of LPs, defined as a two-body contact interaction operator. It describes the exchanges between four polariton modes, leading to the creation of two polaritons at wavevectors $\mathbf{k}+\mathbf{q}$ and $\mathbf{k}'-\mathbf{q}$ from the annihilation of two

polaritons at wavevectors $\mathbf{k}$ and $\mathbf{k}'$. This type of process is the polariton analogue of the optical four-wave mixing in nonlinear media.

Energy renormalization. To give a simple intuition of the effect of the interactions on the polariton dynamics, one can restrict the description of the system to two polaritonic modes with respective wavevectors $\mathbf{k}_1$ and $\mathbf{k}_2$. The energy of the $\mathbf{k}_1$ mode is given by the Heisenberg equation

$$i\hbar\frac{d}{dt}\hat{p}_{k_1} = [\hat{p}_{k_1}, \mathcal{H}_{LP}] = [\hat{p}_{k_1}, \mathcal{H}_{lin}] + [\hat{p}_{k_1}, \mathcal{H}_{int}]\,, \tag{2.43}$$

where the contribution of interactions is equal to

$$[\hat{p}_{k_1}, \mathcal{H}_{int}] = \frac{V_{pp}}{2}\hat{p}^\dagger_{k_2}\hat{p}_{k_2}\hat{p}_{k_1} = \frac{\hbar g}{A}\hat{N}_2\hat{p}_{k_1}, \tag{2.44}$$

with $\hat{N}_2$ the number operator in the mode $\mathbf{k}_2$, $\hbar g = V_{pp}A/2$ the polariton-polariton interaction constant and A the quantization area, equal to the surface of the quantum wells. Provided that the $\mathbf{k}_2$ mode is macroscopically populated, $\hat{N}_2$ can be replaced by its expectation value $\langle\hat{N}_2\rangle$ via the mean field approximation. By normalising the equations by the quantization area A, one introduces the polariton density $n_2 = \langle\hat{N}_2\rangle/A$ in the $\mathbf{k}_2$ mode. Thus, $\hbar g n_2$ defines an interaction potential felt by the $\mathbf{k}_1$ mode polaritons.

In the end, the complete calculation of Eq. (2.43) yields

$$i\hbar\frac{d}{dt}\hat{p}_{k_1} = \left[\hbar\omega_{LP}(\mathbf{k}_1) + \hbar g n_2\right]\hat{p}_{k_1}, \tag{2.45}$$

where $\hbar\omega_{LP}(\mathbf{k}_1)$ is the linear dispersion relation of polaritons in the mode $\mathbf{k}_1$. For repulsive interactions ($g > 0$), the polaritons in the $\mathbf{k}_1$ mode undergo a blue-shift proportional to the density of polaritons in the $\mathbf{k}_2$ mode. Under coherent excitation, where polaritons are generated by resonant injection of a laser beam in the vicinity of the LP branch at $\mathbf{k}_2$, the effect of interactions is described as the renormalization of the $\mathbf{k}_1$ mode energy by the pump mode. This also occurs on the pump mode itself, inducing a mixing of four polaritons in the same mode. Such a parametric process is related to the optical self Kerr effect, also involving four-wave mixing in a single mode. It is responsible, as we will see, for the appearance of a bistable regime in the microcavity.

2.4 Polariton dynamics in resonant excitation

Let us summarize: the strong coupling between a quantum well exciton and a photon in an optical cavity creates a new type of quasi-particle, the polariton, behaving like an interacting boson of finite lifetime. Now, in order to achieve a complete description of the fundamental physics at stake in semiconductor microcavities, we need to address the optical stimulation of such particles. It is done in our experiments under a quasi-resonant excitation, with a coherent

and continuous laser beam illuminating the cavity in the vicinity of the LP resonance. We already know that the conservation of momentum and energy laws implies that only exciton modes matching the photon modes, i.e. its in-plane wavevector, energy and phase, can be created. The same applies for the polariton, as it inherits the properties of its constituent photon and exciton. This makes such an excitation scheme an ideal tool to generate and control a specific polariton mode in the system. However we have not yet discussed how the density of polaritons, thereby the strength of interactions and the resulting particle dynamics, can be optically monitored. This is what we will investigate in this section, by considering for the excitation field a single mode continuous plane wave of frequency ω_{P} and wave vector $\mathbf{k}_{\mathrm{P}}$

$$F_P(r,t) = F_P^0 e^{i(\mathbf{k}_{\mathrm{P}}\mathbf{r}-\omega_{\mathrm{P}}t)}. \tag{2.46}$$

2.4.1 Mean-field approximation

So far we have carried out a quantum description of polaritons. However, in order to solve the system dynamics under laser excitation, it is usual to employ a mean field approximation [37], remaining valid as long as the number of involved particles N is very large, i.e. $N \simeq N+1$. In this approximation, the creation and annihilation operators $\hat{p}_{\mathbf{k}}^{\dagger}$ and $\hat{p}_{\mathbf{k}}$ are replaced by their classical field terms, $\psi(\mathbf{r},t) = \langle\hat{\psi}(\mathbf{r},t)\rangle$ and $\psi^*(\mathbf{r},t) = \langle\hat{\psi}^{\dagger}(\mathbf{r},t)\rangle$, where $\hat{\psi}(\mathbf{r}) = 1/\sqrt{V}\sum_{\mathbf{k}}\hat{p}_{\mathbf{k}}\exp(\mathrm{i}\mathbf{k}\cdot\mathbf{r})$ is the polariton field operator and the particle density is defined as $|\psi(\mathbf{r},t)|^2 = n(\mathbf{r},t)$.

Gross-Pitaevskii equation. Excitation and losses aside, the evolution of ψ is already well known in the framework of quantum gas theory. It is a classical partial differential equation for the order parameter of a superfluid, expressed by Gross [65] and Pitaevskii [137] in 1961 to describe the behaviour of liquid helium

$$\mathrm{i}\hbar\frac{\partial}{\partial t}\psi(\mathbf{r},t) = \left[-\frac{\hbar^2}{2m}\nabla_{\mathbf{r}}^2 + V_{ext}(\mathbf{r}) + \hbar g|\psi(\mathbf{r},t)|^2\right]\psi(\mathbf{r},t), \tag{2.47}$$

where $V_{ext}(\mathbf{r})$ is an external potential in which the system evolve and $g = 4\pi\hbar a_s/m$ the interaction constant, proportional to the diffusion length a_s between particle. It is the well known *Gross-Pitaevskii* equation (GPE), describing the collective dynamics of a macroscopic fraction of particles assimilated to a classical field [100, 138]. It is used to describe thermal Bose gases at equilibrium, such as the condensates of cold atoms in weak interaction.

De Broglie thermal wavelength. A simple criterion to postulate whether an assembly of particles can be described as a collective system was proposed by de Broglie in 1924 [49]. In the context of the development of the wave–particle duality, he suggested that, as for photons, matter particles can be associated to a wavelength, defined as $\lambda_T = h/p$ at thermal equilibrium. The particle momentum p is governed by a Maxwell Boltzmann thermal distribution, equal to $\sqrt{2m\pi k_B T}$, leading to the following expression

$$\lambda_T = \sqrt{\frac{2\pi\hbar^2}{mk_BT}}. \tag{2.48}$$

When λ_T becomes larger than the mean interparticle spacing, the wavepackets of particles overlap. As a result, the system can no longer be described as a set of distinguishable particles. In the case of bosons, it undergoes a phase transition (Bose-Einstein condensation) that yields an accumulation of a macroscopic fraction of particles in the same quantum state, which is well described as a single wave function. At cryogenic temperatures typically around 4K, the de Broglie wavelength for polaritons in our system is of the order of 15 µm, much larger than the average distance between polaritons for densities near the optical saturation $n_{sat}\lambda_T^2 \gg 1$. We can therefore safely assume the mean field approximation for the polaritons operators and refer to the Gross-Pitaevskii equation to describe the evolution of a classical wave function.

Out-of-equilibrium Bose gas. We now include the excitation and the losses as they fundamentally change the dynamics of polaritons compared to those of Bose gases in thermal equilibrium. These differences appear in the global phase of the fluid wave function. For the case of thermal equilibrium, ψ oscillates at a frequency fixed by the chemical potential μ, defined as the energy necessary for the addition of one particle to the system. In the case of the microcavity system, the thermal equilibrium is never reached due to the decay and the continuous injection of polaritons [37]. Consequently, the phase of ψ can no longer be derived by a chemical potential governed only by the intrinsic properties of particles: its definition has to take into account the balance of the exchanges between the fluid and its environment, i.e. it depends on the driving and losses parameters. This leads to a generalization of the GPE for polaritons.

2.4.2 Driven-dissipative Gross-Pitaevskii equation

Since the operator associated to the laser field acts on photon states, it is practical to write first the Schrödinger equation of our system in the exciton-photon wave functions basis $(\psi_X(\mathbf{r},t), \psi_\gamma(\mathbf{r},t))$. In the mean field approximation, the laser field $F_p(\mathbf{r},t)$ is simply added as an external driving force imposing its phase to to the photon field $\psi_\gamma(\mathbf{r},t)$. This yields

$$\mathrm{i}\hbar\frac{d}{dt}\begin{bmatrix}\psi_\gamma(\mathbf{r},t)\\ \psi_X(\mathbf{r},t)\end{bmatrix} = \begin{bmatrix}\hbar F_p(\mathbf{r},t)\\ 0\end{bmatrix} + \tag{2.49}$$

$$\left(\mathcal{H}_{lin}(\mathbf{r}) + \begin{bmatrix}V_\gamma(\mathbf{r}) - \mathrm{i}\hbar\frac{\gamma_{cav}}{2} & 0\\ 0 & V_X(\mathbf{r}) - \mathrm{i}\hbar\frac{\gamma_X}{2} + \hbar g_{XX} n_X(\mathbf{r},t)\end{bmatrix}\right)\begin{bmatrix}\psi_\gamma(\mathbf{r},t)\\ \psi_X(\mathbf{r},t)\end{bmatrix},$$

where $V_\gamma(\mathbf{r})$ and $V_X(\mathbf{r})$ are the mean external potentials felt by photons and excitons respectively , typically induced by local structural defects in the system; $g_{XX} = AV_{XX}/2\hbar$ is the exciton

interaction strength, $n_X = |\psi_X|^2$ is the exciton density and $\mathcal{H}_{lin}(\mathbf{r})$ is the linear Hamiltonian (2.32), written in the real space by replacing $\mathbf{k}$ with $\mathrm{i}\nabla_{\mathbf{r}}$

$$\mathcal{H}_{lin}(\mathbf{r}) = \begin{bmatrix} \hbar\omega_X & \hbar\Omega_R/2 \\ \hbar\Omega_R/2 & \hbar\omega_\gamma(-\mathrm{i}\nabla_{\mathbf{r}}) \end{bmatrix}. \tag{2.50}$$

The dispersion relation of excitons is assumed uniform $\hbar\omega_X = \hbar\omega_X(\mathbf{k}{=}0)$, due to its negligible curvature in the limit of small wavevectors, compared to that of the photons $\hbar\omega_\gamma$. We then reformulate Eq. (2.49) in the polariton basis [44]. Tthe evolution equation of the LP field $\psi(\mathbf{r}, t)$ reads

$$\mathrm{i}\hbar\frac{\partial}{\partial t}\psi(\mathbf{r}, t) = \left[\hbar\omega^0_{LP} - \frac{\hbar^2}{2m}\nabla^2_{\mathbf{r}} + V_{LP}(\mathbf{r}) + \hbar g n(\mathbf{r}, t) - \mathrm{i}\hbar\frac{\gamma}{2}\right]\psi(\mathbf{r}, t) + \hbar\eta_{LP}F_p(\mathbf{r}, t). \tag{2.51}$$

Here, $V_{LP} = |X_{\mathbf{k}}|^2 V_X + |C_{\mathbf{k}}|^2 V_\gamma$ and g are respectively the external potential and the interaction constant of polaritons. η_{LP} quantifies the coupling efficiency of the pump with the polaritons, proportional to the amplitude of the light transmission through the cavity front mirror. $\hbar\omega^0_{LP}$ is equal to the energy of the LP, calculated at $\mathbf{k}{=}0$ from Eq. (2.36). In the end, we find an equation similar to Eq. (2.47), with two new terms to take into account the specificities of the polariton system: its losses and its excitations. It is the so-called *driven-dissipative* or *generalized Gross-Pitaevskii equation* [37]. We will always refer to it in the following to describe the behavior of the polariton fluid.

2.4.3 Optical bistability

We now address a direct consequence of the dissipation and driving of the system: the emergence of a bistable behavior of the polariton density with respect to the pump intensity. In the nonlinear optics literature [161, 25, 106], the term of optical bistability refers to the ability of a system to adopt two different states over a certain range of input intensities, depending on its internal state. It is commonly encountered in Kerr media: it is therefore natural that such a feature emerge for the polariton system [16], since, as mentioned, the interactions between excitons are equivalent to a Kerr nonlinearity under coherent excitation.

By considering a driving field of the form of Eq. (2.46), the energy-momentum conservation laws imply to look for plane wave-type solutions for the polariton wave function, with a phase equal to that of the pump, i.e. $\psi(\mathbf{r}, t) = \psi^0 \exp(\mathrm{i}\mathbf{k}_\mathrm{P}\mathbf{r} - \mathrm{i}\omega_\mathrm{P}t)$. After inserting this ansatz into the steady-state generalized expression of the GPE for a homogeneous system $V_{LP} = 0$, one obtains

$$\left[\omega_\mathrm{P} - \omega_{LP} - \frac{\hbar\mathbf{k}^2_\mathrm{P}}{2m} - g\left|\psi^0\right|^2 + \mathrm{i}\frac{\gamma}{2}\right]\psi^0 = \eta_{LP}F^0_P. \tag{2.52}$$

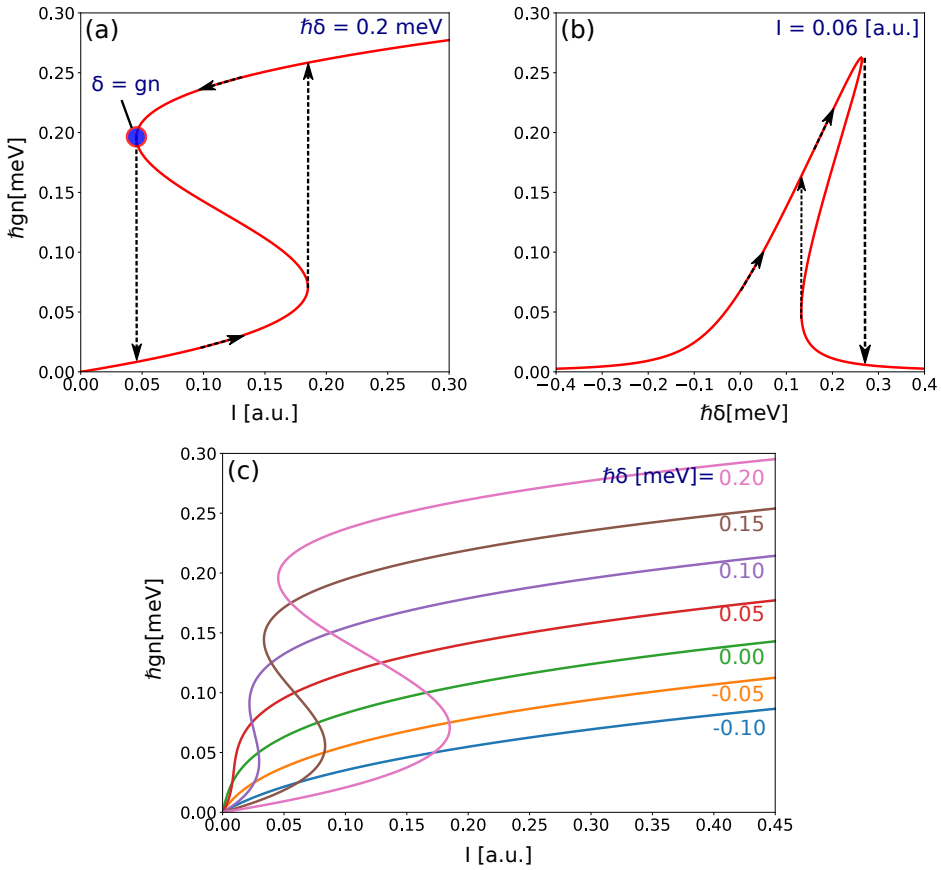

Figure 2.10: **Optical bistability of polaritons under quasi-resonant excitation**, obtained from the numerical resolution of Eq. (2.53) **(a)** Interaction energy of polaritons $\hbar gn$ as a function of the pump intensity I. In the hysteresis loop region, the fluid is in a bistable regime, where its density can either be high (on the higher branch) or low (on the lower branch). The intermediate branch of negative slope is an unstable solution of the GPE, inaccessible in stationary regime. As indicated by the black dashed arrows pointing up (down), at the lower (higher) inflection point, increasing (decreasing) I results in a density switch from the lower (higher) branch to the higher (lower) branch. **(b)** Interaction energy $\hbar gn$ as a function of the pump detuning δ. See (a) for details. **(c)** Interaction energy $\hbar gn$ for different pump detuning δ as a function of pump intensity I. The bistability appears only when $\delta > \sqrt{3}\gamma/2$.

This equation is the analogue of the equation of state of boson gases in thermal equilibrium [138, 37]: here, instead of depending directly on a fixed chemical potential $\mu = gn$, the polariton density $n = |\psi^0|^2$ evolves in a non-trivial way with the pump parameters $\mathbf{k}_\mathrm{P}$, ω_P, F_P^0 and the losses γ. By multiplying this equation by its complex conjugate and denoting $\delta = \omega_\mathrm{P} - \omega_{LP}$ the pump energy detuning with respect to the resonance of LP at $\mathbf{k}_\mathrm{P}$, the following relation for the density is derived

$$n\left[\frac{\gamma^2}{4}+\left(\frac{\delta}{\hbar}+gn\right)^2\right]=\eta_{LP}^2 I, \tag{2.53}$$

with $I=|F_P^0|^2$ the pump intensity. In the general case, this equation exhibits several density solutions for a fixed intensity and detuning of the pump. As an illustration, Fig. 2.10(a) shows the evolution of n with respect to I for a given detuning: all along a certain intensity range, the density can take two values localized on the higher or lower branch of a hysteresis loop. The central branch of negative slope is not considered here because it is dynamically unstable (we will discuss this case later in the manuscript).Therefore, like all other Kerr medium embedded in optical cavities, polaritons exhibit a bistable behavior.

The densities associated to the two bistability turning points, called respectively the higher and lower turning points in the following, can be determined by resolving $\frac{dI}{dn}=0$. This yields the discriminant

$$\Delta=g^2\left(\frac{\delta^2}{\hbar^2}-\frac{3\gamma^2}{2}\right). \tag{2.54}$$

As a result, one deduces that the system is indeed bistable if it possesses at least two different turning points, i.e. if $\Delta>0$, corresponding to a pump energy blue-detuned with respect to the LP branch $\delta>\sqrt{3}\gamma/2$. This will be the dominant excitation regime in the following of this manuscript, and this is why we have emphasized the notion of quasi-resonant excitation from the beginning of this section. On the contrary, when $\delta<\sqrt{3}\gamma/2$, only one solution exists. The polariton density is no longer bistable and its evolution as a function of the laser intensity follows a square root law (see Fig. 2.10 (c)).

From Eq. (2.53), it can be remarkably noticed that, at the higher turning point of the bistability and by neglecting γ with respect to δ, the interaction energy is equal to the pump energy $gn=\delta$. As it will be discussed in the next sections, the excitation of such a point will be crucial in our experiments.

It is also possible to evaluate the variations of the polariton density with respect to the detuning, at fixed pump intensity. Similarly, as it is plotted on Fig. 2.10(b), there is a range of δ in which two density values are possible (those located along the negative slope line are too unreachable because they are dynamically unstable). As well, we find that at the higher turning point $gn=\delta$ (Eq. (2.53)).

Qualitative description of the bistability. To fix the ideas, the emergence of bistability in semiconductor cavities can be explained qualitatively in the following way. (1) At low intensity, the laser is out-of-resonance: the injection of photons in the system has a very low efficiency and produces a small density of polaritons in a finite range of modes $\mathbf{k}$, via the incoherent scattering process $(\mathbf{k}_\mathrm{P},\mathbf{k}_\mathrm{P})\rightarrow(2\mathbf{k}_\mathrm{P}-\mathbf{k},\mathbf{k})$. (2) Ramping up the pump intensity increases the polariton injection rate until it exceeds the cavity loss rate: the density increases

drastically and leads to a renormalization of the resonance energy of the system due to the subsequent growth of polariton interactions. (3) The system jumps to the higher bistability branch. The pump is now in resonance with the LP branch, leading to a very efficient injection. The polariton mode distribution is no longer set by the incoherent scattering processes but locked by the pump. (4) Now, in order to get back to the lower bistability branch, the laser must be taken out-of-resonance again. By lowering its intensity, the polariton density decreases and thus the interaction energy as well. At the higher bistability turning point, the interaction energy is equal to the pump-polariton detuning. As soon as we cross this point, the system is again out-of-resonance with the pump, so the injection is again ineffective and consequently the density falls on lower bistability branch.

Density control knobs. From what we have just discussed, we can derive two ways to control the density of the polariton fluid: either by tuning the intensity I; or by tuning the detuning δ of the pump. These two control knobs are not equivalent, essentially because changing the intensity induces smaller density variations $n \propto I^{1/3}$ than changing the detuning $n \propto \delta$, for the ranges of powers and energies accessible by the laser used in the experiments. Moreover, as we will see in the next section, the change in the polariton interaction energy gn with respect to the laser detuning δ modifies the fluid dynamics, as the values of the GPE terms are modified. The possibility of having access to these two knobs allows to work at a fixed value of $gn - \delta$ for different densities n. In our experiments, we will generally use δ to tune roughly the density (we basically select one of the different bistability curves shown in Fig. 2.10(c)) and then use I to choose the point at which we want to work (corresponding to tune gn).

2.4.4 All-optical control

Before continuing, let us make a brief summary of all the tools we have to control and detect the polaritons, thanks to the rules of optical selection and the laws of conservation of energy and momentum under continuous, single-mode and quasi-resonant excitation. In the same manner that polaritons inherit the properties of pump photons, thus allowing their direct optical control, reciprocally, photons leaking from the cavity preserve the properties of polaritons, providing a direct way to study the dynamics of the quantum fluid. We have an equivalence between the following quantities:

- the pump intensity I and the polariton density n (modulo the bistability relation),
- the polariton density n and the intensity emitted by the cavity, via the cavity coupling mirros (losses),
- the in-plane wavevector of the pump $\mathbf{k}_\mathrm{P}$ and the wavevector of polaritons $\mathbf{k}$.
- the wavevector of polaritons $\mathbf{k}$ and their group velocity $v = \dfrac{\partial \omega_{LP}}{\partial k}(\mathbf{k}_\mathrm{P})$, calculated from Eq. (2.36) and generally referred to as the speed of the polariton flow in the plane of the cavity,
- the polariton wavevector $\mathbf{k}$ and the cavity emission wavevector,

- the polariton energy and the emission energy,
- the polariton lifetime and the emission linewidth.

2.5 Superfluidity

As explained above, polariton fluids exhibit macroscopic coherence at cryogenic temperatures and, acting as bosons, they can massively occupy a single quantum state. Their description must therefore share common characteristics with the equilibrium quantum gases, of which ultra-cold atomic condensates are the paradigmatic representatives. As an example of the investigations that went in this direction after the first experiments in semiconductor microcavities, it is possible to refer to the abundant quantity of papers transposing the theory of polaritons into that of quantum gases [75, 99, 110, 44, 52, 176]. During our demonstrations, we have seen that the dynamics of all these systems are related to each other via the Gross-Pitaevskii equation, common to both systems but enriched with a loss and pump term for polaritons. The question is now to know if the cold atoms/polaritons analogy can be pushed further by studying their collective behavior: in particular, if polaritons, like liquid helium or atomic condensates, can be the seat of superfluidity.

2.5.1 Historical background

Such a particular state of matter was observed in liquid helium by P. Kapitza, then independently by J.F. Allen and A. Don Misener in 1938 [82, 5]. Helium, which has the particularity of not solidifying at low temperatures and atmospheric pressure, undergoes a transition from a normal fluid to a superfluid state, when cooled below a critical temperature threshold, called its lambda point ($T_\lambda = 2.17$ K at saturated vapor pressure). It exhibits striking new behaviors, such as abilities to cross narrow channels without friction or to support quantified vortices within its density. One year later, F. London related these observations to the manifestation of Bose-Einstein condensation, by describing liquid helium as an interacting Bose gas [105]. He calculated that the temperature for condensation, related to the de Broglie wavelength of helium atoms becoming larger than the interparticle spacing, was about 3.09K, very close to the lambda point of superfluidity T_λ. In this picture, helium superfluidity results from the emergence of macroscopic coherence at low temperatures. However, this correspondence is limited as all Bose-Einstein condensates do not necessarily present a superfluid regime, as is the case for instance for the ideal Bose gas, i.e. without interactions. Moreover, in view of the experiments at that time, it does not explain why the friction reappears when, instead of observing its non-viscous circulation through microscopic channels, liquid helium is sent against a macroscopic cylinder [59].

Two-fluid model. L. Tisza [165] followed by L. Landau [96] deepened F. London's idea in 1941, by introducing a two-fluid model to explain the changes in the helium viscosity according to the external perturbation - the macroscopic tube or the microscopic tube - it undergoes. It consists in the interpenetration of a normal fluid component, made of non-condensed atoms,

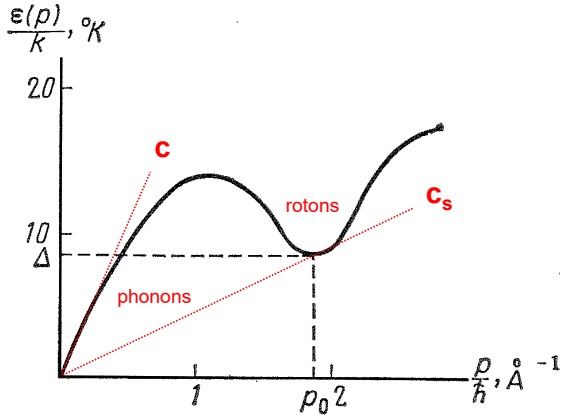

Figure 2.11: **Energy of the elementary excitations of liquid helium predicted by Landau**, at T=1.114K and plotted with respect to wavevector $\mathbf{k} = p/\hbar$. At low-k, the spectrum is linear, corresponding to the excitation of phonon-like particles, moving at the first speed of sound c. At large-k, the inflection of the dispersion curve indicates the emergence of roton-like particles, whose energy minimum is tangent to the line of slope equal to the second speed of sound of helium c_s (note that these do not exist in polariton fluids). When the speed of the flow of helium v is lower than cs, the line of corresponding slope v never crosses the spectrum: no elementary excitation can be created, corresponding to the superfluid regime according to the Landau criterion. Adapted from [97].

with a superfluid component, made of condensed atoms. The condensed part being in the ground state, it cannot contribute to the momentum exchange in helium: it has no viscosity and flows without friction through narrow channels. In contrast, the non-condensed part has a finite viscosity, responsible for the reappearance of viscosity around large obstacles.

Elementary excitations. The fraction of one component compared to the other varies continuously with the temperature: helium is a pure superfluid at zero temperature whereas it is a pure normal fluid at temperature $T > T_\lambda$. The superfluid component is considered as a background fluid, of zero temperature, supporting the normal fluid, described as a sum of elementary excitations, stimulated from the condensed fraction and whose population grows as the temperature increases. These excitations are responsible for the singular behavior of the helium viscosity. Depending on their respective energies, they are classified into two different families of quasiparticles: phonons and rotons. The former are low energy and momentum quantized sound waves that do not collide; the later are excitations of higher energies, associated with motions on a very small area of the fluid, which could result in the generation of elementary vortices. Their spectrum is plotted in Fig. 2.11, where the characteristic signature of the phonons can be observed: it is a linear dispersion relation at low wavevectors, with a slope equal to the speed of sound of helium. The theoretical model underlying such dispersion relations, which we will apply to polaritons in this manuscript, was developed in depth by N. Bogoliubov in 1946 [24].

2.5.2 Landau criterion

From these considerations, it is possible to determine if a fluid is in a superfluid state using the so-called Landau criterion. To this end, let us imagine an obstacle moving without acceleration through a uniform fluid of total mass m, and let us see at which velocity $\mathbf{v}$ it becomes possible for it to create perturbations. To simplify the analysis, it is usual to work for such problems in the reference frame where the obstacle is at rest. If we consider at first an original reference frame R, with an energy E and a momentum $\mathbf{P}$, the co-moving reference frame R' has an energy E' given by the standard Galilean transformations

$$E'(\mathbf{v}) = E - \mathbf{P}\cdot\mathbf{v} + \frac{1}{2}m\mathbf{v}^2. \tag{2.55}$$

In its ground state, the fluid is at rest in the original reference frame, so it has zero momentum. Its energy in the moving frame of reference is simply written as

$$E'_0 = E + \frac{1}{2}m\mathbf{v}^2. \tag{2.56}$$

Now, let us consider a state of the fluid supporting a single excitation of momentum $\mathbf{p}$ and energy $\epsilon_{\mathbf{p}}$. In the original reference frame R, the energy of the fluid is $E+\epsilon_{\mathbf{p}}$, and therefore, in the moving reference frame it becomes

$$E'_{\mathbf{p}} = E + \epsilon_{\mathbf{p}} - \mathbf{p}\cdot\mathbf{v} + \frac{1}{2}m\mathbf{v}^2. \tag{2.57}$$

Thus, to create an excitation of energy ϵ_p and momentum p, the fluid must acquire in the moving reference frame an energy $E'_{\mathbf{p}} - E'_0 = \epsilon_{\mathbf{p}} - \mathbf{p}\cdot\mathbf{v}$. However, in the same reference frame, the defect is at rest and therefore is not able to transfer energy to the fluid. As a result, the appearance of elementary excitations is only possible if their energy cost is zero or negative. Therefore, when the fluid flow velocity is equal to the phase velocity of the excitation, i.e. $v = \dfrac{\epsilon_p}{|\mathbf{p}|}$, the obstacle can create a perturbation of momentum parallel to $\mathbf{v}$. For higher velocities, the excitations with an angle $\cos^{-1}(\epsilon_{\mathbf{p}}/|\mathbf{p}||\mathbf{v}|)$ with respect to $\mathbf{v}$ can also be stimulated, resulting in the onset of phenomena analogous to the Cherenkov effect [78], which described the propagation of a cone-shaped shock wave, when a charged particle moves in a dielectric medium with a velocity larger than the speed of light in that medium.

Critical velocity. Finally, we can deduce the Landau criterion which gives the minimum flow velocity v_c allowing the appearance of perturbations and therefore the departure from the superfluid regime

$$|\mathbf{v}| < v_c = \min_{\mathbf{p}}\left(\frac{\epsilon_{\mathbf{p}}}{|\mathbf{p}|}\right). \tag{2.58}$$

v_c can be found from the spectrum of elementary excitations: it corresponds to the line of maximum slope that no longer crosses the dispersion relation. In the context of liquid helium, it is plotted in Fig. 2.11 and is called the second speed of sound c_s.

2.5.3 Polariton superfluidity

To summarize, the spectrum of the elementary excitations contains the information necessary to know if a fluid can be superfluid. As we will see in the next chapter, it is possible to calculate the polariton spectrum from the Bogoliubov theory [24, 37], which consists in studying the dynamics of small perturbations on top of the fluid. The polariton wave function is decomposed into a background component, stationary solution of the generalized GPE (2.51), and a low-amplitude component, corresponding to the elementary excitations. By injecting it then into the GPE, one can derive the following dispersion relation for the dynamics of weak perturbations

$$\omega_{Bog}(\mathbf{k}) = \hbar\frac{\mathbf{k}_\mathrm{P}\mathbf{k}}{m} \pm \left[\left(\frac{\hbar\mathbf{k}^2}{2m} + 2gn - \delta\right)^2 - (gn)^2\right]^{1/2} - \mathrm{i}\frac{\gamma}{2}. \tag{2.59}$$

To simplify the explanations, let us consider the case where the detuning is exactly equal to the interaction energy of polaritons, i.e. $\delta = gn$. As detailed in the previous section, this regime is reached by tuning the pump intensity to excite the polariton density at the high turning point of the bistability. The dispersion relation becomes

$$\omega_{Bog}(\mathbf{k}) = \hbar\frac{\mathbf{k}_\mathrm{P}\mathbf{k}}{m} \pm \sqrt{\frac{\hbar\mathbf{k}^2}{2m}\left[\frac{\hbar\mathbf{k}^2}{2m} + gn\right]} - \mathrm{i}\frac{\gamma}{2}. \tag{2.60}$$

It is plotted for pump wave vectors $\mathbf{k}_\mathrm{P} = 0$ and $\mathbf{k}_\mathrm{P} = 0.25\ \mu\mathrm{m}^{-1}$ in Fig. 2.12. Two straight lines lie at low-k, corresponding to the spectral signature of phonons. Without flow, i.e. $\mathbf{k}_\mathrm{P} = 0$, their slope is equal to the polariton speed of sound cs, which can be expressed from the Taylor expansion of Eq. (2.60) when $\mathbf{k} \to 0$

$$\hbar\omega_{Bog}(\mathbf{k}) \simeq \sqrt{\frac{\hbar gn}{m}}\mathbf{k} = c_s\mathbf{k}. \tag{2.61}$$

In the case where the fluid has a non-zero flow velocity, $v_{\mathbf{k}_\mathrm{P}} = \dfrac{d\omega_{Bog}}{dk} = \hbar\dfrac{\mathbf{k}_\mathrm{P}}{m}$, the positive and negative slopes of the dispersion relation are asymmetric: phonons co-propagating with the direction of the flow go at velocity $c_s + v_{\mathbf{k}_\mathrm{P}}$; counter-propagating phonons go at velocity $c_s - v_{\mathbf{k}_\mathrm{P}}$.

Historical experiments. Because their spectra reveal phonons under certain excitation conditions, polaritons fluids can behave as a superfluid. The first experimental evidence of a superfluid behavior in semiconductor microcavity was performed by A. Amo in 2009 [9],

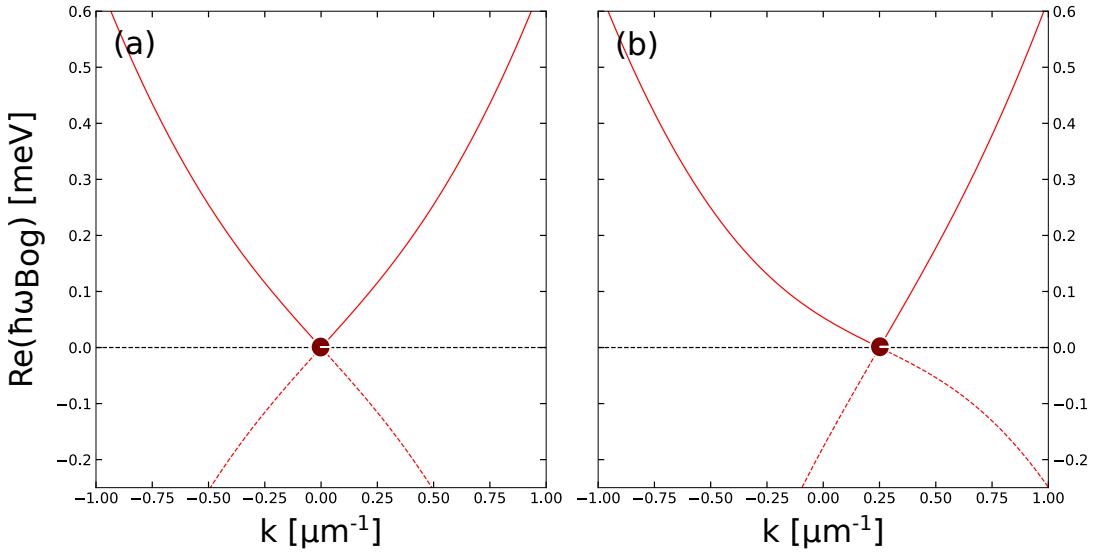

Figure 2.12: **Spectra of elementary excitations of polaritons**, calculated from Eq. (2.60), for a pump detuning $\hbar\delta = 0.2$ meV and at the bistability higher turning point $gn = \delta$. **(a)** Real part of the energy $\hbar\omega_{Bog}$ of the Bogoliubov elementary excitations as a function of their wavevector $\mathbf{k}$. The pump wavevector, highlighted by the red dot, is set at $\mathbf{k}_P$=0, therefore the flow velocity of polaritons is zero. At low-k, two linear branches appear, corresponding to the excitation of phonon particles on top of the fluid. Their slope is equal to the speed of sound c_s. At large-k, the standard parabolic dispersion of single particles is recovered. **(b)** At $\mathbf{k}_P$=0.25 μm^{-}1, the fluid flows in the direction of the positive $\mathbf{k}$ at a speed $v_{\mathbf{k}_P} = \hbar\mathbf{k}_P/m$. As a result, the speed of sound at low-k is modified: it is equal to $cs + v_{\mathbf{k}_P}$ in the direction of flow; $cs - v_{\mathbf{k}_P}$ in the opposite direction.

in a parametric excitation regime. The same year, the demonstration of superfluidity under continuous and quasi-resonant excitation, was reported in our group [10], by exploiting the Landau criterion.

The experiment consisted in sending a flow of polaritons in the wake of a micrometric structural defect. The cavity used at that time was the same one we still use today (see **Annex**). The results are pictured in Fig. 2.13(a), where the top line shows images of the density of the fluid in the real space of the microcavity plane and the bottom line shows the corresponding reciprocal space, i.e. the momentum distribution (k_x, k_y) of polaritons. For each row, the speed of flow, set by the pump angle $\mathbf{k}_P$ = -0.337 μm $^{-1}$, is kept constant and only the pump intensity increases, resulting in an increase of the polariton density and thus in an increase of the speed of sound as described in Eq. (2.61).

At low intensities, in Fig. 2.13(a)-I, the system is in linear regime. The fluid scatters elastically from the defect, leading to the formation of parabolic wavefronts in the direction opposite to the flow in real space and the appearance of a Rayleigh ring in reciprocal space, proving the reflection of polaritons by the defect in all directions of the cavity. At higher intensities, in

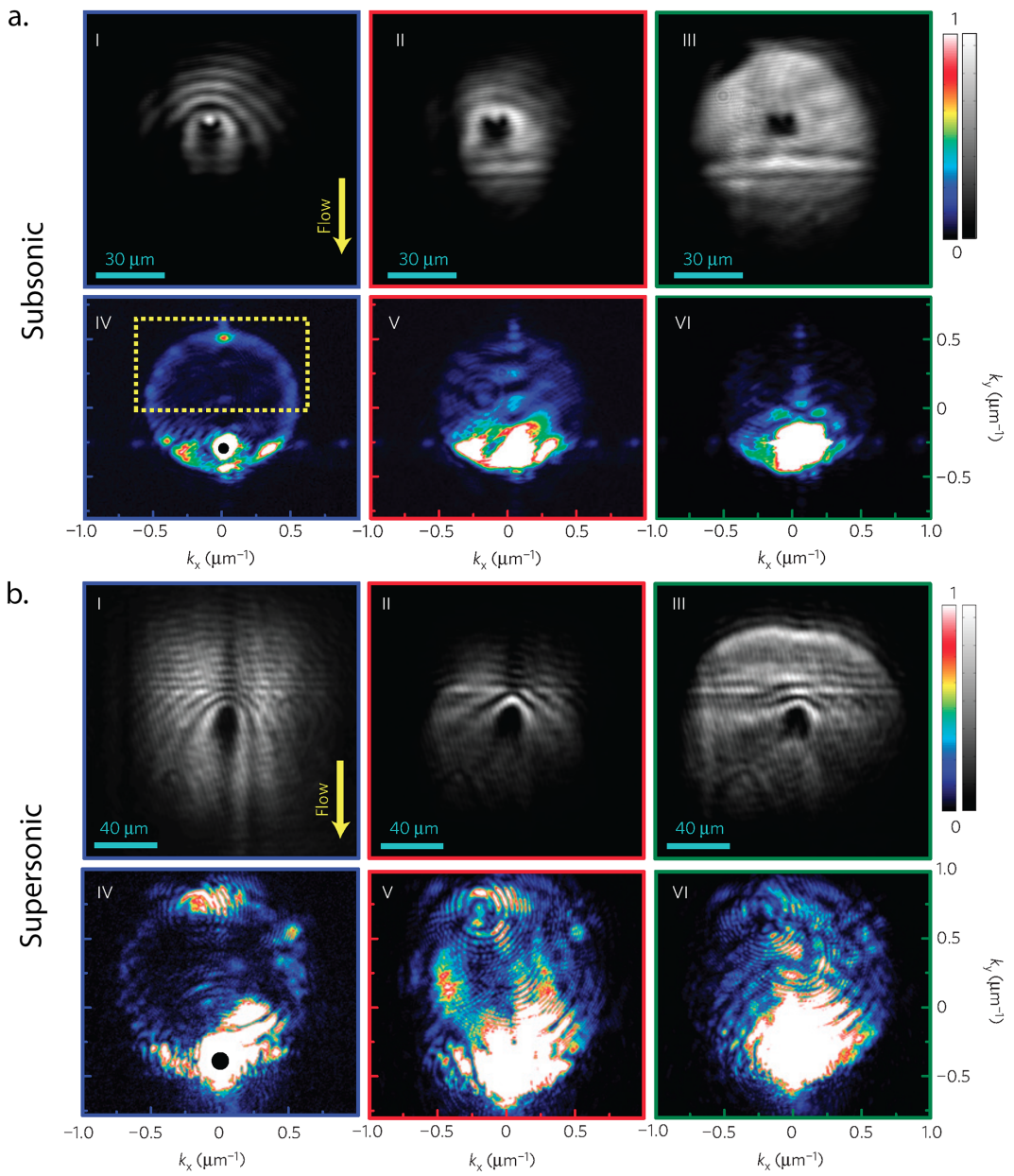

Figure 2.13: **Superfluidity in polariton fluid. (a)** Experimental results of a polariton fluid transition to superfluidity. Top images are real space while bottom ones are the momentum space. The flow goes from top to bottom hitting a defect, the in-plane wavevector is $\mathbf{k}_P$ = -0.337 μm$^-$1 and the detuning $\delta = 0.10$ meV. The polariton density increases from left to right: at low density, the fluid scatters on the defect, as shown by the scattering ring in the far field and the parabolic wavefront in the density map. Those gradually vanish while the density increases, until they completely disappear in the superfluid regime on the right images. **(b)** Same configuration at $\mathbf{k}_P = 0.521\mu$m$^-$1 and $\delta = 0.11$ meV. This time, the increase of density leads to a linearisation of the scattering fringes around the defect, also known as the Cerenkov cone. Adapted from [10].

Fig. 2.13(a)-II and -III, the speed of sound exceeds the speed of the flow. As a consequence, the wave fronts and the Rayleigh ring vanish: the fluid has lost its initial viscosity, it moves therefore without friction around the defect, and does not generate any scattering. Polaritons are in superfluid regime, in accordance with the Landau criterion.

Noteworthy, on the second set of pictures of Fig. 2.13(b) captured for a higher flow velocity, with $\mathbf{k}_{\mathrm{P}} = 0.52\ \mu\mathrm{m}^{-1}$, a Cherenkov-Mach cone clearly appears in the nonlinear regime. The density modulation here has the same shape as that of the air pressure singularities observed for example in the wake of a plane or a bullet when they break the "sound barrier".

Following these discoveries, a whole series of experiments were conducted to study the hydrodynamic nucleation of vortex-antivortex [29, 102] pairs and solitons [8] in the superfluid flowing downstream of the defect. We will details these experiments in details in the following chapter. Although it is very useful to probe the superfluid behavior, the Landau criterion remains an approximation to explain the superfluidity regime [114]. During the last few years, many theoretical and experimental works have led to a refinement of it, taking into consideration for example the shape of the defect or the bistable character of the fluid and allowing to better account for the conditions of superfluidity in polariton systems.

2.6 Bose-Einstein condensation in off-resonance excitation

Bose-Einstein condensation (BEC) is another phenomenon also observed and studied in semiconductor microcavities, pushing the analogy between quantum fluids and polaritons even further. Predicted in 1924 by S. Bose for photons [26] and then generalised in 1925 by A. Einstein to all bosons [55], it arises from the accumulation of a macroscopic fraction of particles in the lowest-energy state. Although the first hints of condensation were initially unveiled in superfluid helium [82, 105], the first observation of a truly BEC dates from 1995 [12, 48], realized in a rubidium atom gas cooled to nano Kelvin temperatures.

The BEC transition is also associated with the idea of spontaneous U(1) symmetry breaking of the phase of the order parameter of the considered system. In the present case of quasi-resonant excitation, this is not achieved as the phase of the polariton wavefunction is pinned by the driving field, preventing the occurrence of BEC, although the experimental conditions are suitable for the formation of a condensate, such as the de Broglie thermal wavelength much larger than the mean spacing between particles at cryogenic temperatures. However, it is still possible to consider other excitation regimes that decouple the dynamics of the polaritons from that of the laser. For instance, in the optical parametric oscillation (OPO) regime, the strong four-wave mixing nonlinearity of the system is exploited to generate from the scattering of coherently injected polaritons, signal and idler polaritons, whose phases are free to evolve. This will be discussed in another chapter of the manuscript. Here we are interested in the off-resonance excitation regime, which, in microcavities designed specifically for this purpose,

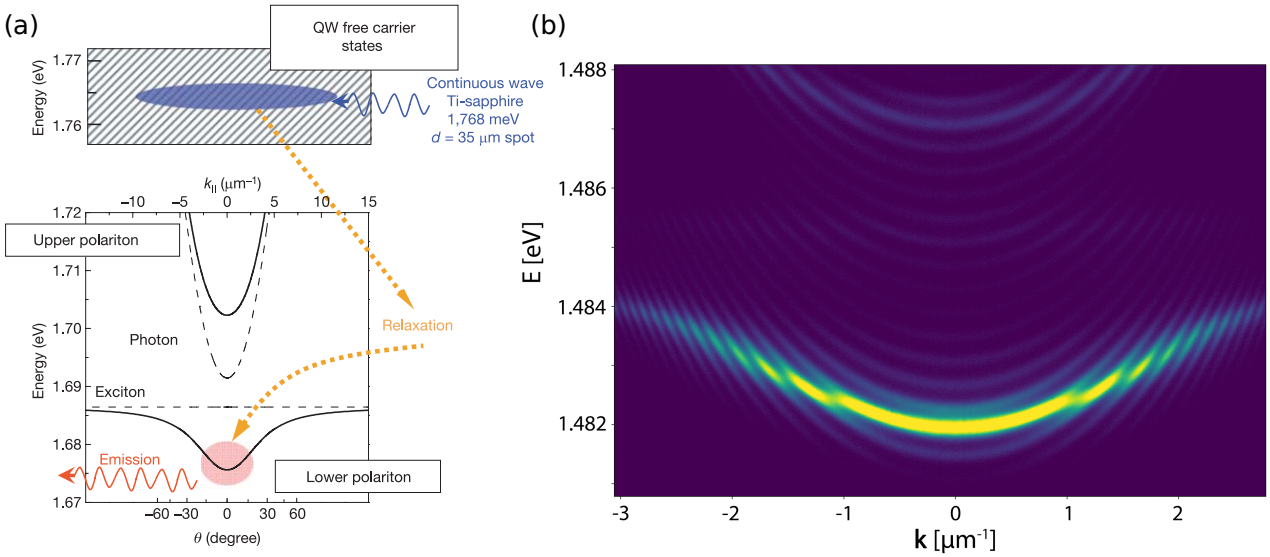

Figure 2.14: **Off-resonance excitation.** **(a)** Scheme of the different steps in the process leading to the off-resonant excitation of polaritons at the bottom of the lower branch. Adapted from [84]. **(b)** Photoluminescence spectrum of polaritons resolved with a spectrometer. Both the upper and lower branches are visible. Note the presence of replica fringes, related to photonic resonance apparent at the frequency of the free spectral range of the effective cavity formed by the association of the two system mirrors with the output substrate.

leads to polariton BEC [35, 85, 23].

2.6.1 Off-resonance pumping

In the off-resonance excitation regime, the laser illuminates the microcavity at much higher energy than the resonance, in the vicinity of one of the reflectivity minima above the stop band of DBRs. Then, the injected photons relax towards the LP branch, via the following steps:

1. Free electron-hole pairs are stimulated and cooled down by phonon emission into an incoherent cloud of bound excitons.
2. These excitons can eventually relax into polaritons accumulating at the wavevectors of the bottleneck region of the LP branch.
3. Finally, collisions between polaritons cause their scattering around the bottom of the LP branch.

Once populated, the LP branch emits a photoluminescence (PL) signal via the optical cavity losses. This signal can be resolved in the reciprocal space (k-space) of the microcavity, collected by a very large aperture objective and then imaged at the level of the slit of a spectrometer coupled to a CCD camera. Since the photons preserve the energy and the planar wavevector of polaritons due to the translational invariance in the cavity plane, we can therefore directly measure the dispersion relation of the LPs, in the linear regime for low excitation intensities as

pictured in Fig. 2.36(b). This is a very useful tool, allowing us to access to the key parameters of our experiments, at the different working points of our sample.

2.6.2 Polariton condensates

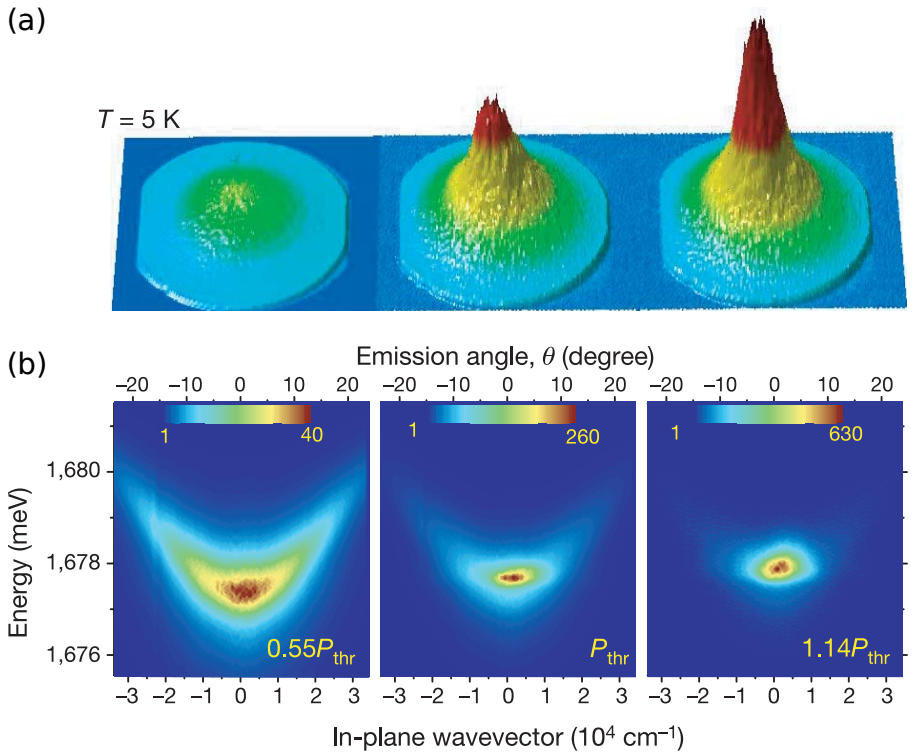

Figure 2.15: **Polariton Bose-Einstein condensation.** The off-resonance driving field power is increased from the left to the right. **(a)** Momentum space emission intensity of the microcavity. With the driving power exceeding the condensation threshold P_{thr}, a sharp and intense peak is formed in the center of the emission distribution ($\theta_x = \theta_y = 0$ °), corresponding to the lowest momentum state $\mathbf{k} = 0$. **(b)** Same data, resolved in energy. Below threshold, the emission is broadly distributed in momentum and energy. Above threshold, the emission comes almost exclusively from the lowest energy state $\mathbf{k} = 0$. Adapted from [84].

A. Imamoglu and R. J. Ram suggested in 1996 that the bosonic character of polaritons could lead to the emergence of a condensate-like state emitting coherent laser light [75]. The creation of such a condensate requires both a macroscopic occupation of a same state by polaritons and the validity of the bosonic approximation mentioned earlier, requiring that the exciton population remains below a certain saturation density ($n_X(a_X^{QW})^2 \ll 1$). It is achieved by ramping up the driving field intensity: the increasing population of polaritons in the bottom of the LP branch stimulates and accelerates the relaxation of the polaritons from the high-k.

If the exciton density exceeds the saturation density before reaching a regime of macroscopic occupation by polaritons, phase-space filling effects and screening of Coulomb interactions lead to the dissociation of excitons into an electron-hole plasma and consequently to the disappear-

ance of polaritons. Note that the stimulated emission of the plasma is similar to that of a laser if the cavity losses are exceeded, making the system equivalent to an optically-pumped vertical surface emitting laser (VCSEL).

The saturation density can be further increased by adding more QWs in the semiconductor microcavity to reduce the mean exciton density per QW. In such a system, above a certain intensity threshold, macroscopic occupation of states is achievable while preserving the bosonic nature of polaritons. Provided that the relaxations of excitons and polaritons are faster than the losses, the competition between the different low-k states favours the lowest energy state along the LP branch, whose macroscopic occupation results in the emergence of a polariton condensate.

The first microcavity BECs were reported by J. Kasprzak in CdTe system, in 2006 [84]. Due to the polariton effective mass, they were produced at temperatures of the order of Kelvin. As shown in Fig. 2.15, above a threshold intensity, a macroscopic accumulation of polaritons in the lowest energy states is clearly observed. The polariton condensates have of course a non-equilibrium nature due to the continuous losses and driving of the system. Therefore, its belonging to the family of Bose-Einstein condensates is still under debate. However, more recent work involving very high quality factor cavities, show the achievement of equilibrium condensation of polaritons at 4K [160] and of microcavity photons at room temperature [87].

Chapter 3

High-resolution coherent pump-probe Bogoliubov modes spectroscopy

As explained in the second chapter, the characterization of the elementary excitations of a quantum fluid is essential to study its collective effects, such as its superfluidity. It is commonly achieved with the help of the Bogoliubov theory.

In the case of polaritons, the behavior of elementary excitations is tightly related to the properties of the driving field and losses via the driven-dissipative nature of the semiconductor microcavity. In this regard, it deviates significantly from that expected for an in-equilibrium cold atom condensate. This is what we will study in this chapter.

The precise detection of the Bogoliubov dispersion in polariton quantum fluids has remained a challenging goal ever since the observation of superfluidity and Bose Einstein condensation therein. In the following, we will present the implementation of a high-resolution angle-resolved coherent probe spectroscopy technique that allows for the measurement of the elementary excitation spectrum in the linear and nonlinear regimes of interactions.

This work is based on the theoretical study carried out by C. Ciuti and I. Carusotto [44, 36] and is reported in Ref. [45].

3.1 Bogoliubov dispersion relation

The dynamics of weak perturbation on top of the polariton fluid is described with the Bogoliubov theory in the mean-field approximation, consisting in the linearization of the generalized GPE around its steady-state solution.

Under a continuous and coherent excitation, we consider first a stationary and homogenous plane wavefunction solution of the GPE $\psi_0(\mathbf{r},t) = \psi_0 \exp(i\mathbf{k}_\mathrm{P}\mathbf{r} - i\omega_\mathrm{P}t)$, of spatial and temporal profiles inherited from the driving field $F_p(\mathbf{r},t) = F_p^0 \exp(i\mathbf{k}_\mathrm{P}\mathbf{r} - i\omega_\mathrm{P}t)$. It represents the background of the fluid, on top of which is introduced a weak perturbation $\delta\psi(\mathbf{r},t)$, typically induced by a weak fluctuation in the driving field amplitude. The polariton wavefunction is then assumed to be the sum of these two components, with the following ansatz

$$\psi(\mathbf{r},t) = \exp(i\mathbf{k}_\mathrm{P}\mathbf{r} - i\omega_\mathrm{P}t)\left[\psi_0 + \delta\psi(\mathbf{r},t)\right]. \tag{3.1}$$

The multiplicative exponential expresses the fact that the main state occupied by polaritons is the pump mode, as expected in coherent excitation and in accordance with the momentum-energy conservation laws. Now, in order to get the energy of the perturbed polariton fluid, we inject $\psi(\mathbf{r},t)$ and $\psi^*(\mathbf{r},t)$ into the generalized GPE and look for the first order solution. This leads to a pair of evolution equations

$$\begin{aligned}\mathrm{i}\hbar\frac{\partial}{\partial t}\delta\psi(\mathbf{r},t) = &\left(\hbar\omega_{LP}^0 - \hbar\omega_\mathrm{P} + \frac{\hbar^2}{2m}\left[\mathbf{k}_\mathrm{P}^2 - 2\mathrm{i}\mathbf{k}_\mathrm{P}\nabla - \nabla^2\right] + 2\hbar g|\psi_0(\mathbf{r},t)|^2 - \mathrm{i}\hbar\frac{\gamma}{2}\right)\delta\psi(\mathbf{r},t)\\ &+ \hbar g\psi_0^2(\mathbf{r},t)\delta\psi^*(\mathbf{r},t),\end{aligned} \tag{3.2}$$

$$\begin{aligned}-\mathrm{i}\hbar\frac{\partial}{\partial t}\delta\psi^*(\mathbf{r},t) = &\left(\hbar\omega_{LP}^0 - \hbar\omega_\mathrm{P} + \frac{\hbar^2}{2m}\left[\mathbf{k}_\mathrm{P}^2 + 2\mathrm{i}\mathbf{k}_\mathrm{P}\nabla - \nabla^2\right] + 2\hbar g|\psi_0(\mathbf{r},t)|^2 - \mathrm{i}\hbar\frac{\gamma}{2}\right)\delta\psi^*(\mathbf{r},t)\\ &+ \hbar g\psi_0^{*2}(\mathbf{r},t)\delta\psi(\mathbf{r},t).\end{aligned} \tag{3.3}$$

The problem is then simplified by expressing the weak perturbations in term of a coherent superposition of counter-propagating plane waves, with respective amplitude $U_\mathbf{k}, V_\mathbf{k} \ll \sqrt{n}$

$$\begin{cases}\delta\psi(\mathbf{r},t) = U_k \cdot \exp(\mathrm{i}\mathbf{k}\mathbf{r} - \mathrm{i}\omega t) - V_k^* \cdot \exp(-\mathrm{i}\mathbf{k}\mathbf{r} + \mathrm{i}\omega t),\\ \delta\psi^*(\mathbf{r},t) = U_k^* \cdot \exp(-\mathrm{i}\mathbf{k}\mathbf{r} + \mathrm{i}\omega t) - V_k \cdot \exp(\mathrm{i}\mathbf{k}\mathbf{r} - \mathrm{i}\omega t).\end{cases} \tag{3.4}$$

Such decomposition allows to express Eq. (3.2) and (3.3) in a new basis, of eigenvectors equal to the $U_\mathbf{k}, V_\mathbf{k}$ plane waves

$$\omega \begin{bmatrix} U_{\mathbf{k}} \\ V_{\mathbf{k}} \end{bmatrix} = \mathcal{L}_{Bog} \begin{bmatrix} U_{\mathbf{k}} \\ V_{\mathbf{k}} \end{bmatrix}, \tag{3.5}$$

where the Bogoliubov operator is defined by

$$\mathcal{L}_{Bog} = \begin{bmatrix} \omega_{LP}^0 + \dfrac{\hbar(\mathbf{k}+\mathbf{k}_\mathrm{P})^2}{2m} + 2gn - \omega_\mathrm{P} - \mathrm{i}\dfrac{\gamma}{2} & gn \\ -gn & -\omega_{LP}^0 - \dfrac{\hbar(\mathbf{k}-\mathbf{k}_\mathrm{P})^2}{2m} - 2gn + \omega_\mathrm{P} - \mathrm{i}\dfrac{\gamma}{2} \end{bmatrix}. \tag{3.6}$$

The spectrum of elementary excitations, i.e. the frequency of $\delta\psi(\mathbf{k})$, is simply given by the eigenvalues of $\mathcal{L}_{Bog}$, equal to the zeros of $\det[\omega - \mathcal{L}_{Bog}]$, with the analytic expression

$$\omega_{Bog}(\mathbf{k}) = \hbar\frac{\mathbf{k}_\mathrm{P}\mathbf{k}}{m} \pm \left[\left(\omega_{LP}(\mathbf{k}_\mathrm{P}) + \frac{\hbar\mathbf{k}^2}{2m} + 2gn - \omega_\mathrm{P}\right)^2 - (gn)^2\right]^{1/2} - \mathrm{i}\frac{\gamma}{2}. \tag{3.7}$$

This is the so-called Bogoliubov dispersion relation of polaritons under a continuous and coherent excitation. It relates the frequency $\omega_{Bog}(\mathbf{k}) = \omega(\mathbf{k} - \mathbf{k}_\mathrm{P}) - \omega_\mathrm{P}$ of weak perturbations of the polariton field to their excitation wavevector $\mathbf{k}$, in the reference frame rotating at the pump frequency ω_P and wavevector $\mathbf{k}_\mathrm{P}$. Note that the consideration of counter-propagative plane waves implies the existence of a solution of negative energy, the so-called polariton ghost-branch, which has the symmetric shape of the positive solution with respect to the polariton condensate.

Comparison with the equilibrium quantum fluid. Here, the out-of-equilibrium nature of our system is evident through the dependence of the elementary excitations energy on the losses γ and the frequencies (ω_P, $\mathbf{k}_\mathrm{P}$) of the pump field. For comparison, in the case of a thermal equilibrium quantum fluid, whose motion is governed by the classical GPE (2.47), the Bogoliubov operator depends only on the interaction energy gn, which is directly linked to the properties of the Bose gas, via its chemical potential μ fixed by the equation of state $\mu = gn$. It is given by

$$\mathcal{L}_{Bog}^{\mathrm{eq}} = \begin{bmatrix} -\dfrac{\hbar\mathbf{k}^2}{2m} + 2gn - \mu & gn \\ -gn & \dfrac{\hbar\mathbf{k}^2}{2m} - 2gn + \mu \end{bmatrix}. \tag{3.8}$$

Its diagonalization gives

$$\omega_{Bog}(\mathbf{k}) = \pm\sqrt{\left(\frac{\hbar k^2}{2m} + gn\right)^2 - (gn)^2}. \tag{3.9}$$

Therefore, the out-of-equilibrium dispersion relation (3.7) is similar to the equilibrium one, except for the additions of an extra energy term equal to $gn - \delta$, coming from the resonant pumping, and of an imaginary term $i\gamma/2$, coming from the polariton finite lifetime.

Moreover, in the driven-dissipative case, the density is a non-trivial function of the intensity $\left|F_p^0\right|^2$ and frequency ω_{P} of the pump, as seen from the bistability analysis. Thus, the slight modifications in the pump field parameters drastically modifies the nature of the elementary excitations and thus the shape of the Bogoliubov dispersion curve. The simple picture of phonons responsible for the onset of the superfluid regime no longer holds and must be completed to account for the diverse phenomena observed in our microcavity quantum fluid.

Stability of Bogoliubov solutions. $\mathcal{L}_{Bog}$ eigenvalues are classified into two main families depending on their imaginary part:

- $\mathfrak{Im}(\omega_{Bog}) < 0$: stable modes,
- $\mathfrak{Re}(\omega_{Bog}) = 0$ and $\mathfrak{Im}(\omega_{Bog}) > 0$: unstable modes, leading to the occurence of dynamical instabilities.

For the last family, instabilities emerge when two different collective excitations modes enter in resonance with each other: either the pump mode with one of the Bogoliubov solutions, ($\omega_{\mathrm{P}} = \omega_{Bog}^{\pm}$ at $\mathbf{k}_{\mathrm{P}}$), involving the onset of a *Kerr instabilities*; either the positive Bogoliubov solution with the negative one, ($\omega_{Bog}^{+} = \omega_{Bog}^{-}$ at $\mathbf{k} \neq \mathbf{k}_{\mathrm{P}}$), responsible for the triggering of *modulational instabilities*. In the latter case, the polariton fluid exhibits the generation of elementary excitation at different finite wavevectors $\mathbf{k}_{\pm}$ on either side of the pump wave vector $\mathbf{k}_{\mathrm{P}}$. Literature generally refers to such wavevectors as lateral bands of instabilities, creating a spatial modulation of the polariton density all along the surface of the fluid. As the system is superfluid, if this modulation is strong enough, it can lead to the creation of topological excitations like vortices.

3.2 Bogoliubov modes characterization

As shown in the previous chapter, depending on the value of δ, two different density regimes are available:

1. The optical bistability, when $\delta > \sqrt{3}\gamma/2$, which exhibits, depending on the pump intensity, a regime of strong interaction, at high density, and a regime of weak interaction, at low density.
2. The optical limiter, when $\delta < \sqrt{3}\gamma/2$. We will not deal with its case here because the different types of elementary excitations it includes are also present in the bistable case.

Without pump, i.e. $\left|F_p^0\right|^2 = 0$, the real part of $\hbar\omega_{Bog}$ matches the parabolic linear-regime dispersion relation of polaritons (2.39), with an imaginary part determined by the polaritons decay rate γ. It gives the single particle response of the microcavity system to a weak intensity

excitation. It will serve us as a reference as we will look for the deviation from its shape when a high-density, nonlinear fluid is generated.

We will now discuss the modifications of elementary excitations depending on the density variation of the fluid along the bistability loop. Accordingly, we have chosen to work at constant detuning $\hbar\delta = 0.2$ meV ($\delta > \sqrt{3}\gamma/2$) and to modify the interaction energy $\hbar gn$ with the laser intensity $\left|F_p^0\right|^2$. The corresponding dispersion relations, plotted from the numerical calculation of Eq. (3.7), are presented in Fig. 3.0.

3.2.1 Interplay with the optical bistability

i- Sonic dispersion relation

Let us begin by analyzing the most spectacular case, which allows us to directly link polaritons to the paradigmatic representatives of quantum fluids: the excitation of the bistability turning point at zero incidence $\mathbf{k}_\mathrm{P} = 0$. Here, the interaction energy is exactly equal to the laser detuning $\delta = gn$. Such relation is analogue to that between the density of the thermal in-equilibrium quantum fluids and their chemical potential $\mu = gn$. The dispersion relation (3.7) simplifies as follows

$$\omega_{Bog}(\mathbf{k}) = \pm\sqrt{\frac{\hbar\mathbf{k}^2}{2m}\left(\frac{\hbar\mathbf{k}^2}{2m} + gn\right)} - \mathrm{i}\frac{\gamma}{2}. \tag{3.10}$$

It is plotted in Fig. 3.0(b) D, where two different regimes are distinguishable according to the value of $\mathbf{k}$ compared to the inverse value of the healing length $\xi = \sqrt{\hbar^2/mgn}$.

In the small wavevector limit, $\mathbf{k} \ll 1/\xi$, the dispersion curve is linear with respect to $\mathbf{k}$

$$\mathfrak{Re}\left(\omega_{Bog}(\mathbf{k})\right) = c_s k, \tag{3.11}$$

with $c_s = \sqrt{\hbar gn/m}$ the polariton speed of sound. In the high wavevector limit, $\mathbf{k} \gg 1/\xi$, we recover the standard parabolic dispersion curve of the linear regime, with a renormalization of the energy due to the interactions (blue shift)

$$\mathfrak{Re}\left(\omega_{Bog}(\mathbf{k})\right) = \frac{\hbar\mathbf{k}^2}{2m} + gn. \tag{3.12}$$

The low-k behaviour is a direct consequence of the disappearance of the dependence of the generalized GPE on the pump energy that occurs at the bistability turning point, leading to an oscillation frequency of the polariton field governed only by the value of gn as it is the case for liquid helium or ultra-cold atomic condensates. It results in the emergence of sound modes in our system, reminiscent of its superfluidity.

This feature as been indirectly reported in several of our previous experiments, in particular in those concerning the generation of vortices and dark solitons [9, 102, 109], which required to excite polaritons as close as possible to the turning point. The precise measurement of such a linear dispersion relation thus embodies a leaps in the understanding of a large variety of phenomena studied in the past by the team.

ii- High-density regime

At high intensity, all along the higher bistability branch, the interaction energy increases with respect to the pump detuning, $gn > \delta$. It results in a shift toward the higher/lower energies of the positive/negative Bogoliubov solution (Fig. 3.0(b) E-F). A gap appears between the two branches, centered on the pump energy and of width increasing as the intensity is ramped up. This behaviour is accompanied with a modification of the shape of the dispersion curve at low-wavevectors: as the intensity goes further away from the turning point, the two linear branches of the Bogoliubov sonic dispersion relation progressively vanish and turn into a single-particle parabola. Consequently, the collective excitations have no longer a phonon-like character.

In the team, this excitation scheme is often referred to as the regime of fixation of the polariton phase, since the fluid wavefunction ψ is entirely governed by the properties of the pump. Ref. [109] is a good illustration of the phenomena observed in such a regime, where dark solitons generated upstream of a flow fail to propagate towards the downstream excited at high intensity, as they cannot dig their characteristic π-phase jump in the density because the fluid phase is pinned by the driving field.

iii- Low-density regime

The excitation on the lower branch of the optical bistability, near its turning point, reveals a drastic modification of the Bogoliubov solutions, as shown in Fig. 3.0(B).

As the interaction energy drops such that $gn < \delta/3$, the positive and negative branches cross each other. This causes the energy of elementary excitations to become purely imaginary at wavevectors for which the argument of the square root in Eq. (3.7) becomes negative

$$\delta - 3gn < \frac{\hbar k^2}{2m_{LP}} < \delta - gn. \tag{3.13}$$

For a fixed δ, the wavevector range of purely imaginary modes grows as gn becomes larger. Therefore, if one wishes to detect such spectral features, the system must be excited as close as possible to its lower turning point.

Importantly, the coupling of the positive and negative Bogoliubov branches drastically modifies the behaviour of $\mathfrak{Im}(\omega_{Bog})$. If the imaginary part turns out to be positive, the solutions are unstable, as it is the case along the bistability branch of negative slope. However on the bistability lower branch, the losses γ stabilize the solutions by keeping their imaginary part negative

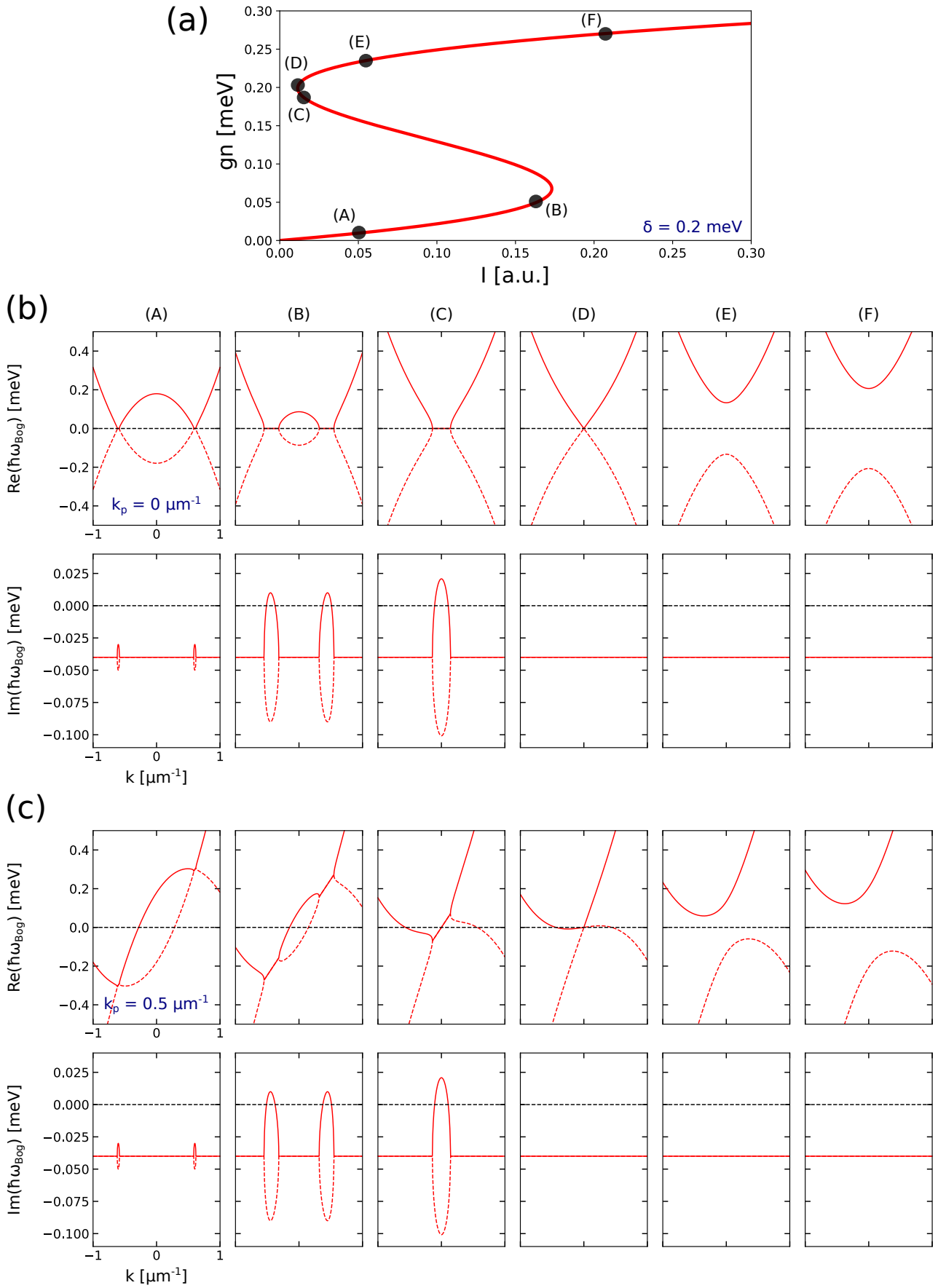
(a)
gn [meV]
I [a.u.]
(A)
(B)
(C)
(D)
(E)
(F)
δ = 0.2 meV
(b)
(c)
Re(ħω_Bog) [meV]
Im(ħω_Bog) [meV]
k [μm^-1]
k_p = 0 μm^-1
k_p = 0.5 μm^-1

Figure 3.0: **Analytical Bogoliubov dispersion relations.** (a) Bistability curve of the fluid density n as a function of the pump intensity I, calculated from Eq. (2.53), for a pump detuning $\hbar\delta = 0.2$ meV. (b) Positive (solid red lines) and negative (dashed red lines) solutions of the Bogoliubov dispersion relation in the fluid reference frame, computed from Eq. (3.7), at the pump wavevector $\mathbf{k}_P = 0$ (zero flow velocity), at the pump detuning $\delta = 0.2$ meV and for pump intensities indicated by the points A, ..., F in (a). Upper line: real part of the energy of elementary excitations. The black dotted line highlights the pump energy. Lower line: imaginary part of the energy of the elementary excitations. As long as it remains negative (below the black dashed line), the Bogoliubov solutions are dynamically stable. Note that near and all along the negative slope branch of the bistability, the modes are unstable, giving rise at the point B and C respectively to modulation instabilities (coupling of the positive solution with the negative solution at $\mathbf{k} \neq 0$) and Kerr instabilities (coupling of the positive and the negative solutions with the pump mode at $\mathbf{k} = 0$). At the other points A, D, E, F, the system losses fix the imaginary part at $-\gamma/2$, stabilizing the fluid. (c) Same considerations as for (b) but at a pump wavevector $\mathbf{k}_P = 0.5\ \mu\text{m}^{-1}$. The fluid speed of flow is no longer zero, leading to an asymmetrization of the Bogoliubov solutions. In both (a) and (b) cases, the linearization of the solutions at low-k, relating the generation of phonon-type elementary excitations, appears only at the turning point D.

over a large intensity range. In this case, the elementary excitations are related to precursors of instabilities and can be studied in a steady state regime. Their linewidth $\gamma_{Bog} \propto \mathfrak{Im}(\omega_{Bog})$ is narrower than the polariton decay rate, inducing an accumulation of particles at the wavevectors given in Eq. (3.13), in addition to those injected by the driving field. This leads to a reshaping of the spatial distribution of the fluid density.

3.3 Reservoir

The previous theoretical analysis considers the ideal case of a fluid in which the only energy contributions come from the polariton-polariton interactions. However, previous works have proven the presence of a long-lived incoherent reservoir of dark excitons in the semiconductor microcavity systems that adds a parasitic exciton-polariton interaction channel to the fluid.

Ref. [111, 158] have reported it by analyzing the decay time of polaritons stimulated in a coherent regime. For this purpose, a quasi-resonant pulse was sent in the cavity. From the temporal analysis of the resulting photoluminescence, two exponential decays were revealed: a first one short-lived, associated to polaritons; a second one long-lived, associated to excitons although the system were excited well below the excitonic resonance.

This reservoir of incoherent excitons adds an interaction channel to the polariton fluid [158, 6]. Its contribution to the spectrum of elementary excitations is taken into account by adding to the generalized GPE its energy $g_r n_r$ and an additional equation describing the evolution of

the exciton reservoir population

$$\begin{aligned} \mathrm{i}\hbar\frac{\partial}{\partial t}\psi(\mathbf{r},t) = & \left[\hbar\omega_{LP}^{0} - \frac{\hbar^2}{2m}\nabla_{\mathbf{r}}^{2} + V_{LP}(\mathbf{r}) + \hbar g n(\mathbf{r},t) + \hbar \mathrm{g_r n_r}(\mathbf{r},\mathrm{t}) - \mathrm{i}\hbar\frac{\gamma_{\mathrm{c}}+\gamma_{\mathrm{in}}}{2}\right]\psi(\mathbf{r},t) \\ & + \hbar\eta_{LP}F_p(\mathbf{r},t), \end{aligned} \tag{3.14}$$

$$\frac{\partial}{\partial t}\mathrm{n_r} = -\gamma_{\mathrm{r}}\mathrm{n_r} + \gamma_{\mathrm{in}}\mathrm{n}. \tag{3.15}$$

γ_{in} is the decay rate of polaritons into the reservoir and γ_c the previously defined polariton decay-rate, dominated by the optical cavity losses. Consequently the total polariton decay rate is equal to $\gamma = \gamma_c + \gamma_{in}$.

The reservoir density population $\mathrm{n_r}$ involves two terms: a source term fed by the polariton density and a loss term fixed by the decay rate γ_r of excitons. In steady state regime, the population of the exciton reservoir is directly proportional to the density of polaritons $\mathrm{n_r} = \frac{\gamma_{\mathrm{in}}}{\gamma_{\mathrm{c}}}\mathrm{n}$.

Effects of the reservoir. To include the reservoir in our model, we consider an effective interaction term $\mathrm{g_{eff}n_{eff}} = \mathrm{gn} + \mathrm{g_r n_r}$, which allows to integrate in a very simple way the contribution of the exciton-polariton interactions to the dynamics of polaritons. Moreover, the description of the effect of the reservoir on the collective excitations requires a redefinition of the Bogoliubov operator. In addition to taking into account in the eigenvector basis of $\mathcal{L}_{Bog}$ the $U_{\mathbf{k}}, V_{\mathbf{k}}$ plane waves associated to the fluid perturbation, we also add the fluctuations of the dark reservoir density $\delta\mathrm{n_r}$ around these perturbations. This leads to write the Bogoliubov matrix as follows

$$\mathcal{L}_{Bog} = \begin{bmatrix} -\frac{\delta}{\hbar} + \frac{\hbar(\mathbf{k}+\mathbf{k}_{\mathrm{P}})^2}{2m} + \mathrm{g_{eff}n_{eff}} - \mathrm{i}\frac{\gamma_{\mathrm{c}}+\gamma_{\mathrm{in}}}{2} & gn & \mathrm{g_r}\psi_0 \\ -gn & \frac{\delta}{\hbar} - \frac{\hbar(\mathbf{k}-\mathbf{k}_{\mathrm{P}})^2}{2m} - \mathrm{g_{eff}n_{eff}} - \mathrm{i}\frac{\gamma_{\mathrm{c}}+\gamma_{\mathrm{in}}}{2} & -\mathrm{g_r}\psi_0 \\ \mathrm{i}\gamma_{in}\psi_0 & \mathrm{i}\gamma_{in}\psi_0^* & -\mathrm{i}\gamma_r \end{bmatrix}, \tag{3.16}$$

with $(U_{\mathbf{k}}, V_{\mathbf{k}}, \delta\mathrm{n_r})$ its eigenvector basis. The reduced 2x2 matrix is simply the previously derived Bogoliubov operator in Eq. (3.6); the third row/column correspond to the coupling terms between polaritons, the reservoir and the microcavity radiative field. Its diagonalization leads to the following expression of the Bogoliubov dispersion relation

$$\omega_{Bog}(\mathbf{k}) = \hbar\frac{\mathbf{k}_{\mathrm{P}}\mathbf{k}}{m} \pm \left[\left(-\delta(\mathbf{k}_{\mathrm{P}}) + \frac{\hbar\mathbf{k}^2}{2m} + 2gn + \mathrm{g_r n_r}\right)^2 - (gn)^2\right]^{1/2} - \mathrm{i}\frac{\gamma}{2}. \tag{3.17}$$

Note in this expression that the reservoir energy is only added to the average energy of polaritons, fixed by the laser detuning δ, and not to the intrinsic dynamics of the fluid, governed

primarily by the interaction energy gn between polaritons. Therefore, it does not contribute to the elementary excitations dynamics.

For instance, at the bistability higher turning point, the polariton density is now associated to both the laser and reservoir energy via $\delta = gn + g_r n_r$. Correspondingly, one calculates the following Bogoliubov equation, same as before

$$\omega_B(k) = \pm\sqrt{\left(\frac{\hbar k^2}{2m_{LP}}\right)\left(\frac{\hbar k^2}{2m_{LP}} + 2gn\right)} - i\gamma/2. \tag{3.18}$$

One recovers at low-k two linear branches, corresponding to the onset of phonon-like excitations, of speed of sound $c_s^r = \sqrt{\hbar g n / m_{LP}}$ which does not depend on the reservoir energy.

The only significant effect of the reservoir is to lower the renormalization of the system energy due to the interactions between polaritons, with respect to the laser detuning, i.e. $gn = \delta - g_r n_r$ at the TP. Accordingly, the speed of sound as expressed a function of δ is also changed by a factor of proportionality α with respect to the speed of sound of the pure polariton fluid

$$c_s^r = \alpha\, c_s = \alpha\sqrt{\frac{\hbar\delta}{m_{LP}}}. \tag{3.19}$$

From this one can identify the reservoir contribution to the blue shift

$$g_r n_r = (1 - \alpha^2)\,\delta. \tag{3.20}$$

3.4 Numerical analysis

In order to compare the experimental results with our model, we resolve numerically the eigenvalues of the Bogoliubov operator $\mathcal{L}_{Bog}$, based on the methods of Ref. [6]. In our case, the collective excitations are probed with a weak laser beam, assumed to be a plane wave of sufficiently small energy $\delta\omega$ and wave vector $\delta\mathbf{k}$ distributions to be several order of magnitude below the key parameters of our system, respectively its decay rate γ and the inverse of its healing length $1/\xi$.

Such a probe is included in our model by performing a linear-response analysis of the different field involved in Eq. (3.16), leading to the relation

$$\hbar\omega(\mathbf{k}) \begin{bmatrix} U_k \\ V_k \\ \delta \mathrm{n_r} \end{bmatrix} = \mathcal{L}_{Bog}(\mathbf{k}) \begin{bmatrix} U_k \\ V_k \\ \delta \mathrm{n_r} \end{bmatrix} + \delta F_{pr}, \tag{3.21}$$

where $\delta F_{pr} = \beta[1,0,0]^T$ represents the weak probe field, considered as a plane wave driving the perturbation in the $U_{\mathbf{k}}$ mode. $\beta \propto \gamma_c$ is a factor reflecting the coupling efficiency of the probe with the elementary excitations.

The intensity response of the system is given by

$$|U_{\mathbf{k}}|^2 \propto \hbar^2\gamma_c^2|\chi_{11}|^2, \tag{3.22}$$

$$|V_{\mathbf{k}}|^2 \propto \hbar^2\gamma_c^2|\chi_{21}|^2, \tag{3.23}$$

with χ_{ij} the elements of the susceptibility response matrix

$$\chi_{ij}(\mathbf{k},\omega) = \left[\frac{1}{\hbar\omega_{Bog}(\mathbf{k},\omega) - \hbar\mathcal{L}_{Bog}(\mathbf{k},\omega)}\right]_{ij}. \tag{3.24}$$

Thus, by considering a probe at ($+\mathbf{k}$, $+\hbar\omega$), i.e. by stimulating the collective excitation in the $U_{\mathbf{k}}$ mode, one can compute and measure from the cavity output intensity the resulting population density in the respective $U_{\mathbf{k}}$ and $V_{\mathbf{k}}$ modes from the χ coefficients, up to the coupling efficiency factor β we did not determine yet.

Moreover, the simultaneous analysis of the $U_{\mathbf{k}}$ and $V_{\mathbf{k}}$ modes allows the measurement of two different processes of generation of the Bogoliubov modes. According to the decomposition (3.4), whereas $U_{\mathbf{k}}$ is occupied by elementary excitations in the same mode as the probe ($+\mathbf{k}$, $+\omega_{Bog}$), the population of $V_{\mathbf{k}}$ includes modes of opposite wavevector and energy ($-\mathbf{k}$, $-\omega_{Bog}$), which are generated by the scattering between the probe and pump polaritons following the four-wave mixing process

$$(+\mathbf{k}, +\omega_{Bog}), (+\mathbf{k}_{\mathrm{P}}, +\omega_{\mathrm{P}}) \rightarrow (-\mathbf{k}, -\omega_{Bog}), (+\mathbf{k}_{\mathrm{P}}, +\omega_{\mathrm{P}}). \tag{3.25}$$

3.5 State of the art

Before continuing with the experiments at the heart of this chapter, we review here the current state of the literature in the measurement of Bogoliubov excitations in polariton systems, as there have been several proposals, in order to understand the technical issues behind the realization of our own spectroscopy setup.

The spectroscopy experiments can be first classified into two different categories, depending on the polariton driving scheme: the off-resonance experiments, measuring the spectrum of polariton condensates; the quasi-resonance experiments, measuring the photo-luminescence spectrum of coherent polariton fluids, which include our system.

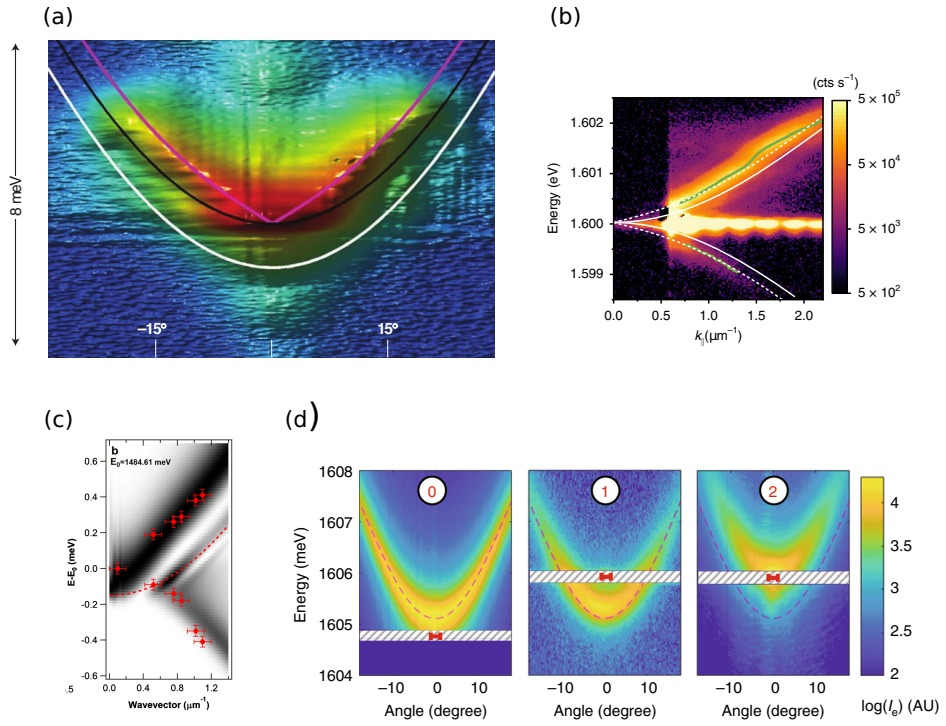

Figure 3.1: **Experimental spectra of elementary excitations. (a-b)** Spectra of the luminescence signal in off-resonance excitation. The sonic dispersion relation is highlighted by the purple and green curves. **(c)** Spectrum of the parametric signal (4WM) in quasi-resonant excitation. Red dots: experimental measurements. Map in the background: theoretical spectrum. **(d)** Spectrum of the luminescence signal in quasi-resonant excitation, in the linear regime, on the lower and higher branch of the bistability. The hatched rectangle indicates the frequency band rejected by a notch filter to eliminate the pump from the detection. Figures from Refs. [168, 133, 90, 158] respectively.

Off-resonance excitation. The most common used scheme of driving of polaritons is the off-resonance pumping, at very high blue detuning with respect to the polariton resonances. The photons are injected in one of the reflectivy dips of the Bragg mirrors, generating an incoherent reservoir of excitons below the energy of the pump. These excitons then reduce their kinetic energy by interacting with phonons, resulting in their relaxation into the lower-polariton branch. In such configuration, the fundamental difference with our resonant cavities comes from the spontaneous emergence of coherence in the polariton fluid. Due to the intermediary relaxation process, the phase and density properties of the fluid are not directly inherited from the pump field: the polaritons and their collective excitations are free to evolve. As presented in the first chapter, such polariton fluids undergo Bose Einstein condensation, so it was historically natural to seek to measure their elementary excitations to study the properties of polariton condensates.

The first report of an experimental measurement of the linear branches of the Bogoliubov sonic dispersion relation was made by S. Utsunomiya et al. in 2008 [168]. The photolumi-

nescence emission of an off-resonance polariton condensate was collected with a spectrometer. When the driving field intensity exceeded the condensation threshold, its spectrum exhibited two linear branches at low-wavevectors, corresponding to the excitation of phonon-like particles on top of the condensate. Further refinements of this technique improving the detection of photoluminescence spectra have been achieved in 2015 to observe the very weak signal of the ghost branch [133, 73]. In particular, in Ref. [132, 131], the detection of such negative Bogoliubov solution showed that its population is driven by quantum fluctuations, leading to a spontaneous depletion of the condensate towards negative energy modes.

However, we will not discuss here in more detail the measurements made with polariton condensates, primarily because their spectrum can differ significantly from that expected in resonant excitation. In particular, it has been shown both analytically [**?**] and experimentally [15] that the polariton condensate dispersion relation exhibits a low-k diffusive Goldstone mode, due to the spontaneous symmetry breaking associated with the condensation process: instead of having only phonon-type collective excitations, the spectra may exhibit an intertwining of its two sonic linear branches with a zero energy plateau over a finite range of wavevectors, not expected in our coherent driving scheme.

Quasi-resonance excitation. The case of coherent driving turns out to be more complicated. The physics differs significantly from that of condensate systems because the dynamics of polaritons is driven by the pump: it seems less obvious that collective excitations, such as phonons, can be spontaneously excited and propagate freely on top of the fluid. Moreover, the presence of the pump conceals the photoluminescence signal of polaritons in an intense photon bath, making difficult to observe directly the spectrum of elementary excitations at small wavevectors, precisely where the dispersion curve deviates from the single-particle parabola. However, as a significant advantage to mention over the off-resonance case, the coherent driving field directly excites the polaritons without the stimulation of intermediate branches that can add additional interaction terms to the dynamics of the system. As such, the analysis of the Bogoliubov spectrum can thus give an estimation of the polariton-polariton interaction energy gn, via the measurement of the speed of sound (although the contribution of a dark reservoir must still be accounted for).

The polariton literature presents a large variety of spectroscopy experiments, each of them innovating in their strategies to reconstruct the elementary excitations dispersion relation. The previous observation of phonon-like particles under coherent excitation is reported in Ref. [91, 90] in 2011, where a pulsed laser pump drives the fluid at quasi-resonance with the LP branch. In addition, a probe laser stimulates at different $\mathbf{k}$ the parametic scattering of polariton into ($+\mathbf{k}$, $-\mathbf{k}$) pairs, via the high Kerr nonlinearity of the system. Then, using a heterodyne detection to extract the four wave mixing emission signal from the pump, the spectrum of the scattered polaritons, observed with a spectrometer, reveals both the linear branches of the Bogoliubov sonic dispersion relation and the ghost branches. Thus, this technique is the first one to prove that it is possible to directly observe elementary excitations in the coherent regime, by means of the scattering between polaritons to populate the Bogoliubov modes. Its

main limitation lies in the use of pulsed lasers: the excitation energy of the system is not well defined, preventing to study the interplay of the elementary excitations dynamics with specific pump parameters.

Ref. [148] and [179] are other quasi-resonance experiments worth mentioning, focused on the detection of the ghost branch. The first one was performed under a pump-probe excitation scheme, revealing for the first time a dispersion of negative mass; the second one achieved a high resolution observation of the PL emission of the negative branch over a large continuous range of wavevectors, after the excitation of polaritons with a weak intensity pulse. However, these did not show the specific signature of elementary excitation, such as the sonic branches of phonon particles, as they were operating in a low intensity regime (low interaction), in order not to be blinded by the pump photons.

Ref. [158] is the latest experimental implementation to our knowledge in which a very accurate measurement of the polariton velocity is achieved in order to measure the contribution of the dark exciton reservoir to the fluid interactions, under continuous and resonant excitation. Here again, the photoluminescence of polaritons is studied. Its observation is realized by eliminating from the detection the pump photons, by filtering the polarization and the energy of the driving field.By a careful processing of the obtained spectra, a precise sound velocity of the polaritons is measured and its deviation from the theoretical case of the polaritonic fluid involving only the pure polariton-polariton interaction allows to measure the dark reservoir interaction strength. This technique exploits the non-zero cross-polarization component due to low residual birefringence and low TE-TM splitting of polaritons, which allows the photoluminescence polarization emitted by the fluid to be filtered in the cross-polarized direction with respect to the laser. This requires the incident field to be linearly polarized, addressing the two circular eigenspins of polaritons: in addition to the interactions between polaritons of same polarizations, interactions between polaritons of crossed polarizations exists, making the analysis of spectra more difficult.

3.6 Experimental implementation

Here are the critical points that we have sought to improve when implementing our setup, with the ultimate goal of making the measurement of the Bogoliubov spectrum as versatile as possible.

- We want to show the dependence of the Bogoliubov spectrum on the excitation. This means that the pump field parameters, such as its intensity and its energy, must be both well defined and precisely tunable. For this purpose, the use of pulsed laser is not adequate: we will rely on cw lasers.
- A complete study of the Bogoliubov modes is only possible if both the real and imaginary parts of the elementary excitations energy are well resolved. The latter, given by the linewidth of the spectrum, can reach values below 1 μeV. The use of a spectrometer as

it is the case in most of the other experiments based on the measurement of the photoluminescence, with a typical resolution of the order of 50 μeV is in consequence not compatible. We must find another tool to measure the energy of collective excitations.

- The number of interaction channels at stake must be as small as possible. Ideally, one wishes to have as unique contribution to the energy of the fluid, the interactions between polaritons. For instance, we do not want to excite different polarization states, which would add new contributions originating from the interactions between polaritons of parallel and antiparallel spins. Therefore, the method used by [158] to filter the Bogoliubov spectrum of the pump signal cannot be exploited in our case.

3.6.1 Experimental setup

The scheme of the experimental setup is shown in Fig. 3.2. It contains three different optical paths: the pump and the probe at the input of the cavity; the detection at the output. It is drawn in this case for a detection in reflection: the input and the output are on the same side of the cavity. However, in our experiments, we can easily change from a detection in reflection, to a detection in transmission. For this last case, in order to keep this scheme valid, one just needs to translate the detection arm from the front to the back of the cavity. All information on the sample and the shaping of the intensity profiles of the laser beams are in the appendices.

Pump path. The pump laser, driving the high-density polariton fluid, is chosen to be as tunable as possible in order to stimulate a broad range of collective excitations. Here we use a circularly polarized cw Titane:Sapphire laser, embedding in its optical cavity a thin etalon allowing a high precision tuning of its energy, centered around the LP resonance at 836 nm. Its intensity is slaved with a proportional–integral–derivative (PID) controller retroacting on the RF driving signal of an AOM, to be able to accurately tune the density excitation point all along the optical bistability. Furthermore, its spatial intensity and phase profiles can be reshaped at will with a spatial light modulator SLM.

Probe path. We decided in our experiments to not rely on the observation of the photolumionescence spectrum of polaritons to measure the spectrum of Bogoliubov. Instead, we look at the modification of the cavity resonances induced by the nonlinearity of the fluid on the transmission or reflection of a probe beam. This one is provided by another cw Titane:Sapphire laser, whose wavelength can be tuned around the polariton energy (836 nm). Its circular polarization is the same as that of the pump.

The experimental main loop consists in the scan of the quantum fluid resonances by tuning the angle of the probe over a discrete range of wavevectors lying in the parabolic bottom area of the dispersion curve. To this end, we use an SLM on which are displayed blazed gratings of tunable steps size, corresponding to different reflection angles of the light sent on it. Therefore, with a cat eye conjugation setup between the cavity and SLM planes, the wavevector of the probe is controlled without changing its working point position in the fluid.

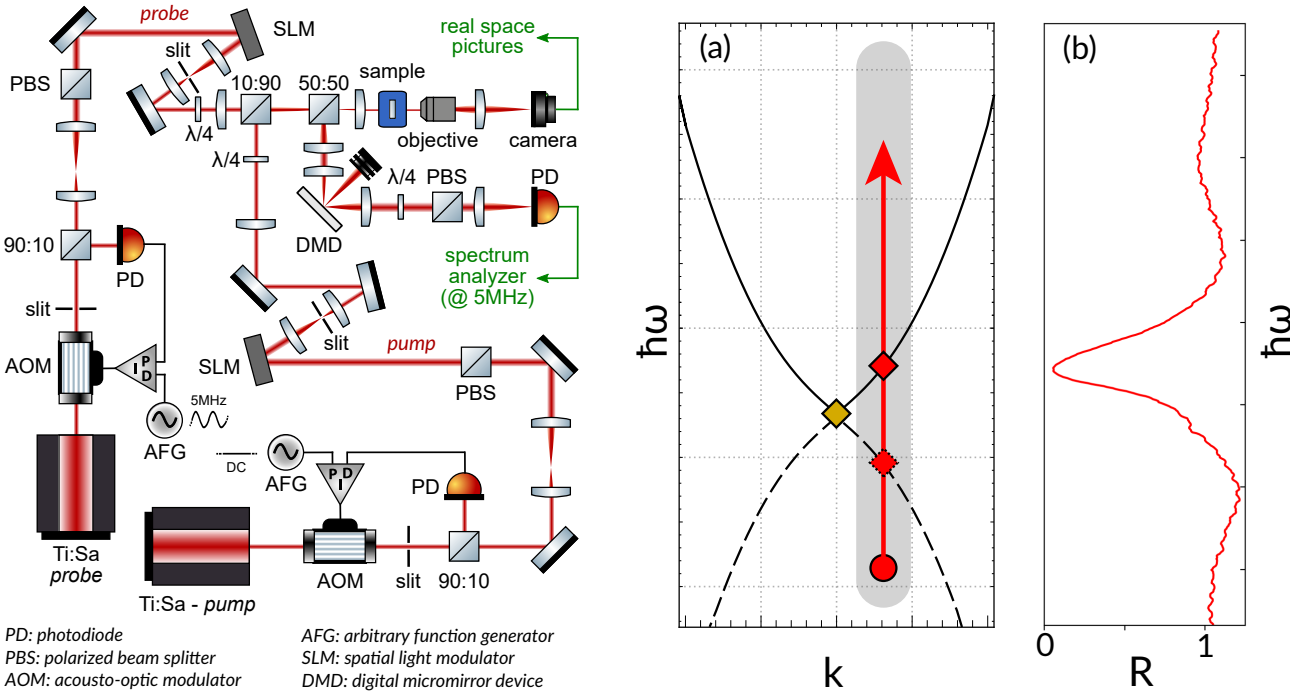

Figure 3.2: **Pump-probe scpectroscopy.** Experimental setup. The sample is placed in a helium cryostat cooled down to 3.8K. Two cw Ti:Sa lasers illuminate it, with the same circular polarization to excite a single spin state. **The pump** injects a high density fluid in the area of its 100µm diameter waist in the plane of the sample. Its intensity I_P is controlled by mean of a proportional-integral-derivative loop (PID) which feedbacks on the RF amplitude of an acousto-optic modulator (AOM). Its phase and intensity profiles can be reshaped with a spatial light modulator (SLM), imaged in the sample plane. **The probe** is recombined with the pump beam thanks to a 90:10 beam splitter. Its waist in the sample plane has a diameter of about 50 μm and an intensity of about 0.1% of I_P. Its wavevector $\mathbf{k}$ is monitored with an SLM, also imaged in the cavity plane, displaying a blazed grating of controllable step size, to change the angle of the first diffraction order, filtered by means of an automatically tunable position slit in the reciprocal space. Its amplitude is modulated with an AOM at $f_{mod} = 5$ MHz, also slaved with a PID loop. The reflection of the cavity is recovered using a 50:50 beam splitter, placed just before the cavity. A DMD in the reciprocal space displays a pinhole of configurable position and size selecting the wavevectors of the signal sent to the detection. In addition, a quarter-wave plate and a PBS operate a polarization selection, to recover only the same polarization state as the pump and the probe. The signal is then focused on a photodiode (PD) and demodulated at f_{mod} with a spectrum analyzer to isolate the probe signal from the pump signal. The transmission of the probe can be easily deduced from this scheme. **(a)** Principle of pump-probe spectroscopy: the pump (yellow square), creates a high density fluid, of dispersion relation depicted by the black lines. The probe scans the resonances of the fluid (red squares), at a fixed $\mathbf{k}$, over an energy range of 150 GHz (red vertical arrow). **(b)** When the probe resonates with the positive branch, a Lorentzian reflectivity dip appears in the reflection signal. The position of the minimum and the full width at the half height of the dip give the real and imaginary parts of the energy of the Bogoliubov mode respectively. In transmission, the signal trace features a Lorentzian peak instead of a dip.

For each of these wavevectors, an energy scan of the probe is operated over 120 GHz (0.5 meV) by tuning the lenght of the laser thin etalon cavity. When its energy matches one of the Bogoliubov modes resonances, the probe is efficiently transmitted by the cavity. Consequently, a transmission peak (reflectivity dip) is observed in the probe signal. In this way, it is possible to reconstruct the dispersion relation of polaritons by measuring both the energy and the momentum of probe transmission (reflection) peaks (dips).

Detection path. In order to separate the probe signal from that of the pump on the detection side, the amplitude of the probe is modulated with an AOM before entering the cavity, at a frequency of $f_{mod} = 5$ MHz which is at least one order of magnitude above the noise bandwidths of the lasers and the various detection devices used. Then, at the output of the cavity, the transmission/reflection signal is focused on a photodiode and then demodulated with a spectrum analyzer centered on f_{mod} to detect only the probe power. In this way, the spectral resolution of the measurements is only limited by the spectral width of the probe laser, here lower than 500 kHz (2 neV).

Fig. 3.2(b) shows a typical reflectivity trace of a probe scan retrieved from the spectrum analyser. A dip is observed, corresponding to the detection of a resonance of the polariton fluid. To find the energy at which it appears, the scan window of the spectrum analyzer is triggered on a TTL reference signal of width matching the beginning and the end of the probe energy scan. In parallel, a wavemeter, also triggered on the same reference signal records at regular intervals the energy of the probe. From these data, we can then directly calibrate the energy scale displayed along the horizontal axis on the spectrum analyzer.

Scan resonances analysis. The shapes of the probe transmission and reflection peaks are directly related to the real and imaginary parts of the energy $\hbar\omega_{Bog}$ of the Bogoliubov dispersion relation. If we consider plane wave like excitations

$$\psi(t) \propto \exp(-\mathrm{i}\omega_{Bog}t) = \exp\left(-\mathrm{i}\mathfrak{Re}(\omega_{Bog})t\right) \cdot \exp\left(\mathfrak{Im}(\omega_{Bog})t\right), \tag{3.26}$$

one easily verifies by taking its temporal Fourier transform that its spectral density has the following Lorentz-distribution law

$$I(\omega) = |\psi(\omega)|^2 \propto \frac{1}{\left(\omega - \mathfrak{Re}(\omega_{Bog})\right)^2 + \left(\dfrac{\mathfrak{Im}(\omega_{Bog})}{2}\right)^2}. \tag{3.27}$$

Such a relation applies for both the detection in transmission and in reflection. For the last case, when a resonance occurs, the trace exhibits a reversed Lorentzian dip rather than a peak. It is related to the probe being injected inside the system when a resonance occurs, therefore to a dip of reflectivity in the intensity trace. Far from resonance, the signal corresponds to that of the total reflection of the probe by the cavity mirrors, so it is renormalized to $R = 1$.

Then, we can directly identified $\mathfrak{Re}(\hbar\omega_{Bog})$ and $\mathfrak{Im}(\hbar\omega_{Bog})$ to be equal to the energy and the HWHM linewidth of the transmission (reflection) peak (dip).

k-space filtering. In order to select the wavevector of the detected resonance, the reciprocal space of the cavity is imaged on a digital micromirror device (DMD), on which a pinhole of tunable shape and spatial position is displayed. It is thus possible to target a specific wavevector $\mathbf{k}_{DMD}$ in k-space with an uncertainty range $\delta\mathbf{k} = 0.0005\ \mu\text{m}^{-1}$ given by the radius of the pinhole. This device will be typically used to detect the scattering of $+\mathbf{k}$, $-\mathbf{k}$ polariton pairs: by adjusting the pinhole position we can detect one specific mode.

Helium cryostat. The experiments are performed at low temperature in order to generate the excitons and thus the polariton fluid. Therefore, we use an Oxford Instrument open-flow helium cryostat, with two circular windows on both side of the cold finger which supports the sample, allowing to detect the polariton emission both in reflection and transmission. A 10^{-6} mbar vacuum is reached thanks to a primary pump and a turbopump. As the cryostat is quite old (2008) and has a few leaks, we usually keep the pumps running while doing the experiments, inducing small vibrations of the sample of the order of 1 μm. Such a cryogenic setup achieved a cooling down of the sample up to 3.6 K, suitable to reach the strong coupling regime.

3.7 Linear regime measurements

As a prelemenary test, we measured first the resonance of the sample in the linear regime. Its energy and wavevector distribution is already well-known thanks to off-resonance PL measurements made previously with a spectrometer.

Spectrum reconstruction. Fig. 3.3 (a) presents the typical reflectivity map we obtain from the differents energy scans of the LP branch operated with the weak probe at different $\mathbf{k}$ and without the pump. One of these scans is plotted in Fig. 3.3 (b), where a reflectivity dips is observed at the energy of the polariton resonance. By iterating such scans at sufficiently close steps of wavevector ($\Delta\text{k} = 0.0189 \pm 0.0005\ \mu\text{m}^{-1}$), one can reconstruct slice by slice the polaritons spectrum of Fig. 3.3 (a).

Polariton parameters By comparing this dispersion relation with the PL off-resonance one, we can ensure that our technique provides consistent measurements, and in particular that the energy and wavevector of the probe associated to the axes of Fig. 3.3 (a) are well calibrated. Furthermore, because the resonance of the LP branch changes along the wedge, it is mandatory to realize at each working point such linear-regime measurement in order to extract the crucial parameters necessary for the data analysis. For each experiments, we need to make sure we measured the following polariton parameters:

- The mass m, given by the inverse of the second derivative of the parabola
- The resonance frequency ω_0, at $\mathbf{k} = 0$ and without interactions. It is the reference for the laser detuning $\delta = \omega_{\text{P}} - \omega_0$.

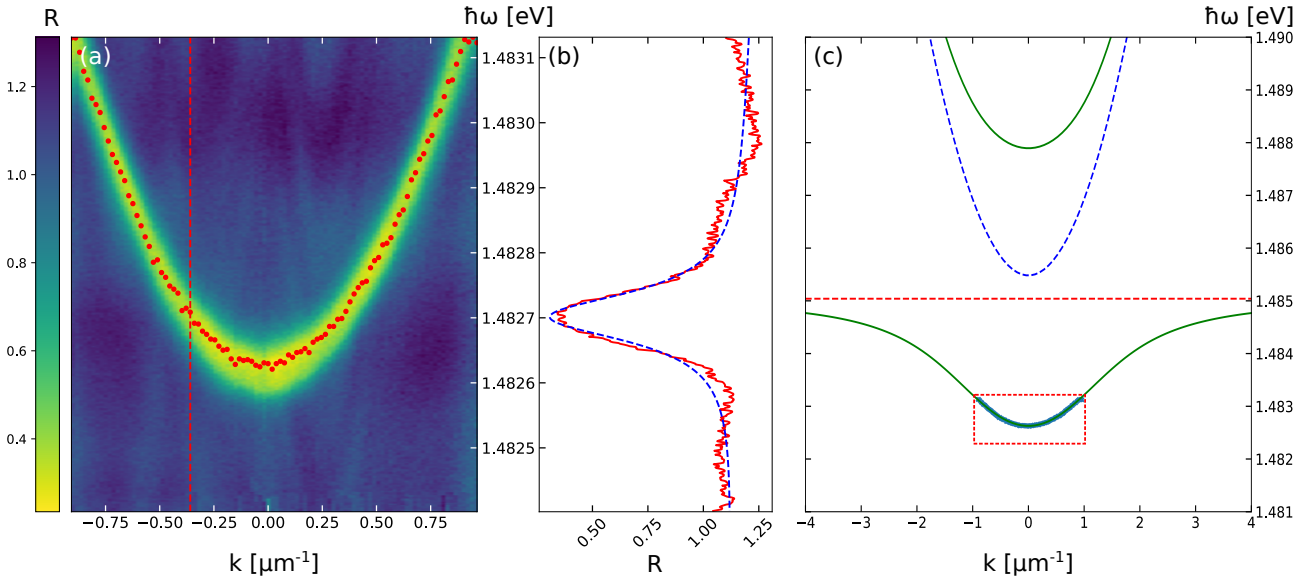

Figure 3.3: **Spectrum of polaritons in linear regime.** **(a)** Reflectivity map plotted as a function of the probe energy $\hbar\omega$ and wavevector $\mathbf{k}$. The red dots indicate the energy of the reflection minima at the different k addressed with the SLM. They give the real part of the Bogoliubov dispersion relation. **(b)** Red line: trace of the probe signal taken along the vertical slice in red dashes on (a); blue line: corresponding Lorentzian fit, used to extract the polariton decay rate $\gamma = 90$ μeV. **(c)** Theoretical plots of the LP, UP (green), photon (blue) and excitons (red) branches. The LP branche is fitted from the minima of (a) lying in the red dashed rectangle.

- The decay rate γ given by the FWHM linewidth of the dispersion relation.

All these parameters are extracted from the fits of the minima/maxima of the reflection/transmission maps with the dispersion relation (2.36), plotted in Fig. 3.3 (c). Notice that the probe scan region lies in the parabolic region of the LP branch.

3.8 Speed of sound measurement

Now that all our analysis and measurement tools have been described, we can discuss experimental results. In order to test the reliability of our setup, our first effort focused on measuring the speed of sound of polaritons.

3.8.1 Preparation of the polariton fluid

The experiments were performed with a pump beam of Gaussian spatial profile, with a diameter of the order of 100 μm and a detuning of at least $\hbar\delta = 0.2$ meV $> \sqrt{3}\hbar\gamma/2$ to be in bistable regime. Each time we want to operate in the high-density regime, we have to tune carefully the pump intensity $I_P = \left|F_p^0\right|^2$. In particular, to address densities lying on the higher branch

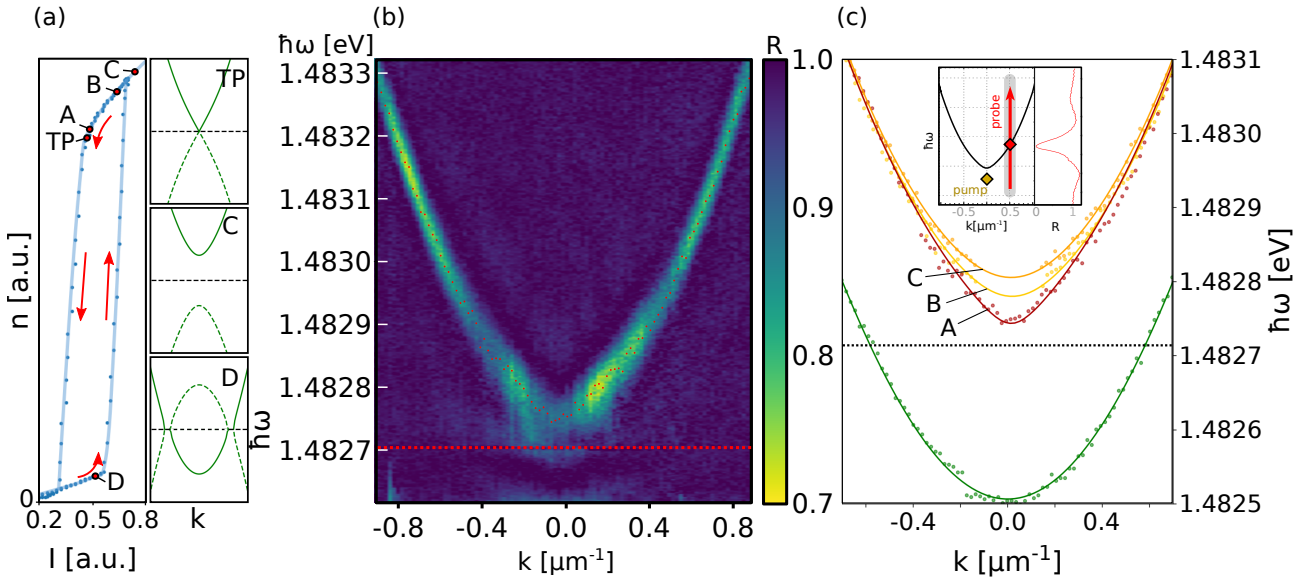

Figure 3.4: **Spectrum of polaritons at different densities. (a)** Left panel: Experimental bistability of the fluid as a function of pump intensity I, at a detuning $\hbar\delta = 0.2$ meV. Points A, B, C and D indicate the densities at which spectrum measurements are carried out. TP highlights the turning point of the bistability. Right-hand panels: expected theoretical dispersion relations at points TP, C and D. **(b)** Reflectivity map plotted as a function of probe energy $\hbar\omega$ and wavevector k, at the point A of the bistability. The horizontal dashed red line gives the pump energy; the red dots the reflectivity minima for each k scanned by the probe. **(c)** Real parts of the Bogoliubov dispersion relations extracted from the reflectivity minima of the spectra captured in nonlinear regime at points A, B and C of the bistability (red, yellow and orange dots) and in linear regime (green dots). The plotted curves are the corresponding fits, calculated from the dispersion relation (3.17). The black dashed line indicates the pump energy. The panel shows the measurement procedure: the probe performs an energy scan at a given k. When it enters into resonance with the polariton dispersion relation, a dip appears in its reflectivity trace (red line). The energy of the minimum of this dip is equal to the real part of the Bogoliubov spectrum.

of the hysteresis loop shown in Fig. 3.4(a), I_P must first be ramped up to the lower turning point, near D, where a sudden jump in density happens, before being smoothly adjusted to reach points A, B or C.

Fig. 3.4(b) shows a typical reflectivity map of the probe with respect to the wavevector k and energy $\hbar\omega$, measured for a pump intensities I_P at the point A, as close as possible to the turning point. At large-k, the dispersion relation matches the parabolic shape of the linear resonance of polaritons. However at low-k, it changes significantly, exhibiting a shape between two linear lines and a parabola. To visualize the modifications of the shape of the dispersion relations as a function of the excitation point A, B and C of the bistability, we extract from each of the reconstructed spectra and at each of the **k** scanned, the real part of the energy of

the Bogoliubov modes, by measuring the energy at which the minimum of reflectivity appears in the trace of the probe (indicated by the dots in Fig. 3.4(b) for the curve A in Fig. 3.4(c) for example). This yields the curves plotted in Fig. 3.4(c), where we have also added the dispersion relation in linear regime, measured at the same working point.

Energy renormalization. First of all, the renormalization of the polariton energy by the interactions is well observed, as evidenced by the energy jump of at least $\hbar\delta = 0.2$ meV of the dispersion curves measured in nonlinear regime compared to the bare cavity resonance. The energy shift depends on the position of I_P on the bistability. As expected in theory, the energy gap decreases as the density is approaching the higher turning point.

Low-k shape. Secondly, the density change is accompanied by a modification of the shape of the dispersion curve. Indeed, a linearization of the spectrum is expected as the turning point is approached by I_P. This is what is observed here: far from the turning point, the dispersion relation has the parabolic shape of the linear regime; in the vicinity of the turning point, a departure from the parabolic regime is observed (see Fig. 3.4 (c) A), leading to a closing of the gap as the interactions strength decreases.

Limitations. The observation of the two linear branches of the Bogoliubov sonic dispersion relation requires to reach precisely the turning point of bistability, below A. In our case, the fluctuations of the laser intensity I_P and detuning δ, as well as the temperature fluctuations in the cryostat, make the direct excitation of this point very challenging: as soon as I_P is lower than that of point A, the system drops from the higher-branch to the lower-branch of the bistability. In order to directly measure the polariton speed of sound, it is therefore necessary to find a way to lock the fluid on the higher-branch of the bistability, exactly at the turning point. Such a solution will be discussed in the following. However, it is possible to develop first a simple model to explain the particular features observed in the spectrum at the point A, and then to extract the behavior at the turning point.

3.8.2 Linewidth analysis

In Fig. 3.5,(a) we excite the fluid with a Gaussian intensity profile, leading to the excitation of a given density distribution governed by the bistability distribution law on the higher branch. As a consequence, the observed spectrum is an average of several dispersion relations corresponding to different density modes. This results in an effective broadening of the linewidth, which exceeds the polariton decay rate $\gamma = 86$ μeV.

High-k broadening. For $\mathbf{k} \gg \xi$, the broadening of the spectrum is not significant, as shown by the plot of the scan at large k in Fig. 3.5 (c), where the fit of the resonance dip allows to measure a linewidth about 5% larger than the polariton decay rate calibrated in linear regime. It results from the excitation of a finite range of interaction energies by the Gaussian pump beam, which, given the evolution law $n \propto I_P^{1/3}$ of the density with respect to the laser intensity, remains small compared to the standard polariton linewidth.

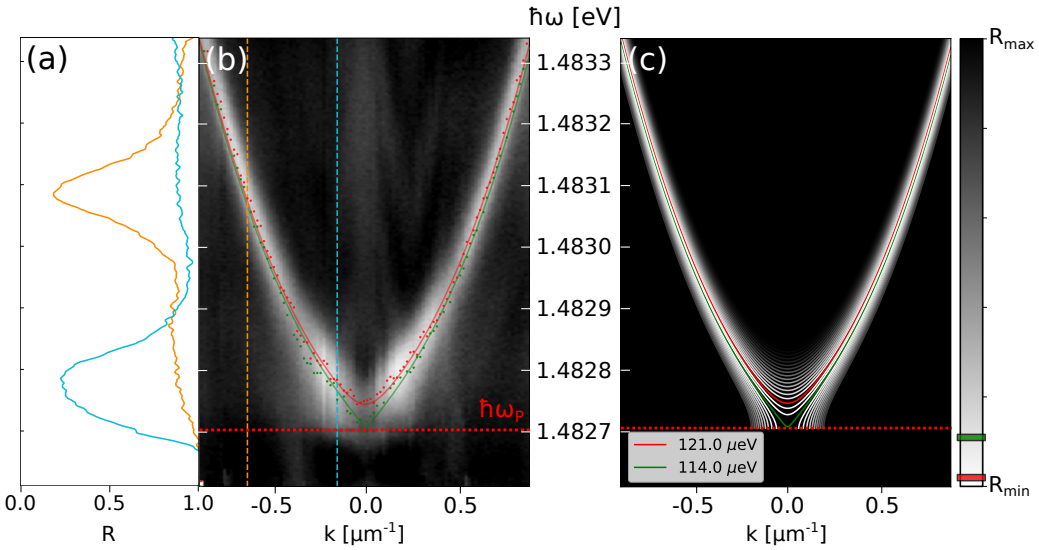

Figure 3.5: **Analysis of the shape of the spectrum linewidth. (a)** Vertical slices taken along the blue dashed lines at $k = 0.16\mu m^{-1}$ and orange dashed lines at $k = 0.64\mu m^{-1}$ of the spectrum shown in (b). **(b)** Reflectivity map of the probe with respect to its wavevector k and energy $\hbar\omega$, at a detuning $\hbar\delta = 0.2$ meV. The horizontal red dotted line indicates the energy of the pump $\hbar\omega_P$. The red points highlight the minima of reflectivity R_{min}; the green points correspond to the reflectivity dips at $R = 0.11 \times (R_{max} - R_{min})$. The red and green curves are the corresponding theoretical fits, obtained for $\hbar gn = 122\mu eV$ and $\hbar gn = 114\mu eV$ respectively. **(c)** Analytical dispersion curves corresponding to concentric rings of equal width in the Gaussian pump, of reflectivity calculated assuming a Gaussian probe. The red curve corresponds to $\hbar gn = 122\mu eV$; the linear green curve to $\hbar gn = 114\mu eV$.

Low-k broadening. At low-k, however, the broadening of the resonance reflects the change in shape of the dispersion curve (including its linearization) as the pump intensity is close to the turning point. This results in an asymmetrical trace of the probe scan, plotted in blue in Fig. 3.5 (c), of linewidth up to 40 % greater than the polariton decay rate.

Phenomenological model. In order to explain such observations, as a first approach one can evaluate analytically the different density modes n excited by the pump by discretising its Gaussian intensity distribution. The pump profile is modelized as a set of concentric rings of equal width w_i and of inner radius r_i, to which are associated a mean value of gn following the bistability relation (2.53). Accordingly, the Gaussian intensity profile of the probe is divided into rings of same width and radius. Then, by considering that the probe beam and fluid area are overlapping and have roughly the same waist, as it is the case in our experiment, each ring of the probe resonates with the pump ring of same width and radius, at an energy depending on its assigned gn value. The real part of the dispersion relations deduced in this way are represented in Fig. 3.5 (c).

In order to reproduce accurately the experimental spectrum, the reflection of each probe ring must be weighted according to its intensity $I(r_i)$, with respect to the total intensity I_{pr} of

the probe. By denoting $A(r_i)$ the area of the ring of radius r_i and $g(r_i)$ a Gaussian distribution evaluated at r_i, the relative intensity for each ring of the probe is expected to be proportional to

$$\alpha_i = \frac{A(r_i) \times g(r_i)}{\sum_i A(r_i) \times g(r_i)}. \tag{3.28}$$

Subsequently, assuming that when the α_i intensity ring enters in resonance with the fluid, the other rings are out-of-resonance and then totally reflected, we can associate to each of the dispersion relations a reflection coefficient proportional to 1 - α_i, color-coded in Fig. 3.5 (c).

For instance, the ring of largest α_i contributes the most to the decrease in the reflectivity of the probe when it resonates. Thus, its dispersion relation should match the distribution of the reflectivity minima of the probe. Since the pump intensity distribution along the optical bistability is not known precisely, we can use it as a reference: its $g_0 n_0$ value is determined by fitting with Eq. (3.17) the minima of the reflectivity map corresponding to the red dots of Fig. 3.5 (b). From this, we can extrapolate the gn of the other rings.

Results. In the end, from the fit of the spectrum minima, plotted in red in Fig. 3.5 (a) and (b), we evaluate $g_0 n_0 = 122.0$ μeV. From there, we compute in Fig. 3.5 (a) the real part of the dispersion curves for each of the model rings, for gn varying from $\pm 20\mu$eV around $g_0 n_0$. Their colors reflects their respective contribution to the total reflectivity of the probe. In this way, it can be seen that, from this very simple model, the shape of the experimental spectrum is adequatly reconstructed.

Speed of sound extraction. Importantly, we manage to discern in Fig. 3.5(c) the Bogoliubov sonic dispersion relation of the bistability turning point, plotted in green and corresponding to the ring of $gn = 114$ μeV, i.e a speed of sound $c_s = 0.58$ μm/ps. From the weighting factors α_i, we can attribute to it a reflectivity of the order of 10%. Then, by following the isoline of same reflectivity on the experimental spectrum corresponding to the green dot in Fig. 3.5(b), we remarkably recover the same linear dispersion.

Therefore, we can deduce with the help of this very simple model the speed of sound of polaritons from the slope of the linear branches of the dispersion curve extracted by isolating the relevant reflectivity isoline.

3.8.3 Direct measurement of c_s

With this model in mind, we decided to directly measure the Bogoliubov sonic dispersion relation by reducing the range of interaction energy felt by the probe during the scans of polaritons. It has been accomplished by reshaping with an SLM the probe intensity profile into a ring of narrow 10 μm width, to spatially select a small range of the density distribution during the scans. We tuned the ring radius to spatially overlap the inner border of the fluid in

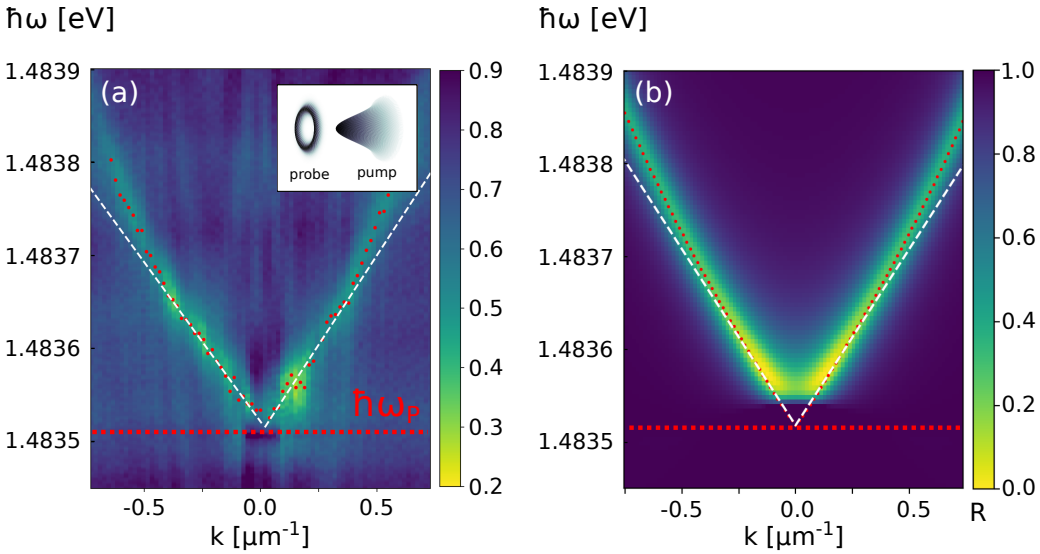

Figure 3.6: **Polariton spectrum at the bistability turning point,** measured at a detuning $\hbar\delta = 0.5$ meV. **(a)** Reflectivity map, plotted as a function of the energy $\hbar\omega$ and wavevector k of the probe. The red dots indicate the reflectivity minima at each of the k scanned; the dashed red horizontal line the pump energy $\hbar\omega_P$. At low-k, two linear branches with no gap with the pump are clearly visible, with slopes equal to the speed of sound, highlighted by the two white dashed lines. They demonstrate the presence of phonon-type elementary excitations in the fluid. **Inset:** Excitation scheme: the probe is reshaped into a 10µm thick ring using an SLM, in order to scan a reduced range of densities in the fluid, whose distribution is governed by the Gaussian intensity profile of the pump. Its radius is chosen to match the density regions closest to the turning point. **(b)** Numerical calculation, performed under the same conditions as the experiment.

the cavity real space, i.e. at the boundary just before the density falls from the higher- to the lower-bistability branch, where the interaction energy is the closest to the turning point.

The resulting reflectivity map as a function of $\mathbf{k}$ and $\hbar\omega$ is shown in Fig. 3.6 (a), where the two linear branches of the sonic dispersion relation are clearly vissible at low-k. The reduction of the energy range experienced by the probe is reflected by the observation of the same resonance linewidth at all wavevectors. The numerical calculation of the model (3.16) in Fig. 3.6 (b), performed with the same parameters as the experiments accurately reproduces the spectrum. Then, from the slope at low-k of the linear branches, the polariton speed of sound is directly measured to be $c_s^r = 0.54\mu$m/ps.

Dependance with the density. This measurement was repeated for different fluid densities, selected by changing the detuning δ of the pump and then the intensity I_{P} to operate as close as possible to the turning point. The speeds of sound c_s^r measured with the fit (3.17) are plotted in Fig. 3.7 (a) as a function of δ. We recover here the expected square root dependence.

Reservoir factor. As already mentioned above, in the case of a pure polariton fluid with only polariton-polariton interactions at stake, c_s is directly related to the laser detuning $\hbar\delta = \hbar g n$. However, the values measured here are twice lower than expected in such ideal case: this is due to the energy contribution $\hbar \mathrm{g_r n_r}$ of the incoherent exciton reservoir to the total blue shift of the fluid $\hbar \mathrm{g_{eff} n_{eff}}$. As the renormalization of the fluid energy to the pump energy still holds at the turning point, i.e. $\hbar \mathrm{g_{eff} n_{eff}} = \hbar\delta$, it follows that the energy of the polariton interaction is lower than expected $\hbar g n < \hbar\delta$, hence a lower speed of sound.

Thus, such speed of sound measurements represent a robust method of assessing the interaction energy of the exciton reservoir. From the calculation of the ratio α between the speeds of sound calculated with and without the addition of the contribution of the dark reservoir, respectively c_s^r and c_s, one can directly infer $\mathrm{g_r n_r}$ associated to the working point of the sample where the experiment is performed

$$\alpha = \frac{c_s^r}{c_s} = \frac{\sqrt{\delta - \mathrm{g_r n_r}}}{\sqrt{\delta}}, \tag{3.29}$$

$$\mathrm{g_r n_r} = (1 - \alpha^2)\delta. \tag{3.30}$$

Fig. 3.7 (b) and (c) show the reservoir factor α and the renormalization energy $\mathrm{g_r n_r}$ extracted from the data of Fig. 3.7 (a) respectively. Note that $\mathrm{g_r n_r}$ depends linearly on δ, so is proportional to the polariton density n. Such behaviour was expected when we assumed in Eq. (3.15) the reservoir to be filled by the non-radiative losses of the polaritons $\gamma_{in} n$. As a result, the reservoir factor $\alpha = 0.59$ is almost constant with respect to δ for the given working point.

Moreover, as a final remark, we noticed experimentally that α can be tuned by changing the exciton-photon detuning $\Delta E_{X-\gamma}$, that is the photonic C and excitonic X Hopfield coefficients, by working at different points of the sample. In general, the more excitonic the fluid is, i.e. for

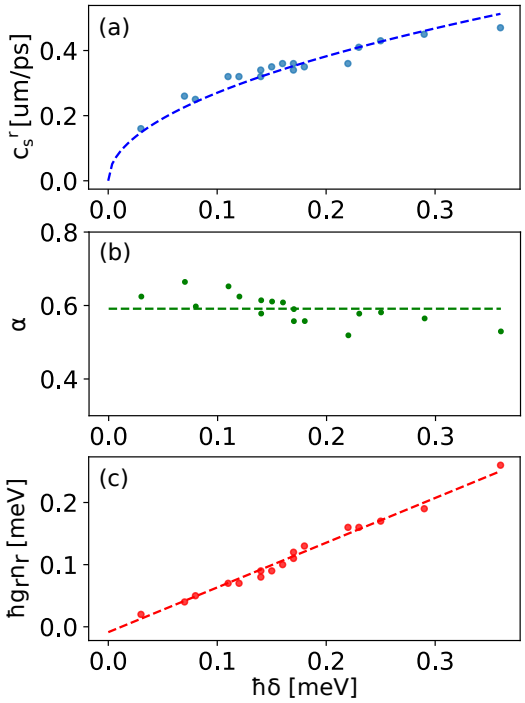

Figure 3.7: **Polaritons speeds of sound.** **(a)** Measurements of the speed of sound c_s for different detunings δ of the pump, carried out at the same working point of the sample and at $\mathbf{k}_P = 0\ \mu m^{-1}$. They are extracted from the fit of the polariton spectra with (Eq.) 3.17. The dashed line corresponds to the fit of the experimental data points. It demonstrates the dependence of c_s on the square root of the density, as $\delta \propto gn$. **(b)** Corresponding reservoir factor α as a function of δ, calculated from the ratio between the speed of sound measured in (a) and the expected speed of sound without reservoir. The green dashed line shows that the reservoir contribution is independent of δ. **(c)** Corresponding energies of the dark exciton reservoir $\hbar g_r n_r$ as a function of δ, also extracted from the fit of spectra with (Eq.) 3.17. The red dashed line indicates the linear dependence of the reservoir population n_r with the polariton density n, as predicted by the theory.

larger values of $|X|^2$, the larger the reservoir factor is. It manifests a more efficient stimulation process of the incoherent excitons. The analysis of such a phenomenon will be carried out in a systematic way in future works.

3.8.4 Dark reservoir spectral signature

As briefly explained above, the reflectivity maps can be analyzed numerically by computing the eigenvalues of the Bogoliubov operator (3.16) at different wavevectors $\mathbf{k}$ and energies $\hbar\omega$ scanned by the probe. In order to reproduce with accuracy the shape of the experimental spectra, the measured key polariton parameters, δ, γ, m and α, are used to calculate $\mathcal{L}_{Bog}$; the remaining unknown parameters, namely the coefficients γ_{in}, γ_r, which give the feeding and decay rates of the exciton reservoir, are tuned iteratively, by comparing the numerical and

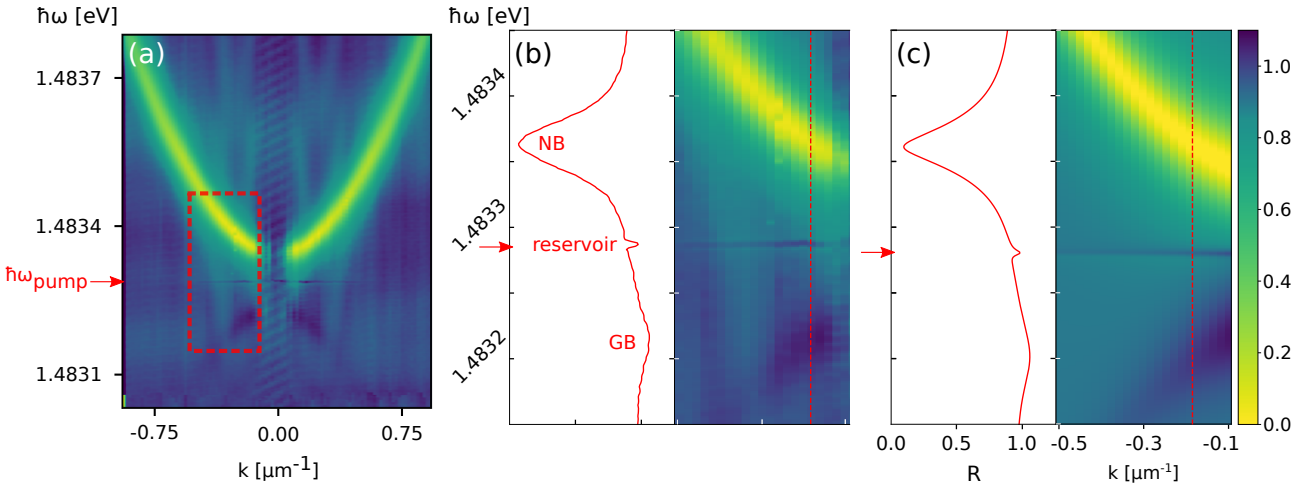

Figure 3.8: **Spectrum of the dark exciton reservoir**, obtained for a detuning and pump wavevector of $\hbar\delta = 0.3$ meV and $\mathbf{k}_\mathrm{P} = 0\ \mu\mathrm{m}^{-1}$. **(a)** Reflectivity map of the probe as a function of its energy $\hbar\omega$ and wavevector $\mathbf{k}$. The pump energy is indicated by the red arrow. The striped area at low-k is due to the saturation of the photodiode in detection by the pump intensity, masking the probe signal. **(b)** Right panel: zoom into the red dashed frame of (a). Left panel: trace of the probe reflection taken along the vertical red dashed line. The normal branch (NB) and the ghost branch (GB) appear as a dip and a peak respectively. An additional signal peak of very narrow linewidth is visible at the pump energy. It is identified as the emission signal from the dark exciton reservoir, originating from the scattering of pump polaritons seeded by the probe. Its spectrum corresponds to the horizontal line of $R > 1$ in (a). **(c)** Numerical calculations performed under the same conditions as the experiment. When the contribution of the dark exciton reservoir is included, the flat spectral line on the right panel and the narrow emission peaks on the left panel are well reproduced. Without the addition of the reservoir, these signatures disappear.

experimental results.

With the help of such numerical calculations, we managed to highlight the spectral signature of the dark exciton reservoir in Fig 3.8. By adding to the model the relaxation of polaritons towards the dark reservoir ($\gamma_r \neq 0$), the numerical result in Fig 3.8(c) shows a flat and very narrow spectral line at the same energy $\hbar\omega_{\mathrm{P}}$ as the pump. These features are typical of the excitations of heavy, long-lived and static particles compared to polaritons, that is, of excitons. For sufficently slow probe energy scans performed around the pump energy in order to achieve a high resolution of the dispersion relations linewidth at the spectrum analyzer, such a flat branch can be observed in Fig 3.8(b), making possible to precisely characterize the exciton reservoir, in particular its decay rate $\hbar\gamma_r = 1.5$ μeV given by the fit of its linewidth and corresponding to a lifetime $\tau_r = 440$ ps, in accordance with the typical expected value [158].

Notice that the reflectivity of the reservoir branch is greater than 1: the probe gains intensity when it enters into resonance with the excitons. We do not detect here a proper resonance behavior, which would have led to a reflectivity dip associated with the injection of the probe, but rather a seed-like phenomenon typical of parametric excitation schemes. Here, the probe is the seed, stimulating the scattering process of polaritons from the pump to the reservoir when at resonance. Thus, the exciton population results indeed from an incoherent process, i.e. not directly stimulated by the pump laser, originating from interactions between polaritons.

3.9 Ghost branch

So far, the detection of the Bogoliubov negative solution has still not been observed in our experiment. This is due to the fact that its resonance, an inverted parabola, does not match any proper resonance of the optical cavity, and, as a consequence, the efficiency of its direct excitation by the probe is expected to be very low.

Gain detection. Nevertheless, its observation can be achieved by enhancing the indirect population of its modes as much as possible, via the exploitation of the four-wave mixing (4WM) process consisting in the scattering of two polaritons from the pump mode ($\mathbf{k}_{\mathrm{P}}$, ω_{P}) toward one mode of the positive branch ($+\mathbf{k}$, $\omega_{\mathrm{P}} + \omega_{Bog}$) and one mode of the negative branch ($-\mathbf{k}$, $\omega_{inc} - \omega_{Bog}$). In such an excitation scheme, the probe fulfills the role of a seed enforcing the parametric scattering of polaritons toward the mode ($\mathbf{k}_{pr}$, ω_{pr}) when at resonance with one of the Bogoliubov branches. In order to reach the most efficient 4WM possible to get the highest polariton population possible in the ghost branch, the driving of polaritons has to be as single-mode as possible, i.e. the distribution of wavevectors $\delta\mathbf{k}$ and energies $\hbar \times \delta\omega$ of the fluid must be as small as possible.

Top-hat excitation scheme. To this end, the probe and pump waists are first chosen to be as large as possible (of the order of 150 μm), corresponding to a wavevector distribution $\delta\mathbf{k} = 0.042$ $\mu\mathrm{m}^{-1}$. Secondly, in order to narrow the energy distribution of the fluid ($\hbar \times \delta\omega = \hbar g \times \delta n$), the polariton density n has to be as homogeneous as possible in the area of the

working point. Therefore, we reshaped the pump intensity profile with a SLM to drive the fluid with a top-hat beam, thus a uniform intensity, leading to the excitation of a very small range of density along the higher-branch of the bistability.

Obviously, one could have also considered using a top-hat beam as well in order to precisely target the turning point of the bistability to observe the Bogoliubov sonic dispersion relation, and to spare the analyses we performed in order to extract the linear branches from the linewidth of the measured spectra. Unfortunately, because of the temperature, intensity and frequency fluctuations inherent to our setup, as soon as the turning point is reached with the top-hat pump, the fluid falls on the lower branch of the bistability, making impossible to capture a spectrum, which requires several seconds of scans. The Gaussian pump that we used previously had the advantage of featuring an intense center, locking on the higher branch of the bistability the neighboring regions of lower intensity, including the one at the turning point, by means of a seed-support effect well known by the team [135].

3.9.1 Reflection detection

Fig 3.9(a) shows the typical reflectivity map observed with the top hat excitation. In addition to the positive branch already presented, here the negative Bogoliubov branch is clearly detected, thanks to an increase in the intensity of the probe, exceeding that at the input of the cavity $R > 1$ (see the color bar of the reflectivity map or the energy scan of the probe taken along the red dashed line). Unlike the normal branch, there is no resonant injection of the probe: we rather detect the creation of polaritons by the aforementioned stimulated 4WM process, hence an increase in the intensity of the probe, provided by the radiative losses of the polaritons scattered in the ghost branch from the pump mode. Such a gain process also occurs at the energy of the positive branch. But, it is masked by the resonance dip because the excitation efficiency of the polaritons at its level is very high compared to that of at the negative branch. However, at very low-k, a decrease in the depth of the reflectivity dip, or even a reflectivity greater than 1 can be observed. Indeed, the 4WM process is more efficient as $\mathbf{k}$ approaches $\mathbf{k}_{\mathrm{P}}$, as the phase matching conditions become close to degeneracy.

3.9.2 Transmission detection

4WM detection scheme. Another possibility to observe the ghost branch is to directly select the scattering modes resulting from the 4WM of the probe and the fluid with the DMD placed in the reciprocal space of the cavity: instead of filtering with the pinhole displayed in the k-space, the cavity emission at the same wavevector as that of the probe ($\mathbf{k}_{DMD} = \mathbf{k}_{pr}$), one can rather select the opposite wavevector ($\mathbf{k}_{DMD} = -\mathbf{k}_{pr}$). Fig. 3.11 shows what is typically observed. Fig. 3.11(b) corresponds to the reflectivity spectrum, obtained under the same top-hat excitation and detection conditions as above, with the DMD selecting the wavevector of the probe ($\mathbf{k}_{DMD} = \mathbf{k}_{pr}$). Fig. 3.11(c) corresponds to the transmission spectrum obtained in 4WM detection, i.e. $\mathbf{k}_{DMD} = -\mathbf{k}_{pr}$. In this case, we looked at the transmission signal as we

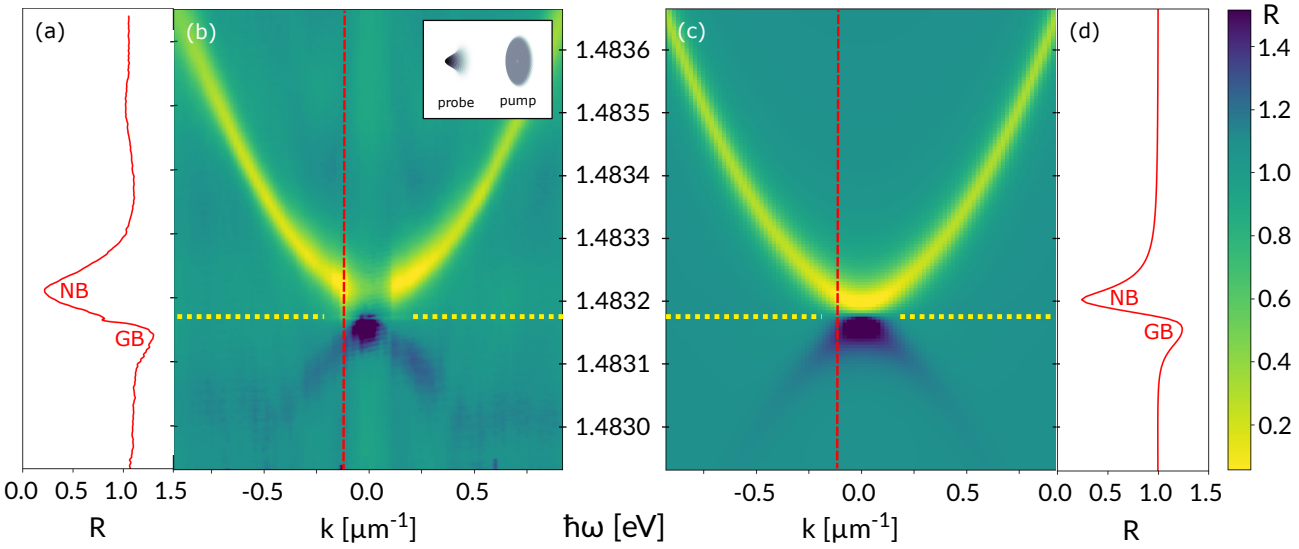

Figure 3.9: **Normal and ghost branches spectrum.** Obtained for a pump detuning and wavevector $\hbar\delta = 0.2$ meV and $\mathbf{k}_\mathrm{P} = 0\ \mu\mathrm{m}^{-1}$. The pump intensity is chosen as close as possible to the bistability turning point. **(a)** Trace of the probe scan taken along the red dashed vertical slice of the map (b). In addition to the $R < 1$ reflectivity dip of the normal branch (NB) resonance, a n $R > 1$ gain peak is discernible under the pump energy highlighted by the yellow dashed line, revealing the ghost branch (GB) resonance by seeding of the 4WM process leading to the scattering of two polaritons from the pump mode toward positive and negative modes. **(b)** Reflectivity map plotted as a function of the energy $\hbar\omega$ and wavevector $\mathbf{k}$ of the probe. The inset shows the top-hat excitation pattern, which increases the efficiency of the 4WM processes between the probe and the pump. The NB appears at $R < 1$; the GB appears below the pump energy at $R > 1$ and is of greater intensity the closer the probe wavevector is to the pump wavevector, since the 4WM becomes more efficient as its phase matching conditions become quasi-degenerate. **(c, d)** Corresponding numerical calculations, made under the same conditions as (a, b).

.

did not achieve to observe the ghost branch signal in reflection with this configuration. These two maps were obtained for the same experimental parameters and at the same working point. In the latter, we have deliberately masked the transmission at low-k, as we recover the direct signal of the probe $\mathbf{k}_{DMD} \simeq -\mathbf{k}_{DMD} \simeq \mathbf{k}_{pr} \simeq 0$.

U and V coefficients. These two types of detections are of primary importance for us, because they give access to the densities of the Bogoliubov excitations, via the measurement of the $|U_k|^2$ and $|V_k|^2$ intensities of the two counterpropagating perturbations described in Eq. (3.21). In direct detection ($\mathbf{k}_{DMD} = \mathbf{k}_{pr}$), the response of the system is proportional to the population in the U_k mode, while in 4WM detection ($\mathbf{k}_{DMD} = -\mathbf{k}_{pr}$), it is proportional to the population in the V_k mode. Therefore, for a given perturbation, i.e. a given ($\mathbf{k}_\mathrm{pr}$, ω_pr), we can directly reconstruct the resulting Bogoliubov field, up to a coupling factor, weighting

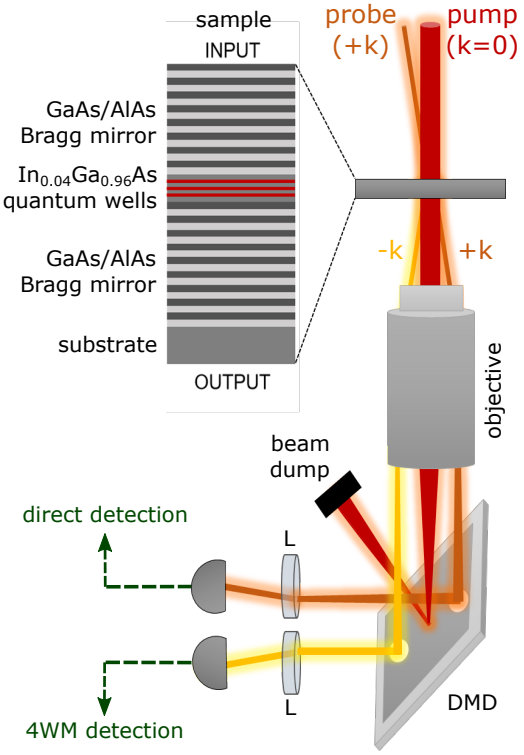

Figure 3.10: **Spectroscopy detection scheme.** The cavity is illuminated at $\mathbf{k} = 0$ μm^{-1} by an intense pump beam. The elementary excitations of the resulting polariton fluid are stimulated with a probe beam injected at $+\mathbf{k}$, modulated at $f_{mod} = 5MHz$ using an acousto-optic modulator (AOM). A large aperture objective ($\theta/2 = 40.5°$) collects the photons emitted at the output, including those from the pump, the probe and the four-wave mixing (4WM) of the probe with the pump at $-\mathbf{k}$. It images the reciprocal space of the cavity on the chip of a digital micromirror device (DMD), which displays a pinhole of precisely tunable radius and position $\mathbf{k}_{DMD}$, selecting either photons from the probe $\mathbf{k}_{DMD} = +\mathbf{k}$ (direct detection) or photons from the 4WM $\mathbf{k}_{DMD} = -\mathbf{k}$ (4WM detection). Other non-selected photons are eliminated by means of a beam dump. At the output of the DMD, a photodiode collects the filtered signal. It is linked to a spectrum analyzer which demodulates the total signal at f_{mod}, allowing the signal of the probe (or its 4WM) to be isolated from the intense bath of pump photons when the pinhole of the DMD is close to the pump wave vector.

the efficiency of stimulation of elementary excitations with the probe. Now, we do not have a direct access to the value of such a factor: we will try to evaluate in future works. As it is, however, this detection scheme provides already a sufficient tool to study the evolution of the elementary excitation densities as a function of the parameters of the pump and the probe.

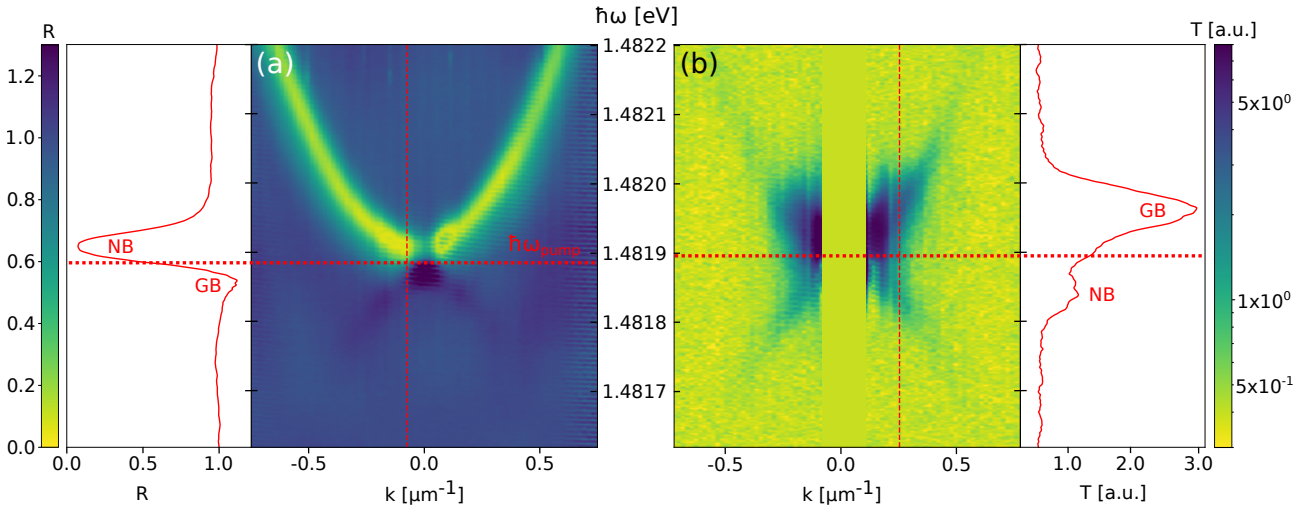

Figure 3.11: **Direct and 4WM detection spectra,** obtained for a pump detuning and wavevector $\hbar\delta = 0.05$ meV and $\mathbf{k}_\mathrm{P} = 0mu\mathrm{m}^{-1}$. **(a)** Left-hand panel: Reflection trace of the probe taken along the red dashed vertical line of the spectrum. Right-hand panel: Reflectivity map as a function of the energy $\hbar\omega$ and the wavevector $\mathbf{k}$ of the probe, made in direct detection, with the DMD monitored to select the $k_{DMD} = \mathbf{k}$ signal. The pump energy is indicated by the red dotted horizontal line. . The normal branch (NB) and the ghost branch (GB) appear as a dip and a peak in the reflectivity signal respectively. **(b)** Left-hand panel: Transmission map of the probe as a function of its energy and wavevector. The detection is in 4WM configuration, i.e. $k_{DMD} = -k$. Right-hand panel: Trace of the probe transmission taken along the red dashed line. When the probe is at resonance with NB ($\omega > \omega_{pump}$), the detection collects the 4WM scattering at the wavevector opposite to the probe, related to the GB emission. Plotted as a function of the probe energy, GB appears as a peak at $\omega > \omega_{pump}$. It has been confirmed with a spectrometer that its energy is indeed $\omega_{GB} < \omega_{pump}$. When the probe is at resonance with GB ($\omega < \omega_{pump}$), the scattering towards the NB is also detected via a second peak in the energy scan.

3.10 Dynamical instabilities

Polaritons are now excited as close as possible to the turning point of the lower bistability branch, in the low-density regime. Consequently, the interaction energy drops with respect to the previous cases, leading to a shift towards the red of the spectrum, recovering the standard parabolic shape of linear regime. However, unlike the spectra obtained in linear regime, a residual density remains here, sufficient to induce a local modification of the polariton dispersion curve.

Direct detection. Indeed, thanks to the high resolution of our spectroscopy technique, we detect in the direct detection reflectivity spectrum pictured in Fig. 3.12(b), two very narrow plateaus corresponding to the crossing of the positive and negative Bogoliubov branches at the pump energy, highlighting the signature of weak interactions. Such plateaus are detected via the

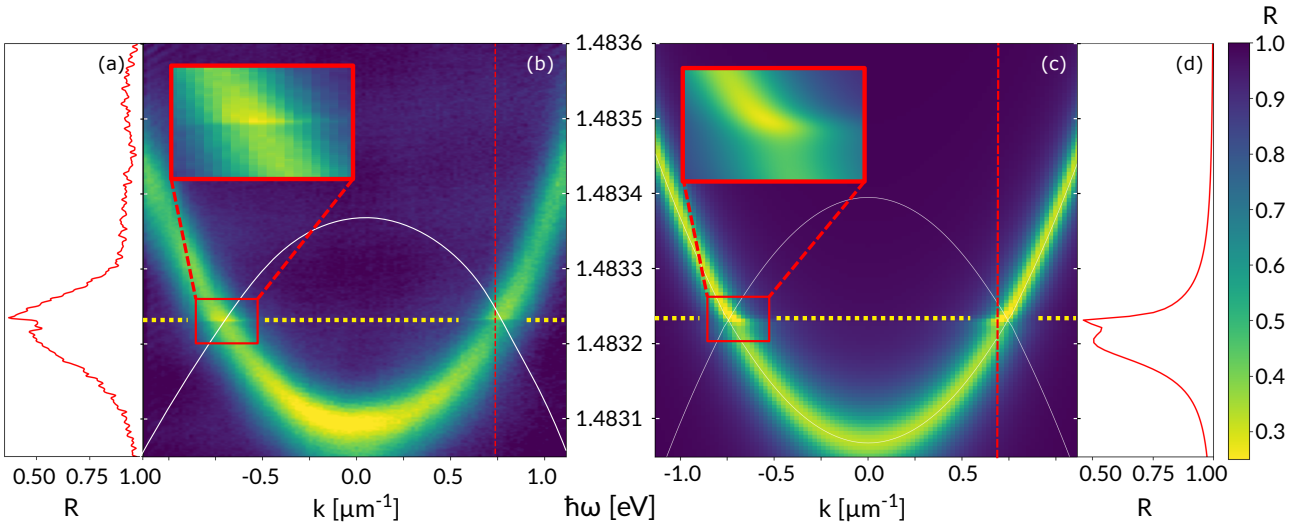

Figure 3.12: **Precursors of modulation instability spectrum**, obtained at pump detuning and wavevector $\hbar\delta = 0.14$ meV and $\mathbf{k}_P = 0$ μm^{-1}. The pump intensity is adjusted to be as close as possible to the lower turning point of the bistability. **(a)** Trace of the reflectivity of the probe taken along the horizontal red dashed line of the spectrum in (b). The resonance of the normal branch corresponds to the dip in the signal. **(b)** Reflectivity map of the probe as a function of its energy $\hbar\omega$ and its wavevector $\mathbf{k}$. The yellow dashed line indicates the pump energy; the white inverted parabola corresponds to the theoretically expected ghost branch dispersion relation. At the intersection of the normal and ghost branches, narrow plateaus are visible in the spectrum (see zoom in the red box), due to the local onset of gain on the probe, as evidenced by the narrow peak in the reflectivity dip shown in the scan (a). They result from the real part of the Bogoliubov spectrum being equal to zero (here the pump energy) over a finite range of wavevectors, and from the imaginary part having a modulus smaller than the standard polariton linewidth, set by the polariton decay rate γ. **(c-d)** Corresponding numerical calculations performed with the same parameters as the experiment.

modification of the shape of the probe reflectivity dip (see the energy scan of Fig. 3.12(a) and (d) taken along the vertical line in red dotted line), which exhibits a narrow peak, corresponding to the detection of gain. Still, the shape and linewidth of the spectrum remains governed by the transmission of the probe through the bare resonance of the sample in the fluid background, partially concealing the effects of interactions between polaritons and therefore making difficult to extract the properties of modes associated to the gain peaks.

4WM detection. To further improve the detection of these spectral narrow features, we implemented again the aforementioned 4WM detection scheme, presented in Fig 3.13. The 4WM transmission map in Fig. 3.13(b), obtained under the same experimental conditions than the direct reflectivity map in Fig. 3.13(a), shows the detection of the ghost branch, crossing the normal branch at the plateaus energies and wavevectors, which confirms that local transformation of the spectrum is originating from the coupling of the positive and negative Bogoliubov solutions. Remarkably, since the 4MW detection only captures the modes resulting from the

scattering with pump polaritons and thus eliminates from the signal the bare resonance of the cavity (i.e. the direct transmission of the probe), the spectrum only includes the resonance of the fluid associated to the excitation of the lower bistability branch. In particular, at the level of the plateaus, we can extract precisely the linewidth of the elementary excitations, from which $\mathfrak{Im}(\hbar\omega_{Bog})$ is measured equal to 10 μeV, much smaller than the decay rate of polaritons γ.

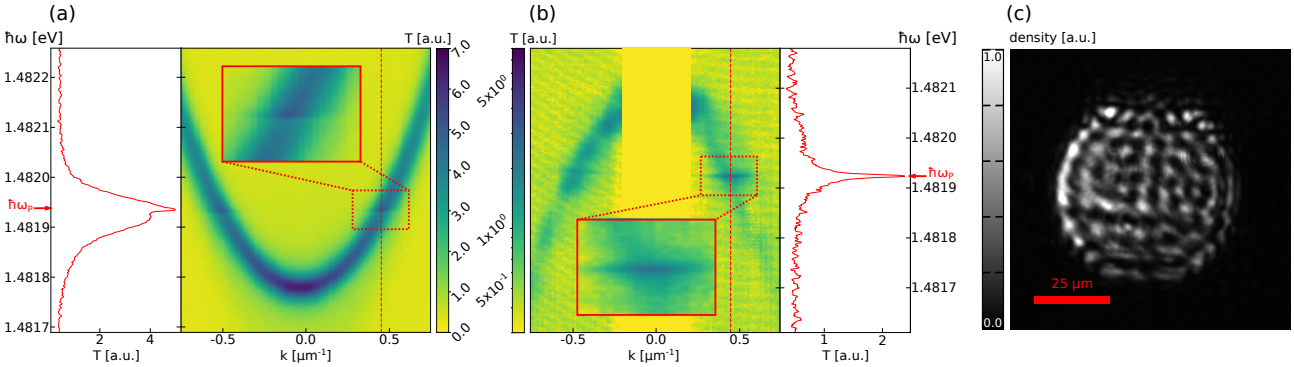

Figure 3.13: **Direct and 4WM detection of modulation instability precursor spectra,** for a pump intensity near the lower bistability turning point and a detuning $\hbar\delta = 0.16$ meV. **(a)** Right panel: transmission map of the probe in direct detection. Left panel: slice along the vertical red dashed line of the spectrum. At the pump energy, a narrowing and amplification of the probe is visible, related to the change in the imaginary part of the energy of the elementary excitations. The zoom in the red dashed inset highlights a narrow plateau in the spectrum, signature of the onset of precursor of modulation instabilities at the pump energy $\hbar\omega_{\mathrm{P}}$ indicated by the red arrow. **(b)** Left panel: transmission map of the probe in 4WM detection, under the same experimental conditions as (a). k and $\hbar\omega$ are respectively the energy and wavevector of the 4WM emission. The ghost branch is detected. The plateau is clearly visible at the crossing point with the normal branch, with a better resolution than in (a). Right panel: slice along the vertical red dashed line of the spectrum. The sub-γ linewidth of the resonance peak gives the imaginary part of the energy of the modulation instability precursor. (c) Density map of the fluid in the cavity plane.

Modulation instabilities. This narrowing reveals the excitation of precursors of modulational instabilities mentioned in the previous part. The associated gain reveals the generation of polaritons at different wavevectors than that of the pump, modulating the polariton density at the spatial frequency of the normal and ghost branch crossing wavevectors. Fig. 3.13(c) shows the density map related to the dispersion relation in Fig. 3.13(a) and (b). A density modulation pattern is observed. Although such turbulent dynamics, with a characteristic evolution time τ of the order of the polariton lifetime, i.e. about 15 picoseconds, cannot usually be resolved by the low temporal resolution of our cameras, here the structural defects in the cavity plane fix the shape of the fluid. This means that the spatial frequency of the density pattern results from a balance between the wavevectors of the instability plateaus of the spectrum and the distribution of the cavity structural defects.

The use of the term precursor comes from the fact that these instability modes remain dynamically stable in the Bogoliubov terminology, i.e. $-\hbar\gamma/2 < \mathfrak{Im}(\hbar\omega_{Bog}) < 0$, thanks to the losses inherent to our system.

3.11 Outlooks

The spectroscopy technique is very versatile and can be generalized to many other of excitation of polaritons.

Analogue gravity

In analogue gravity experiments [20], for instance, the polariton flow is designed to simulate the geometry of the gravitational field around an astronomical black hole. In this picture, phonons in the fluid going at the speed of sound and dragged by the flow represent photons going at the speed of light and trapped by the black hole [76].

1D black hole. In a one-dimensional geometry, a region upstream of a cavity structural defect is driven in the subsonic regime $v < c_s$, whereas another region downstream is driven in the supersonic regime $v > c_s$. The use of a defect, i.e. a local modification of the external potential felt by polaritons, operates an abrupt break between these two flow regimes, thus allowing a clear definition of the position of an event horizon at the point of intersection of the sound and fluid velocity curves $v = c_s$, boundary from which the phonons coming from the upstream region $x < 0$ can no longer oppose the flow of the fluid and thus find themselves trapped in the downstream region $x > 0$ [64]. This is thereby an analogue to a black hole, first achieved experimentally in Ref. [125]. With our spectroscopy technique, we can precisely reconstruct the flow and sound velocity profiles and then adjust the pump parameters to obtain the ideal black hole geometry. Moreover, it is then possible to probe the spectral signatures of the transmission and reflection of elementary excitations at the level of the event horizon, in order to observe effects analogous to the Hawking radiation, responsible for the creation of particle pairs of opposite energies at the boundary of a real black hole [68].

Rotating black hole. Secondly, we have a long track record in the team of giant vortex generation in polariton fluid [30, 76], with the help of Laguerre-Gauss beam profiles shaped with a SLM. The subjacent flow structure can be reinterpreted in terms of a two-dimensional rotating black hole [154]. Indeed, such a geometry siphons the fluid at the level its non-excited core, thanks to the inherent losses of the system, generating a radial acceleration of the flow towards its center at $r = 0$. In addition, by tuning the Laguerre-Gauss mode order, a specific azymuthal acceleration can be added. Thus, in addition to an event horizon $v = c_s$, the giant vortex includes a second boundary, delimiting the ergosurface of a rotating acoustic black hole, where the azymuthal speed of the flow is greater than the speed of sound. In such a region, it is expected that for certain propagating wavevector, the elementary excitations can be amplified by pulling some energy out of the background flow. This is the analogue of the Penrose

phenomenon, that we can also try to measure with the pump-probe spectroscopy, looking in particular for gain signatures on the probe.

Turbulence

As already discussed, our technique can also be used to study turbulent regimes of polaritons. Indeed, it allows a spectral detection of instability modes, which has the advantage of not requiring the use of devices with a high temporal resolution (streak camera and pulsed lasers) to resolve the typical picosecond dynamics of the fluid. We have only presented here the excitation of precursors of modulation instabilities, on the lower branch of the bistability, which remain dynamically stable thanks to the cavity losses. But it is possible to consider other excitation schemes operating a sustaining of the fluid in an unstable dynamic regime.

Dark solitons in channel. As explained in a next section, the generation of dark solitons in a confinement channel dug in the density of the fluid reveals such modulation instabilities, leading to the formation of vortex-antivortex streets [92, 46]. We have investigated in such a configuration these instabilities through the spatial distribution of vortices. But, with the pump-probe spectroscopy, the analysis can be pushed even further by measuring exactly the intensity, energy and momentum of the elementary excitations at stake.

Counter-propagative flows. Second geometry considered, the creation of two counter-propagating fluids, either in collision or in shear configurations, can result in the creation of vortex pairs due to instabilities forced by the pump injecting polaritons at to two opposite and non-zero wavevectors. Depending on the speeds of flow with respect to the speed of sound, different unstable modes can be addressed, such as Kelvin-Helmotz and super-radiant instabilities, with different Bogoliubov spectra, that can potentially be identified with our technique [61].

Chapter 4

Goldstone mode of a planar polariton fluid in Optical Parametric Oscillation regime

The coherent probe spectroscopy technique is versatile enough to be used in completely different excitation regimes of polaritons. In the previous chapter we demonstrated its performance with the analysis of the spectrum of elementary excitations of a coherently driven fluid; here we will present its use on a polariton fluid obtained in Optical Parametric Oscillator (OPO) regime: the resonant pumping in the vicinity of the inflection point of the LP branch generates the scattering of polaritons in a signal and idler condensates, whose phase is not fixed by the driving field. Like Bose-Einstein condensation or laser emission, such an excitation scheme entails a spontaneous breaking of the continuous phase symmetry of the system. Consequently, the Goldstone theorem predicts that the spectrum of the elementary excitations of polaritons should exhibit a vanishing (gapless) energy mode in the long wavelength limit.

The objective of this chapter is therefore to measure with our spectroscopy technique the dispersion curve of such a mode, in order to describe the specificities of an out-of-equilibrium system and to prove that it is indeed the consequence of a spontaneous symmetry breaking transition. This work is based on the theoretical study of M. Wouters and I. Carusotto [177].

4.1 Spontaneous symmetry breaking

As a general definition, a spontaneous symmetry breaking (SSB) occurs when a symmetric system, i.e. with an Hamiltonian $\mathcal{H}$ invariant under a unitary transformation $\mathcal{U}$, has a ground state $|\Psi\rangle$ that is no longer symmetric with respect to this same transformation. The following two conditions must therefore be met

$$[\mathcal{U}, \mathcal{H}] = 0 \quad \& \quad |\Psi\rangle \neq \mathcal{U}\,|\Psi\rangle\,. \tag{4.1}$$

As a consequence, one can associate a new state to every symmetry-broken ground state: if $|\Psi\rangle$ exists, then $\mathcal{U}\,|\Psi\rangle$ also exists. Furthermore, the symmetry of the Hamiltonian implies

$$\mathcal{H}\left(\mathcal{U}\,|\Psi\rangle\right) = \mathcal{U}\mathcal{H}\,|\Psi\rangle = \mathcal{U}E_\Psi\,|\Psi\rangle = E_\Psi\mathcal{U}\,|\Psi\rangle\,, \tag{4.2}$$

with E_Ψ the eigen-energy of $\mathcal{H}$ related to the state $|\Psi\rangle$. The two different states $|\Psi\rangle$ and $\mathcal{U}\,|\Psi\rangle$ have the same energy. Thus, if we consider a continuous symmetry, a whole collection of degenerate broken symmetry states can be mapped by performing the transformation $\mathcal{U}$.

4.2 Goldstone mode

As a consequence of the spontaneous breaking of a continuous symmetry, the spectrum of elementary excitations of the system under consideration exhibits massless particles. These stem from the so-called Goldstone mode, predicted by the eponymous theorem following the work of Y. Nambu [122] and J. Goldstone [63]. In its non-relativistic version [98], the theorem states that the Goldstone mode emerges in the Bogoliubov spectrum in the form of an elementary excitation whose energy tends to 0 (gapless) in the long-wavelenght limit $\mathbf{k} \to 0$.

As a paradigmatic illustration of Goldstone modes, one can mention those originating from systems with a second-order phase transition, responsible for SSB at the vicinity of some critical points. For instance, the magnon branch is associated with the spontaneous breaking of the rotational symmetry of the magnetic moment orientation of ferromagnets, when the temperature falls below the Curie critical temperature [97]. Another example, more related to quantum fluids, is the zero-sound mode, which is a manifestation of the spontaneous breaking of the U(1) gauge symmetry of the mean field of thermal equilibrium Bose-Einstein condensates [128, 74, 56]. The characteristic long-range spatial and temporal coherences observed in such systems witness the vanishing spectrum in the low-k limit. Finally, works linking the laser threshold to a second-order phase transition evidence also an SSB [50]. Similar to ferromagnets, where each spin aligns itself with the direction of the mean magnetic field generated by all the other spins, each atom in a laser develops a radiative dipole aligned with the mean electromagnetic field emitted by all the other atoms, when the critical threshold level of population inversion is reached. Therefore, a laser system should be the seat of a Goldstone mode.

In the following, we will present the measurement of a Goldstone mode in the polariton system, excited under optical parametric oscillation (OPO) regime, which, as we will see, embodies an SSB whose description lies at the boundary between the laser and BEC systems.

4.3 Optical parametric oscillation

Parametric processes in semiconductor microcavities arise from the large third order nonlinearities induced by the interactions between the QWs excitons. We first present here the nonlinear equations governing the evolution of the field in such a medium, first from the point of view of nonlinear optics in order to explicit the four-wave mixing (4WM) that emerges in our system, then from the point of view of polaritons.

4.3.1 Parametric conversion

In the language of nonlinear optics, the response of matter to an incident electromagnetic wave $\mathbf{E}$ is described by the generation of a new field $\mathbf{P}$, called the dielectric polarization. For sufficiently large optical powers, $\mathbf{P}$ is a nonlinear function of $\mathbf{E}$

$$\mathbf{P} = \mathbf{P}^{(1)} + \mathbf{P}^{(2)} + \mathbf{P}^{(3)} + ..., \tag{4.3}$$

with,

$$\mathbf{P}^{(n)}(\omega = \omega_1 + \omega_2 + ... + \omega_n) = \epsilon_0 \chi^{(n)}(\omega_1, \omega_2, ..., \omega_n) \otimes E(\omega_1)E(\omega_2)...E(\omega_n), \tag{4.4}$$

where ϵ_0 is the vacuum permittivity and $\chi^{(n)}$ the susceptibility tensor of order n. The expression of the latter can in principle be entirely determined by the intrinsic properties of the matter, for instance, the linear susceptibility $\chi^{(1)}$ is directly related to the medium refractive index n via the equality $n^2 = \mathrm{Re}\left(1 + \chi^{(1)}\right)$. To each of the higher orders $n > 1$ is assigned a different nonlinear optical process. These are described by the propagation equation of monochromatic plane waves in an isotropic medium

$$\nabla \mathbf{E} - \frac{1}{c^2}\frac{\partial^2}{\partial t^2}\left(\mathbf{E} + \frac{\mathbf{P}^{(1)} + \mathbf{P}^{(NL)}}{\epsilon_0}\right) = 0, \tag{4.5}$$

in which $\mathbf{P}^{(1)} = \epsilon_0 \chi^{(1)} \mathbf{E}$ and $\mathbf{P}^{(NL)} = \sum_{i>1} \mathbf{P}^{(i)}$ are respectively the linear and the nonlinear dielectric polarizations, and $\mathbf{E}(z,t) = \sum_i A_i \exp(\mathrm{i}k_i z - \mathrm{i}\omega_i t)$. Then, under the approximation of slowly varying amplitude, Eq. (4.5) is written in the following simplified form

$$\sum_i 2\mathrm{i}k_i \frac{\partial A_i}{\partial z} \exp(\mathrm{i}k_i z - \mathrm{i}\omega_i t) = \frac{1}{\epsilon_0 c^2}\frac{\partial^2 \mathbf{P}^{(NL)}}{\partial t^2}, \tag{4.6}$$

with $k_i^2 = n_i^2 \omega_i^2 / c^2$. By decomposing $\mathbf{P}^{(NL)}$ into a sum of monochromatic plane waves

$$\mathbf{P}^{(NL)}(z,t) = \sum_i \mathcal{P}_{\omega_i}^{(NL)}(z)\exp(-\mathrm{i}\omega_i t), \tag{4.7}$$

we obtain a final set of equations relating the amplitudes of the input field A_i to the component $\mathcal{P}_{\omega_i}^{(NL)}$ of the induced dielectric polarization

$$\frac{\partial A_i}{\partial z}\exp(ik_i z) = \mathrm{i}\frac{\omega_i}{2\epsilon_0 n_i c}\mathcal{P}_{\omega_i}^{(NL)}. \tag{4.8}$$

In what follows, only the third order linear process is relevant, arising from the dielectric polarization of amplitude

$$\mathcal{P}_{\omega_i}^{(3)}(z) = \sum_{jkl}\epsilon_0\chi_{jkl}^3 A_j A_k^* A_l \exp\left[\mathrm{i}\left(\mathbf{k}_j - \mathbf{k}_k + \mathbf{k}_l\right)\cdot\mathbf{z}\right]. \tag{4.9}$$

It describes a four wave mixing process (4WM), of frequencies $(\omega_i, \omega_j, \omega_k, \omega_l)$ and wavevectors (k_i, k_j, k_k, k_l) . By injecting it into Eq. (4.8) and then integrating along the length L of the nonlinear medium, one obtains the output intensity

$$|A_i(L)|^2 = \left(2\frac{\omega_i\chi_{jkl}^{(3)}}{n_i c}\right)^2 |A_j|^2|A_k|^2|A_l|^2\left(\frac{\sin\Delta\mathrm{k}\cdot\mathrm{L}/2}{\Delta k}\right)^2, \tag{4.10}$$

with $\Delta k = k_i - k_j + k_k - k_l$. Thus, in order to achieve the longest possible propagation of the four-wave mixing, the following ideal condition must be verified

$$\Delta k = 0, \tag{4.11}$$

which is generally referred to as the spatial phase matching condition of the four-wave mixing. Its temporal equivalent, related to the conservation of energy, reads

$$\Delta\omega = \omega_i - \omega_j + \omega_k - \omega_l = 0. \tag{4.12}$$

Parametric conversion. Among the different types of processes arising from third-order non-linearity, it is the four-wave parametric conversion process that interests us in this manuscript. It consists in the creation of one signal and one idler photon from two pump photons provided by a single laser.

4.3.2 Optical parametric oscillator

By inserting the nonlinear medium into an optical cavity at resonance with one or more of the field involved in the nonlinear process, one creates an effective optical oscillation system featuring multiple fields. As it is generally the case with such devices, the oscillations of the

resonant fields arise if the gain of the parametric process dominates the losses for each round trip in the cavity, regime which is reached above a specific pump power threshold. If this condition is fulfilled, the cavity emits coherent and amplified waves in the cavity resonant modes. As a result, the power of the pump decreases to feed the resonant fields, leading to a parametric gain saturation above the oscillation threshold.

Optical Parametric Oscillators (OPO) are categorized into different types according to the number of fields at resonance with their cavity [143]: the single (SROPO), double (DROPO) and triple (TROPO) resonance OPOs. In general, the higher the number of resonant fields is, the lower the parametric oscillation threshold is, typically from a few watts for the SROPO [27] to a few milliwatts for the TROPO [149]. OPOs are often used both for their high tunability and for the generation of wavelengths that cannot be reached by more conventional lasers. Typically, those based on KTP and BBO crystals cover a range of wavelengths from the visible (500-800 nm) to the mid-infrared (1-5 μm) [140, 150]. In addition, they can be employed as a source of highly correlated non-classical states, for example to generate entangled [112, 164] or squeezed [69] states. For this reason, they are widely spread in the field of quantum optics, for experiments in quantum cryptography [136], teleportation [33, 31] or memory [80].

In this chapter, we will focus on the polariton analogue of TROPO. Instead of mixing photons, here we will look at parametric processes between polaritons. Two ingredients are needed: a nonlinear medium and a spectral selection of the output modes. The former is obtained via the scattering processes between polaritons, which are equivalent to four-wave mixing in Kerr medium; indeed the original shape of the spectrum of lower polariton branch allows to satisfy both the parametric conversion phase matching conditions seen above and the simultaneous triple-resonance of the pump, signal and idler modes with the microcavity system.

4.4 Polariton parametric oscillations

4.4.1 Theoretical description

Parametric amplification. The first experiments demonstrating a parametric gain effect in a polariton planar cavity date from 2000 [147, 22], using a pump-probe excitation scheme depicted in Fig. 4.1: a high-intensity pump beam injects polaritons in the vicinity of the LP branch inflection point, at wavevector and energy ($\mathbf{k}_\mathrm{P}$, ω_P); a low-intensity probe beam resonates with the lowest energy state of the LPs, at ($\mathbf{k}_\mathrm{S}$=0, ω_S). By increasing the pump power above a certain threshold, the authors observe a huge gain on the probe, up to 70, which is concentrated in a very narrow spectral width, blue-shifted with respect to the bare resonance of polaritons. They thus highlight a parametric conversion process, involving the scattering of two polaritons in the mode set by the pump at $\mathbf{k}_\mathrm{P}$, into a signal polariton, seeded by the probe to enhance the conversion at $\mathbf{k}_\mathrm{S}$, and an idler polariton, whose emission can also be detected at a larger wavevector $\mathbf{k}_\mathrm{I}$.

It is crucial to note that such a process is enabled by the "S" shape of the polariton dispersion

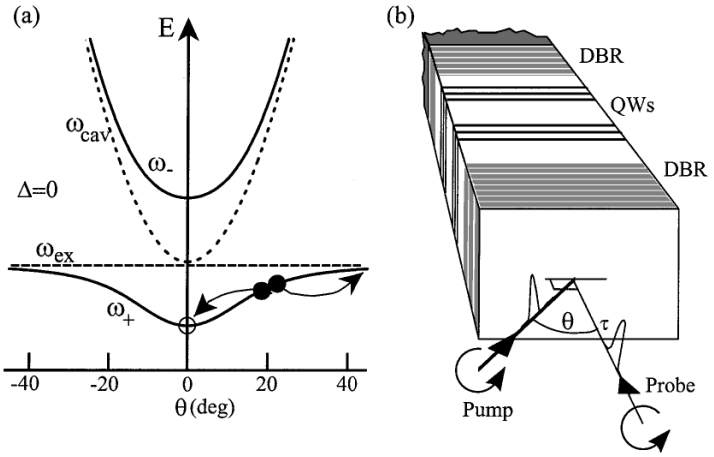

Figure 4.1: **Excitation scheme in parametric amplification regime. (a)** Energies and wavevectors of the pump, idler and signal modes of the OPO along the LP resonance. The two black dots highlight two pump polaritons injected in the vicinity of the LP branch inflection point at $\mathbf{k}_\mathrm{P}$. They scatter via the polariton-polariton interactions to generate a polariton in a signal mode at $\mathbf{k}_\mathrm{S} = 0$, highlighted by the transparent dot, and a polariton in an idler mode at $\mathbf{k}_\mathrm{I} = 2\mathbf{k}_\mathrm{P}$, highlighted by the red dot. **(b)** Injection of lasers into the cavity in parametric amplification regime. The pump illuminates the cavity at its magic angle θ; the probe around $\mathbf{k} = 0$. In [147], when the probe has a polarization aligned with that of the pump (right circular) and a wavevector matching that of the signal mode, a gain is observed, attesting the establishment of a parametric amplification regime. Adapted from [147].

relation around the inflection point, allowing the simultaneous fulfillment of the temporal and spatial phase matching conditions of the 4WM

$$\begin{cases} \mathbf{k}_\mathrm{I} = 2\mathbf{k}_\mathrm{P} - \mathbf{k}_\mathrm{S}, \\ \omega_\mathrm{I} = 2\omega_\mathrm{P} - \omega_\mathrm{S}. \end{cases} \tag{4.13}$$

This means that the parametric conversion observed here is an intrinsic feature of the strong coupling: it results from a mixing between polariton modes and not between photon modes.

Analytical description. The underlying processes in this excitation scheme are explained theoretically by the quantum model of C. Ciuti [42, 43] and by the classical model of D. Whittaker [174]. In both cases, the driving mechanism of the parametric conversion is the interaction between polaritons, given by the Hamiltonian

$$\mathcal{H}_{PP}^{OPO} = V_{pp}\left(\hat{p}_{\mathbf{k}_\mathrm{S}}^\dagger \hat{p}_{\mathbf{k}_\mathrm{I}}^\dagger \hat{p}_{\mathbf{k}_\mathrm{P}} \hat{p}_{\mathbf{k}_\mathrm{P}} + h.c.\right), \tag{4.14}$$

coupling two polaritons in the pump mode $\mathbf{k}_\mathrm{P}$ to one polariton in the probe mode $\mathbf{k}_\mathrm{S}$ and another in the ilder mode $\mathbf{k}_\mathrm{I}$. Its addition to the generalized GPE, expressed from Eq. (2.51)

for the mean field wave function of each of the resonant modes, leads to the derivation of a set of evolution equations

$$\mathrm{i}\hbar\frac{\partial}{\partial t}\psi_{\mathrm{S}} = \left[\hbar\omega_{LP}(\mathbf{k}_{\mathrm{S}}) - \mathrm{i}\hbar\frac{\gamma_{\mathrm{S}}}{2}\right]\psi_{\mathrm{S}} + \hbar g\psi_{\mathrm{I}}^{*}\psi_{\mathrm{P}}^{2} + \mathcal{F}_{\mathrm{S}}(t), \tag{4.15}$$

$$\mathrm{i}\hbar\frac{\partial}{\partial t}\psi_{\mathrm{P}} = \left[\hbar\omega_{LP}(\mathbf{k}_{\mathrm{P}}) - \mathrm{i}\hbar\frac{\gamma_{\mathrm{P}}}{2}\right]\psi_{\mathrm{P}} + 2\hbar g\psi_{\mathrm{P}}^{*}\psi_{\mathrm{S}}\psi_{\mathrm{I}} + \mathcal{F}_{\mathrm{P}}(t), \tag{4.16}$$

$$\mathrm{i}\hbar\frac{\partial}{\partial t}\psi_{\mathrm{I}} = \left[\hbar\omega_{LP}(\mathbf{k}_{\mathrm{I}}) - \mathrm{i}\hbar\frac{\gamma_{\mathrm{I}}}{2}\right]\psi_{\mathrm{I}} + \hbar g\psi_{\mathrm{S}}^{*}\psi_{\mathrm{P}}^{2}, \tag{4.17}$$

where $\mathcal{F}_{\mathrm{P}}(t)$ and $\mathcal{F}_{\mathrm{S}}(t)$ are respectively the high-intensity pump and the weak probe fields, γ_{S}, γ_{P} and γ_{I} the FWHM linewidths of the three considered parametric modes. $\hbar\omega_{LP}(k_i)$ is equal to the polariton energy in the i mode, including the self-interaction energy renormalisation $\hbar g|\psi_i|^2\psi_i$. The population in the signal mode is then derived from the following coupled linear system

$$\hbar\omega\begin{bmatrix}\psi_{\mathrm{S}}^{0}\\ \psi_{\mathrm{I}}^{0^*}\end{bmatrix} = \begin{bmatrix}\hbar\omega_{LP}(\mathbf{k}_{\mathrm{S}}) - \mathrm{i}\hbar\dfrac{\gamma_{\mathrm{S}}}{2} & \hbar g\psi_{\mathrm{P}}^{2}\\ -\hbar g\psi_{\mathrm{P}}^{2} & 2\hbar\omega_{\mathrm{P}} - \hbar\omega_{LP}(\mathbf{k}_{\mathrm{I}}) - \mathrm{i}\hbar\dfrac{\gamma_{\mathrm{I}}}{2}\end{bmatrix}\begin{bmatrix}\psi_{\mathrm{S}}^{0}\\ \psi_{\mathrm{I}}^{0^*}\end{bmatrix} + \begin{bmatrix}\mathcal{F}_{\mathrm{S}}^{0}\\ 0\end{bmatrix}, \tag{4.18}$$

calculated by writing Eq. (4.15) and the conjugate complex of Eq. (4.17) in stationary regime. ψ_{S}^{0} and ψ_{I}^{0} are the amplitudes of the signal $\psi_{\mathrm{S}} = \psi_{\mathrm{S}}^{0}\exp(-\mathrm{i}\omega_{LP}(\mathbf{k}_{\mathrm{S}})t)$ and idler $\psi_{\mathrm{I}} = \psi_{\mathrm{I}}^{0}\exp(-\mathrm{i}\omega_{LP}(\mathbf{k}_{\mathrm{I}})t)$ wave functions; $\mathcal{F}_{\mathrm{S}}^{0}$ is the amplitude of the probe $\mathcal{F}_{\mathrm{S}} = \mathcal{F}_{\mathrm{S}}^{0}\exp(-\mathrm{i}\omega t)$ at the frequency ω.

The signal mode amplitude is given by

$$\psi_{\mathrm{S}}^{0} = \frac{\mathcal{F}_{\mathrm{S}}^{0}\left(\hbar\omega - 2\hbar\omega_{\mathrm{P}} + \hbar\omega_{LP}(\mathbf{k}_{\mathrm{I}}) + \mathrm{i}\hbar\dfrac{\gamma_{\mathrm{I}}}{2}\right)}{\left(\hbar\omega - E_{-}\right)\left(\hbar\omega - E_{+}\right)}, \tag{4.19}$$

with $E_{\pm}$ denoting the eigenvalues of the matrix (4.18).

One can show that ψ_{S}^{0} is maximal when the diagonal elements of Eq. (4.18) are equal, i.e. $\hbar\omega_{LP}(\mathbf{k}_{\mathrm{S}}) = 2\hbar\omega_{\mathrm{P}} - \hbar\omega_{LP}(\mathbf{k}_{\mathrm{I}})$. This is equivalent to express the energy conservation of the parametric process. The pump wavevector $\mathbf{k}_{\mathrm{P}}$ satisfying this condition determines the "magic" angle of the polariton amplification. Correspondingly, the eigenvalues $E_{\pm}$ are equal to

$$E_{\pm} = \hbar\omega_{LP}(\mathbf{k}_{\mathrm{S}}) - \mathrm{i}\hbar\left[\frac{\gamma_{\mathrm{S}} + \gamma_{\mathrm{I}}}{4} \pm \frac{1}{2}\sqrt{\left(2g|\psi_{\mathrm{P}}|^{2}\right)^{2} + \left(\frac{\gamma_{\mathrm{S}} - \gamma_{\mathrm{I}}}{2}\right)^{2}}\right]. \tag{4.20}$$

From this, the density in the signal mode $|\psi_{\mathrm{S}}^{0}|^2$ diverges when $\mathrm{Im}(E_{-}) \to 0$ for the probe frequency $\omega = \omega_{LP}(\mathbf{k}_{\mathrm{S}})$. This yields the expression of a threshold density in the pump mode

$$\left|\psi_{\mathrm{P}}^{thr}\right|^{2} = \frac{1}{g}\sqrt{\frac{\gamma_{\mathrm{S}}\gamma_{\mathrm{I}}}{4}}, \tag{4.21}$$

to be reach and in order to achieve the amplification of the probe.

This result simply expresses similar gain condition as for lasers: the population rate of polaritons from the pump mode toward the signal and idler modes must be faster than the polariton decay rates, i.e. the losses of the system, in order to achieve gain on the probe. From it, we define an oscillation threshold for the pump intensity $\left|F_P^{thr}\right|^2$, related to $\left|\psi_{\rm P}^{thr}\right|^2$. Its expression is not trivial since the relationship between the polariton density and the pump intensity is not linear. Indeed, under the detuning condition $\delta > \sqrt{3}/2\gamma$, a bistability regime can also appear in the OPO configuration.

In the end, the gain on the probe amplitude reads

$$G(\omega_{\rm S}) = \frac{|\psi_{\rm S}^0|^2 - \left|\psi_{\rm S}^{lin}\right|^2}{\left|\psi_{\rm S}^{lin}\right|^2} = \left[\frac{1}{1 - \frac{\left(2g|\psi_{\rm P}|^2\right)^2}{\gamma_{\rm S}\gamma_{\rm I}}}\right]^2 - 1, \tag{4.22}$$

where $\left|\psi_{\rm S}^{lin}\right|^2$ is the population in the signal mode in linear regime, with the probe only.

Optical parametric oscillation. In the above experiment (Fig. 4.1, scattering processes in the signal mode are enhanced by a probe beam resonating with it. Further experiments carried out shortly after the reports in Ref. [22, 159] revealed the generation of macroscopic populations in the signal and idler modes without the use of a probe beam ($|F_S^0|^2 = 0$), thereby demonstrating the achievement of a true OPO regime in semiconductor microcavities.

In such an excitation scheme, a multiplicity of modes are generated from the scattering of pump polaritons, since there is no probe to favor the population of specific signal and idler modes. Those with loss rates higher than their generation rate will decay. Thus, in a process similar to mode selection in laser, the signal mode with the lowest decay rate will dominate, depleting the pump at the expense of other modes, until it is the only one to survive. When the pump is at the inflection point of the LP branch, corresponding to the so-called magic angle of the cavity, the dominant signal mode is at $\mathbf{k}_{\rm S} = 0$, which is expected since it corresponds to the ground state of polaritons, implying a higher stability. However, in more elaborate models [54, 53], it is shown that usually several modes survive from this competition, which could complicate the analysis of the OPO process in our experiments.

4.4.2 SSB in OPO regime

Let us now consider the following transformation

$$\mathcal{U}: \qquad \psi_{\rm S} \to \psi_{\rm S} \times \exp(\mathrm{i}\Delta\phi) \quad \& \quad \psi_{\rm I} \to \psi_{\rm I} \times \exp(-\mathrm{i}\Delta\phi). \tag{4.23}$$

It consists in a simultaneous and opposite phase rotation $\Delta\phi$ of the polariton wave functions $\psi_{\rm S}$ and $\psi_{\rm I}$ in the signal and idler modes respectively. By removing the contribution of the probe

($|\mathcal{F}_{\rm S}|^2 = 0$ in OPO regime), one can easily demonstrate that the evolution equations (4.15), (4.17) and (4.16) are invariant under application of $\mathcal{U}$. It follows directly that the Hamiltonian of the system driven in OPO regime is invariant under the application of $\mathcal{U}$. Moreover, if we apply $\mathcal{U}$ to the wave function ψ of the OPO, expressed with the following ansatz

$$\psi(x,t) = \psi_{\rm P}\exp(\mathrm{i}[\mathbf{k}_{\rm P}x - \omega_{\rm P}t]) + \psi_{\rm S}\exp(\mathrm{i}[\mathbf{k}_{\rm S}x - \omega_{\rm S}t]) + \psi_{\rm I}\exp(\mathrm{i}[\mathbf{k}_{\rm I}x - \omega_{\rm I}t]), \tag{4.24}$$

the signal and idler wave functions $\psi_{\rm S}$ and $\psi_{\rm I}$ acquire respectively a $\Delta\phi$ and $-\Delta\phi$ phase shift, whereas the pump wave function $\psi_{\rm P}$ remains unchanged. The OPO wave function ψ is therefore not symmetric with respect to $\mathcal{U}$.

Consequently, all the prerequisites for SSB are met: the pump polaritons driving the parametric process undergo a $U(1)$ phase-rotation symmetry breaking which should result in the emergence of Goldstone mode in the signal and idler polariton spectra.

Signal and idler fluid as BEC. Off-resonance polariton condensates and OPO signal/idler polaritons share the feature of being excited without phase fixation by the pump. In the off-resonance configuration, the initial phase of the driving field is lost via the process of spontaneous relaxation of the pump photons to the smallest k-states of the LP branch; in the OPO configuration, although the phase-matching conditions of the 4WM process impose the global phase of the scattered polaritons to be equal to that fixed by the pump, the respective relative phases of the signal and idler polaritons are free to evolve. These decouplings between the polaritons and the driving field phases enable the SSB, which is responsible for the emergence of a Goldstone mode in both OPO and off-resonance quantum fluids. For this reason, polaritons generated in OPO regime have historically been studied as a candidate for BEC, leading to a whole series of experimental works dedicated to the measurement of the signatures of such a process, with for example the macroscopic occupancy of a single mode or the spontaneous onset of large-scale spatial and temporal coherences. In the following, we will therefore assimilate polariton fluids in the signal and idler modes to condensates. For more details on the differences between polariton lasers, condensates and OPO, one can refer to the Ref. [85, 35, 23].

4.5 OPO elementary excitations

To characterise the Godstone mode, we first calculate the spectrum of elementary excitations of polaritons in OPO regime, as explained by M. Wouters in Ref. [177]. This is done again with the help of the Bogoliubov theory: the generalized GPE equation is linearized around the stationary solutions of the S, P and I polaritons. The wave functions of the system read

$$\begin{cases} \psi_{\rm S}(\mathbf{r},t) = \exp(i\mathbf{k}_{\rm S}\mathbf{r} - i\omega_{\rm S}t)\left[\psi^0_{\rm S} + \delta\psi_{\rm S}(\mathbf{r},t)\right], \\ \psi_{\rm P}(\mathbf{r},t) = \exp(i\mathbf{k}_{\rm P}\mathbf{r} - i\omega_{\rm P}t)\left[\psi^0_{\rm P} + \delta\psi_{\rm P}(\mathbf{r},t)\right], \\ \psi_{\rm I}(\mathbf{r},t) = \exp(i\mathbf{k}_{\rm I}\mathbf{r} - i\omega_{\rm I}t)\left[\psi^0_{\rm I} + \delta\psi_{\rm I}(\mathbf{r},t)\right]. \end{cases} \tag{4.25}$$

The weak perturbations $\delta\psi_i$ of polaritons in the mode $i = (S, P, I)$ are then described as the superposition of two counterpropagating plane waves of respective amplitudes U_k^i and V_k^i

$$\delta\psi_i = U_k^i \exp(i\mathbf{kr} - i\omega_{Bog}t) - V_k^{i^*} \exp(-i\mathbf{kr} + i\omega_{Bog}t), \tag{4.26}$$

leading to linearize the GPE in the following simplified form

$$\hbar\omega_{Bog}(\mathbf{k}) \cdot \mathcal{U}_k = \mathcal{L}_{Bog}(\mathbf{k}) \cdot \mathcal{U}_k, \tag{4.27}$$

with $\mathcal{U}_k = \left[U_k^S, U_k^P, U_k^I, V_k^S, V_k^P, V_k^I\right]^T$. We recover an equation similar to that seen in the third chapter for the evolution of the amplitude of weak perturbations. Here, in the OPO case, the Bogoliubov operator $\mathcal{L}_{Bog}$ is defined in an extended space of dimension 6x6, in order to account for the polaritons in the signal and idler modes in addition to those directly injected by the pump. It can be expressed in the form

$$\mathcal{L}_{Bog}(\mathbf{k}) = \begin{bmatrix} M(\mathbf{k}) & Q(\mathbf{k}) \\ -Q^*(\mathbf{k}) & -M^*(\mathbf{k}) \end{bmatrix}, \tag{4.28}$$

which is analogue to the 2x2 Bogoliubov operator of the single-mode polariton fluid in (Eq.) 3.6. The 3x3 matrices $M(\mathbf{k})$ and $Q(\mathbf{k})$ are defined as follows

$$M_{mn}(\mathbf{k}) = \left[\hbar\omega_{LP}(\mathbf{k}_m + \mathbf{k}) - \hbar\omega_m - \mathrm{i}\hbar\frac{\gamma}{2}\right]\delta_{m,n} + 2\sum_{rt=1}^{3} \hbar g_{k_m+k,k_n+k,k_t}\delta_{m,n+r-t}\psi_r^*\psi_t, \tag{4.29}$$

$$Q_{mn}(\mathbf{k}) = \sum_{rt=1}^{3} \hbar g_{k_m+k,k_r,k_s}\delta_{m+n,n+t}\psi_r\psi_s, \tag{4.30}$$

where the three modes (S, P, I) are identified respectively with the values (1, 2, 3) and $\hbar\omega_{LP}(\mathbf{k}_m + \mathbf{k})$ is the linear dispersion relation of polaritons given by (Eq.) 2.36. We have taken into account that the strength of these interactions depends on the exciton Hopfield coefficient, by writing g as a function of the wavevectors of the different polariton modes involved

$$g_{k,q_1,q_2} = X^*(k)X^*(q_1 + q_2 - k)X(q_1)X(q_2)g. \tag{4.31}$$

From this, one can note that the diagonal terms of $\mathcal{L}_{Bog}(\mathbf{k})$ are equal to the diagonal terms of the single-mode operator, expressed for each of the S, P and I modes, while the off-diagonal terms are equal to the interaction energies between each of all possible combinations of two modes.

S-polaritons spectrum computation. The real and imaginary parts of the energy of the elementary excitations are computed from the eigenvalues of the Bogoliubov operator, after

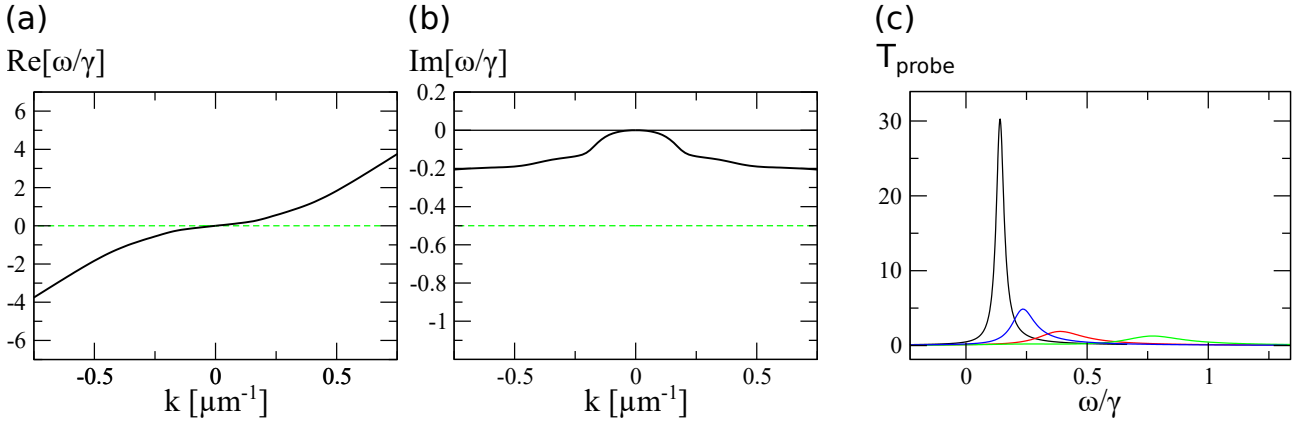

Figure 4.2: **Theoretical spectrum of elementary excitations in OPO regime. (a)** Real part (**(b)** Imaginary part) of the Bogoliubov dispersion relation around the stationary state. The green dashed line highlights the frequency ω_S of the signal condensate (the decay rate of signal polaritons $\gamma_S/2$). The Goldstone mode has almost zero curvature and a linewidth tending towards 0 in the low-k limit. **(c)** Response spectrum to a probe beam for several values of probe wavevectors $\mathbf{k} - \mathbf{k}_S = 0.1, 0.15, 0.2, 0.3\ \mu\text{m}^{-1}$, around the signal wavevector $\mathbf{k}_S$. Adapted from [177].

considering the linear response of the system to a weak external probe $\delta\mathcal{F}_{pr} \propto [1,0,0,0,0,0]^T$, injecting perturbations in the same mode as the signal condensate

$$\hbar\omega_{Bog}(\mathbf{k}) \cdot \mathcal{U}_k - \mathcal{L}_{Bog}(\mathbf{k}) \cdot \mathcal{U}_k = \delta\mathcal{F}_{pr}. \tag{4.32}$$

The results are plotted in Fig. 4.2(a) and (b) for a pump intensity F_p above the OPO threshold. The parameters used are very close to those corresponding to our cavity, with a Rabi energy $\hbar\Omega_R = 5$ meV, exciton-photon detuning $\Delta E_{X-\gamma}(k=0) = 0$ meV, an interaction constant $\hbar g = 5\ \mu\text{eV}\cdot\mu\text{m}^2$ and a polariton decay rate $\hbar\gamma = 100\ \mu$eV.

Goldstone dispersion relation. The dispersion relation of the Goldstone mode is calculated from the diagonalization of the Bogoliubov operator (4.28). It displays a real and imaginary part equal to 0 when $\mathbf{k} = 0$. Remarkably, its shape differs from that observed for thermal equilibrium Bose-Einstein condensates, where the Goldstone mode manifests as two sonic branches $\text{Re}\,[\omega_{Bog}(\mathbf{k})] = c_s|k|$ with a singularity at k=0. In the out-of-equilibrium case, the Goldstone mode does not show any singularity. Instead, its real part features an energy plateau with a very small slope, corresponding to a group velocity that is also almost zero with respect to the typical speed of sound expected for phonon-type elementary excitation. The Goldstone mode of polariton condensates is thus diffusive rather than propagative: a perturbation introduced locally at the surface of the S-condensate relaxes without moving, feeding the spatial twist of the polaritons phase. This is a specific feature of out-of-equilibrium systems, without in-equilibrium counterpart and still under investigation today [116, 70, 117].

Probe response. The response of the system transmission to a weak probe is shown in Fig. 4.2(c). The imaginary part of the spectrum tends towards 0 at low-k and results in a strong narrowing of the linewidth with respect to the polariton decay rate γ and in an amplification of the amplitude, expected as the probe acts as a seed of the OPO process. At large-k, the probe recovers a behavior similar to that it would have in linear regime: a linewidth around γ and an amplitude unchanged compared to the input one. These are the typical features that we will reveal by exploring the high resolution spectroscopy technique presented in the previous chapter.

4.5.1 OPO experiments

Before dealing with the experiments, we can mention a set of experiments reporting the implementation of the OPO regime in polariton systems, where the emission of signal and idler condensates exhibits some of the features of the Goldstone mode.

As already discussed, the first experimental demonstration of parametric optical amplification in microcavity has been carried out in 2000 by P. Savvidis [147], where a seed probe send through the S-condensate is amplified in a narrow band of gain up to 7000%. Then, just after this first achievement, the same teams demonstrated the successful implementation of OPO with only the pump drinving polaritons [159, 22]. They revealed a spontaneous drastic change in the spectrum, becoming maximal and non-thermal around the signal mode wavevector. Pioneering measurements of coherence have been made in 2006 [17], pointing out the preservation of the first-order spatial coherence of S polaritons at macroscopic scales of the order of the quantum fluid dimension. The article [155] presents further coherence measurement, demonstrating that the S-polaritons spatial and temporal long-range orders disappear when moving from a 2D to a 1D fluid geometry. Such a behaviour is related to an increase in fluctuations with decreasing dimensionality, in agreement with predictions for standard condensates in thermal equilibrium. Finally, Ref. [18] is the last experimental report to our knowledge which explicitly refers to a Goldstone mode measurement in OPO regime . It shows a significant increase in the lifetime of the S mode emission in response to a weak pulsed probe injected in the I condensate, proving the presence of a critical slowing down associated to the elementary excitation spectrum vanishing in the long wavelength limit.

4.5.2 Bogoliubov spectrum in out-of-equilibrium condensates

These OPO works can be completed by the observation of Goldstone modes in off-resonance excitation, with microcavities suitable for condensation.

Numerical calculation. Calculations of collective excitations spectra in off-resonance condensates have been carried out in Ref. [162] and [176], the first using a microscopic model to evaluate the polariton dynamics; the second using a mean-field description of the condensate, similar to the one we used to calculate the Bogoliubov dispersion relations. Both lead to the

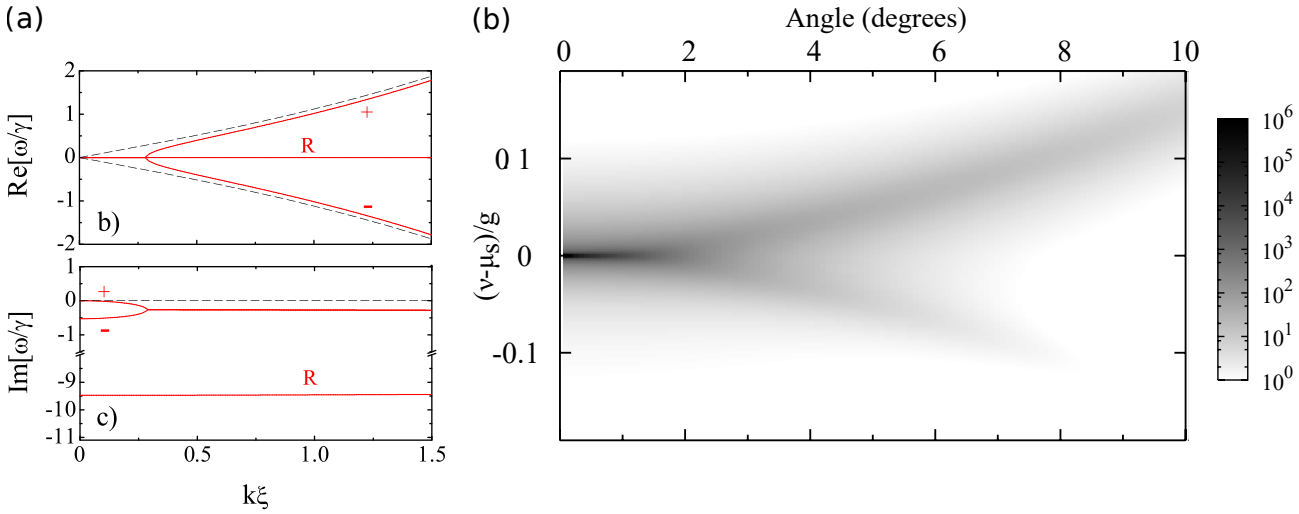

Figure 4.3: **Theoretical spectrum of elementary excitation of a polariton condensate.** **(a)** Upper (lower) line: real (imaginary) part of the Bogoliubov dispersion relation. The Goldstone mode at low-k is evidenced by the vanishing of the gap between the positive (+) and negative (-) branch in the real part and the zero positive branch in the imaginary part. **(b)** Photoluminescence spectrum of the condensate. The Goldstone mode corresponds to the plateau of zero energy and very narrow linewidth at low-k. Adapted from [162].

same result: the spectrum exhibits a Goldstone branch whose energy tends to 0 as $\mathbf{k} \to 0$. It is again a diffusive mode, of analytical expression

$$\omega_{Bog}(\mathbf{k}) = -\mathrm{i}\frac{\Gamma}{2} \pm \sqrt{\left(\omega_{Bog}^{in-eq}(\mathbf{k})\right)^2 - \frac{\Gamma^2}{4}}, \tag{4.33}$$

with Γ the effective polariton decay rate in the off-resonance excitation scheme and ω_{Bog}^{in-eq} the standard Bogoliubov dispersion relation of in-equilibrium quantum fluids given by

$$\omega_{Bog}^{in-eq} = \sqrt{\frac{\hbar k^2}{2m}\left(\frac{\hbar k^2}{2m} + 2gn\right)}. \tag{4.34}$$

For small $\mathbf{k}$, such as the argument under the square root is negative, $\omega_{Bog}(\mathbf{k})$ is purely imaginary, leading to a gapless diffusive plateau in $\mathrm{Re}\left(\omega_{Bog}(\mathbf{k})\right)$ in the long wavelength limit.

Such a result is interesting because the same type of analytical expression can be inferred for the Goldstone mode in OPO regime. It shows especially that the length of the plateau depends on the loss rate of the system: the larger Γ is, the larger is the range of the wavevectors in which the real part of ω_{Bog} is purely imaginary; conversely, when Γ tends to 0, this range becomes infinitely small and the plateau is replaced by two sonic branches, as expected for systems in equilibrium. This is a proof that the intrinsic dissipation of polaritons is indeed responsible for the formation of a diffusive rather than a propagative Goldstone mode.

Experiments. Although hints of spectral signatures of a narrow diffusive mode can be found in historical experiments measuring polariton condensate spectra [84, 168], first explicit mention to a Goldstone mode are given in Ref. [15, 120, 121]. The most advanced analysis was carried out by D. Ballarini [19], by measuring the spectrum of elementary excitations of a polariton condensate from the Fourier transform of the first-order correlation function $g^{(1)}(\Delta x, \Delta t)$. The Goldstone mode has been observed. However, its diffusive character could not be evidenced due to the use of a very long lifetime microcavity. Moreover, the spectral resolution of the technique prevented the detection of any spectral narrowing.

4.6 Experimental implementation

Our objective is to propose a fully detailed experimental characterization of the Goldstone mode: we wish to demonstrate its diffusive character, to quantify precisely its spectral narrowing and to prove that it is indeed the consequence of a spontaneous symmetry breaking by explicitly destroying the initial symmetry of the system, and then observing the disappearance of the Goldstone mode.

4.6.1 Experimental setup

The same pump-probe spectroscopy setup described in the previous chapter is used to measure the Goldstone mode spectrum with the same sample. The main difficulty lies in the necessity to have simultaneous access to the signal mode around $\mathbf{k}_\mathrm{S} = 0\ \mu\mathrm{m}^{-1}$ (at angle $\theta_\mathrm{S} = 0°$) and the idler mode at $\mathbf{k}_\mathrm{I} = 2.5\ \mu\mathrm{m}^{-1}$ ($\theta_\mathrm{I} = 19.2°$). For this purpose, a lens with a large aperture of 32.4° (of focal length $f = 40$ mm and radius $R = 25.4$ mm) is chosen to focus the following three laser beams in the cavity plane:

- The pump, at the magic angle $\mathbf{k}_\mathrm{P} = 1.25\ \mu\mathrm{m}^{-1}$ ($\theta_\mathrm{P} = 9.6°$), when working at points of the sample corresponding to near zero exciton-photon detuning $\Delta E_{X-\gamma} \simeq 0$ meV. It is provided by a Ti:Sapphire Matisse TR laser with a bandwidth of 500 kHz (2.1 neV).
- The probe, at $\mathbf{k}_\mathrm{S}$. It is provided by a Ti:Sapphire M2 Solstis laser with a bandwidth of less than 50kHz (<0.21 neV). Its role is to scan the polariton spectrum in the signal mode, in order to detect the Goldstone mode.
- A third laser, at $\mathbf{k}_\mathrm{I}$. It is provided by a motorised Littman/Metcalf Laser System LION diode, operating between 790 and 840 nm and with a bandwidth of less than 100 kHz (<0.42 neV). It will be used to destroy the Goldstone mode.

The aforementioned bandwidths are significantly narrower than the typical linewidths that are observed in the polariton spectrum (of the order of 1 GHz, i.e. 4 μeV): they do not limit the spectral resolution in the experiments.

In order to minimize the deformation of the Gaussian profile of the laser beams by the optical aberrations at the edge of the lens before the cavity, the sample is tilted by -$\mathbf{k}_\mathrm{P}$ with respect

to the normal incidence. In this way, the pump beam goes through the center of the lens and the probe and idler beams go through the angles ± 9.6°. Thus, in the plane of the cavity, the beam profiles remain Gaussian, with a waist of about 100 μm diameter for the pump and the idler, and about 50 μm diameter for the probe.

In the following, measurements are always achieved with a pump intensity well above the OPO threshold $|F_{\mathrm{P}}|^2 > \left|F_{\mathrm{P}}^{thr}\right|^2$.

4.6.2 OPO excitation procedure

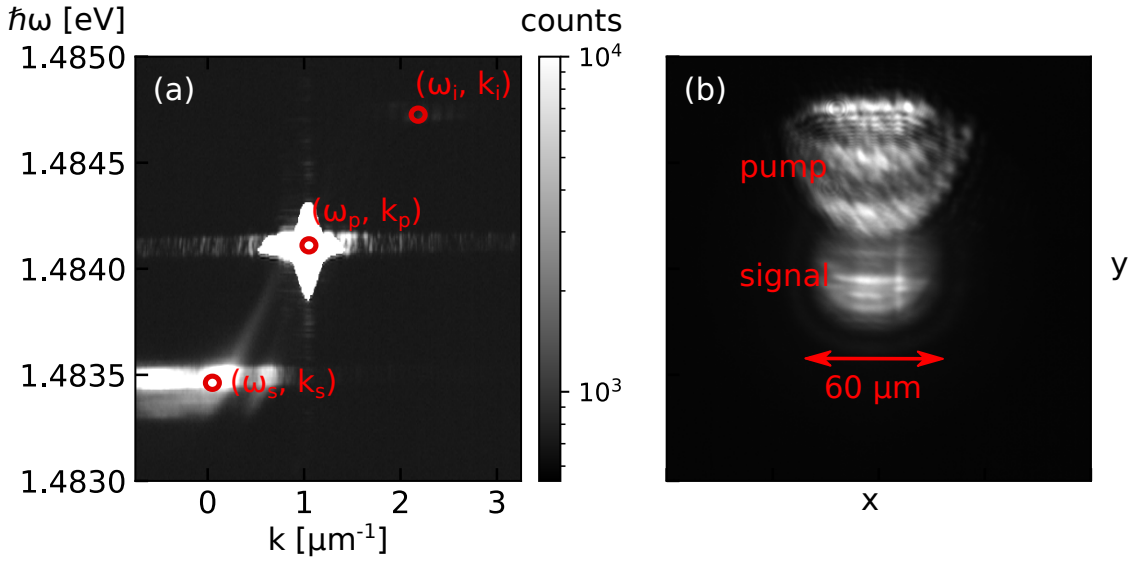

Figure 4.4: **Microcavity emission signal in OPO regime.** **(a)** Photoluminescence spectrum, obtained with a spectrometer. **(b)** Image of the cavity plane in real space.

Finding the pump configuration leading to the OPO regime is not trivial, especially when one wants to avoid the appearance of multimode regime, making the analysis of the Goldstone mode more challenging. The main difficulty lies in the large range of tunable parameters: the laser detuning δ, intensity $I_{\mathrm{P}} = |F_{\mathrm{P}}|^2$, wavevector $\mathbf{k}_{\mathrm{P}}$ and diameter $\varnothing_{\mathrm{P}}$ have to be adjusted simultaneously to obtain the OPO regime. Moreover, the choice of the working point, in addition to modify the exciton-photon detuning $\Delta E_{X-\gamma}$ and thus the wavevector of the magic angle of the LP branch, leads to modifications in the potential felt by polaritons, depending on the distribution of the local structural disorder. In order to converge in the most efficient way to the set of parameters allowing the onset of the OPO, we use the reflection R (transmission T) probe at $\mathbf{k} = 0$ $\mu\mathrm{m}^{-1}$ is observed in order to monitor the onset of the signal and idler condensates. The procedure consists in optimizing the amplitude and the linewidth of the reflection (transmission) dip (peak) of the probe as described in the following steps:

1. The pump starts at $\mathbf{k}_{\mathrm{P}} = 0$ $\mu\mathrm{m}^{-1}$, at a high enough intensity I_{P} to ensure to be above the oscillation threshold when the magic angle is reached. Its energy is blue detuned $\hbar\delta \simeq 0.5$ meV to keep it above the resonance of LPs when $\mathbf{k}_{\mathrm{P}}$ is increased. The probe resonance

signal is a Lorentzian, with a FWHM linewidth equal to the polariton decay rate $\hbar\gamma_0 \simeq 80$ μeV and a transmission peak amplitude T_0 close to that of the linear regime. It is blue-shifted with respect to the LP resonance due to the interactions between polaritons.

2. We increase $\mathbf{k}_\mathrm{P}$ by a few 100 mm^{-1}, inducing a decrease in $\delta(\mathbf{k}_\mathrm{P})$, thus a decrease in pump polariton density and a red-shift of the probe transmission peak energy. This is compensated for by increasing the driving field energy, in order to recover the initial polariton density. This step is repeated until the magic angle is roughly reached, by proceeding in small steps of $\mathbf{k}_\mathrm{P}$ to remain blue-shifted with respect to the LP branch.

3. Near the magic angle, the amplification $T > T_0$ and narrowing $\gamma < \gamma_0$ of the probe begins occurring in accordance with the trigger of the OPO regime. In the cavity real space, an additional emission signal appears, overlapping the polariton fluid driven by the pump (Fig. 4.4 (a)). The latter flows ballistically at the velocity set by $\mathbf{k}_\mathrm{P}$, transforming the input Gaussian profile of the pump beam into a comet shape; the first corresponds to the generation of polaritons in the signal mode of the OPO, of shape depending on the flow velocity of polaritons, therefore on the wavevector $\mathbf{k}_\mathrm{S}$ at which it is generated. Here, our cameras are not sufficiently sensitive in order to detect the emission of the idler mode. Indeed, it is generated at very large-k, where the exciton fraction of polaritons is largely dominant over the photon fraction, thus where polaritons emit very few photons.

4. In order to be as close as possible to the magic angle, corresponding to the OPO scattering process preferentially feeding the $\mathbf{k}_\mathrm{S} = 0$ and $\mathbf{k}_\mathrm{I} = 2\mathbf{k}_\mathrm{P}$ modes, we try to cancel the flow of the signal polaritons. We found that the most efficient way to proceed was to make the signal condensate density profile in the real space as symmetrical as possible with respect to a rotation around its center, in addition to shift the signal peak emission wavevector in the reciprocal space at $\mathbf{k}_\mathrm{S} = 0$ μm^{-1}. To this end, we tune slightly $\mathbf{k}_\mathrm{P}$ and δ.

5. Once properly done, the other remaining parameters are changed. In particular, the aim now is to have a resonance peak of the probe at $\mathbf{k}_\mathrm{S}$ as close as possible to a Goldstone mode resonance, i.e. with a gain T/T_0 as big as possible and a linewidth narrowing γ/γ_0 as small as possible. At this stage, we detect usually several probe transmission peaks at distinct energies, manifesting the onset of a multi-mode OPO regime. These can be canceled by tuning the pump diameter and/or slightly shifting the sample position to change the working point. Once done, the pump intensity $|F_\mathrm{P}|^2$ is ramped up to obtain the highest transmission and smallest linewidth of the probe peak, expected at the highest intensity. It is then followed by a new optimization of k and δ as described in the previous step and so on, until the gain and the linewidth are no longer respectively increasing and decreasing .

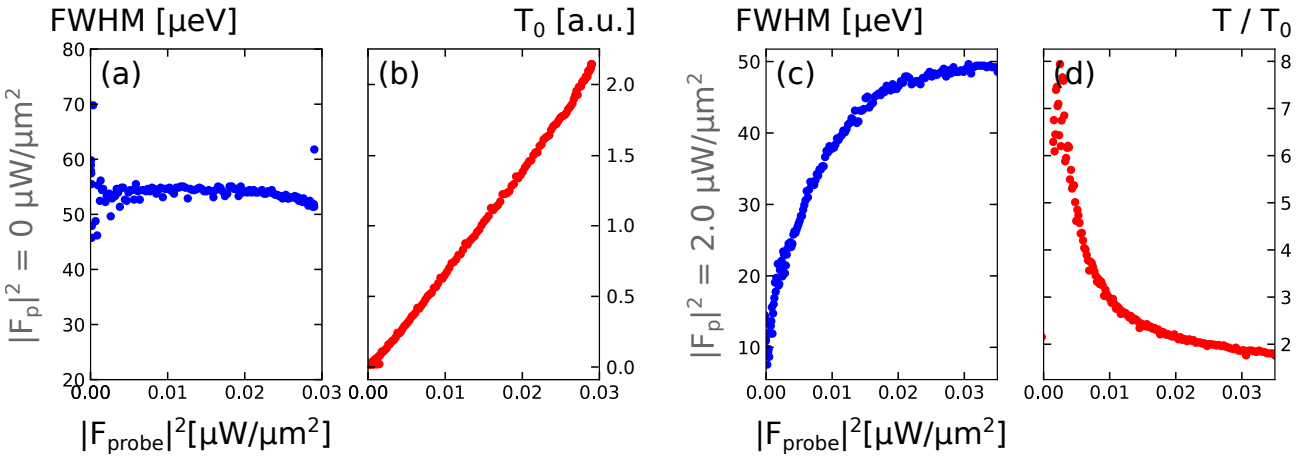

Figure 4.5: **Probe intensity scans.** **(a)** FWHM and **(b)** maximum transmssion amplitude T_0 of the probe in linear regime ($|F_{\rm P}|^2 = 0$ μW/μm^2), at wavevector $\mathbf{k} = 0$ μm^{-1}, plotted as a function of the probe intensity $|F_{\rm probe}|^2$. The first is fixed by the polariton loss rate; the second is linear with the incident probe intensity. **(c)** HWHM and **(d)** maximum gain on probe transmission T/T_0 in OPO regime ($|F_{\rm P}|^2 = 2.0$ μW/μm^2), at wavevector $\mathbf{k} = 0$ μm^{-1} near the signal mode wavevector $\mathbf{k}_{\rm S}$. The first increases and the second decreases when the probe intensity is increased.

4.7 Spectroscopy of the S-condensate

4.7.1 Probe effects on the spectrum

The signal condensate spectroscopy is now performed using the same technique as described in the previous chapter. As the existence of the Goldstone mode is intrinsically linked to the phase degeneracy of the S and I polaritons, it is crucial to ensure that the probe does not fix the phase of the condensates during the resonance scans. Its intensity is thus chosen low enough to avoid to be in the injection regime.

Probe intensity tuning. Fig. 4.5 shows the probe maximum transmission intensity T and FWHM linewidth $\gamma/2$, for scans of the sample at a specific wavevector choosen near $\mathbf{k}_{\rm S} = 0$ μm^{-1} and for different intensities $|F_{\rm probe}|^2$.

In Fig 4.5(a) and (b), the pump intensity is zero: the probe scans the polariton resonance in linear regime. As expected, in Fig. 4.5(a), the linewidth is fixed by the polariton decay rate γ_0. In addition, as shown in Fig. 4.5(b), the intensity of the transmission peak T_0 evolves linearly with the probe intensity $|F_{\rm probe}|^2$.

In Fig 4.5(c) and (d), the pump is set at the magic angle and to high intensity $|F_{\rm P}|^2 = 2.0$ μW/μm^2, well above the OPO threshold $\left|F_{\rm P}^{thr}\right|^2 \simeq 0.5$ μW/μm^2 at the detuning $\hbar\delta = 0.5$ meV. Consequently, the probe, scanning the signal condensate, exhibits a different behavior with respect to the linear one. As shown in Fig. 4.5(c), its linewidth depends on the probe intensity:

at very low intensity, it is well below the standard polariton linewidth set by the decay rate γ_0 = 54 μeV; while at higher intensity, it tends towards 0. Thus, the adequate intensity range for observing the smallest possible linewidths should be no more than three orders of magnitude below the pump intensity $|F_{\text{probe}}|^2/|F_{\text{P}}|^2 \simeq 10^{-3}$. Here we do not show the transmission for lower probe intensities, as the signal is too weak and lost in the noise of the detection. As a result, we will still have a residual phase pining by the probe in our experiments, which limits the minimum Goldstone mode linewidth that can be observed.

4.7.2 Preliminary results

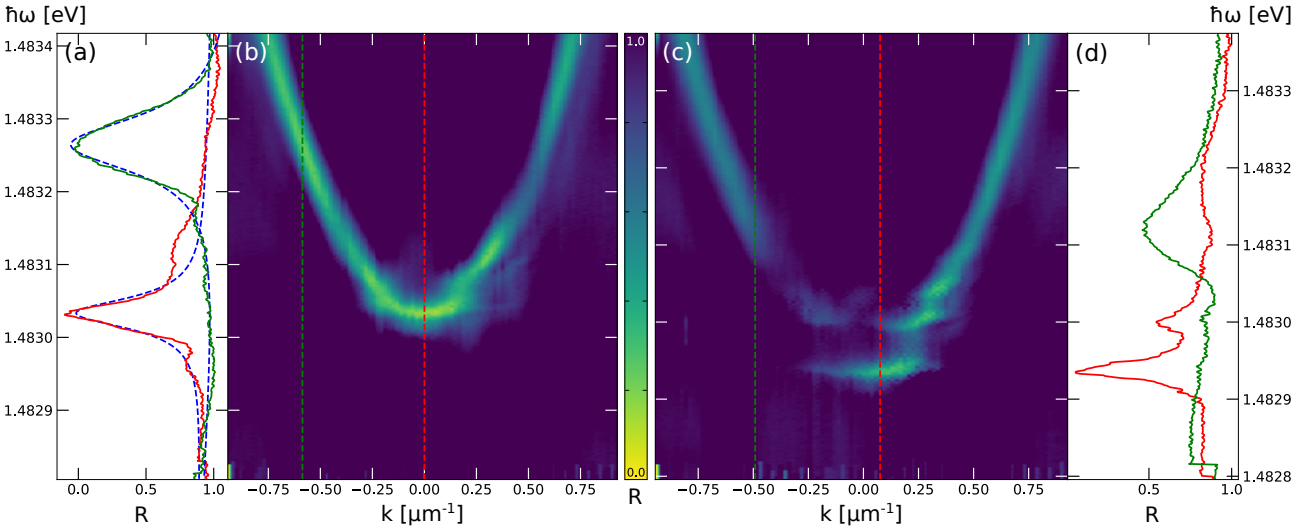

Figure 4.6: **Reflection spectrum of S-polaritons. (b)** Reflection map plotted as a function of the probe energy $\hbar\omega$ and wavevector $\mathbf{k}$, with the pump at the magic angle. The Goldstone mode corresponds to the appearance of a narrow and flat plateau at low-k. **(a)** Red line (green line): probe trace taken along the red (green) dashed line on (a), fitted from Lorentzian law in a blue dashed line, from which the linewidth of the S-polaritons is extracted. **(c)** Reflection map obtained under the same conditions as (b) but at a different working point, corresponding to an energy difference along the cavity wedge of 30 μeV. The spectrum shows several resonances at a same $\mathbf{k}$, indicating the presence of a multimode OPO regime. **(d)** Traces of the probe corresponding to the dashed lines in (c)

Initially, our first attempts to observe the Goldstone mode were made in reflection, among other reasons to avoid the presence of spurious photon transmission branches in the reconstructed spectrum, related to the subtrate at the sample output which creates in association with the two Bragg mirrors of the main Fabry-Perot, an effective optical cavity whose free spectral range $\Delta_{\text{FSR}} \simeq$ 75GHz falls within the energy range of the probe scan $\hbar\Delta\omega \simeq$ 200 GHz. These photonic resonances are not observed in reflection, making it easier to analyze the polariton spectrum.

Spectrum analysis. Fig. 4.6(b) shows an example of a reflectivity spectrum, when the

pump shines the sample at the magic angle. The first feature to be noticed is the atypical shape of the dispersion relation around the signal wavevector $\mathbf{k}_S \simeq 0$ μm^{-1}: instead of a standard parabolic or sonic dispersion, here we observe a flat plateau over $\pm$ 0.15 μm^{-1}, blue-detuned of about $\hbar(\omega_S - \omega_{LP}) = 0.7$ meV with respect to the bare resonance of the LP branch due to the energy renormalization induced by interactions. This is the signature of a diffusive mode ($d\omega/dk = 0$), as predicted by the theory.

The second striking feature observed at the plateau level is the narrowing of the FWHM linewidth γ of the reflection dip, which is significantly smaller compared to the polariton decay rate γ_0, up to $\gamma = 0.4\gamma_0$ at $\mathbf{k}_S$. We measured it from the Lorentzian fit of the probe scan signal. As shown in Fig. 4.6(a), such a fit law does not match exactly the experimental data. We will explain later how we will refine our model with the help of the theoretical analysis to best reproduce the experimental measurements.

All these observations are consistent with the expected behavior of the Goldstone mode in polariton fluids, i.e. a dispersion relation of a diffusive mode, with a linewidth approaching 0 when $\mathbf{k} \to 0$.

Multimode OPO. As an illustration of the close dependance on the experiment parameters and the wide variety of possible spectra in the OPO regime, Fig. 4.6(c) shows another example of S-polaritons dispersion relation, taken under exactly the same conditions as Fig. 4.6(b), but at a sample working point adjacent to the previous one. Several narrow resonances are observed at the same wavevector, corresponding to several dips in the reflectivity of the probe plotted in Fig. 4.6(d). They are associated with the onset of a multimode OPO regime, probably induced by the change in the energy landscape of the cavity background, shifted by 30 μeV with respect to the previous working point and in proximity to a structural defect.

Limitations of reflection detection. At this point, in order to perform a complete analysis of the spectra, it is important to know how the population of the elementary excitations is distributed along the dispersion relations. This is closely related to the OPO gain, which is an essential information that we do not have access to when looking at the resonances in reflection, as the amplification of the probe is partially hidden by its transmission through the cavity. Moreover, for the same reason, the analysis of the properties of the resonance reflectivity dips becomes difficult when its Lorentzian shape is deformed by the presence of gain on the probe, preventing, for instance, the measurement of the Goldstone mode linewidth. An illustration of this is displayed in Fig. 4.7(a), for OPO regimes optimized to obtain the highest density in the S and I condensates, which correspond to even narrower γ and higher gain T/T_0 than those shown in Fig. 4.6(b) and (c). The reflectivity of the probe exceeds $R = 1$ at some $\mathbf{k}$ and ω, resulting in a local change in the Lorentzian shape of the resonance and thus making impossible a satisfying extraction of a linewidth, as shown in Fig. 4.7(b). Such considerations oblige us to work in transmission and therefore to deal with spurious effects induced by the cavity substrate on the spectrum. Consequently, the spectra in the following may exhibit parasitic resonances that can be caused by the proximity of a photon branch to

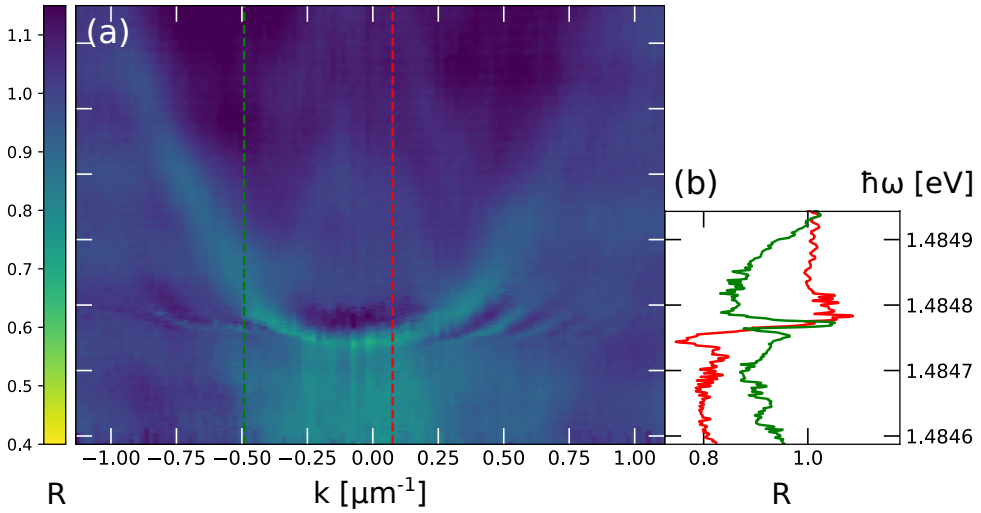

Figure 4.7: **Fano pattern in S-polariton reflection spectrum. (a)** Reflection map plotted as a function of the probe energy $\hbar\omega$ and wavevector $\mathbf{k}$, with the pump at the sample magic angle. The OPO gain induces a local amplification of the probe amplitude, resulting in the appearance of typical Fano patterns where the resonance areas $R \to 0$ mix with the amplification $R > 1$. **(b)** Red line (green line): trace of the probe taken along the red (green) dashed line on (a). The OPO gain hides the expected Lorentzian dip for resonance.

the lower polariton branch.

4.7.3 Goldstone mode linewidth analysis

In Fig. 4.8(a) is presented a transmission spectrum of S-polaritons, obtained with the pump at the magic-angle $\mathbf{k}_\mathrm{P} = 1.2\ \mu\mathrm{m}^{-1}$, of intensity $|F_\mathrm{P}|^2 = 6.11\ \mu\mathrm{W}/\mu\mathrm{m}^2$ and detuning $\hbar\delta = 1.0$ meV, optimized to be in a single mode OPO regime. Again, a flat plateau lies at low-k, in this case with a small slope, revealing that the scattering towards the S-state does not occur exactly at $\mathbf{k} = 0\ \mu\mathrm{m}^{-1}$: the fluid has a non-zero flow velocity which drags the diffusive elementary excitations at its surface. More importantly, we see now the amplification of the probe $T/T_0 \gg 1$ around $\mathbf{k}_\mathrm{S}$, decreasing very quickly as soon as we move away from it.

Fig. 4.8(b) shows three energy scans for different wavevector $\mathbf{k}$ of the probe, corresponding to the vertical slices of the transmission map in Fig. 4.8(a) (red dashed lines). As for the reflection detection, we observe a significant narrowing of the transmission peak width when $\mathbf{k} \to 0$, accompanied by a strong amplification of the probe.

Amplification. To quantify the gain, T is compared to the linear transmission of the probe T_0, measured in linear regime. T/T_0 is plotted in Fig. 4.9(a). with respect to $\mathbf{k}$ for different pump intensity $|F_P|^2$. It decreases rapidly as the probe moves away from $\mathbf{k}_\mathrm{S} = 0.06\ \mu\mathrm{m}^{-1}$, with a power law that tends towards $T/T_0 \propto \mathbf{k}^{-1}$ as F_P increases. Such a behavior is expected as the polariton scattering in the S-condensate is concentrated in a narrow range of wavevectors.

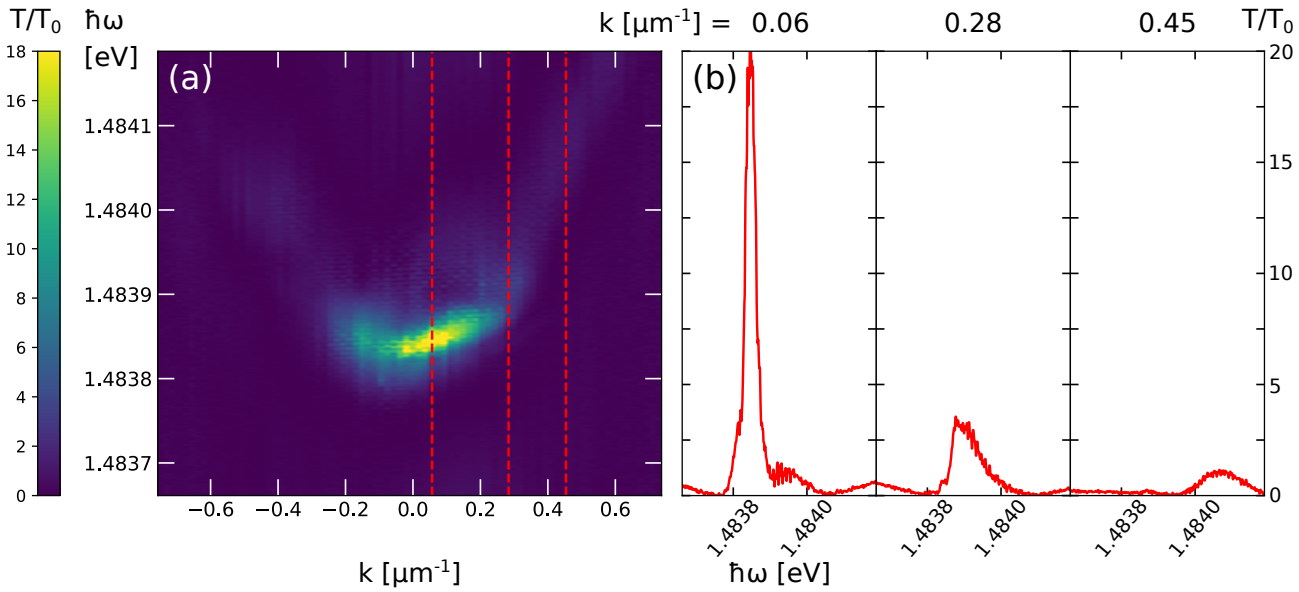

Figure 4.8: **Transmission spectrum of S-polaritons**, in the OPO regime with the pump at the magic angle $\mathbf{k}_\mathrm{P} = 1.2\ \mu\mathrm{m}^{-1}$, at intensity $|F_\mathrm{P}|^2 = 6.11\ \mu\mathrm{W}/\mu\mathrm{m}^2$ and at detuning $\hbar\delta = 1.0$ meV. **(a)** Map of the transmission gain T/T_0 of the probe as a function of its wavevector $\mathbf{k}$ and its energy $\hbar\omega$. The narrow, slightly tilted gain plateau has the expected shape of a diffusive Goldstone mode. **(b)** Traces of the probe scans taken along the vertical red dashed lines of (a). The resonance peaks are amplified and narrow when the probe scans around the central wavevector $\mathbf{k}_\mathrm{S} = 0.06\ \mu\mathrm{m}^{-1}$ of the signal condensate.

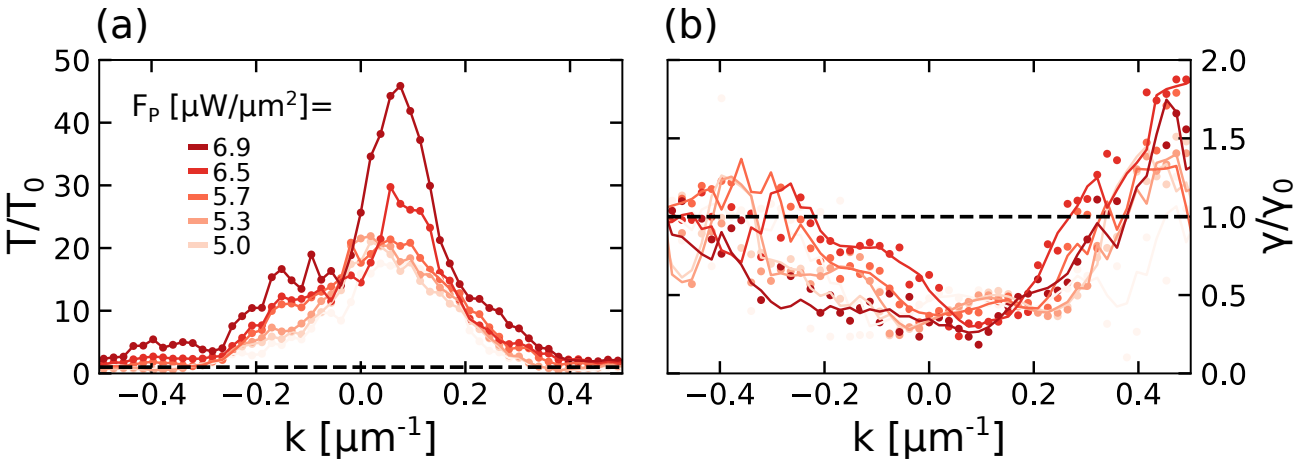

Figure 4.9: **Amplification and spectral narrowing of the Goldstone mode,** in OPO regime. **(a)** Gain on the maximum transmission T of the probe with respect to the linear transmission T_0, plotted as a function of its wavevector $\mathbf{k}$, for different pump intensities $|F_\mathrm{P}|^2$. **(b)** FWHM linewidth γ of probe scans with respect to the polariton decay rate γ_0, plotted as a function of $\mathbf{k}$, for different pump intensities. The solid lines are the moving average of the data.

It is a signature of the emergence of the long-range spatial coherence characteristic of the BEC transition [155]. At large $\mathbf{k}$, T/T_0 is again 1: the phase matching conditions are no longer verified and consequently the probe no longer seeds the parametric process responsible for its amplification.

Spectral narrowing. The evolution of the probe gain as a function of $\mathbf{k}$ is accompanied by a sharp narrowing of the linewidth of the spectrum around $\mathbf{k}_\mathrm{S}$. Such analysis is difficult because the shape of the transmission peaks is not a pure Lorentzian. As a first approximation, the measurement of the FWHM linewidth is sufficient to account for the spectral narrowing. As shown in Fig. 4.8(b), it is compared to that measured in the linear regime γ_0. At low-k, γ/γ_0 is of the order of 0.25, reflecting the vanishing of the imaginary part of the Goldstone mode energy. At high-k, even if the width remains difficult to evaluate because of the small amount of signal, we recover the linear regime behavior with $\gamma/\gamma_0 \simeq 1$.

The amplification and narrowing increase as the pump intensity moves away from the OPO threshold. This is shown in Fig. 4.9(a) and (b), where at the highest reachable intensity the gain approaches $T/T_0 = 45$ and the narrowing $\gamma/\gamma_0 = 0.2$, compared to the linear resonance.

Multimode analysis. It is possible to extend further the analysis on the linewidth, as several spurious modes may be present in the vicinity of the Goldstone mode. These may originate from the photonic resonances at the free spectral range of the optical cavity coupled to the substrate, from the co-existence of several signal and idler modes resulting from the OPO process, or from additional elementary excitation branches predicted by the Bogoliubov theory.

The evidence for such a multimode regime is verified experimentally as illustrated by Fig. 4.10.

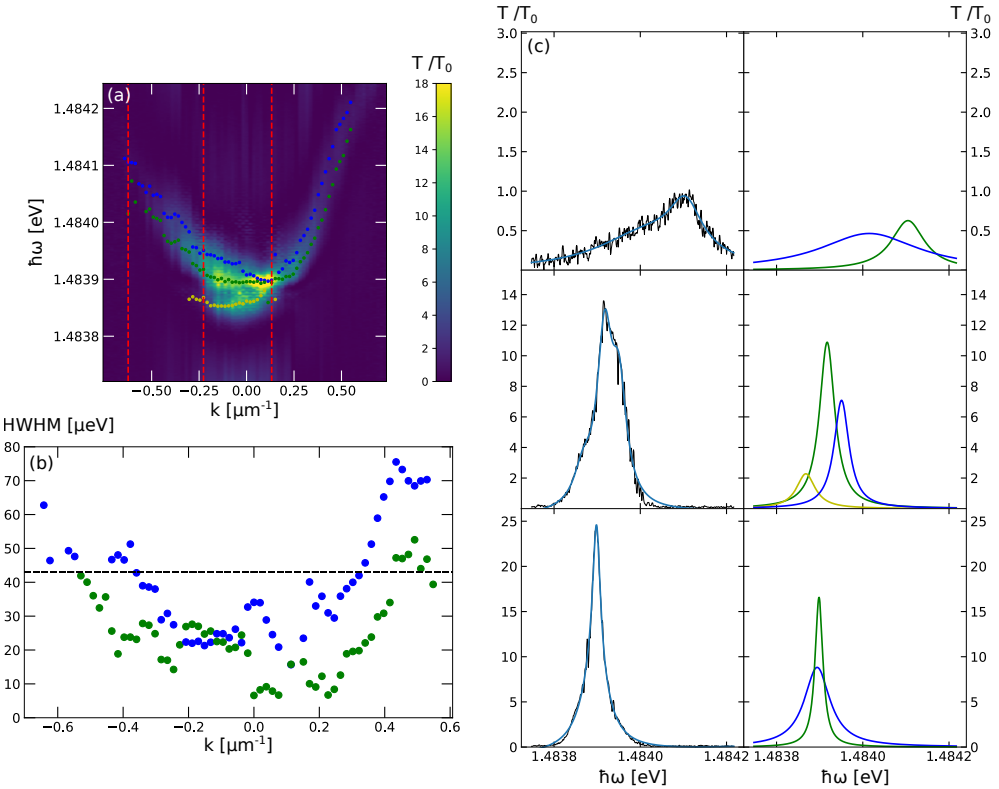

Figure 4.10: **Multimode analysis of the S-polaritons spectrum. (a)** Transmission map plotted as a function of the probe energy $\hbar\omega$ and wavevector $\mathbf{k}$, with the pump at the sample magic, of intensity $F_p = 7.0\ \mu\mathrm{W}/\mu\mathrm{m}^2$ and detuning $\hbar\delta = 1.0$ meV. The blue, green and yellow curves correspond to the energy of the Lorenzian maxima extracted from the fits of the probe traces at each of the scanned $\mathbf{k}$. **(b)** HWHM linewidths of the different Lorentzians fitted at each of the scans of the map (a). **(c)** Left panel: scan of the probe plotted in black line and its multimode fit plotted in blue line, at the wavevectors -0.62, -0.23 and 0.12 $\mu\mathrm{m}^{-1}$ respectively (from the upper to the lower row), indicated by the red dashed line in the map (a). Right panel: individual Lorentzian components of the multimode fit.

In Fig. 4.10(c), the probe traces extracted from Fig. 4.10(a) does not have a purely Lorentzian shape. In order to reproduce their peculiar linewidth at the base of the transmission peak, one has to consider the sum of several Lorentzians. Around $\mathbf{k}_S$ (lowest panel), the peak of larger amplitude and smaller width corresponds to the Goldstone mode, whereas the second and third ones corresponds to spurious modes. The resulting fit closely matches the experimental peaks.

By iterating this fitting procedure to each of wavevectors scanned by the probe, three different dispersion relations are identified, of real $\hbar\omega$ and imaginary γ parts plotted respectively in Fig. 4.10(a) and (b). The Goldstone mode is the green branch, with almost zero curvature and a linewidth tending to $\gamma \simeq 0.05 \times \gamma_0$ around $\mathbf{k}_S$.

All these results are consistent with the spectral features that are expected at the onset of

the Goldstone mode in the OPO process, i.e. a diffusive dispersion relation, of width close to zero. Now, we can bring a final proof of what we claim here by explicitly destroying the spontaneous symmetry breaking of the OPO process.

4.8 Destruction of the Goldstone mode

4.8.1 Injection scheme

Similarly to the observation of a gap opening in the magnon spectrum of ferromagnets under application of an external magnetic field, which fixes a privileged alignment direction of the magnetic moments and results in the loss of the spontaneous symmetry breaking [97], the injection of an additional laser into the signal or idler mode of the OPO fixes the phase of polaritons and should therefore leads to the loss of the SSB. Indeed, the parametric conversion process occurs preferentially at the phase set by the additional laser. Therefore the SSB no longer takes place and thus the Goldstone mode vanishes.

In this way, we want to demonstrate that the observed narrow spectra are indeed the result of a SSB. Theoretically, the destruction of the Goldstone mode is evidenced by the broadening of the linewidth around the signal mode wavevector $\mathbf{k}_{\mathrm{S}}$ when injecting the additional laser at resonance with the signal or the idler condensates. Accordingly, it results in a broadening of the transmission peak of the probe. Its FWHM linewidth is larger the higher the additional laser intensity, as the phase fixation gets stronger [177].

In our experiments, a laser diode is used for the injection. Its spectral bandwidth is less than 0.42 neV (100 kHz), thus several order of magnitude below the typical linewidths observed for polaritons and well below the narrowest Goldstone modes that we managed to detect. Therefore we can assume that the linewidths measured in the following are determined by the dynamics of polaritons and not by the lasers.

4.8.2 Injection in the S-condensate

Our first experiment to destroy the SSB of the OPO involved the phase pinning of the signal condensate, as its position in real and reciprocal space is clearly resolved by CCD cameras (unlike the idler polaritons), facilitating the mode matching with the injection laser.

Scan of the energy. The experiment is performed in the same conditions used for the preparation of the OPO regime in the previous section. In Fig. 4.11, the additional laser is injected at the central wavevector of the signal mode $\mathbf{k}_{\mathrm{S}} \simeq 0\ \mu\mathrm{m}^{-1}$, at an intensity $|F_i|^2 = 0.4\ \mu\mathrm{W}/\mu\mathrm{m}^2$, one order of magnitude below the pump intensity $|F_{\mathrm{P}}|^2 = 5\ \mu\mathrm{W}/\mu\mathrm{m}^2$ and two orders of magnitude above the probe intensity $|F_{probe}|^2 = 0.005\ \mu\mathrm{W}/\mu\mathrm{m}^2$. The diameter of its waist in the plane of the cavity is similar to the diameter of the signal condensate, of the order of 75 μm. The probe scans the cavity over 70 GHz at $\mathbf{k}_{\mathrm{S}}$. Its transmission is displayed in Fig. 4.11(a), for different energy detunings $\hbar\delta_i$ of the injection laser with respect to the signal mode resonance,

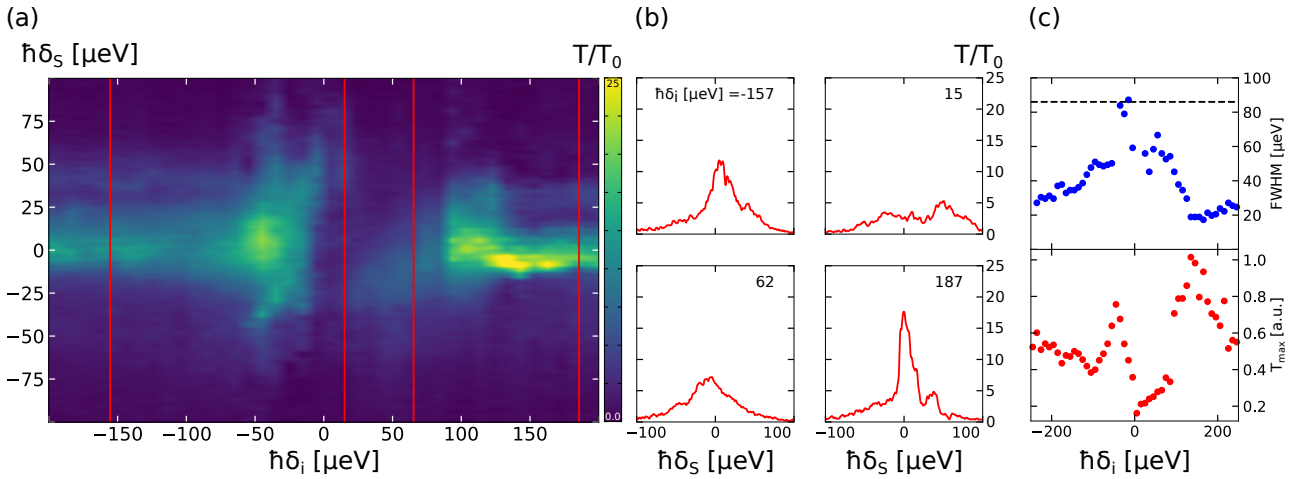

Figure 4.11: **Destruction of the Goldstone mode by laser injection into the signal mode.** The pump is at the magic angle, at intensity $|F_p|^2 = 5\ \mu\mathrm{W}/\mu\mathrm{m}^2$ (above the OPO threshold) and at detuning $\hbar\delta = 0.5$ meV. The injection laser has an intensity of $|F_i|^2 = 0.2\ \mu\mathrm{W}/\mu\mathrm{m}^2$. **(a)** Transmission gain T/T_0 map of the probe at $\mathbf{k} = \mathbf{k}_S$ as a function of the detuning of the probe δ_S and of the injection laser δ_S, with respect to the energy of the signal polaritons at $\mathbf{k}_S \simeq 0\ \mu\mathrm{m}^{-1}$. **(b)** Traces of the probe gain T/T_0, taken for different δ_i along the red vertical lines of (a). **(c)** Upper panel: Full width at half maximum (FWHM) of the probe transmission peak versus δ_i. Lower panel: Maximum amplitude T_{max} of the probe transmission T as a function of δ_I. When the injection laser energy is far from the signal polaritons resonance, the Goldstone mode is detected via the spectral narrowing of the linewidth of the probe resonance peak relative to the polariton decay rate γ indicated by the horizontal back dashed line; when the injection laser energy is near resonance, the Goldstone mode vanishes, as evidenced by the decrease in the amplification and the broadening of the probe resonance peak.

going from the red $\delta_i < 0$ to the blue $\delta_i > 0$. Out of resonance, $\hbar\delta_i > 100\ \mu$eV, the probe trace reveals the narrow linewidth peak (of FWHM $= 20\ \mu\mathrm{eV} = 0.24\ \hbar\gamma$) characteristic of the Goldstone mode analysed before. Close to resonance, $\hbar\delta_i < 100\ \mu$eV, this peak broadens and drops in amplitude, until reaching a linewidth close to γ when $\hbar\delta_i \to 0\ \mu$eV: the Goldstone mode vanishes. The asymmetry of the injection range with respect to $\hbar\delta_i = 0\ \mu$eV is due to the coupling efficiency of signal polaritons with the additional laser that remains significant for slight blue shifts (as it is observed in the standard scheme of coherent excitation), while for red shifts it is very low. The Goldstone mode is therefore recovered as soon as $\hbar\delta_i < 0\ \mu$eV. Note that we checked that the OPO regime was still operating, by observing that the signal mode emission remained unchanged when the injection laser was in resonance with it.

Scan of the intensity. In Fig. 4.12, in addition to its energy, the intensity of the additional laser is ramped up. As soon as the injection is in the vicinity of the signal condensate ($\hbar\delta_i < 0.075\ \mu$eV), the destruction of the Goldstone mode happens for intensities $|F_i|^2$ as low as two

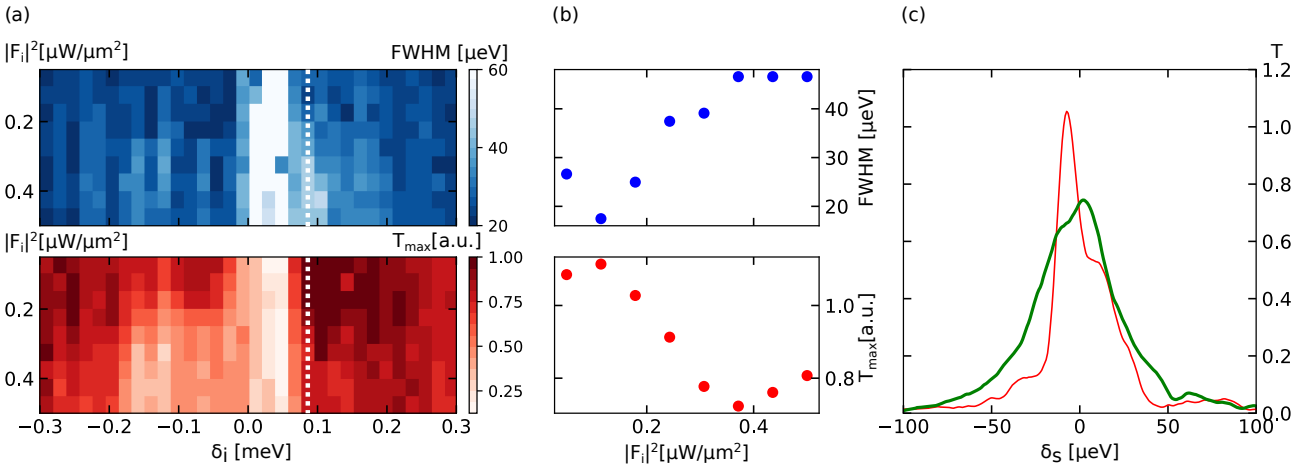

Figure 4.12: **Intensity of the injection signal scan.** The pump illuminates the sample in the OPO conditions. **(a)** Upper (lower) panel: The color scale shows the map of the full width at half maximum FWHM (maximum transmission T_{max}) of the probe resonance with the signal mode at $\mathbf{k} = \mathbf{k}_S$, displayed as a function of the detuning δ_i between the injection laser energy and the signal polariton resonance at $\mathbf{k}_S \simeq 0$ μm^{-1}, and of the injection laser intensity $|F_i|^2$. **(b)** Upper (lower) panel: FWHM (T_{max}) of the probe resonance as a function of $|F_i|^2$, for δ_i chosen along the vertical white dashed line of (a). **(c)** Red (green) curve: probe transmission signal at $|F_i|^2 = 0.2$ (0.5) μW/μm^2 and $\hbar\delta_i = 0.08$ meV. The linewidth and amplitude of the probe resonance peak increases and decreases respectively as $|F_i|^2$ is ramped up. This reveals the destruction of the Goldstone mode as the phase fixation of the signal polaritons by the injection laser becomes stronger.

orders of magnitude below the pump intensity $|F_p|^2$. As illustrated in Fig. 4.12(b) and (c), the broadening of the FWHM and the decrease in the transmission peak of the probe is greater the higher the injection intensity, meaning that the phase fixation is stronger.

4.8.3 Injection in the I-condensate

Fig. 4.13 presents the destruction of the Goldstone mode when the additional laser is injected at resonance with idler polaritons. The transmission of the probe scanning the S-polariton resonance near $\mathbf{k}_S = 0$ μm^{-1} is measured, for different values of detuning $\hbar\delta_i$ between the energies of the injection laser and the I-polaritons at the wavevector $\mathbf{k}_I \simeq 2.5$ μm^{-1}. For an injection intensity an order of magnitude below the pump intensity, there is a broadening of the linewidth and a vanishing of the gain when the additional laser is near resonance $0 < \hbar\delta_i < 15$ μeV. This evidences that the Goldstone mode is destroyed by phase fixation of the I-polaritons as well, and thus it results indeed from the invariance of the simultaneous phase rotation of S- and I-polaritons.

Fig. 4.14 shows a detailed analysis of the transformation of the probe resonance with the signal condensate when the third laser is close to the resonance of the idler condensate. Around $\hbar\delta_i$

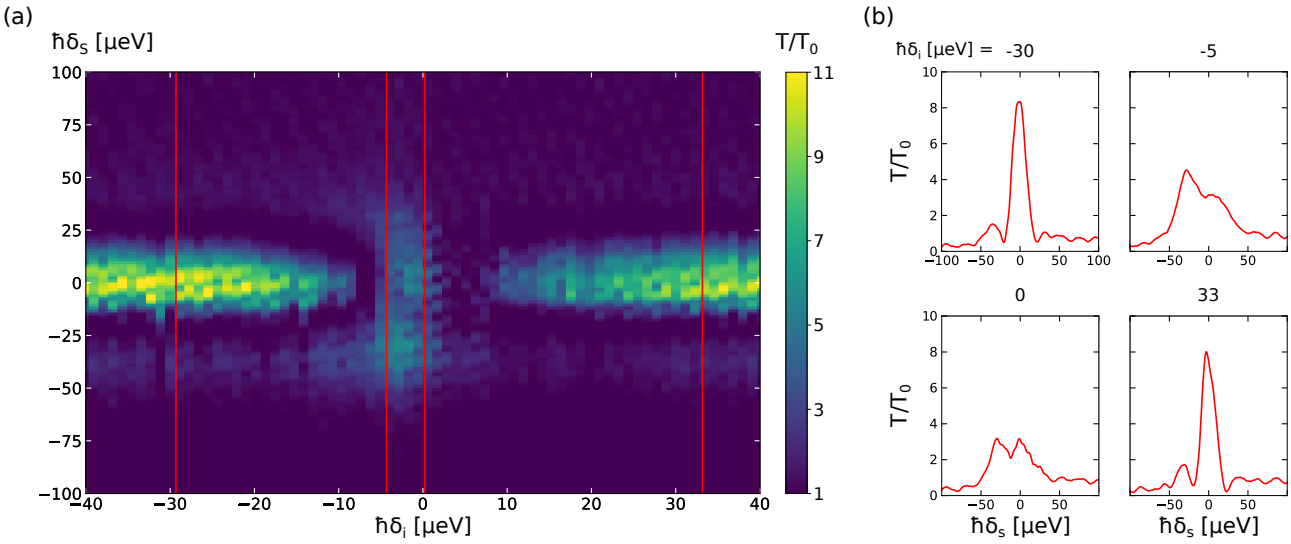

Figure 4.13: **Destruction of the Goldstone mode by laser injection into the idler mode.** The pump is at the magic angle, at intensity $|F_p|^2 = 5\ \mu\mathrm{W}/\mu\mathrm{m}^2$ (above the OPO threshold) and at detuning $\hbar\delta = 0.5$ meV. The injection laser has an intensity of $|F_i|^2 = 0.5\ \mu\mathrm{W}/\mu\mathrm{m}^2$. **(a)** Transmission gain T/T_0 map of the probe at $\mathbf{k} = \mathbf{k}_\mathrm{S}$ as a function of the detuning of the probe $\hbar\delta_\mathrm{S}$ with respect to the energy of the signal polaritons at $\mathbf{k}_\mathrm{S} \simeq 0\ \mu\mathrm{m}^{-1}$ and of the injection laser δ_I, with respect to the energy of the idler polaritons at $\mathbf{k}_\mathrm{I} \simeq 2.5\ \mu\mathrm{m}^{-1}$. **(b)** Traces of the probe gain T/T_0, taken for different δ_i along the red vertical lines of (a). When the injection laser energy is far from the idler polaritons resonance, the Goldstone mode is detected via the spectral narrowing of the linewidth of the probe resonance peak; when the injection laser energy is near resonance, the Goldstone mode vanishes, as evidenced by the decrease in the amplification and the broadening of the probe resonance peak.

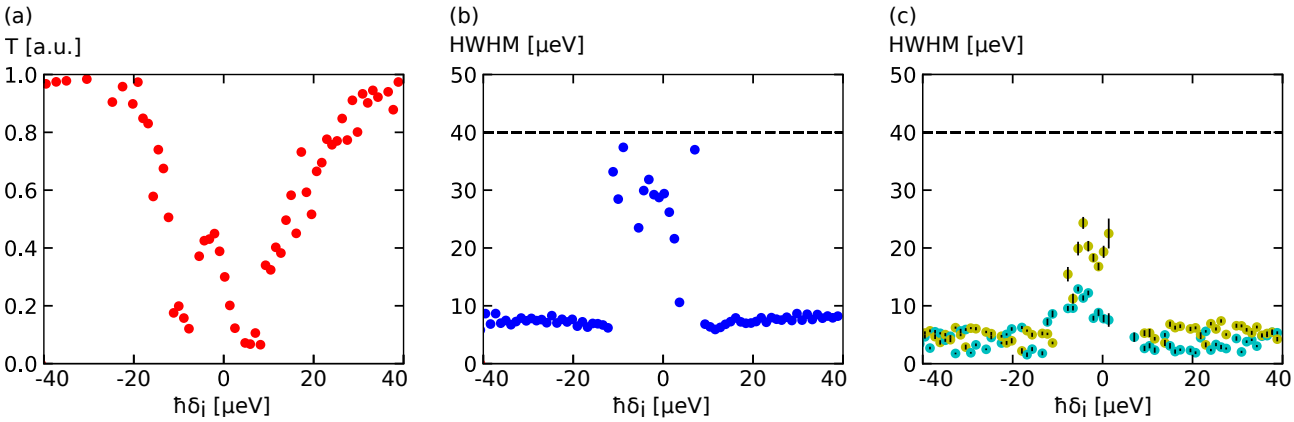

Figure 4.14: **Transmission and linewidth of the probe laser in the vicinity of the signal condensate**, for different injection energies of an additional laser in the idler condensate. **Panel (a)** (**Panel (b)**) Maximum transmission intensity T (HWHM linewidth) of the probe resonance with the signal condensate as a function different detuning values δ_i of the injection laser energy with respect to the idler condensate. **(c)** Corresponding HWHM linewidths resulting from the multimode analysis of the probe resonance signal. The shape of the probe transmission peak is adequately reproduced with a fitting law corresponding to the sum of two Lorentzian, whose respective HWHM linewidths are plotted in yellow and blue.

$= 0$ meV, the maximum transmission amplitude of the probe drops as presented in Fig. 4.14(a), as a consequence of the loss of gain; the HWHM linewidth broadens and tends towards a value governed by the polariton decay rate ($\hbar\gamma_0/2 = 40$ μeV at the considered working point) as presented in Fig. 4.14 (b). All these features confirm the vanishing of the Goldstone mode due to the fixation of the idler condensate phase.

However, as was revealed by the multimode analysis of the Goldstone mode, the probe resonance peaks displayed on the map in Fig. 4.14 may result from the sum of several Lorentzian peaks. To ensure that the increase in HWHM observed upon injection of the third laser into the idler condensate is indeed related to a linewidth broadening of the resonance, and not, for instance, to an energy splitting of the different modes detected that would produce also an effective broadening of the peak in the trace of the probe, a multi-Lorentzian analysis is performed. Here we find that the probe signal is well reproduced when the fit corresponds to the sum of two Lorentzians. The HWHM linewidths of these two peaks plotted in Fig. 4.14(c) display a broadening when the energy of the third laser is in the vicinity of the idler condensate resonance $\hbar\delta_i \rightarrow 0$ meV: this analysis also reveals the destruction of the Goldstone mode.

Chapter 5

Snake instabilities of dark solitons in static polariton fluid

In the investigations of polariton Bogoliubov modes, we briefly mentioned the modulational instability modes as a type of elementary excitation that is out of reach in stationary regime due to its dynamically unstable nature, i.e. $\mathfrak{Im}(\omega_{Bog}) > 0$. In the regime of continuous quasi-resonant excitation, under homogeneous driving, we were therefore limited to study the precursors of such instabilities. However, thanks to the close dependence between the pump properties and the polariton dynamics, it is possible to design a driving scheme suitable for the stimulation and observation of modulational instabilities in steady state.

This work, presented in this chapter, is part of the study of the stability of dark solitons in planar semiconductor microcavities. Indeed, because of their one-dimensional nature, solitons placed in a two-dimensional environment are inherently unstable due to the presence of transverse modulational instabilities, called "snake instabilities", leading to their decay into chains of quantized vortex-antivortex pairs [86, 94]. This results in the onset of a quantum turbulent regime equivalent of the von Karman vortex street.

In the previous works of our team, the snake instabilities could not be recorded because the solitons were always generated in a stabilizing supersonic flow. Moreover, the typical picosecond relaxation time makes their observation unfeasible without very fast time-resolution measurements. In the following, we will discuss the experimental implementation of a technique of reshaping of the pump intensity profile in order to dig in the polariton superfluid a static low-density channel embedding dark solitons. Such a confined geometry will allow us to observe in stationary regime the snake-instabilities.

Our work is based on the theoretical study carried out in collaboration with the group of G. Malpuech in Clermont-Ferrand [92]; and the experimental results are reported in Ref. [46].

5.1 Dark soliton in polariton superfluid

5.1.1 Definition

The concept of soliton refers to solitary non-linear waves, maintaining their shape and velocity during propagation and upon collision with other solitary waves. Their first historical description was made by J. Russel in 1834 [79], who reported an unusual wave propagating without dispersion broadening while moving along a narrow water channel. A first attempt to explain this observation was proposed in 1872 by J.V. Bussinesq, by deriving an equation with solutions featuring the peculiar property of conserving their initial shape when they intersect with each other. In 1895, D. Korteweg and G. de Vries developed a simplified form of this equation, the so-called KdV equation, offering an exactly solvable model of wave propagation on the surface of shallow water [93]. The concept of soliton, however, did not appear until the 1960s, when researchers associated the solitary wave shape-retaining properties during propagation and collision with the behaviour of particles. Today, it refers to a broad class of solitary waves, including some that do not preserve their shape, accelerate, divide into multiple waves or form interacting bound states during propagation [107]. The common characteristic of such a diversity of waves, whereby they can be described as solitons, lies in the complete integrability of the equations describing their motion.

The original behaviour of solitons results from the balance between the classical dispersive broadening of a wave, which tends to spread out temporally and spatially, and the modifications on the field induced by a non-linear medium, which, on the contrary, tends to compress the wave. Thus, nonlinearity is a crucial ingredient in soliton generation, as demonstrated in 1962 by G.A. Askaryan, who showed that the correction to the refractive index proportional to the illumination intensity in self-focusing media can suppress the diffraction broadening of a beam [14]. As already reported several times in this manuscript, the physics of such media is based on the GPE, of which the soliton is a particular solution [107]. For a self-focusing medium (attractive interactions), solitons are bright: they take the form of an intense peak propagating over a continuous background. In contrast, for a self-defocusing medium (repulsive interactions), like the microcavity polaritons, the solitons are dark: they have the form of an intensity dip in a continuous background.

Dark soliton solution. For the latter case, the one we are interested in, the expression of the soliton wave function is inferred from the one-dimensional time-dependent GPE, without application of an external potential

$$\mathrm{i}\frac{\partial}{\partial t}\psi(x,t) = -\frac{\hbar^2}{2m}\frac{\partial^2}{\partial^2 x}\psi(x,t) + g|\psi(x,t)|^2\psi(x,t), \tag{5.1}$$

with g positive in the case of a self-defocusing medium. Then, one finds, from a judicious choice of variable and ansatz, the following solution [166]

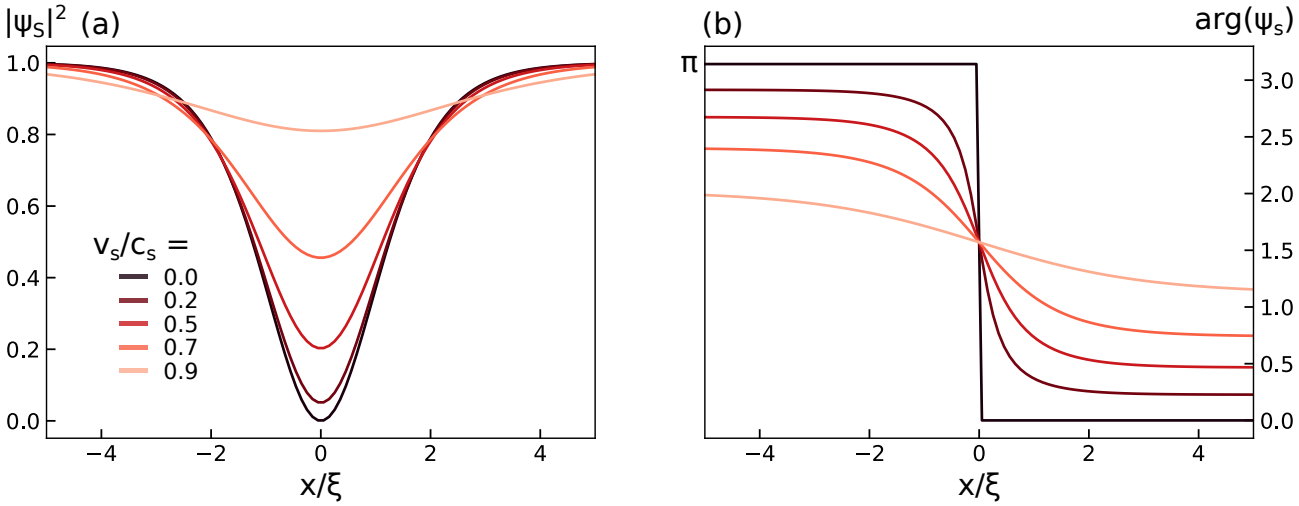

Figure 5.1: **Theoretical intensity and phase profiles of a 1D dark soliton** calculated from Eq. (5.2). **(a)** Intensity profiles of the dark soliton for different values of its velocity v_s relative to the speed of sound c_s. Its half-width with respect to its density minimum is equal to one healing length ξ, fixed by the density of the fluid. **(b)** Corresponding phase profiles. The soliton is really "dark" only in a static regime $v_s = 0$, otherwise its characteristic density dip and phase jump are not at zero and π respectively. It is then rather called a "gray" soliton.

$$\psi_S(x - v_s t) = \sqrt{n}\left[\sqrt{1 - \frac{v_s^2}{c_s^2}}\tanh\left(\frac{\mathrm{x - v_s t}}{\xi\sqrt{2}}\sqrt{1 - \frac{\mathrm{v_s^2}}{\mathrm{c_s^2}}}\right) + \mathrm{i}\frac{\mathrm{v_s}}{\mathrm{c_s}}\right], \tag{5.2}$$

where v_s is the propagation speed of the soliton. The corresponding density $|\psi_S|^2$ and phase $arg(\psi_S)$ profiles are plotted for different values of v_s in Fig. 5.1(a) and (b), where the characteristic dark soliton density dip, of depth tending towards 0 when $v_s/c_s \to 0$, accompanied by a π-phase jump are shown. Predicted in the 1970s [166], such dark solitons were only observed experimentally two decades later. Since then, they have been studied in a wide variety of nonlinear systems, such as cold atom condensates [58, 51, 57], thin magnetic fims [1, 41], liquid helium [175], optical fibres [171, 157] and at the surface of water [39].

5.1.2 Dark soliton pair generation

Regarding polariton fluids, the first observation of dark solitons was made in the Quantum Fluids of Light team by A. Amo in 2011 [8], following the demonstration of superfluidity in 2009 [10]. The experiment consisted in resonantly exciting a polariton flow at a specific velocity v, upstream of a structural defect. When the flow velocity exceeds the speed of sound $v > c_s$, a pair of oblique dark channels appears downstream of the defect, in the density map of the fluid in Fig. 5.2(a). Their solitonic nature is confirmed by the π-phase jump on either side of their dip in Fig. 5.2(b). Obviously, the planar geometry and the driven-dissipative character of the polariton system make the theoretical description of the solitons observed here different

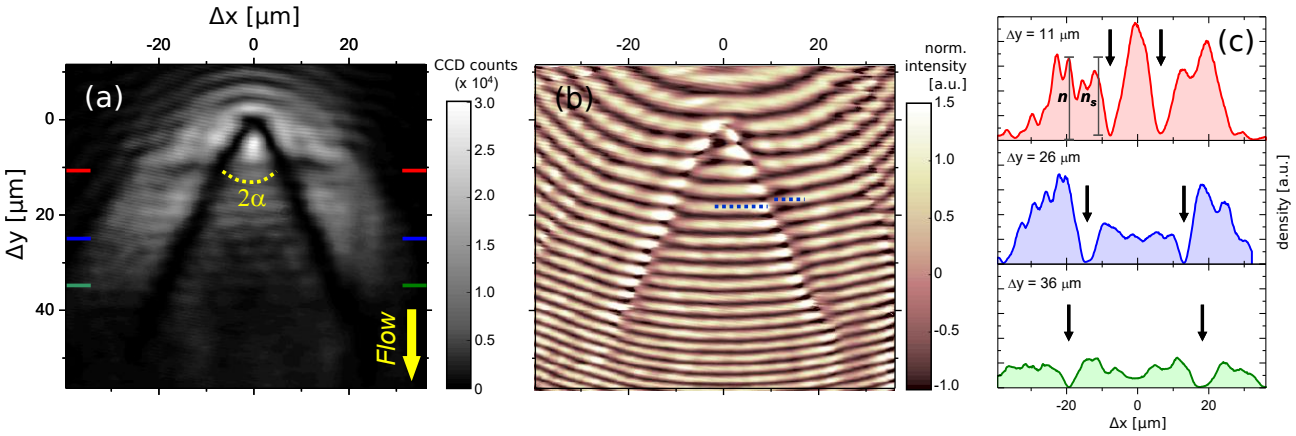

Figure 5.2: **Generation of a pair of oblique dark solitons in a planar polariton fluid.** **(a)** Density map of the fluid in the cavity plane. **(b)** Corresponding phase map obtained by interferometry method. **(c)** Density profiles taken along the lines of (a) indicated by the coloured markers. The black arrows indicate the position of the solitons along x. – The dark solitons of the pair correspond to the two black channels in the fluid density in (a), associated with the π phase jumps in (b). They are generated within a supersonic fluid, flowing in the wake of a micrometer-sized structural defect, located just below their junction. The α separation angle is determined by the Mach number of the fluid $M = v/c_s$. Figure adapted from [8].

from that of the GPE pure 1D case. Nevertheless, one can relate the two configurations by considering that the direction of the flow is equivalent to an effective time axis. Looking at successive horizontal slices of Fig. 5.2(c) one observes two solitons of shape similar to those described in Fig. 5.1, which move away from each other in time.

Interestingly, the aperture angle α between the two solitons is linked to the Mach number c_s/v of the flow after the defect. From Eq. (5.2), it is possible to associate the density dip phase jump θ to the soliton velocity v_s via the relation $v_s = c_s\cos(\theta/2)$. In addition, to follow a straight line during its propagation, the soliton has a velocity in the laboratory reference frame matching $v_s = v\sin(\alpha)$. Thus, from the combination of these two relations, the following expression is found

$$\sin(\alpha) = \frac{\mathrm{c_s}}{\mathrm{v}}\cos\left(\frac{\theta}{2}\right). \tag{5.3}$$

In this experiment, the generation of solitons under resonant excitation, i.e. in a regime where the phase of polaritons is directly inherited from the phase of the driving field, is achieved thanks to the exploitation of the ballistic propagation of the fluid outside the pump injection area [134], where the phase is free to evolve and thus undergoes a π-phase jump. In this case, the distance of propagation of solitons is limited to a length governed by the microcavity losses in the ballistic area, restraining the study to small scales of the order of twenty microns. Overcoming such a limitation has been the focus of the team works over the last few years, to

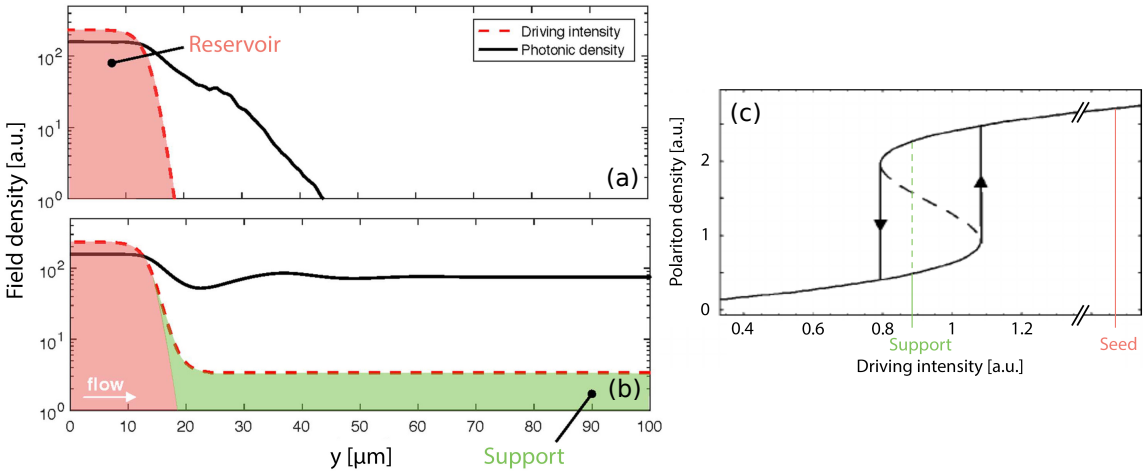

Figure 5.3: **Polariton density in seed/support configuration. (a)** Polariton density profile with only the seed. The black solid line shows the intracavity density (logarithmic scale); the red dashed line the incident intensity. The seed excites a high density polariton reservoir, highlighted by the red area. It has a small incidence angle with respect to the plane of the cavity, imposing a flow to the fluid (towards towards increasing x), which decays exponentially outside the illuminated region. **(b)** Polariton density profile with only the seed and the support. Even if the support creates in the green area a density two orders of magnitude below that excited by the seed, the flow of the fluid outside the reservoir region sustains a high density on a macroscopic scale, no longer limited by the finite lifetime of polaritons. **(c)** Density of polaritons as a function of the incident intensity. Individually, the seed excites a very high density, far away from the bistability loop; the support a density lying on the lower branch, in the bistability loop. Adapted from [135].

make solitons propagate over macroscopic distances.

5.1.3 Superfluid propagation enhancement

In order to generate a superfluid flow on macroscopic scales without pinning its phase, S. Pigeon numerically revealed in 2017 [135] a method to keep the fluid density at high level over distances of several hundred microns. Two driving fields are considered, with the same frequency ω_P and in-plane wavevector $\mathbf{k}_P$ but with different intensities. The first one, at a very high intensity I_P chosen far from the bistability hysteresis loop, plays the role of a seed. It is localized in a small region of the sample and generates a high density fluid whose dynamic is frozen by phase pinning. The second, called the support, has an intensity $I_S < I_P$ lying in the bistability hysteresis loop. It covers an area of several hundred microns length over the cavity, generating a fluid that is initially in the lower density regime. Then, remarkably, the localized application of the seed at a point of the support results in a locking of the total illuminated area of the microcavity density on the higher branch of the bistability. This is shown in Fig. 5.3: when the seed alone is applied, the fluid flows in the $\mathbf{k}_P$ direction over a distance governed by the

exponential decay of polaritons; with application of the support, under an intensity I_S here two orders of magnitude below that of the seed, the propagation is maintained over macroscopic distances, thus resulting in an effective enhancement of the superfluid propagation.

Back to topological excitations, with this method, the support phase is not pinned by the driving field as it is excited in a weak intensity regime. Moreover, the addition of the seed maintains a high density regime suitable for the formation of vortices and solitons. Such a behavior has been demonstrated empirically, both numerically [135] and experimentally [102], in a configuration similar to the oblique soliton experiment, with the seed upstream and the support downstream a structural defect. In a subsonic regime, $v < c_s$, the turbulence created in the wake of the defect generates a stream of vortex-antivortex pairs of shape preserved all along the entire length of the support, proving that the phase of the fluid under weak intensity excitation is free to evolve. Today, a true analytical demonstration of such an observation has yet to be made.

5.1.4 Parallel dark solitons observation.

Similarly, the pump/support configuration was used to improve the propagation of solitons downstream the structural defect [101]. To do so, the flow velocity is supersonic $v > c_s$, resulting in the propagation of a pair of dark solitons in the region of the support over a hundred microns, instead of the twenty microns observed in 2011 [8]. The modification of the excitation scheme is accompanied by a change in the dynamics: surprisingly, the solitons are no longer oblique, but parallel to the flow, with a constant spacing between them, suggesting the onset of a bound state. Such a phenomenon was unexpected as the repulsive interactions between dark solitons should have repelled them from each other [181].

Solitons imprinting. As the latest technical refinement of the team dedicated to such studies, an all-optical method has been implemented to generate solitons at will in order to no longer have to rely on structural defects and therefore to better control the parameters of the experiment [109]. It involves the modulation of the phase profile of the seed with a SLM, to include in it two π-phase jumps. In doing so, the formation of a soliton pair in the sample is triggered, as the seed sets the phase of polaritons. Then, by giving a sufficient velocity to the flow in the direction of the support, the solitons propagate freely over distances of several hundred microns.

The great strength of the imprinting lies in the ability to tailor the initial conditions of the generation of solitons as desired. In particular, it allowed us to show that the spacing between the two solitons of the bound pair did not depend on the initial spacing, suggesting the involvement of a balance between the repulsive force intrinsic to dark solitons and an attractive force, which tends to reduce the size of the region enclosed by the pair, energetically costly to sustain as it is out-of-phase with the the rest of the fluid. Further studies of the mechanisms behind this attractive force have shown that the spacing between solitons is not governed by the hydrodynamic parameters of the flow, related to the Mach number, but rather

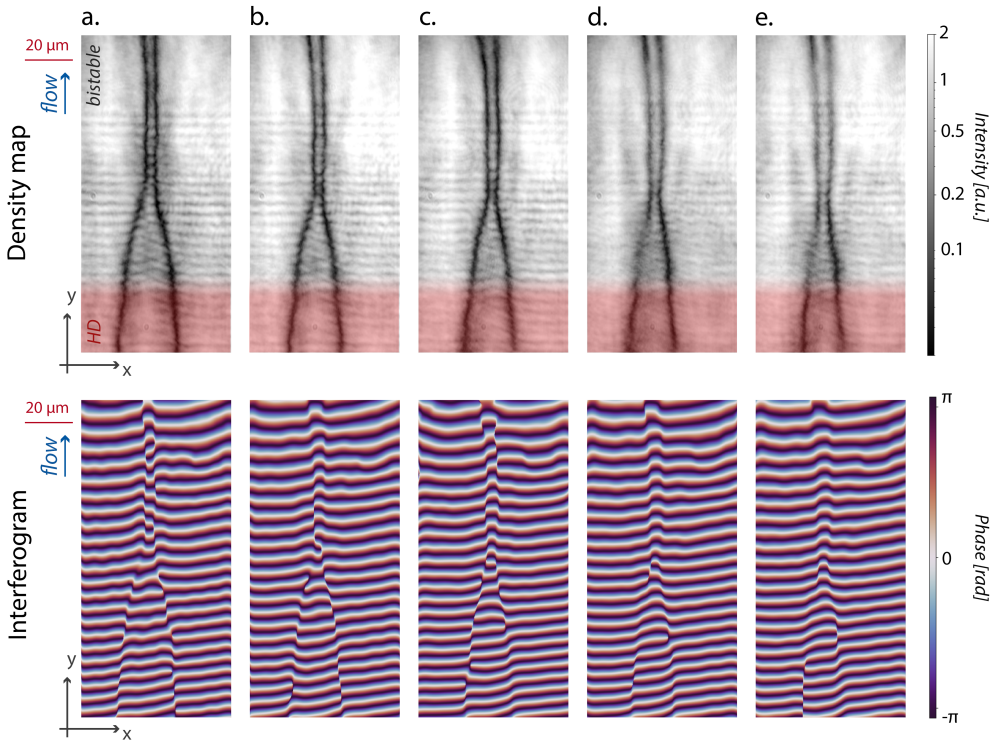

Figure 5.4: **Scan of the initial separation distance between two imprinted dark solitons**. Upper (lower) panels: density (phase) maps of the polariton fluid. A pair of dark solitons are imprinted with a high intensity seed, of phase profile reshaped with an SLM to include two π-phase jumps separated from each other by a controllable distance. They are generated in the high density region of the cavity (HD in red), where the phase of the fluid is fixed by that of the seed. By operating at supersonic velocity and illuminating the rest of the cavity with a low-intensity support, which injects a bistable fluid locked on the higher branch by the presence of the seed, the solitons propagate over several hundred microns. Their separation distance is tuned from 24 μm in panel **a.** to 15 μm in panel **e.**. When they enter the bistable fluid, the solitons propagation is maintained, but not their separation distance: they get closer to one another until reaching an equilibrium separation distance. Adapted from [109].

by the decay rate of polaritons γ, highlighting that the soliton bound state is a feature peculiar to out-of-equilibrium quantum fluids [109].

5.2 Snake instabilities

So far, we have investigated flow regimes suitable for the emergence of stable solitons. However, contrary to the ideal 1D case, it is well known that usually 2D solitons undergo transverse instabilities [180, 32] leading to their deformation and decay into vortex-antivortex pairs. These are the so-called snakes-instabilities [11], which we will discuss in this section.

5.2.1 Soliton stability in 2D

The stability of the fluid is derived from the Bogoliubov theory, which, as already mentioned, consists in linearising the generalized GPE around its steady state solution ψ_0. When the imaginary part of their energy is negative, the elementary excitations of polaritons correspond to the stable modes of the problem, stationary if a continuous pump exactly compensates the losses. On the contrary, when their imaginary part is positive, the elementary excitations experience a growth of their amplitude over time, until it becomes comparable to the amplitude of the stationary solution ($\propto \sqrt{n}$), making the linearisation of the GPE no longer valid. These are the unstable solutions. Now, the Bogoliubov problem can be solved in the presence of dark solitons by simply choosing the soliton wavefunction ψ_S of Eq. (5.2) as the steady state solution ψ_0 of the GPE. We assume here that the geometry of the system is invariant in the direction of the soliton axis, chosen along y. The linearization leads to the definition of a new set of relations between the amplitudes (U_k, V_k) of the elementary excitations and their energy $\hbar\omega$, called the Bogoliubov-de Genne equations [92]

$$\hbar\omega \begin{bmatrix} U_{\mathbf{k}} \\ V_{\mathbf{k}} \end{bmatrix} = \begin{bmatrix} L(x,k_y) & \hbar \mathrm{g}|\psi_0(\mathrm{x},\mathrm{k_y})|^2 \\ -\hbar \mathrm{g}|\psi_0(\mathrm{x},\mathrm{k_y})|^2 & -L(x,k_y) \end{bmatrix} \begin{bmatrix} U_{\mathbf{k}} \\ V_{\mathbf{k}} \end{bmatrix}. \tag{5.4}$$

$L(x,k_y)$ is defined as follows

$$L(x,k_y) = -\frac{\hbar^2}{2m}\left[\frac{\partial^2}{\partial x^2} - k_y^2\right] + 2\hbar \mathrm{g}|\psi_0(\mathrm{x},\mathrm{k_y})|^2 - \hbar\omega_{\mathrm{P}} - \mathrm{i}\hbar\frac{\gamma}{2}, \tag{5.5}$$

where the translational invariance allows to replace the nabla operator of the GPE by $\nabla^2 \rightarrow \partial^2/\partial x^2 - k_y^2$, with k_y the wavevector of the elementary excitations along y. Thus, we find a Bogoliubov operator similar to those studied previously, except that here the density distribution $|\psi_0|^2$ is no longer homogeneous and matches the profile of a dark soliton.

In order to get a simple picture of why the solutions of such a problem are generally unstable, one can refer to the study of the interplay between the energy of elementary excitations and the bistability of polaritons. It was seen in this section that the densities between the higher- and lower- branches of the bistability hysteresis loop correspond to unstable solutions of the Bogoliubov equation. And precisely, the dark solitons density profile switches smoothly from the bistability higher branch at $x \gg \xi$ to the lower branch at $x = 0$, thus explores a large range of these intermediate densities. Consequently, a set of unstable modes exists locally in the fluid, causing a modulation of the density at specifics wavevectors, which leads to a breaking of the soliton shape into energetically more favorable vortex-antivortex pairs.

The apparent stability of the aforementioned experiments comes from the supersonic flow and losses that wash away the transverse modulation instabilities [81]. For flow velocities at the boundary of the supersonic and subsonic regimes, though, several experiments performed also in the wake of a structural defect under resonant excitation [145, 123], report the formation of vortex streams, which can be understood as the decay of solitons by snake instabilities.

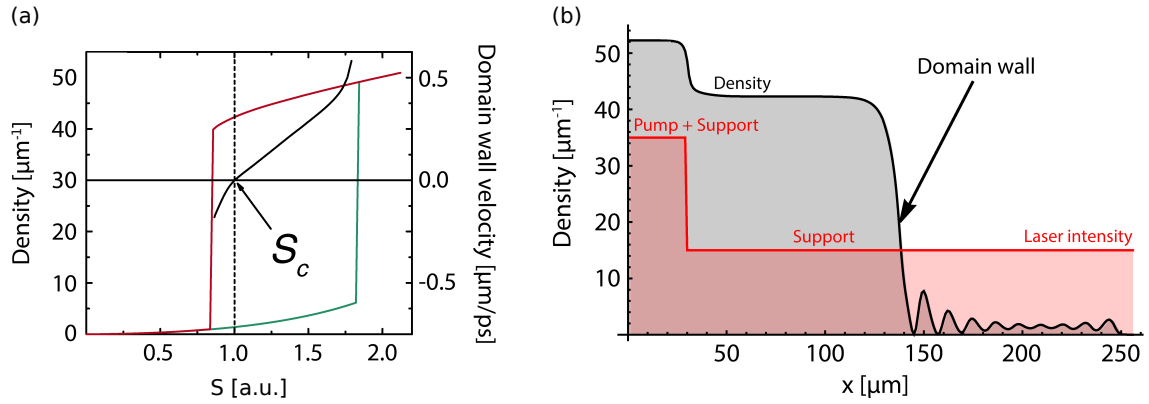

Figure 5.5: **Implementation of a domain wall (DW). (a)** Polariton bistability. Red and green plots: density (left vertical axis) as a function of the support intensity S. Black plot: DW velocity (right vertical axis). S_c denotes the critical intensity of the support at which the DW velocity is zero. **(b)** Steady state density profile after the DW propagation along the support. A high-intensity seed (called pump here) is injected at $\mathbf{k}$=0 μm^{-1} into the half-space $x < 30$ μm; a low-intensity support illuminates the entire cavity. The high density reservoir injected by the seed propagates along the support $x > 30$ μm until it stabilizes at an equilibrium position. Its abrupt slope edge models a DW. Adapted from [92].

However, such measurements rely on the use of a pulsed laser and a streak camera with a resolution of a few ps in order to capture snapshots of the vortices, of evolution time similar to the lifetime of polaritons. Therefore, it prevents a consistent study of the dynamics of the instabilities which requires a precise definition of both the energy and the intensity of the driving field. Nonetheless, based on the previous work of the team and the theoretical work of S.V. Koniakhin [92], it is possible to consider an excitation scheme suitable for the study of snake instabilities under continuous pumping and with low temporal resolution devices.

5.2.2 Domain walls

The trick is to confine the solitons and vortex-antivortex (VA) pairs in a static low-density channel, dug into the fluid, in order to freeze the spatial and temporal dynamics. The edges of the channel form domain walls (DW) [7, 104], separating two areas of the cavity under two different excitation regimes: one driven by an intense seed; the other driven by an intermediate-intensity support beam. Now, before discussing the appearance of topological excitations within such a geometry, one must first investigate under which conditions such a channel may exist. This requires first of all to study the motion of the DWs, to know the conditions of operation that ensure its stability in order to preserve the shape of the channel.

Stability of DW. Polaritons are again excited in a seed/support configuration at zero incidence $\mathbf{k} = 0$ μm^{-1} so that no preferential flow direction is imposed, within a cavity assumed to be translationally invariant along y. The support covers the entire cavity in simulations, while the seed shines only the $x < 30$ μm half-space, switching the density from the lower- to

the higher-branch of the bistability. The resulting high density reservoir then propagates along the support in the $x > 30$ μm direction, before decaying abruptly over a distance equal to one healing length ξ, setting up the DW of the problem, with a velocity that can be derived from the generalized steady-state GPE

$$\left[-\delta - \frac{\hbar^2}{2m}\nabla^2 + \hbar g|\psi_0|^2 - i\hbar\frac{\gamma}{2}\right]\psi_0 + S = 0, \tag{5.6}$$

with S the support field term, of detuning δ with respect to the LP branch and assumed to be real without loss of generality. By initially neglecting the polariton decay rate γ compared to the laser detuning frequency $\delta/\hbar$, such equation can be written in the well-known form of a Newton equation of motion for a material point, from which one can deduce the conditions required to maintain the DW around a given equilibrium position [92].

This leads to the definition of a critical value of the support intensity

$$S_c = \frac{2\delta^{3/2}}{3\sqrt{3}g}. \tag{5.7}$$

When $S < S_c$, the DW moves along the decreasing x; when $S > S_c$, it moves along the increasing x. Otherwise, when $S = S_c$, the DW remains stationary.

5.2.3 Solitons in channel

We can now proceed with the construction of the channel by adding a second seed occupying the $x > 54$ μm area of the cavity, thus separated by 24 μm from the first one, i.e. about 13 ξ by considering the typical densities of the higher branch of the bistability. The intensity of the support is chosen at $S = 0.25\ S_c$, so that the two DWs do not propagate within the channel. Then, thanks to the numerical simulation of the generalized GPE applied to such a geometry, one can reveal the spontaneous onset of a pair of dark solitons in the channel. This phenomenon can be explained by the destructive and constructive interference at work in the low density region, between polaritons of opposite wave vectors originating from the two DWs.

Instabilities. The modulation instabilities are thereafter triggered by the addition of a noise which breaks the translation invariance along the y direction. Consequently, the solitons bend and then break up into VA chains. Interestingly, the distriubtion of vortices within the channel depends critically on the intensities of the seed P and the support S. As shown in Fig. 5.6(c) and (d), the switch from $P = 1.25S_c$ to $P = 2S_c$ leads to the transition from an anti-symmetric regime, where two vortices of the same charge face each other on each side of the channel, to a symmetric regime, where, on the contrary, two vortices of opposite charge face each other. This is caused by the coexistence of two different instability modes within the channel, competing with each other. The imaginary parts of their energy, calculated from the Bogoliubov-de Gennes equation (5.4), are plotted in red and green on Fig. 5.6(b), as a

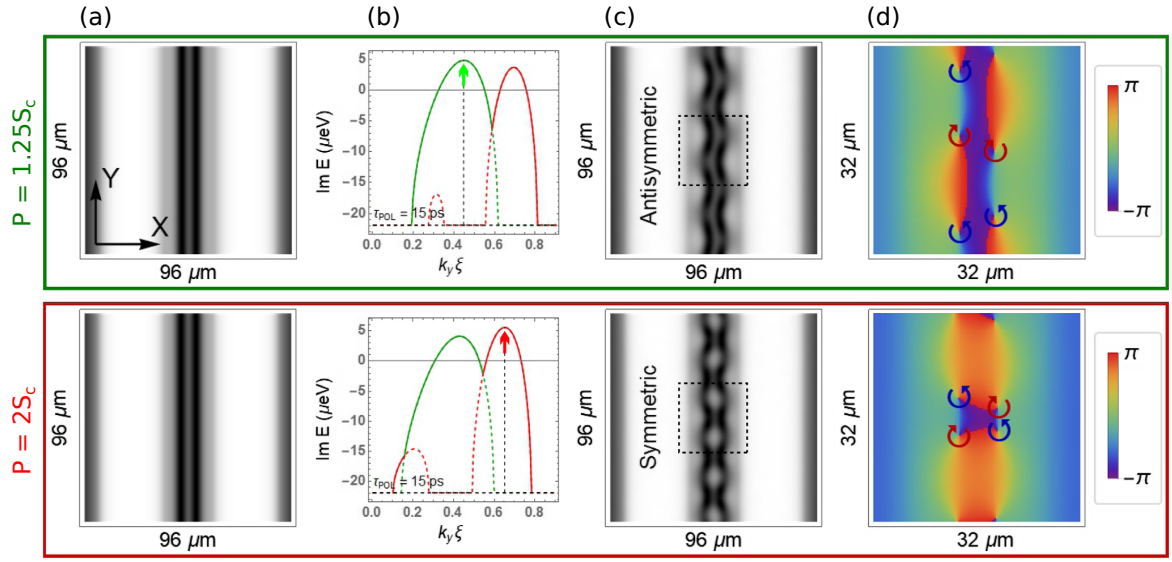

Figure 5.6: **Simulation of snake intabilities of solitons embedded in a channel. (a)** Density maps of the fluid before instabilities are triggered. The channel has a width of L = 25 μm, driven by the support of intensity $S = 0.25S_c$. It is enclosed between two regions of higher density, excited at high intensity P+S, by the seed P in addition to the support S. On the upper (lower) line, $P = 1.25S_c$ ($P = 2S_c$). Under these conditions, the channel exhibits a pair of dark solitons at its center. **(b)** Imaginary parts of the energy of the instability modes calculated from Eq. (5.4) under the conditions of (a) and plotted as a function of the wavevector k_y of the elementary excitations along the channel axis. The green and red colors highlight two different instability modes, competing with each other. The arrows indicate the highest energy mode, of k_y varying with P. **(c)** Density maps of the fluid after instabilities are triggered by the introduction of a weak disorder. The solitons break up and then transform into a chain of vortex-antivortex frozen in time due to the confinement induced by the channel. The change of dominant mode with P results in a transformation of the vortex distribution, from a symmetric to an antisymmetric state. **(d)** Phase maps corresponding to the black dashed square region in (c). They reveal the existence of vortex-antivortex pairs, with topological charges given by the direction of rotation of the blue and red arrows. Adapted from [92].

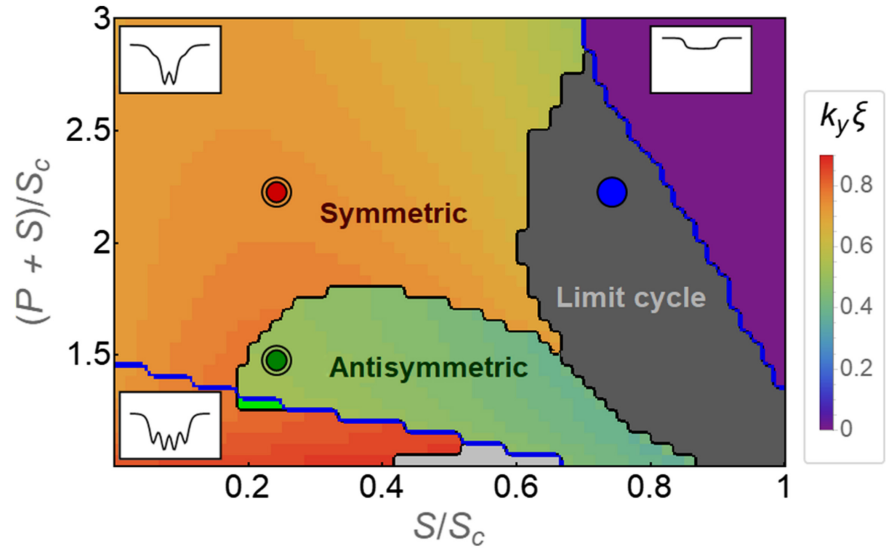

Figure 5.7: **Phase diagram of solitons embedded in a confinement channel** as a function of intensities of the seed P and the support S. The color-code indicates the value of k_y corresponding to the maximum of the imaginary part of the elementary excitations energy calculated from the Bogoliubov-de Genne equation. The black lines demarcate different geometries of instabilities, with in particular symmetric modes in orange, antisymmetric modes in green and breathing modes in black. The red and green dots indicate the fluid excitation conditions of each of the two lines in Fig. 5.6. The blue lines delineate the regimes of different numbers of solitons (zero, two or four), of density profiles displayed in the insets. Figures adapted from [92].

function of the wavevector of the elementary excitations in the k_y direction. It can be seen that by changing the intensity of the seed S, one modifies the maximum values of $\mathfrak{Im}(E)$ and consequently privileges the excitation of one mode at the expense of the other, resulting in a transformation of the vortex distribution observed in Fig. 5.6(c), as the dominant wavevector k_y of the instabilities changes.

Phase diagram. From the two previous examples, we can see that such a configuration is a powerful tool to address and study specific k_y modes of instability. To do this, one simply needs to tune the intensities of the support and the seed. Such a study is summarized in the phase diagram in Fig. 5.7, where the dominant instability mode, calculated from the Bogoliubov-de Gennes equation, has been plotted with different color shades as a function of the intensity S in the region within the channel and the intensity $S + P$ in the outer regions, relative to the critical intensity of the support S_c. Different regions can be identified, depending on the state of solitons:

- In purple, polaritons almost completely fill the channel, washing away solitons. This regime occurs for support values below S_c, as the particle flow comes from two DWs instead of one.

- In dark grey, the solutions are non-stationary. and correspond to breathing modes of solitons. They feature a pair of breathing solitons oscillating in time.
- In light grey, the channels embeds four solitons. These are stables ($\omega_{Bog}(k_y) < 0$) as the small seed P and large support S intensities ensure weak transverse flows.
- At the bottom left corner, the four solitons decay into symmetric streets of VA pairs, as the flow from the DWs increases at lower support intensity S.
- In the orange regions (between the blue lines), the channel embeds a soliton pair that decays into a symmetric street of VA pairs.
- In green regions, the channel embeds a soliton pair that decays into an anti-symmetric street of VA pairs.

5.3 Experimental implementation

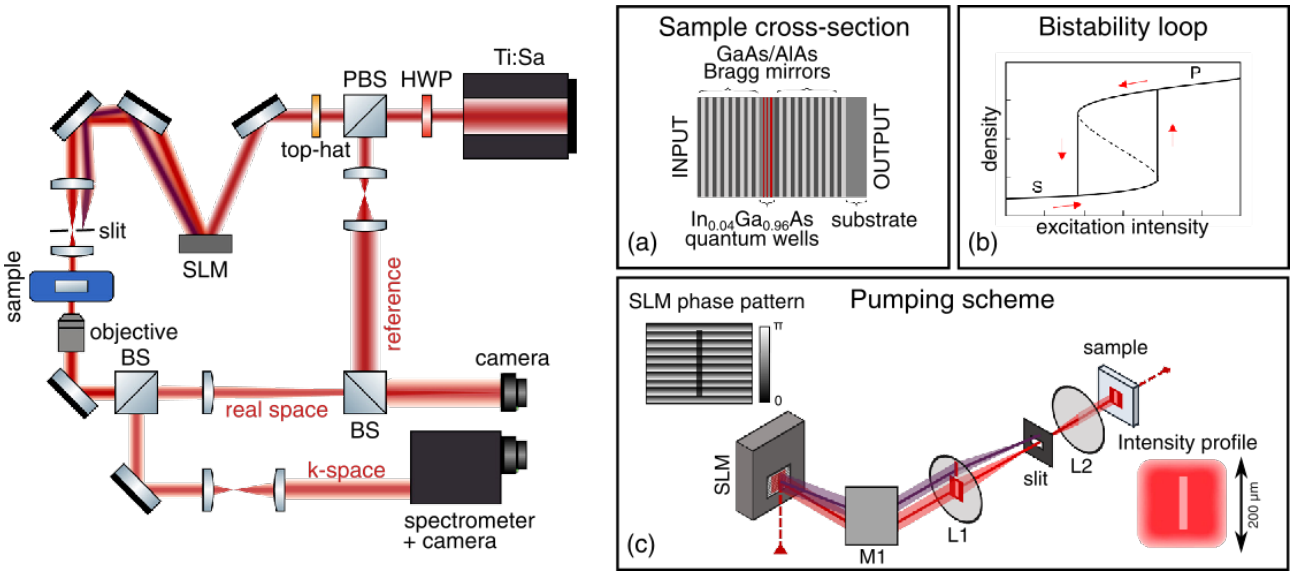

Figure 5.8: **Experimental setup**. **(a)** Cross-section skecth of the microcavity. **(b)** Sketch of the bistability loop obtained with a quasi-resonant excitation. **(c)** Detail of the shaping method to dig a rectangular vertical channel in the center of the driving field. In the scheme of the experimental set-up the red beam after the SLM corresponds to the laser intensity diffracted by the grating; the non-diffracted purple beam corresponds to the zero order of the grating, which is cut by a slit in the Fourier plane to obtain the intensity profile shown in the input plane of the cavity. The laser spot is flat and square due to the use of a top-hat lens. The real space detection arm gives access to the density and phase maps of the fluid, while the k-space detection to the energy-momentum distribution of the fluid by using a spectrometer.

5.3.1 Setup

The setup used for our experiments is schematized in Fig. 5.8. It involves only one laser beam, provided by a cw Ti:Sapphire Matisse, driving the sample at quasi-resonance and normal incidence. Therefore, contrary to what the theory suggests in the implementation of the seed/support method, we do not use two different beams to excite polaritons. Instead, we reshape the wavefront of the laser beam with a spatial light modulator (SLM), to incorporate within it a channel of tunable shape and intensity. More details on the SLM intensity modulation technique are given in **Appendix**.

Camera. The intensity and phase pictures shown in the following are taken with a mechanical shutter camera PIXIS1024BR eXcellon from Princeton Intruments. Its charge-coupled device (CCD) embeds a back-illuminated chip with 1024x1024 pixels of $13\mu m^2$, and of quantum efficiency around 95% at 830 nm. The readout rate is equal to 100kHz and the integration time is down to 1ms.

Intensity. The intensity images are taken by imaging the cavity plane into that of the camera using a 2-lenses telescope and a polarization filter aligned with the circular polarization of the input drive, in order to eliminate the contribution of any spin-flip effects in the detection. The signal collected originates from the photons leaking through the optical cavity: their dynamics preserve those of polaritons, so no special processing of the image is required after to analyze the fluid properties.

Phase. The phase profiles are extracted from the measurement of the interference pattern of the fluid image in the camera plane with a large-waist reference beam issued from the laser source before any modulation of the phase by the SLM. The overlap between these two beams is deliberately off-axis, in order to create an interferogram with quasi-straight and parallel fringes. By changing the angle between the reference with respect to the signal, the size of the fringes is controlled and set to be as small as possible, about 3 pixels in this case, in order to achieve the best phase resolution. The phase profile is derived from numerical filtering of the spatial frequency of the fringes in Fourier space, shifted to the zero frequency to eliminate the contribution of the global phase shift induced by the angle of the reference beam with respect to the fluid. In doing so, the inverse Fourier transform argument reveals only the local phase changes in the fluid (the 2π-phase windings of vortices and the π-phase jumps of solitons). Its fringes are unwrapped so that the phase map is continuous.

5.3.2 Boundary conditions

A crucial difference with the theory that we had to address at the beginning of our experiments is that we cannot create a channel with a translational invariant geometry along its length, because the size of the excitation beam is finite, with a waist of 200 μm, limited by the power needed to generate polaritons on the higher branch of the bistability (for detunings $\hbar\delta$ around 0.2 meV). Consequently, two ends are present on both side of the channel length, which modify the fluid behaviour depending on their geometry, which can be of two types:

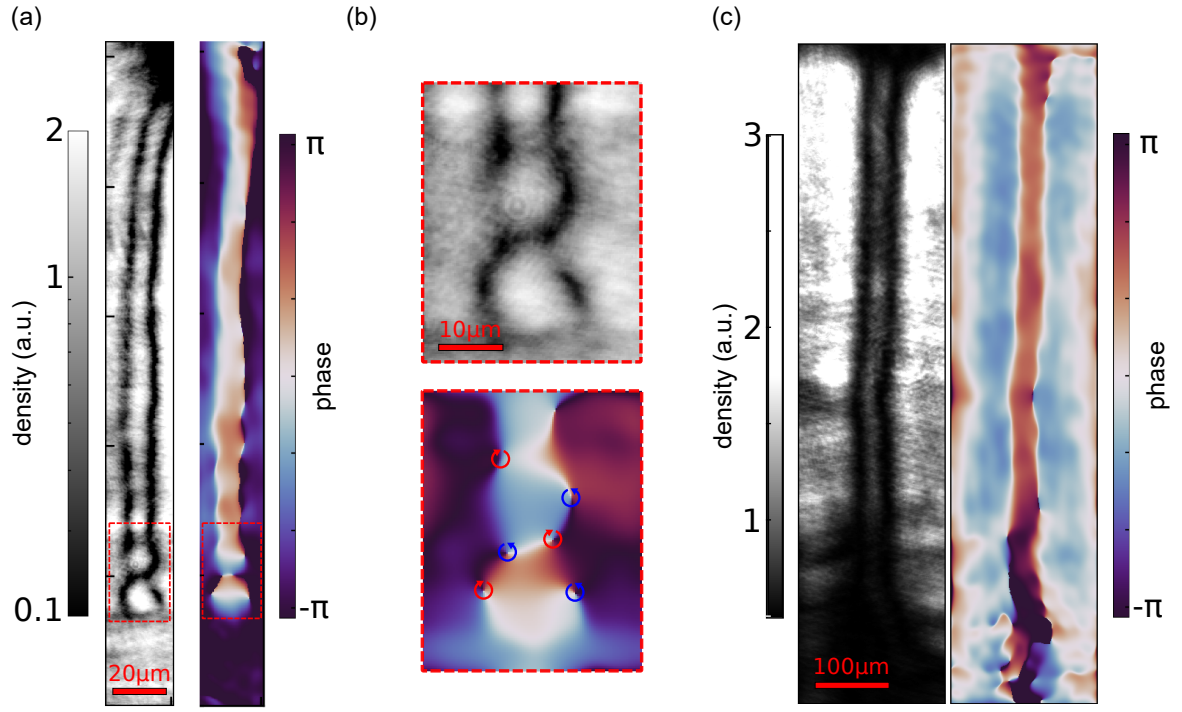

Figure 5.9: **Density and phase of the polariton fluid for different channel end geometries.** **(a)** Channel of length l = 240 μm and width L = 15 μm for a laser detuning δE = 0.2 meV. The upper end of the channel is linked to the edge of the driving field (open-end), while the lower end is closed by a third horizontal wall (dead-end). A pair of dark solitons spreads along the channel, as confirmed by the two phase jumps of π. Its decay in VA pairs is observed in the bottom part of the channel, closed by a high-density wall. **(b)** Zoom in the red dashed region of (a), where several winding of 2π on the phase map are visible. **(c)** Same channel as (a), but open at both ends. The VA pairs due to snake instabilities are not observable.

- dead-end channel, i.e. the channel is closed by a third high density horizontal domain wall,
- open channel, i.e. the channel is linked to the edges of excitation beam, thus linked to the non-excited zero density regions of the cavity.

Fig. 5.9(a) displays a low density channel belonging to these two situations: its upper end is open; its lower end is closed. By setting its width at L=15 μm, a pair of dark solitons appears within it, at $\hbar\delta = 0.2$ meV and $\mathbf{k}_P = 0$ μm^{-1}, as shown by the two near-zero density lines in the density map and the two π jumps in the phase map. At the open end, the solitons remain straight, a behavior that is also seen in Fig. 5.9(c) where both ends are open. The zero density region does not impose a stationary boundary condition on the fluid, making it impossible for the VA pairs to be pinned in the channel and thus to be observed in a steady state regime.

On the other hand, at the dead-end displayed in Fig. 5.9(b), the solitons decay. The breaking of the translational symmetry induced by the third high-density wall triggers the snake insta-

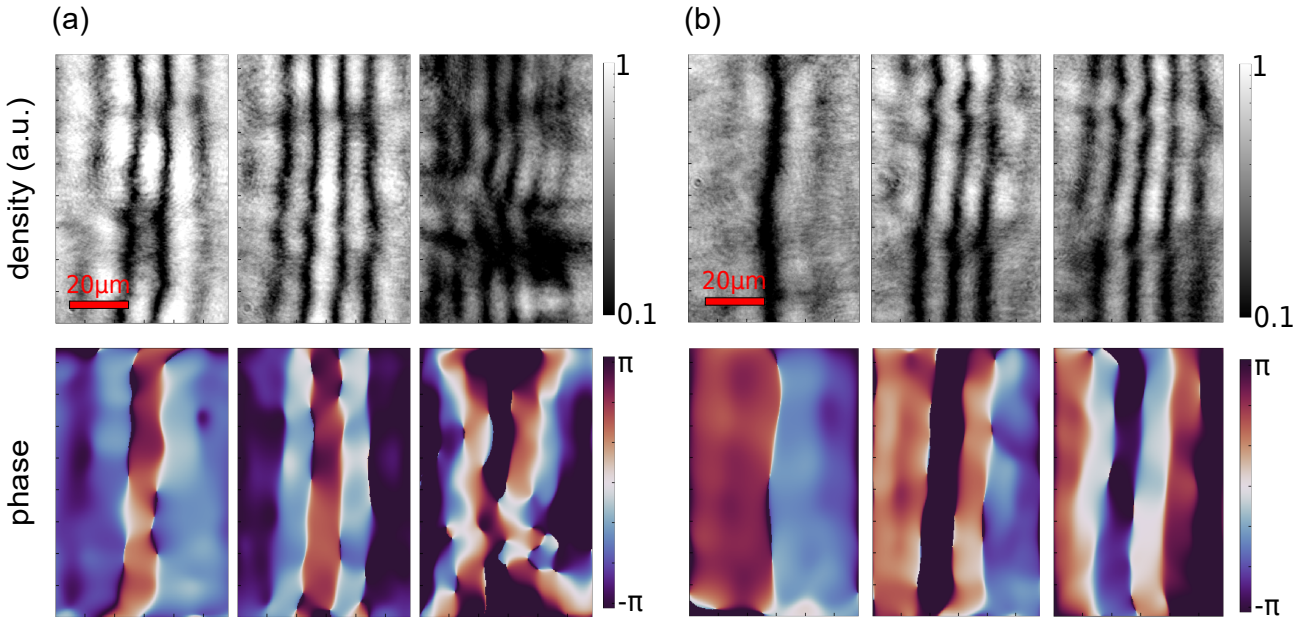

Figure 5.10: **Density and phase of the polariton fluid for different channel widths and phases.** Three open-end channels surrounded by two **(a)** in phase (**(b)** out of phase) walls, imprinted with different widths L = 25, 40, 55 μm for a detuning ΔE = 0.05 meV. The channel contains 2, 4 and 6 (1, 3 and 5) dark solitons.

bilities, which lead to the formation of stationary VA pairs, thanks to the local enhancement of the confinement induced by the DWs. Correspondingly, vortices are detected in the phase map, by locating the 2π-phase windings. The closed channel geometry is thus suitable for the observation of snake instabilities.

5.3.3 Channel width

The channel width is another parameter not clearly investigated in the theory, which can be easily monitored experimentally by modifying the pattern displayed on the SLM. In Fig. 5.10(a), we consider the case of a channel open at both ends, for different widths L = 25, 40, 55 μm, equal to several healing lengths $\xi = 5.3$ μm at detuning $\hbar\delta = 0.05$ meV. In this way, we observe respectively 2, 4 and 6 pairs of dark solitons. Note that the solitons also tend to break up for the largest L due to snake instabilities.

Continuity of the fluid wave function. In this first case presented in . 5.10 (a), the number of solitons is even because the symmetric phase parity (no phase jump) between the two high-density regions on either side of the channel is preserved by the asymmetric phase parity (π-phase jump) of solitons. Now, as presented in Fig. 5.10(b), if we add a π-phase shift between these two regions thanks to the SLM, we see that, for the same channel widths L, the number of solitons is odd, respectively 1, 3 and 5, behaviors also observed in [62]. This gives another proof that the pump, when operating in the high intensity regime, pins the phase of polaritons, whereas when operating in a weak intensity regime, as it is the case in the channel,

it leaves the phase free to evolve.

5.3.4 Channel length

To confirm that the closed geometry does induce an enhancement of the pinning of VA pairs in the channel, Fig. 5.11 presents a data set taken under the same conditions as in Fig. 5.9, where the channel length is varied from $l = 40$ to 240 μm with the SLM.

When the channel is short, l <150 μm, instabilities appear clearly, as illustrated by the periodic breakup of solitons into VA pairs on the phase maps. The boundary conditions imposed by the dead ends fix the number of vortices that appear, at a spatial period determined by the healing length ξ (governing the size of the vortex cores and the mean equilibrium distance between two vortex of same topological charge). For a longer channel, $l > 150$ μm, the instabilities remain clearly visible only at both the ends, suggesting that the observed stabilization of the VAs is closely related to the confinement potential felt locally by polaritons.

5.3.5 Power scans

In order to stimulate different instability modes, the powers of the support S and the pump P are tuned, as suggested by the theory, in closed channel geometry to freeze of the vortex dynamics.

Total power scan. First, by varying the total power $P + S$ of the excitation beam, equivalent to scan the phase diagram in Fig. 5.7 along its diagonal axis as P and S are modified simultaneously, several regimes are distinguishable, presented on the density and phase maps of Fig. 5.12. Here, the total power is expressed as a fraction of the maximum accessible total power $P_{max} = 100$ mW and not of the critical power of the support S_c, since, as shown in the phase diagram, in the channel configuration the threshold at which the two DWs collapse depends non-trivially on S and P and is not clearly defined. In Fig. 5.12, $P + S$ is increased from the left to the right. In practice, we always scan the fluid from higher to lower power, so that we can access all the density range along the higher branch of the bistability.

At low power $P + S < 0.36\ P_{max}$, in the first panel, we observe the imprinted $L = 23$ μm wide and $l = 150$ μm long channel. The polariton density is low because the intensity wall areas lies below of the range of the bistability loop. At high power $P + S > 0.74\ P_{max}$, on the contrary, the channel fills up completely as S is above S_c, resulting in a vanishing of the stiffness of the DWs, which collapse and wash out the pair of dark solitons. Notice that the solitons fade away first by the central region of the channel and then by its ends. This behavior differs from that of simulations: the incident top-hat may not be as flat as expected when injected into the system and the energy landscape felt locally by polaritons features a small energy gradient, of the order of 0.35 μeV/μm along the channel axis, due to the optical cavity wedge. At intermediate powers, the fluid is in a regime that allows the onset of snake instabilities, as evidenced by the modulation of the soliton pattern in both the density and phase maps at

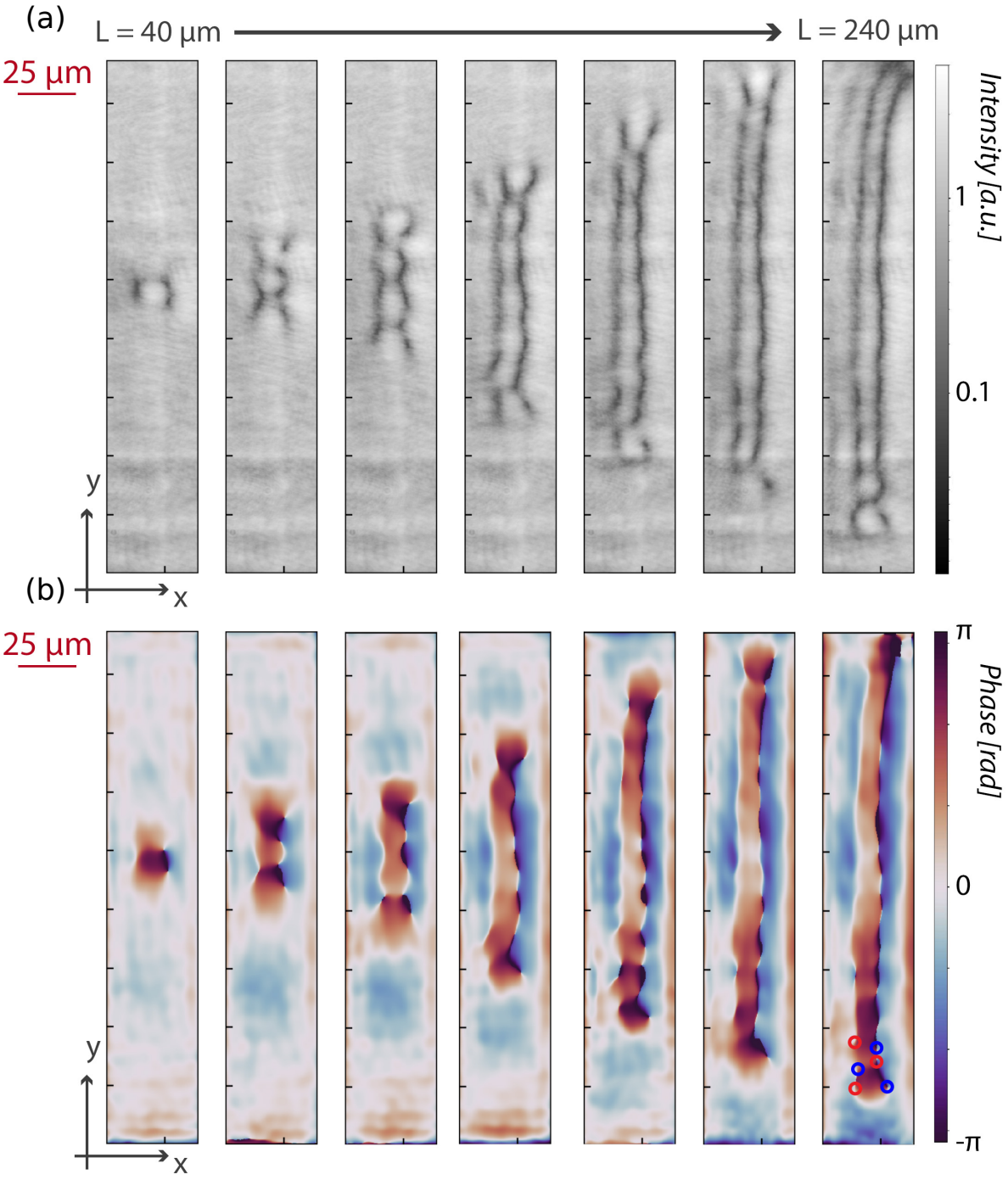

Figure 5.11: **Scan of the length of the channel**, of width $L = 15$ μm and at detuning $\hbar\delta = 0.2$ meV. **(a)** Density map. (**(b)** Phase map). A pair of dark solitons occupies the whole length of the channel, which increases from left to right from $l = 40$ to 240 μm. Snake instabilities are revealed by the break-up of the solitons into chains of vortex-antivortex pairs (red and blue circles) near the regions of confinement enhanced by the presence of a horizontal DW.

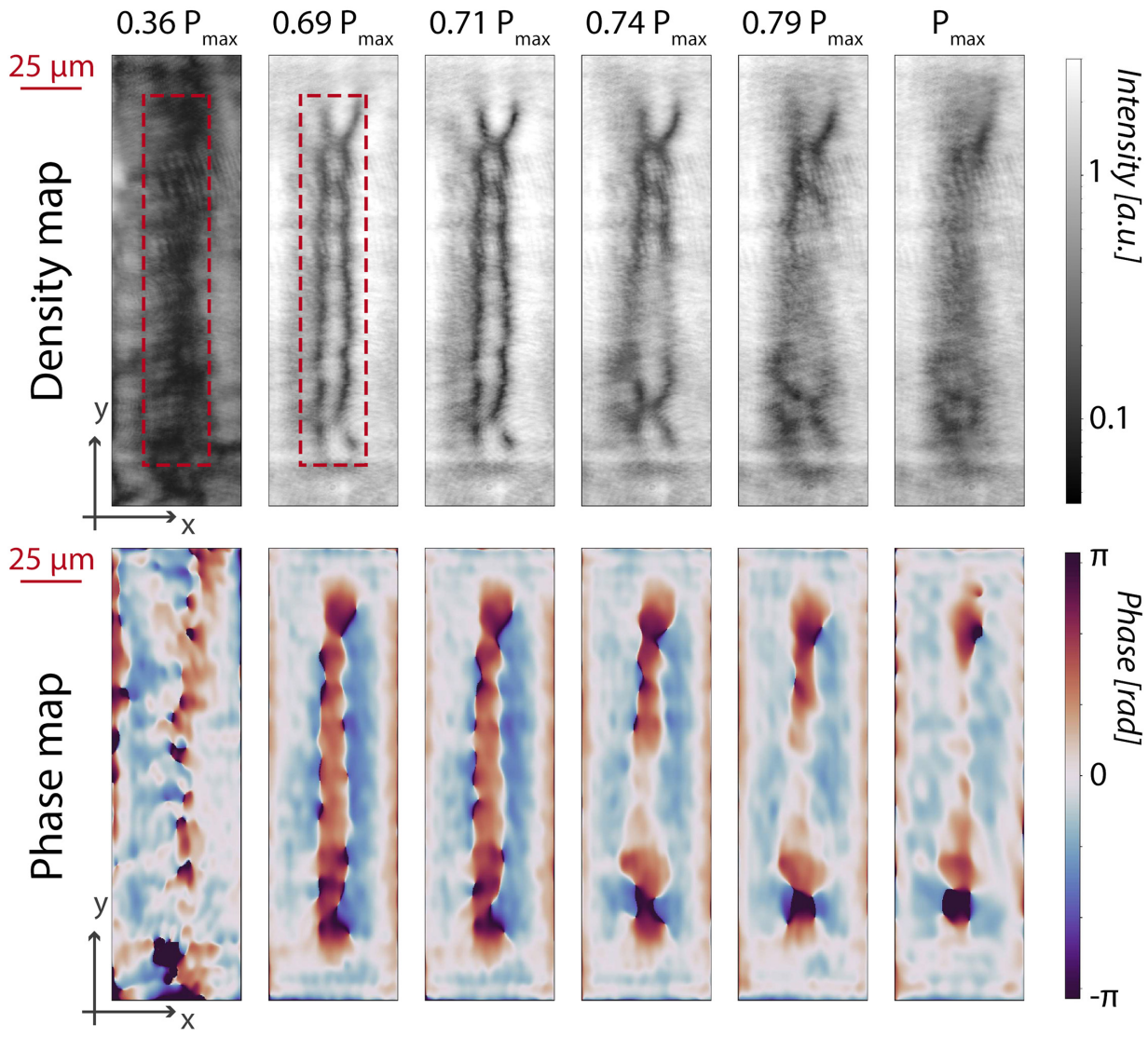

Figure 5.12: **Scan of the total power** $P + S$ of a polariton fluid with an imprinted channel of width $L = 23$ μm and lenght $l = 150$ μm, at a pump detuning $\hbar\delta = 0.2$ meV. **Upper row:** Density maps. (**Lower row:** Phase maps) for different values of $S + P$. The laser power increases form left to right until the maximum value $P_{max} = 100$ mW. At low intensity, the whole fluid is linear. When the pump regions jump into the nonlinear regime, the solitonic pattern appears, best defined for $P = 0.71 P_{max}$, then vanishes for higher intensities.

powers $P + S = 0.69$ and $0.71\ P_{max}$.

Support power scan. Based on these investigations, we then only scan the power S of the support, for different powers P fixed between 0.69 and 0.74 P_{max}, thus coinciding with horizontal scans along the lower part of the phase diagram. For example, in Fig. 5.13(a) is displayed our observations for a total power $P = 0.70\ P_{max}$, with S/P varying between 0.1 and 0.6. We found that the distribution of VA pairs in the channel, indicated by the red (+1 charge) and blue (-1 charge) circles in the phase maps, depends strongly on S.

Most strikingly, we go from an excitation of 4 to a 5 VA pairs when S goes from 0.1 to 0.4 P (at $S = 0.6\ P$, the DWs have collapsed). This is due to the decrease of the healing length ξ that occurs with the increase of the density in the channel as S grows: the number of vortices rises as their size decreases, as shown in Fig. 5.13(c). Secondly, the position of each vortex also changes slightly with S, reflecting the modification of the k_y wave vector of the instability modes. Unfortunately, regardless of the P and S powers, the detuning δ, or the l and L parameters of the channel, we only succeeded in detecting the symmetric mode as dominant, and never the anti-symmetric mode.

Cavity disorder. In order to understand this last issue, simulations were carried out, under conditions that more adequately reproduce the experimental microcavity. In particular, we noticed that the phase diagram in Fig. 5.7 was obtained by breaking the translation invariance of the channel after introducing of a weak disorder of the order of 0.01 meV, which is small compared to the typical amplitude of about 0.05 meV of the disorder in the cavity plane (point and elongated strctural defects), similar to the DW confinement potential energy ($\hbar$gn $\simeq$ 0.1 meV). It is therefore very likely that it also affects the distribution of VA pairs: the pattern exhibited by the channel should result from a balance between the modal distribution k_y of instabilities and the energetic roughness of the cavity background, not initially taken into account, hence the fact that the anti-symmetric pattern is not observed as easily as expected.

In the phase diagram, this results in a blurring of the transitions between the different parameter regions of different instability regimes, as the VAs distributions are no longer regular and well defined as in the ideal case. However, it is still possible to discriminate a symmetric state from an anti-symmetric state by measuring the standard deviation of the X coordinate of the soliton pair mass center $X_c(y)$ along its axis parallel to y

$$\langle \Delta^2 \rangle = \left\langle \left(X_c(y) - \langle X_c(y) \rangle_y \right)^2 \right\rangle_y , \tag{5.8}$$

where $\langle \rangle_y$ is the average over the y coordinate. Based on this definition, a symmetric pattern has its mass centre position quasi-aligned vertically, i.e. $\langle \Delta^2 \rangle \to 0$; the anti-symmetric pattern has its mass centre position undergoing a sinusoidal oscillation, i.e. $\langle \Delta^2 \rangle > 0$.

The new phase diagram is depicted in Fig. 5.14, where the value of $\langle \Delta^2 \rangle$ is color-coded in place of the value of k_y. Once again, different areas are distinguishable:

- in dark grey, the DWs have collapsed and therefore the channel has no soliton,

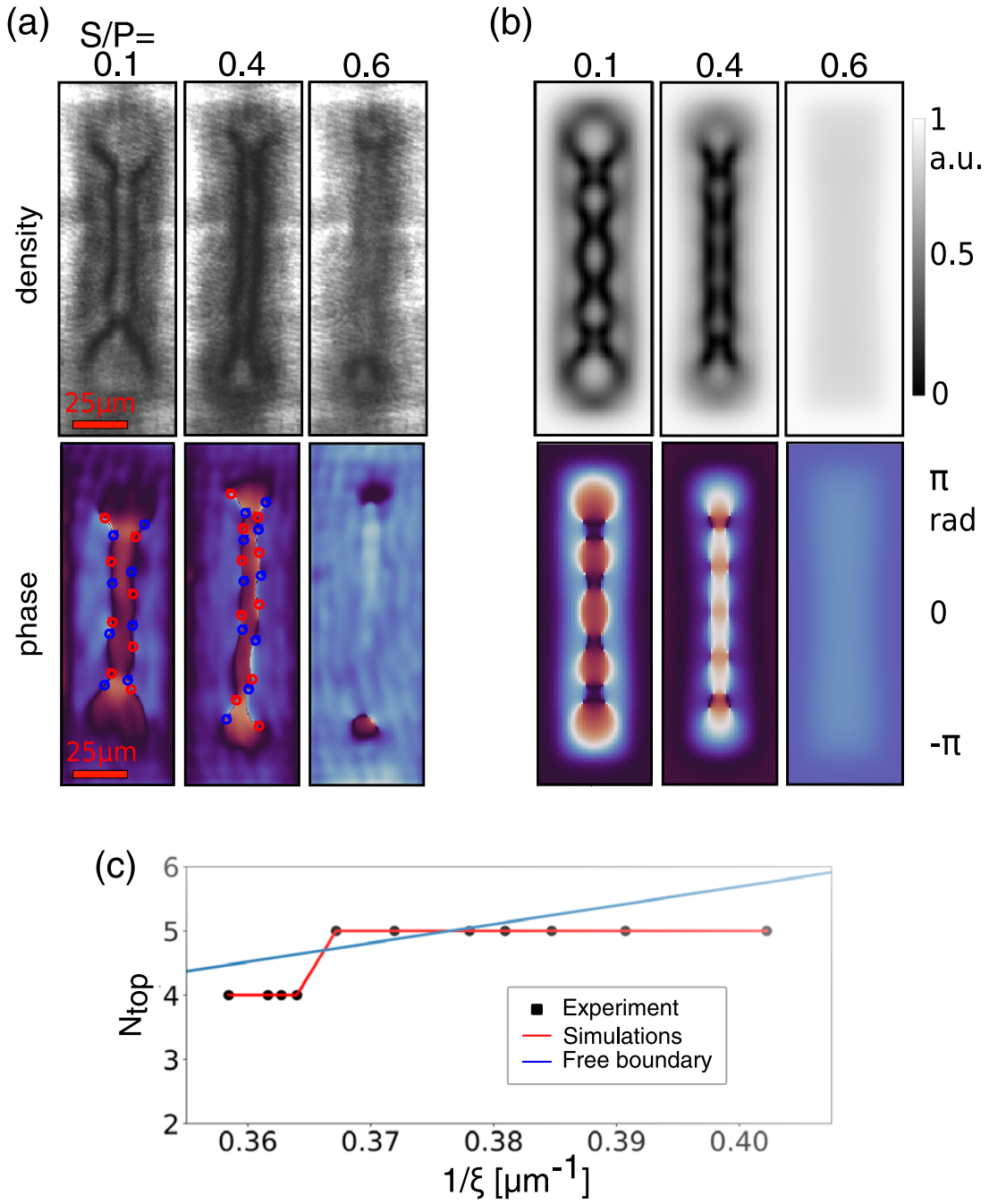

Figure 5.13: **Scan of the support power.** **(a)** Experimental fluid density (upper panels) and phase maps (lower panels) for a channel with length and width respectively l = 150 μm, L = 23 μm; the ratio between the support and the seed S/P increases from left to right. The position of the +1 and -1 charge vortices are indicated in the phase maps by the red and blue arrows respectively. **(b)** corresponding numerical simulations. **(c)** Evolution of the number of VA pairs N_{top} in the channel for different values of the inverse of the healing length $1/\xi$. The black dots are the experimental data. The red curve gives the simulations results under the same experimental conditions whereas the blue curve shows the vortex density for an infinite channel.

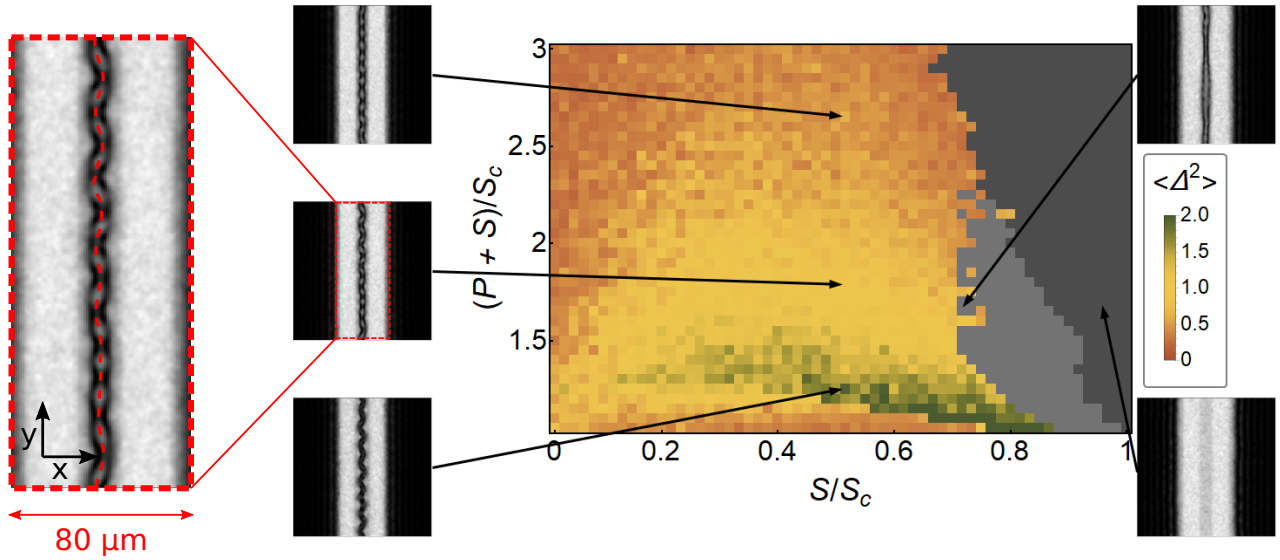

Figure 5.14: **Phase diagram of solitons embedded in a confinement channel**, obtained by simulations with disorder. Color shows the standard deviation $\langle\Delta^2\rangle$ of center between the solitons $X_c(y)$. Light gray area corresponds to limit cycle phase with no solution stationary in time. Dark gray shows the no-soliton phase with the full filling of the channel with polaritons. The insets show examples of soliton and instability distributions in the density, at different values of $\langle\Delta^2\rangle$ indicated by the black arrows. The irregular distribution of vortices in the zoom in red frame reveals that the high amplitude disorder attenuates the boundary of the transition from a symmetric mode to a dominant asymmetric mode. Adapted from [92].

- in light grey, the solutions are not stationary in time and correspond to breathing modes of solitons,
- in dark orange, $0 < \langle\Delta^2\rangle < 0.5$, the dominant instability mode is the symmetric,
- in green, $\langle\Delta^2\rangle \simeq 2$, the dominant mode is anti-symmetric,
- in yellow, no dominant mode can be clearly identified.

For the latter case, the pinning of the VA pairs distribution by the disorder makes it impossible to discriminate between a symmetric and anti-symmetric mode. This results in the pattern shown in the red inset in Fig. 5.14, of shape similar to the experimental observations.

To conclude, the anti-symmetric mode only appears clearly in a very narrow region of the phase diagram, much smaller than expected in the ideal case, which may explain why we did not observe it in our experiments.

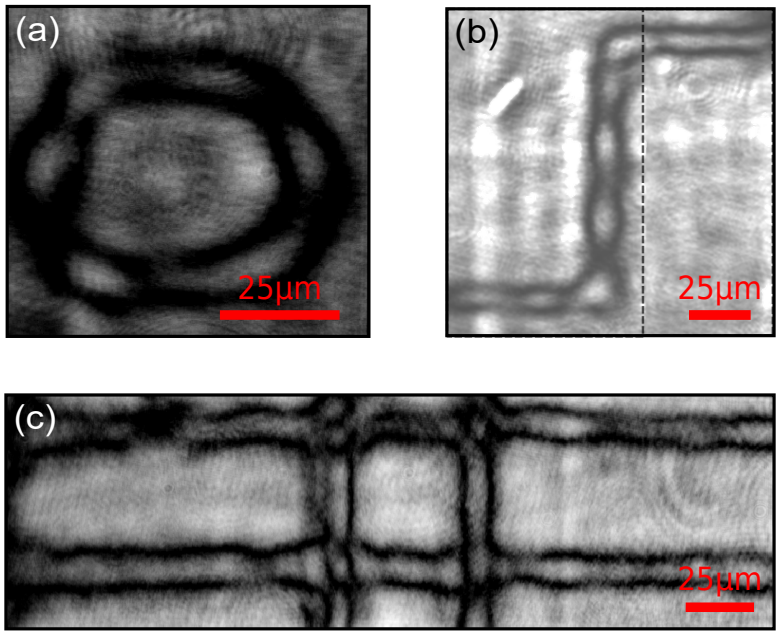

Figure 5.15: **Experimental guiding of solitons** in imprinted channels in **(a)** circular, **(b)** S-shaped and **(c)** multi-crossing geometry.

5.3.6 Solitons guiding

Besides the study of snake instabilities, the experimental versatility achieved by the use of SLM to engineer the intensity profile of the pump beam provides the opportunity to guide solitons into more complicated geometries. As an illustration, Fig. 5.15 shows the density resulting by the impression of different channel shapes in the fluid. It reveals solitons guided in:

- A circular channel in Fig. 5.15(a), demonstrating that the use of DWs is also suitable for cylindrical symmetries.
- A S-shaped channel in Fig. 5.15(b), with both ends open to the non-excited regions. It presents the continuity of solitons at the right angle bends of the DWs.
- A multi-crossing channel in Fig. 5.15(c), where all the ends are open. It shows the possibility to make solitons cross each other without altering their propagation.

5.4 Outlook: maze solving

Let us discuss again the geometry of the channel at its ends. In the dead-end configuration, a third high-density DW closes the channel outlets. This DW has stability conditions different from those of the 1D infinite lateral DWs considered in the theory: it has a higher kinetic energy due to its confinement between the two main walls of the channel. For this reason, its propagation occurs at lower critical support intensities. As a consequence, as plotted in Fig. 5.16 (a), the dead-end channel is completely filled at a critical support intensity S_{cc} below the critical support intensity S_c of the channel open at both ends. Now that we know that it

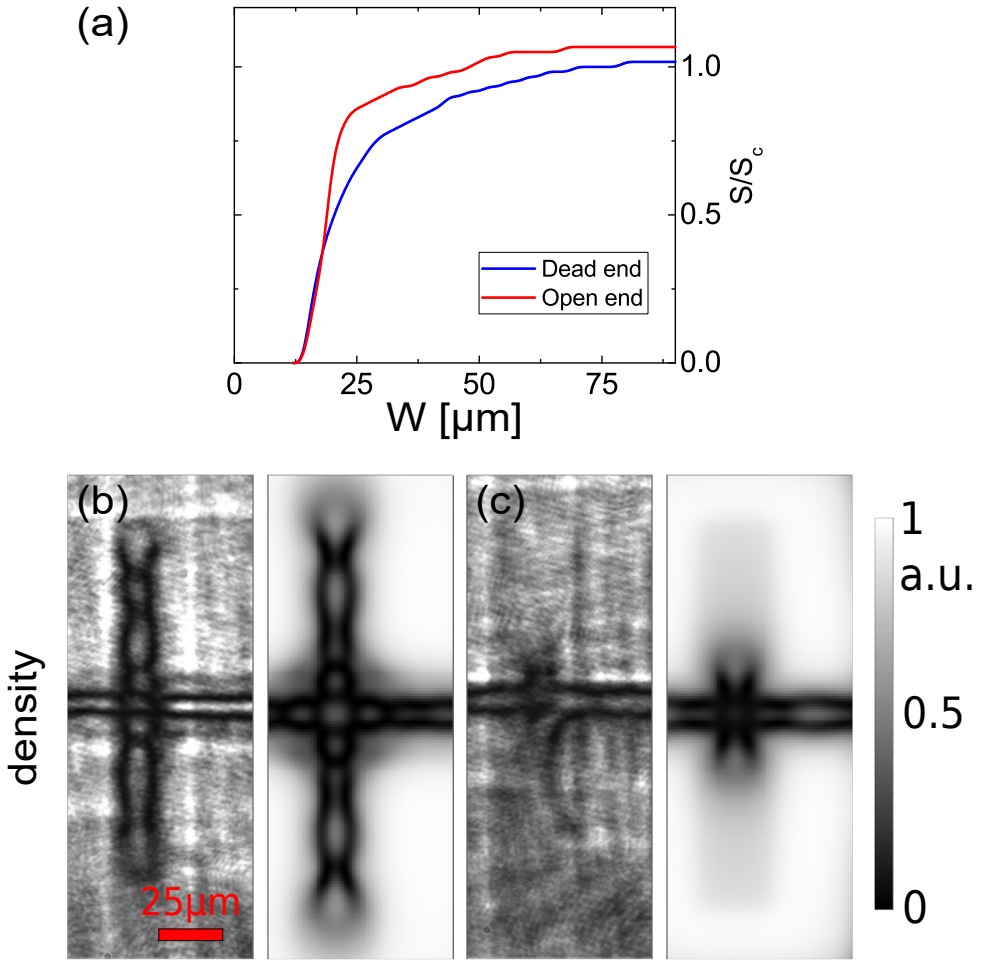

Figure 5.16: **Crossroads maze solving** with a channel width L = 23 μm and a laser detuning $\hbar\delta$ = 0.04 meV. **(a)** Critical support intensities for the motion of the two types of DWs with respect to their width L. The dead end channel geometry (in blue) closes for lower intensities than the open one (in red). Adapted from [92]. **(b-c)** Experimental (left) and numerical (right) density maps of the imprinted cross. The vertical channel is dead-end; the horizontal channel is open at both ends. In Panel (b), the channel intensity with respect to the DW intensity is equal to S/P = 0.3. Solitonic structures are present in both cross arms. In panel (c), S/P is slightly lowered. The soliton pair is formed only in the horizontal arm, connecting the entrance with the exit, thus solving the maze.

is also possible to build complicated shaped channels to guide solitons, we can exploit these differences in stability to solve analogue maze with polaritons.

The all-optical solving of a maze belongs to the interdisciplinary field of algorithms of maze and graph solving. Such works were initiated by the research of L. Euler [4], and considered as precursors of topology. Today, standard maze solving is mostly performed using algorithms implementing the so-called potential method [130], which consists in assigning an energy to a final destination, reached following a series of path choices associated with energy gradients.

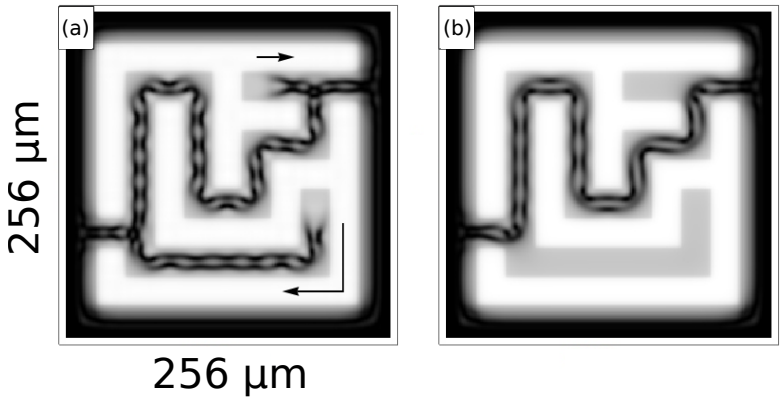

Figure 5.17: **Maze solving simulation.** **(a)** Snapshot of the density map 20 ps after the pump and support have been switched on: the heads of solitons start to be repelled by the dead-ends as indicated by the black arrows. **(b)** Stationary final density map after 1 ns: the solitons fill only the path corresponding to the solution of the maze. Adapted from [92].

It is used in robotics [152, 3], biology [167, 119], microfluidics [60] and plasma physics [139]. One can also mention chemistry experiments based on the velocity map of the reaction front method [156] or optical experiments, via the quantum wavepacket scattering method [36].

Preliminary results. In our setup, the maze solver implements a dead-end filling algorithm [127]. Fig. 5.16(b) gives an experimental example, where two channels of identical intensity cross each other to form a very basic maze: the vertical channel is dead-end; the horizontal channel is open and its two ends simulate the entrance and exit of the maze. By lowering the intensities of both the pump P and the support S, we go from a state where solitons occupy both channels, to a state where solitons occupy only the open channel, solution of the maze. Such a situation is possible thanks to the difference between the support intensity thresholds at which the two channels are filled. When $S_{cc} < S < S_c$, the horizontal DWs at the dead ends move along the vertical channel, erasing the solitons, until they reach the crossroads, where a rigid open 1D channel geometry is restored. Of course, the cross shape remains a rudimentary maze architecture. The addition of more paths was more challenging as it was difficult to prevent the overlapping of the channels with structural defects in the cavity background, which locally modified the stability conditions of the DWs and thus made the solving of the maze impossible.

Nevertheless, we give here a first proof of implementation of a maze solving algorithm in a polariton fluid. By choosing cavities with less structural asperities in their plane, or by using large excitation power in order to raise the energy of the fluid significantly above the potential energy variations in the cavity background, we should be able in the future to solve more intricate mazes, such as that simulated in Fig. 5.17. Theoretically, the polariton maze has a solving time τ governed by the velocity v of the DWs at the ends. For a maze with $N = Z^2/W^2$ cells, with Z the overall system size and W the width of a channel, τ is in the worst case equal to NL/v. The small prefactor $L/v \simeq 0.5$ ns embodies the main strength of our maze solver,

allowing it to outperform modern processors, which require several hundred clock ticks in order to solve a single cell.

Chapter 6

Dissipative phase transition with driving-controlled dimension

The features we have seen in experiments performed under coherent excitation (Bogoliubov spectroscopy and snake intstabilities study) are intrinsically linked to the bistable nature of polaritons arising at quasi-resonance. The precise knowledge of the curve relating the polariton density to the driving intensity is thus necessary to understand the dynamics of quantum fluids in semiconductor microcavities. It has been achieved analytically so far from the mean-field derivation of the generalized GPE.

In this chapter we will deviate from the classical description to operate a quantum description, which includes quantum fluctuations into the polariton dynamics. The stationary solutions of such an approach give at first sight different results from the mean-field approach: in particular, it does not reproduce the bistability loop.

However, still in the quantum description, the critical slowing down of the polariton dynamics in the vicinity of the threshold driving intensity allows to reveal again the bistable behaviour of polaritons. From this perspective, the bistability curve is the manifestation of a first-order dissipative phase transition. We will show in the following that its emergence depends on the quantum fluid dimensionality, via the modification of the characteristic time of quantum fluctuations in the system.

This work is based on the theoretical studies of Z. Li and is reported in Ref.[103].

6.1 Optical metastability

So far, we have investigated the dynamics of polaritons with a mean field (MF) description. We deduced from it the bistable character of the fluid, related to the existence of two density solutions accessible by the system in stationary regime, for a single intensity value of a continuous and blue-shifted quasi-resonant ($\delta > \sqrt{3}\gamma/2$) excitation.

Now, we wish to compare this result with that derived from a quantum description of polaritons. The LP field is represented by the quantum operator $\hat{\psi}(\mathbf{r}, t)$, obeying the standard boson commutation relation $\left[\hat{\psi}(\mathbf{r}), \hat{\psi}^\dagger(\mathbf{r}')\right] = \delta(\mathbf{r}, \mathbf{r}')$. In the reference frame rotating at the pump frequency ω_P, the Hamiltonian of the system reads [37]

$$\begin{aligned}\hat{\mathcal{H}} = &\int \mathrm{d}^2\mathbf{r}\ \hat{\psi}^\dagger(\mathbf{r}) \left[-\hbar\Delta\hat{\psi}(\mathbf{r}) - \frac{\hbar^2\nabla^2}{2m}\hat{\psi}(\mathbf{r})\right] \\ &+ \int \mathrm{d}^2\mathbf{r}\ \frac{\hbar \mathrm{g}}{2}\hat{\psi}^{\dagger 2}(\mathbf{r})\hat{\psi}^2(\mathbf{r}) \\ &+ \int \mathrm{d}^2\mathbf{r}\ \hbar\left[\mathcal{F}(\mathbf{r})\hat{\psi}^\dagger(\mathbf{r}) + \mathcal{F}^*(\mathbf{r})\hat{\psi}(\mathbf{r})\right],\end{aligned} \tag{6.1}$$

where $\mathcal{F}(\mathbf{r})$ describes the amplitude and spatial shape of the coherent pump. The losses, which couple the polaritons to the environment, are accounted for in the dynamics by means of a Lindblad master equation, describing the time evolution of the polariton density matrix $\hat{\rho}$. Under the Born-Markov approximation, assuming a uniform polariton decay rate γ and discarding the thermal fluctuations at cryogenic temperature, such an equation is written [34]

$$\frac{\mathrm{d}\hat{\rho}}{\mathrm{d}t} = \mathcal{L}[\hat{\rho}] = -\frac{\mathrm{i}}{\hbar}\left[\hat{\mathcal{H}}, \hat{\rho}\right] + \mathcal{D}\left[\hat{\rho}\right], \tag{6.2}$$

with $\mathcal{L}$ the Liouvillian non-hermitian superoperator and $\mathcal{D}$ the dissipator, defined as

$$\mathcal{D}\left[\hat{\rho}\right] = \int \mathrm{d}^2\mathbf{r}\ \frac{\gamma}{2}\left[2\hat{\psi}(\mathbf{r})\hat{\rho}\psi^\dagger(\mathbf{r}) - \left\{\hat{\psi}^\dagger(\mathbf{r})\hat{\psi}(\mathbf{r}), \hat{\rho}\right\}\right]. \tag{6.3}$$

Within the MF approximation, the dynamics of the classical parameter derived from the expectation value of the quantum operator $\psi(\mathbf{r}, t) = \left\langle\hat{\psi}(\mathbf{r}, t)\right\rangle$ is given by

$$\frac{\partial\psi}{\partial t} = \frac{\partial}{\partial t}\mathrm{Tr}[\hat{\rho}\hat{\psi}] = \mathrm{Tr}\left[\frac{\mathrm{d}\hat{\rho}}{\mathrm{d}t}\hat{\psi}\right]. \tag{6.4}$$

This equation is identical to the generalized GPE (2.51), from which the steady state density bistability relationship (2.53) is calculated. Beyond the MF approximation, the stationary solution of the Linblad equation is equal to the density matrix ρ_{ss} related to the eigenvalue $\lambda = 0$ of the problem $\mathcal{L}\hat{\rho} = \lambda\hat{\rho}$. Remarkably, ρ_{ss} is usually unique (see Fig. 6.1 (a)). Thus, the density calculated from $n_{ss}(\mathbf{r}) = \frac{1}{S}\int \mathrm{d}^2\mathbf{r}\ \mathrm{Tr}\left[\hat{\rho}\hat{\psi}^\dagger(\mathbf{r})\hat{\psi}(\mathbf{r})\right]$ exhibits a single solution for any value

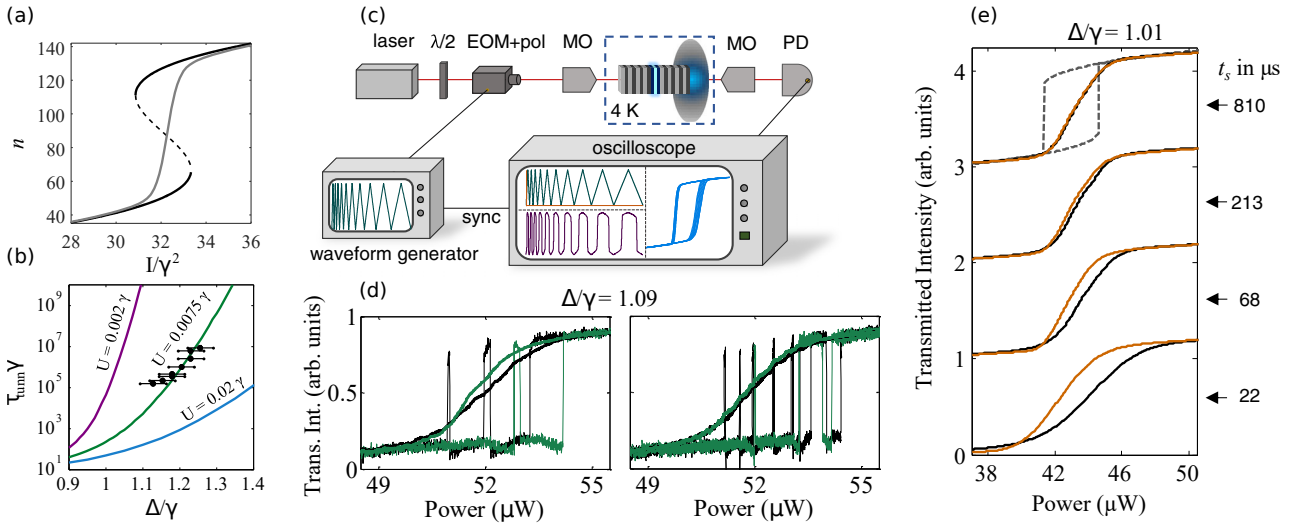

Figure 6.1: **Probing a dissipative phase transition via dynamical optical hysteresis.** **(a)** Theoretical mean-field (black curve) and quantum (gray curve) density solutions with respect to the driving intensity. **(b)** Tunneling time τ_{tunn} between the two mean-field metastable states width respect to the driving detuning Δ, for different interaction strength U. **(c)** Experimental setu. Experimental setup. The driving field intensity is modulated with a set of ramps of different frequencies with an electrical optical modulator (EOM). The transmitted intensity (proportional to the density) is sent to a photodiode (PD) and its signal analyzed with an oscilloscope synchronised with the waveform generator monitoring the EOM. **(d-e)** Transmitted intensity with respect to the pump power. **(d)** Single shot (thin lines) and averages over 1000 realizations (thick lines) of dynamic hysteresis. The intensity ramp time is $t_s = 0.11$ ms (0.43 ms) in the left panel (right panel). **(e)** Dynamic hysteresis loop averaged over 1500 realizations for different values of t_s. The bistability loop of the mean field solution appears when the intensity ramp time approaches that of the quantum fluctuations. Adapted from [142].

of the pump intensity $|\mathcal{F}|^2$. Therefore, at first glance, the mean field and quantum approaches lead to two different results.

Role of fluctuations. This apparent contradiction is resolved by including fluctuations into the analysis: the solutions associated with the MF hysteresis loop are interpreted as metastable realizations of the system, between which the density switches on time scales of the same order of the characteristic time of fluctuations of the polariton field; the unique steady state solution of the Linblad equation is viewed as an average over these realizations.

Thus, the experimental observation of one solution rather than the another is simply a question of the time scale ratio between the measurement time τ_m and the switching time from one metastable state to another τ_f. If $\tau_m \gg \tau_f$, a measurement gives the average of the metastable realizations of the system over time; if $\tau_m \ll \tau_f$ a measurement gives only a single metastable realization. Such time scales were historically investigated first in experiments involving the spontaneous switching of a two-mode laser from one metastable state to another

performed in the 1980s [144]. In polariton system, τ_f can be astronomically long when the fluctuations are small and the number of particles involved is large [71]: we usually detect the solution given by the MF description, i.e. the metastable solutions relative to the higher and lower branches of the bistability.

The role of quantum fluctuations in the emergence of the polariton bistability has been studied in the group of J. Bloch in Ref. [142], where a pillar microcavity is driven by a quasi-resonant excitation whose intensity is ramped up and down over time scales varying from 1.25 ms to 20 μs (Fig. 6.1 (c)). The high polariton interactions achieved in 0D pillar systems allow to reach characteristic fluctuations times below microseconds (see Fig. 6.1 (b)). Consequently, varying the sweep rate of the intensity is equivalent to tuning the number of switches between high and low metastable states experienced by the polariton density during the total sweep time. As shown in Fig. 6.1 (d, e), at long sweep times, the average intensity transmitted by the cavity (proportional to the polariton density) is averaged over a very large number of switching events: the unique solution expected by the quantum approach is found. On the contrary, at short sweep times, the transmission integrates few switching events: two density solutions are evidenced by the opening of the bistability loop, as predicted by the MF approach.

6.2 Dissipative phase transition

In classical systems, thermal phase transitions, such as that from a liquid to a solid phase, takes place at finite temperature and are driven by thermal fluctuations. In a closed quantum system, phase transitions can emerge at zero temperature, where the system is in its ground state. They are driven by the quantum fluctuations that govern the competition between the non-commutative terms of the gapless Hamiltonian (phases of the system). For open quantum systems, such as polaritons, provided that thermal fluctuations are negligible, the dissipative phase transition is driven by both quantum fluctuations and the coupling of the microcavity to the environment. These determine the nonequilibrium steady state in which the system ends up by setting the outcome of the competition between the metastable states.

The Linblad equation encompasses the descriptions of the quantum fluctuations dynamics in open systems. The Liouvillian superoperator has a complex spectrum of eigenvalues $\{\lambda_j \mid \exists \hat{\rho}_j, \mathcal{L}[\hat{\rho}_j] = \lambda_j \hat{\rho}_j\}$ of negative real part $\mathrm{Re}(\lambda_j) \leq 0$. While the zero eigenvalue relates the steady state solution, the non-zero eigenvalues describe the transient relaxation of the density matrix toward the steady state. The Liouvillian gap is defined as the non-zero eigenvalue of smallest real part $\lambda = \min\{|\mathrm{Re}(\lambda_j)|\}$, equal to the inverse of the asymptotic decay rate toward the steady state. Its value governs the characteristic rate of back-and-forth transition from one metastable state to another. In this picture, a phase transition is defined from the closure of the Liouvillian gap $\lambda \to 0$ in the thermodynamic limit [118, 169]. It is linked to the critical slowing down of the rate of switching events between the metastable states (phases) of the system.

Such a dissipative phase transition is highlighted by adiabatically varying a parameter of

the system to switch from one metastable state to another. In our case, the hysteresis loop is observed in the evolution of the polariton density as a function of the pump intensity, corresponding to the transition from a low- to a high-density phase upon Liouvillian gap closure at a critical driving strength.

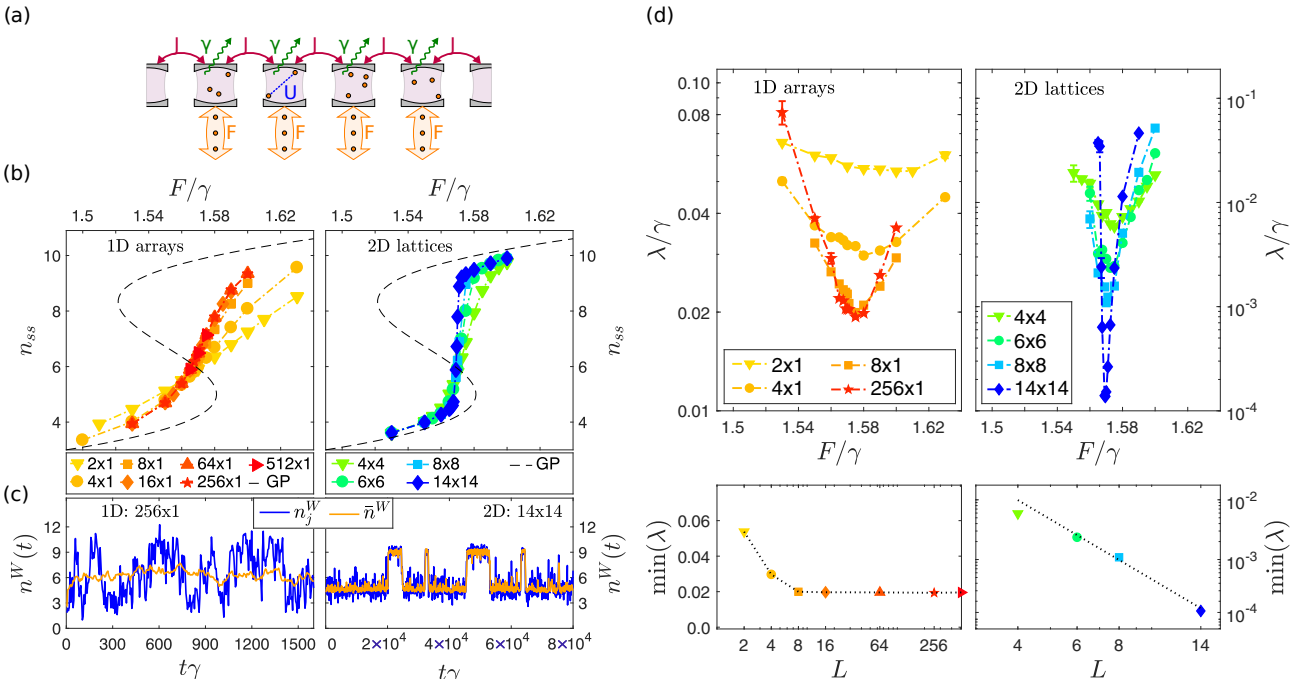

Figure 6.2: **Critical slowing down in driven-dissipative Bose-Hubbad lattices. (a)** Schematic representation of the Bose-Hubbard lattice. **(b-d)** The left (right) column correponds to the simulation results for the 1D (2D) lattice. **(b)** Average steady state population per site n_{ss} as a function of the driving field strength F (in units of the dissipation rate γ) for arrays of different sizes. The black dashed line corresponds to the solution given by the mean field GPE. **(c)** Time-dependent single-trajectory of the population in a single site n^W (blue line) and the average population $\hat{n}^W$ over all sites (orange line). **(d)** Upper row: Liouvillian gap λ as a function of the driving field amplitude for different array sizes L. Lower row: Minima of the Liouvillian gap as a function of the array size L. Note that the critical slowing down of fluctuations appears in the thermodynamic limit of $L \to \infty$ only for the 2D lattice. Adapted from [169].

System dimension. Here we will study the role of the spatial dimension of the polariton fluid in the onset of criticality. This research follows theoretical work on driven-dissipative bosonic resonator lattices with Kerr-type nonlinearity. In the model of Ref. [169], depicted in Fig. 6.2 (a), a coherent and homogeneous driving field illuminating the system injects a macroscopic population of bosons in the wavevector mode $\mathbf{k} = 0$. The nonlinearity induces a local boson-boson interaction denoted U and a boson can hop from one site to another neighbouring site at a frequency given by the hopping coupling J.

The numerical resolution of the Lindblad equation derived from the Halmiltonian (described

by the Bose-Hubbard model) shows that the behavior of the Liouvillian gap with respect to the driving intensity is closely related to the $N \times M$ dimension of the lattice. For a 1D system (M=1), λ converges to a finite value when N is increased; for a 2D system it decreases continuously when the area $N \times M$ is increased without convergence.

In 1D, the non-closure of the gap proves the absence of critical slowing down and thus of phase transition as the driving field intensity is scanned. The rate of switching events between two metastable states remains very fast, as shown in Fig. 6.2 (c) where one observes that the fluctuations induce fast variations of the boson population. Consequently, the average steady-state population integrates over a large number of realizations. Its plot as a function of the intensity shows a single-valued curve, very different from the bistability of the MF description and whose S-shape slope converges to a finite value as the Liouvillian gap saturates when the length N increases.

In 2D, the closure of the Liouvillian gap results in a critical slowing down of the fluctuations. In Fig. 6.2 (b) the different metastable states taken up by the population are clearly discernible. As a result, the average population curve in steady state approaches the MF bistability. Its slope does not saturate as the area increases, suggesting the emergence of a discontinuous jump in the thermodynamic limit, thus the appearance of a first-order phase transition.

6.3 Experimental implementation

In this section, we present the experimental implementation in our planar semiconductor microcavity of the critical slowing down theoretically studied in driven-dissipative Bose-Hubbard networks. Thanks to the all-optical control achieved in quasi-resonant excitation, the study of the dimensionality dependence is enabled by the spatial reshaping of the driving field profile. In doing so, we seek to examine the dissipative phase transition with respect to the pump intensity for different dimensions of the polariton fluid (which are not spatially discretized, contrary to the Bose Hubbard lattice). The same behaviors as described above are expected.

6.3.1 Theoretical model

The steady-state density of polaritons averaged over a disk D of diameter l_d at the centre of the pumping region is given by

$$n_D^{SS} = \frac{1}{\mu(D)} \int_D \mathrm{d}^2\mathbf{r} |\psi_{SS}(\mathbf{r})|^2, \tag{6.5}$$

with $\mu(D)$ the area of the disk D. ψ_{SS} is the steady-state polariton field, computed from the mean field GPE (2.51) such that $\partial_t \psi_{SS} = 0$.

Formally, a phase transition of order M is defined as

$$\lim_{I\to I_c}\left|\frac{\partial^M}{\partial I^M}\lim_{l\to\infty} n_D^{SS}\right| = +\infty, \tag{6.6}$$

describing a divergent behavior of n_D^{SS} when the intensity I of the driving field tends to a critical value I_C, in the thermodynamic limit of the parameter $l \to \infty$ denoting one of the spatial dimension of the fluid. In the following, we want to compare the critical behavior of n_D^{SS} for a 2D and 1D fluid geometry. In the first case, the polaritons are injected by a circular spot of diameter l; in the second case, by an elliptical spot of major axis l and minor axis $b \ll l$. Our goal is therefore to see if a phase transition of order 1 (M=1) emerges in the 2D case and not in the 1D case, in the limits given by Eq. (6.6).

6.3.2 Setup

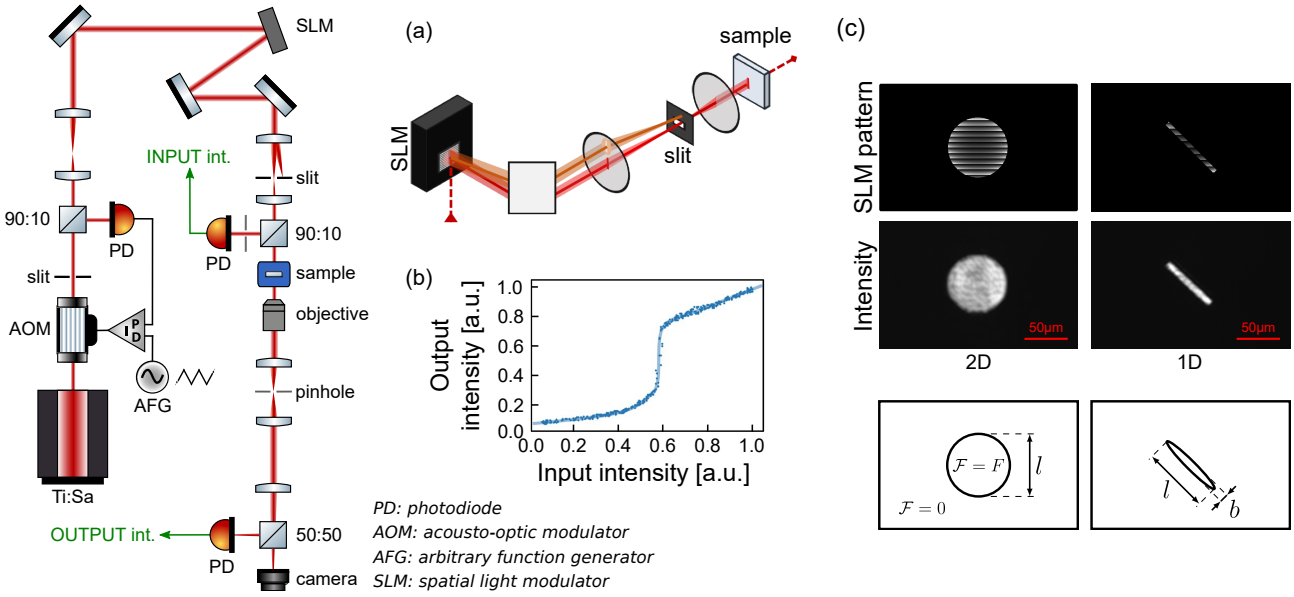

Figure 6.3: **Sketch of the experimental setup**. The laser is slaved using a proportional–integral–derivative (PID) controller, an arbitrary function generator (AFG) and an acousto-optic modulator (AOM) loop to produce a power ramp; its intensity profile is reshaped using a spatial light modulator (SLM). Two photodiodes (PD) measure the power inside disks of diameter $l_D = 5$ μm at the center of the beams at the sample input and output. **(a)** Pump intensity profile shaping method: the light (dark) beam represents the zero (first) order of the diffracted beam from the SLM. **(b)** Output intensity from the sample with as a function of the input intensity, plotted for a pump detuning of $\delta = \gamma$ and a 2D top-hat drive of diameter $l = 30$ μm. **(c)** SLM phase pattern (upper) for obtaining 2D (left) and 1D (right) flat-top beam profiles (middle) of different sizes and intensities (bottom).

The sample used is the same as for the other experiments. At the working point of our experiments, the effective mass of the polaritons is $m = 5.2 \times 10^{-35}$ kg and the decay rate $\hbar\gamma = 80$ μeV. The interaction constant is equal to $\hbar g = 0.01$ meV$\cdot\mu$m^2.

A cw Ti:Sapphire Matisse laser excites polaritons with a circular polarization and at normal incidence. Its Gaussian profile is reshaped by a Spatial Light Modulator (SLM), whose liquid crystal matrix plane is imaged in that of the cavity, as shown in Fig. 6.3 (a).

Beam profile reshaping. The phase pattern displayed on the SLM includes a blazed grating of controllable constrast, in order to tune the intensity fractions diffracted in the 0 and +1 orders. In this way, a flat top-hat intensity profile is produced in order +1, sent at normal incidence through the cavity, while order 0 (not-diffracted by the SLM) is blocked in the Fourier space using a slit. Moreover, by adding a non-diffracting mask on top of the grating, it is possible to select which regions of the laser spot are sent to the cavity. Thus, as shown in Fig. 6.3 (c), the shape of the driving field follows the shape of the mask contours: we switch from a 2D circular spot to a 1D elliptical one by just configuring the SLM with a circular aperture mask to a narrow slit one. In the following, we adjust the diameter of the circular spot and the length of the major axis of the elliptical spot, both denoted l, by controlling the corresponding dimension of these masks. In the 1D case, the minor axis b of the ellipse is chosen equal to 6.4 μm, i.e. small enough with respect to the values swept by l to measure the transformation of the density slope during the scans of the driving intensity and large enough compared to the diffraction limit (at 3.1 μm) to avoid undesirable diffraction effects at the edges. More details on the methods to reshape the intensity profiles at the SLM are given in Appendix.

Intensity scan. To probe the phase transition, the driving field power is modulated with a low-frequency ramp (200 Hz) by an acousto-optic modulator (AOM). With the help of a PID feedback loop, its maximum and minimum values are kept constant for each modulation period and chosen to scan a wide range of density.

Detection. The intensities at the input and output of the cavity are measured using two photodiodes which are positioned behind two pinholes selecting the central $l_d = 5$ μm diameter region of the driving field and the fluid in the plane of the cavity respectively. Consequently, as illustrated in Fig. 6.3(b), the density is directly measured with respect to the driving field intensity by plotting the powers detected by the two photodiodes (one with respect to the other).

6.4 Results and discussion

6.4.1 Experimental measurements

We now compare the change in the density behavior as a function of pump intensity by scanning l between 15 and 45 μm. The results for the 1D and 2D geometries are plotted on the upper and lower parts of Fig. 6.4.

The pump-polariton detuning is chosen to be equal to $\delta = \gamma > \sqrt{3}\gamma/2$, in order to operate in a regime where one usually expects to observe a bistability according to the steady-state mean-field equation. Remarkably, in the present case, the experimental curves of the steady-state

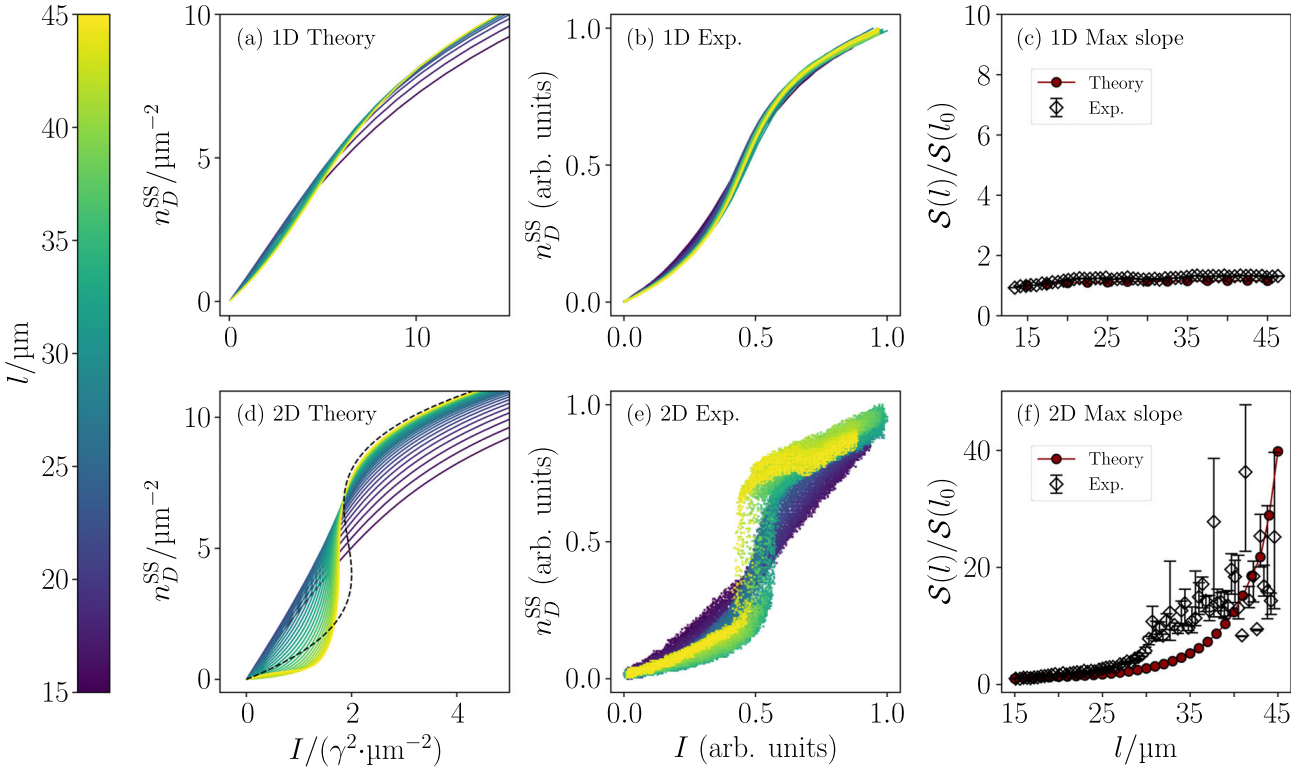

Figure 6.4: **(a)** Theoretical (**(b)** experimental) results for the steady-state polariton density n_D^{SS} averaged over the probing disk as a function of the drive intensity I for different top-hat spot sizes l (see colorbar) in the 1D configuration with detuning $\delta = \gamma$. **(c)** The maximum derivative $\mathcal{S}(l)$ for each top-hat size l normalized by the maximum derivative at $l_0 = 15$ μm, for both theoretical and experimental results (see legend). **(d)-(f)** The same quantities as in (a)-(c) for the 2D configuration. The dashed line in (d) is the prediction of the mean-field theory in Eq. (2.53). Note that as the top-hat increases in size, the slope in the 1D configuration quickly saturates for increasing size l, while in the 2D configuration the slope sharply increases in both theory and experiment, as expected for a first order phase transition.

density n_D^{SS} averaged over the area of the probing disk D with respect to the pump intensity I shown in Fig. (b) and (e) do not exhibit any hysteresis loop for most values of l. The maxima of the slope $\mathcal{S}(l) = \max_I\{\frac{\partial n_D^{SS}(I,l)}{\partial I}\}$ of the transition from the low- to the high-density (calculated with a noise-robust numerical differentiation method [40]) are plotted in Fig. 6.4(c) and (f), to evidence the emergence of the phase transition as defined in Eq. (6.6).

In 1D geometry, $\mathcal{S}(l)$ quickly saturates to a finite value such that $\mathcal{S}(l)/\mathcal{S}(l_0) < 2$ with $l_0 = 15$ μm, as its length l increases: the slope of the crossover remains smooth, implying the absence of a phase transition. On the opposite, in 2D geometry, the slope $\mathcal{S}(l)$ increases drastically up to a factor $\mathcal{S}(l)/\mathcal{S}(l_0) \simeq 40$ as the diameter l increases, indicating the emergence of a phase transition in the thermodynamic limit of $l \to \infty$. Moreovere, at the largest diameters $l > 35$ μm, the onset of a hysteresis loop is even visible, indicating the critical slowing down of the dynamics with respect to the detection time of photodiodes. The broadening of the uncertainty

on the measurement of the slope $\mathcal{S}(l)$ at large dimensions comes from the quasi-verticality of the crossover ($\tan^{-1} \simeq 84°$), causing the calculation of the derivative to be more sensitive to noise. For $l > 45$ μm, the digital sampling of the photodiode signal was not sufficiently resolved to capture the diverging slope variations in the thermodynamic limit.

Note that, while the resolution of the generalized GPE should normally lead to bistable solutions for any dimension due to the absence of fluctuation term, we unexpectedly observe here the closure of the hysteresis cycle at low-dimension. This can be explained by a coupling between different modes of the fluid, at different wavevectors. In addition to the dominant mode at $k = 0$, the top-hat excitation scheme induces the generation of spurious modes at $k \neq 0$: while the mode at $k = 0$ is responsible for the phase transition, its coupling with the $k \neq 0$ modes leads to effective fluctuations in the system, and as a result to a vanishing of the bistability.

To justify the use of the GPE, its results were compared to those obtained from the truncated Wigner approximation method, which explicitly involves a quantum fluctuation term. Comparing the temporal evolution of the density for each of these two methods, the relative errors measured are below 5%, and decrease below 1% once the steady-state is reached. This result was found to be robust for different excitation intensities and system dimensions.

6.4.2 Numerical analysis

These results are consistent with the theoretical predictions made within the driven-dissipative Bose-Hubbard lattice. They are also adequately reproduced by the mean-field simulations of the generalized GPE (2.51) with diffusive boundary conditions (since polaritons can diffuse out of the pumping region) and with the same parameters as the experiment, as shown in Figs. 6.4(a) and (d) for the 1D and 2D geometry respectively.

Liouvillian gap closure. The study of the dynamic properties of criticality arising in 2D geometry is further investigated by simulating the time evolution of the polariton density $n_D(t)$ averaged over the probe disk towards the steady state density n_D^{SS}. Fig. 6.5(a) reports the results: when the driving intensity I is close to the critical value I_c, the density difference $n_D(t) - n_D^{SS}$ decreases exponentially towards zero in the limit of large time scales with respect to the polariton lifetime $t \ll 1/\gamma$. This decay exhibits a critical slowing down as l increases, of characteristic time fixed by the Liouvillian gap value λ. By fitting it with a function of the form $n_D(t) = n_D^{SS} + A\exp(-\lambda t)$, one extracts the dependence of λ on the diameter l as a function of the intensity I. The corresponding curves plotted in Fig. 6.5(b) reveal that λ does indeed show a dip around a critical intensity which decreases as l increases. This demonstrates the closure of the Liouvillian gap in the thermodynamic limit and thus confirms the emergence of a first order dissipative phase transition.

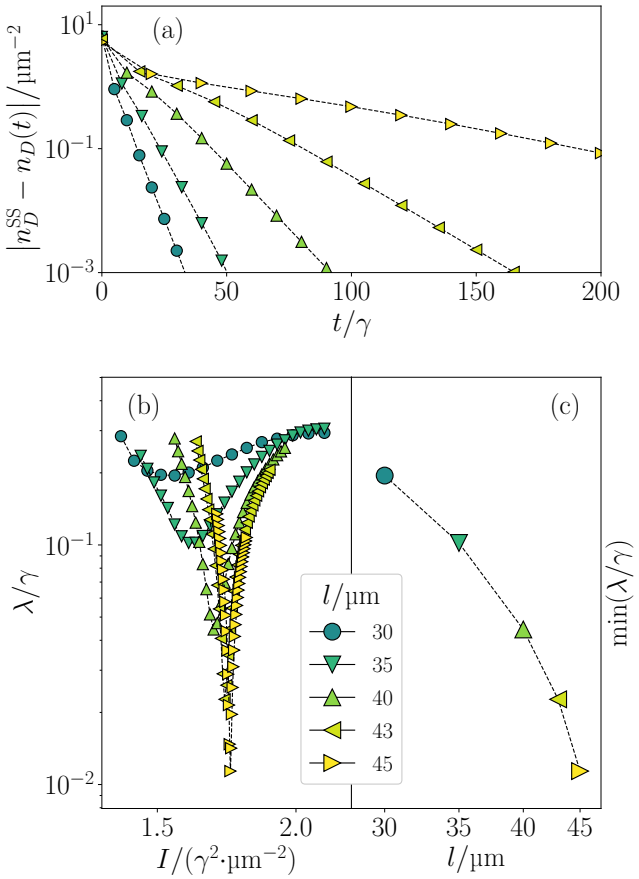

Figure 6.5: **Critical slowing down and the closing of the Liouvillian gap** for a 2D top-hat drive observed in numerical simulations. **(a)** Relaxation of $n_D(t)$ towards the steady state n_D^{SS} for difference driving spot sizes l (see legend) at driving intensity $I = 1.7689\ \gamma^2/\mu m^2$. The other parameters are the same as in the experiment. **(b)** The Liouvillian gap λ evaluated from the asymptotic decay rate as a function of the driving intensity I for different values of l. **(c)** The minimum of λ as a function of l.

Chapter 7

Conclusion

The starting point of this thesis was to introduce the semiconductor microcavity system in the **second chapter**. While photons are interacting-free bosons in vacuum, their strong coupling with quantum well excitons leads to the generation of new particles, the exciton-polaritons. These particles, inheriting the interactions of their charged constituents, act as a quantum fluid. Their dynamics is described by the generalised Gross-Pitatevskii equation, i.e. the same equation used in ultra-cold atomic condensates, with the addittion of a pumping and a loss terms to take into account the driven-dissipative nature of the system.

Although similar in many respects to quantum fluids in thermal equilibrium, as evidenced by the demonstration of superfluidity or Bose-Einstein condensation, polariton fluids are nonetheless out of equilibrium: their behaviour depends critically on the way they are driven. This is manifested by the transformation of their elementary excitations, the emergence of phase transitions or the appearance of vortices and dark solitons, depending on the pumping parameters.

Thus, in the **third chapter**, we have presented the implementation of a high-resolution coherent probe spectroscopy technique in order to investigate the interplay between the elementary excitations of polaritons and the bistability loop, relating the fluid density to the pump intensity in a quasi-resonant excitation regime. In doing so, in addition to the particular case of the onset of phonon-like excitations at the turning point of the bistability, from which we measured the polariton speed of sound and quantified the contribution of a reservoir of dark excitons to the dynamics of the system, we demonstrated that in the lower density regime (lower bistability branch), the fluid exhibits precursors of modulational instabilities, while in the higher intensity regime (higher bistability branch, far from the turning point), the Bogoliubov spectrum displays the opening of an energy gap. Moreover, we have also presented the observation of the Bogoliubov negative solution (ghost branch), via the parametric scattering of polariton pairs.

Such a spectroscopy technique is very versatile and can be used with other excitation schemes. Typically, as presented in the **fourth chapter**, it can be exploited to study the

spectrum of a Goldstone mode, arising in the parametric polariton oscillation regime due to a spontaneous symmetry breaking. Thanks to it, we have measured very precisely the narrowing of the linewidth of an elementary excitation mode of almost zero group velocity in the small wavevector limit, identified as a diffusive Goldstone mode. Then, by fixing the phase of the signal and idler condensate with an additional laser, we succeeded in explicitly destroying the spontaneous symmetry breaking of the OPO regime and we observed the subsequent vanishing of the Goldstone mode.

In the **fifth chapter**, we presented the implementation of an excitation scheme allowing the observation of modulational instabilities in stationary regime. It consisted in embedding in an imprinted static channel of low intensity a pair of dark solitons, decaying into a vortex-antivortex street due to the onset of transverse snake instabilities. These instabilities presented different symmetries that we were able to study, as well as different behaviors depending on the open or dead-end nature of the channel, providing a very first implementation of a fast maze resolver in a polariton fluid.

Finally, in the **sixth chapter**, we demonstrated the possibility to control the dynamics of the quantum fluctuations of our system by changing the dimension of the polariton fluid. In particular, we have shown that for a two-dimensional fluid, the fluid density switching time between its two metastable solutions exhibits a critical slowing down in the large diameter limit. This corresponds to the emergence of a first order phase transition and is manifested by the appereance of a bistability loop.

The experimental and analysis tools developed in this manuscript can be used for a wide variety of applications. For instance, our spectroscopy technique can be implemented together with the driving field intensity and the phase profile reshaping techniques in the context of analog gravity experiments, in order to probe the Hawking radiation or the super-radiance phenomena in an acoustic black hole in 1D and 2D geometries [76].

In the context of the quantum turbulence, we are also considering to study precisely the spectral signatures of dark solitons snake instabilities [92], and the Bogoliubov spectrum of an optical lattice of polariton condensates [21]. Besides the fundamental study of elementary excitations, the control of such excitations could open the way to the implementation of a complex analog maze solver [92].

In the context of the phase transition in driven-dissipative systems, our analysis of the spontaneous symmetry breaking in OPO configuration can be pushed further; indeed, the theory predicts that the Goldstone mode should be accompanied by the apparition of an overdamped partner mode, the Higgs mode, which could also be of great interest to characterize. Moreover, our spectroscopy technique can be easily adapted to investigate the phase transitions in quasi-equilibrium polariton condensates obtained in out-of-resonance pumping regime [162, 176] revealing specific features of such systems.

Appendix A

Microcavity sample design and fabrication

All the experiments performed during this thesis were carried out on the same semiconductor microcavity fabricated by molecular beam epitaxy at the Ecole Polytechnique Fédérale de Lausanne (EPFL) by Romuald Houdré in 1995.

Quantum wells. The sample embeds N=3 $In_{0.04}Ga_{0.96}As$ quantum wells, achieving a compromise between a large Rabi splitting $\Omega_R \propto \sqrt{N}$ and strong polariton-polariton interactions gn $\propto N^{-1}$. Note that N is not high enough to use the microcavity under off-resonance excitation in order to observe polariton condensation.

Bragg reflectors. The two distributed Bragg reflectors (DBR) are made of alternating layers of $Ga_{0.9}Al_{0.1}As$ and AlAs, of thickness $\lambda_0/4n_i$, with $\lambda_0 = 836$ nm the resonance wavelength of the optical cavity in vacuum and $n_{i=(Ga_{0.9}Al_{0.1}As,AlAs)}$ the respective refractive indices of the two materials. The top has 40 alternating layers; while the bottom has 53 layers, in order to compensate for the reflectivity decrease induced by its contact with the high refractive index GaAs substrate. Such a substrate has been used as a base for depositing each of the layers of the sample and polished such that the system can be used in transmission. The respective reflectivity of the top and bottom mirrors are equal to $R = 0.9985$ and $R = 0.9993$. This gives a cavity finenesse close to $\mathcal{F} = 3000$.

Optical cavity. The intracavity space is made of GaAs, with a thickness of $2\lambda_0$, suitable for the onset of three antinodes of the electromagnetic field, at the position of which the three quantum wells are placed to maximise the light-matter coupling. In order to tune precisely the resonance of the cavity with that of excitons, a small wedge was introduced between the mirrors, with an angle of about 10^{-6} radians. The corresponding energy gradient felt by photons leads to an energy gradient in the LP branch energy, measured to be 0.7 μeV/μm. It is large enough to explore exciton-photon detuning ranging from +7 meV to -4 meV on either side of the sample; but also small enough, relative to the polariton decay rate γ, to be able to work

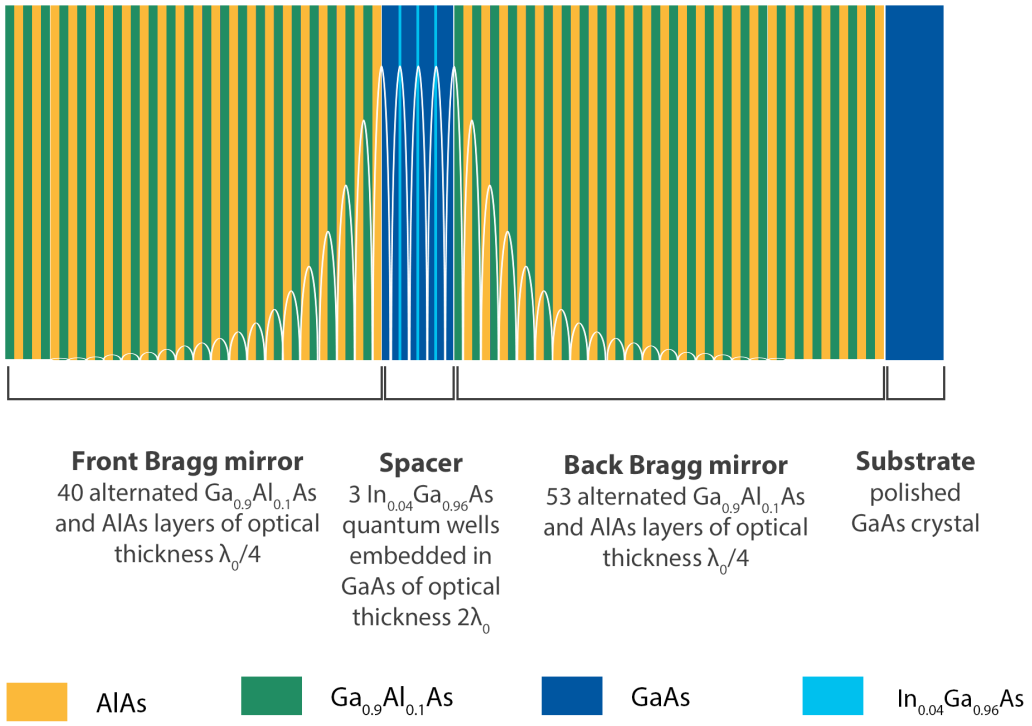

Figure A.1: **Semiconductor microcavity.** Two Bragg mirrors of alternated layers of $Ga_{0.9}Al_{0.1}As$ and AlAs of optical thickness $\lambda_0/4$ (40 and 53 layers respectively), surrounding a spacer of GaAs of optical thickness $2\lambda_0$, in which three quantum wells of $In_{0.04}Ga_{0.96}As$ are embedded at the antinodes of the electromagnetic field, whose amplitude distribution is highlighted by the white line. The cavity is grown on a substrate of GaAs, previously polished to allow working in transmission. The excitation takes place on the thin mirror side, while the detection is done on the substrate side. From [108].

over macroscopic distances of the order of 100 μm without significantly experiencing its effects.

Anticrossing. Fig. A.2(a) shows the measurement of the strong coupling anticrossing in our sample. The energies of the UP and LP branches are extracted from the photoluminescence spectrum emitted by the microcavity, under off-resonant excitation at $\mathbf{k} = 0$ μm^{-1} at different working points. The energies of the photon and exciton branches are deduced from Eq. 2.36. At their intersection $\hbar\Delta E_{X-\gamma} = 0$ meV, the Rabi energy is measured equal to $\hbar\Omega_R = 5.07$ meV.

Structural defects. Fig. A.2(b) pictures the transmission of the cavity illuminated at two different wavelengths (837.21 and 837.05 nm) at zero incidence. The resonance of the lower polaritons appears as two visible bright lines orthogonal to the direction of the wedge between the two mirrors of the optical cavity. Several structural defects are visible. The regular square lattice shape pattern originates from the mosaic phenomenon induced by the mechanical stresses applied to the sample. The thick and irregular black lines on the upper side of Fig. A.2(b) are dislocations attributed to mechanical shocks that have been exerted on the cavity during its

use over time. Finally, point defects are randomly distributed in the sample. They are dark or bright depending on whether the local modification of the potential they induce is blue-shifted (potential well) or red-shifted (potential barrier) with respect to the resonance of polaritons. Their diameter varies from sub-microns to ten microns.

Sample parameters				
	Material	N	δ (nm)	$n(\lambda_0)$
DBR_1	$Ga_{0.9}Al_{0.1}As$	40	60.1	3.48
DBR_2	AlAs	40	70.8	2.95
SP	GaAs	3	275	3.54
QW	$In_{0.04}Ga_{0.96}As$	3	8	3.54
SP	GaAs	3	275	3.54
DBR_1	$Ga_{0.9}Al_{0.1}As$	53	60.1	3.48
DBR_2	AlAs	53	70.8	2.95
SUB	GaAs	1	400×10^3	3.54

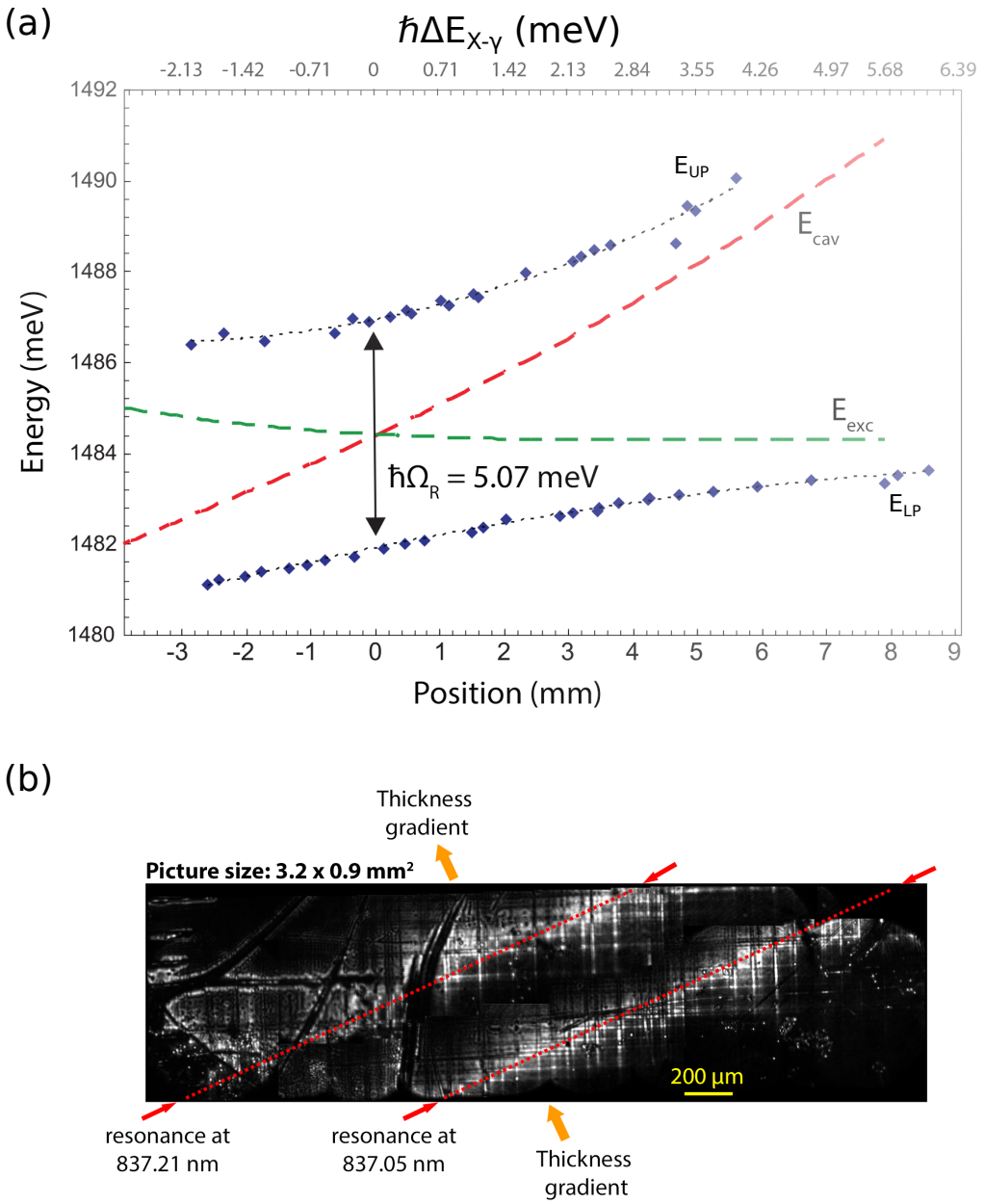

Figure A.2: **(a) Experimental anticrossing**. The blue dots represent the upper and lower polariton branches, obtained under off-resonant pumping at $k = 0\ \mu\text{m}^{-1}$. Changing the position changes the photon-exciton detuning $\Delta E_{X-\gamma}$ (horizontal axis); the exciton and photon energies are plotted in green and red dashed line, respectively. The experimental value for the Rabi splitting is extracted at zero detuning: $\hbar\Omega_R = 5.07$ meV. **(b) Cavity transmission.** Picture of a sample area of 3.2x0.9 mm^2, excited at two different wavelengths (837.05 and 837.21 nm). The resonances are clearly visible orthogonal to the wedge, as well as the different types of defects of the cavity: the regular pattern of mosaicity, some elongated dislocations and point-like defects.

Appendix B

Spectroscopy experiment routine

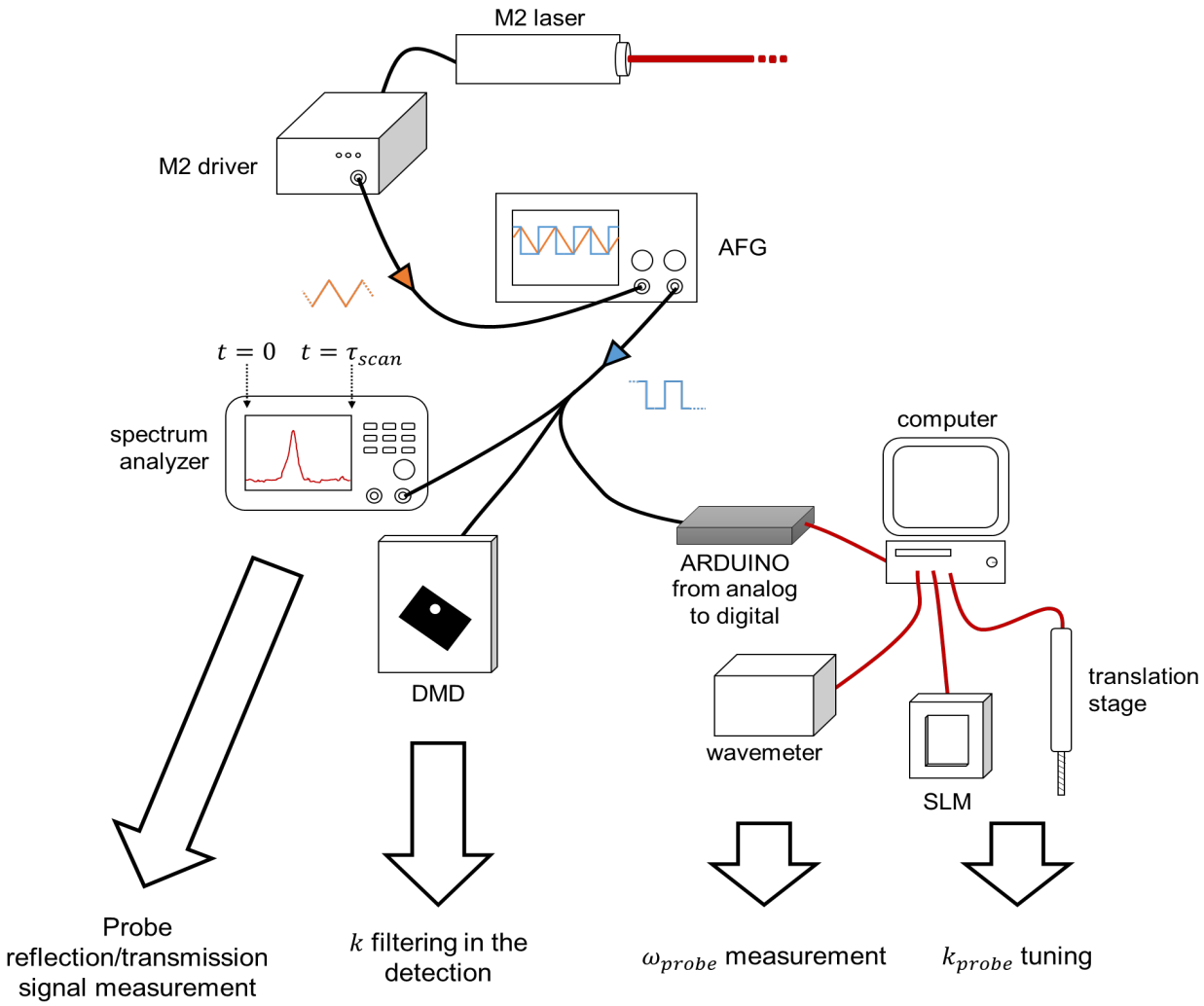

Figure B.1: **Setup automation.**

We detail in Fig. B.1 the automation routine of the spectroscopy experiment as the quality of the results relies a lot on it. Indeed, the parameters chosen at the beginning of the experiment slowly deviate from their initial values due to low-frequency fluctuations ($1/\tau \sim 1/100$ Hz) that are technically difficult to eliminate. In particular, the drifts of the laser energy and of the cryostat temperature significantly modify the dynamics of polaritons on time scales of the order of a hundred seconds. It is therefore crucial to automate the experiment in order to capture the Bogoliubov spectrum as quickly as possible, before the excitation regime deviates significantly from its initial state.

The routine core time, corresponding to the running a complete iteration of the experiment, is limited by the time of one scan of the probe energy τ_{scan}. This parameter is tunable with the M2 laser driver which automatically adjusts the scan speed of the length of the laser etalon cavity via the voltage of the piezo mirrors. For energy scans of 120 GHz, it cannot be lowered below 500 ms. Thus, for a hundred consecutive energy scans at probe wavevectors equally distributed between -1 and +1 μm^{-1}, the incompressible duration time of the total execution of the experiment is about 50 s, which remains relatively low compared to the time scale of the system fluctuations.

To achieve a spectrum acquisition time as close as possible to 50 ms, we slaved all the setup instruments with the triggering signal of the probe energy scan, provided by an analog output of the M2 driver. It is sent directly to the analog trigger input of the spectrum analyzer, setting its sweep time at τ_{scan}, and of the DMD, modifying the $\mathbf{k}$ position of the filtering pinhole at the beginning of each new scan. The other instruments, respectively the SLMs, the wavemeter and the servo-motors, do not have an accessible analog input to trigger them. They are controlled via a numerical trigger signal, synchronized with the analog one. For this purpose, we use an Arduino programming board: an FPGA with both analog and digital inputs and outputs. One of its input is connected to the analog trigger signal, which is then converted into a digital signal sent to the computer. Thanks to a home-made Python interface, all the changes of state of the instruments are in this way synchronized with the scan of the probe: the change of the phase pattern displayed by the SLM (i.e. the change of the probe wave vector), the recording of the laser wavelength measurements by the wavemeter, and the translation of the various servo-motors.

This ensures that the execution time of one measurement differs little from the incompressible time of the scans.

Appendix C

SLM intensity/phase profiles reshapping

All the experiments presented in this manuscript are based on a precise control of the spatial intensity and phase profile of the involved laser fields. This is achieved by using a spatial light modulator (SLM), embedding a reflective matrix of micrometric liquid crystals. Each pixel is addressed with a tunable voltage, in order to control its refractive index. This thus allows to control the local phase of a laser field reflected on the SLM.

SLMs are generally used as a holography device: for a target wavefront, wished in the focal plane of a lens, it is possible to compute a hologram, i.e. a phase pattern displayed on the SLM (corresponding to a distribution of voltages applied to each liquid crystal), modulating the incident wavefront and generating the desired phase and intensity distributions. This method has the drawback of requiring the numerical calculation of holograms. For relatively simple wavefront geometries, it is perfectly adequate as the algorithms quickly converge to a hologram solution, but in our case, we want to generate more complex profiles.

Our technique is based on the implementation of a blazed grating on the SLM, diffracting the incident beam at tunable angle α (order 1). Its phase pattern has a spatial distribution given by

$$\phi_{grat}(x,y) = mod_{2\pi}\left[\frac{2\pi}{\lambda}y\right] \times C(x,y), \tag{C.1}$$

with y the space coordinate along which the grating is modulated and λ the grating step size. $C(x,y) \in [0,1]$ denotes the local contrast of the grating modulation at the coordinate (x,y). By changing locally its value, we change the diffraction efficiency of the blazed grating, so the intensity distribution between the orders 0 (direct reflection) and 1 (diffracted reflection).

By cutting in the Fourier plane of the SLM the zero order and aligning the first order along the optical axis of the setup, the laser intensity distribution matches the $C(x,y)$ map when the

SLM plane is imaged at the output focal point of a $2f$-$2f$ telescope configuration.

In this way, in order to reshape the Gaussian intensity profile $I_{in}(x, y)$ of lasers, $C(x, y)$ is set equal to the ratio $I_{out}(x, y)/I_{in}(x, y)$, with $I_{out}(x, y)$ the target intensity profile. This leads to express the phase pattern to display on the SLM as follows

$$\phi_{SLM}(x, y) = \frac{I_{out}(x, y)}{I_{in}(x, y)} \left(\phi_{out}(x, y) + mod_{2\pi} \left[\frac{2\pi}{\lambda} y \right] \right), \tag{C.2}$$

where the possibility to modify the phase profile of the field is accounted for, via the addition of a target phase map $\phi_{out}(x, y)$ to the blazed grating phase.

Publications

- S. V. Koniakhin, O. Bleu, D.D. Stupin, S. Pigeon, A. Maître, **F. Claude**, G. Lerario, Q. Glorieux, A. Bramati, D. Solnyshkov and G. Malpuech. "Stationary Quantum Vortex Street in a Driven-Dissipative Quantum Fluid of Light", *Phys. Rev. Lett.* **123**, 215301, 2019.
- A. Maître, G. Lerario, A. Medeiros, **F. Claude**, Q. Glorieux, E. Giacobino, S. Pigeon and A. Bramati. "Dark-Soliton Molecules in an Exciton-Polariton Superfluid", *Phys. Rev. X*, **10**, 041028, 2020.
- **F. Claude**, S. V. Koniakhin, A. Maître, S. Pigeon, G. Lerario, D.D. Stupin, Q. Glorieux, E. Giacobino, D. Solnyshkov, G. Malpuech and A. Bramati. "Taming the snake instabilities in a polariton superfluid", *Optica*, **7**, 1660-1665, 2020.
- M.J. Jacquet, **F. Claude**, A. Maître, T. Boulier, E. Cancellieri, C. R. Usciati, I. Carutotto, E. Giacobino, A. Bramati and Q. Glorieux. "High-resolution coherent probe spectroscopy of a polariton quantum fluid", *Phys. Rev. Lett.*, **129**, 103601, 2022.
- A. Maître, **F. Claude**, G. Lerario, S.V. Koniakhin, S. Pigeon, D. Solnyshkov, G. Malpuech, Q. Glorieux, E. Giacobino and A. Bramati. "Spontaneous generation, enhanced propagation and optical imprinting of quantized vortices and dark solitons in a polariton superfluid: Towards the control of quantum turbulence", *EPL*, **134**, 24004, 2021.
- Z. Li*, **F. Claude***, T. Boulier, R. Usciati, E. Giacobino, Q. Glorieux., A. Bramati and C. Ciuti. "Dissipative Phase Transition with Driving-Controlled Spatial Dimension and Diffusive Boundary Conditions", *Phys. Rev. Lett.*, **128**, 093601, 2021.
- **F. Claude**, M.J. Jacquet, R. Usciati, I. Carutotto, E. Giacobino, A. Bramati and Q. Glorieux. "High-resolution coherent probe spectroscopy of a polariton quantum fluid", *Phys. Rev. Lett.*, **129**, 103601, 2022.
- M.J. Jacquet, M. Joly, **F. Claude**, L. Giacomelli, Q. Glorieux, A. Bramati and E. Giacobino. "Analogue quantum simulation of the Hawking effect in a polariton superfluid", *The European Physical Journal D*, **76**, 152, 2022.

In preparation

- **F. Claude**, M. J. Jacquet, I. Carusotto, Q. Glorieux, E. Giacobino and A. Bramati. "Spectrum of elementary excitations of a quantum fluid of polariton".
- **F. Claude**, M. J. Jacquet, Q. Glorieux, M. Wouters, E. Giacobino, I. Carusotto and A. Bramati. "Experimental observation of the diffusive Nambu-Goldstone mode of a non-equilibrium phase transition"

Bibliography

[1]

[2] Ioffe institute electronic archive, 2022.

[3] Andrew Adamatzky, Alessandro Chiolerio, and Konrad Szacilowski. Liquid metal droplet solves maze. *SOFT MATTER*, 16(6):1455–1462, FEB 14 2020.

[4] Imperatorskaja akademija nauk (Rusko). *COMMENTARII ACADEMIAE SCIENTIARVM IMPERIALIS PETROPOLITANAE.*, volume 10. typis Academiae, 1747.

[5] J. F. Allen and A. D. Misener. Flow of liquid helium ii. *Nature*, 141:75–75, 1938.

[6] Ivan Amelio, Anna Minguzzi, Maxime Richard, and Iacopo Carusotto. Galilean boosts and superfluidity of resonantly driven polariton fluids in the presence of an incoherent reservoir. *Phys. Rev. Research*, 2:023158, May 2020.

[7] A. Amo, S. Pigeon, C. Adrados, R. Houdré, E. Giacobino, C. Ciuti, and A. Bramati. Light engineering of the polariton landscape in semiconductor microcavities. *Phys. Rev. B*, 82:081301, Aug 2010.

[8] A. Amo, S. Pigeon, D. Sanvitto, V. G. Sala, R. Hivet, I. Carusotto, F. Pisanello, G. Leménager, R. Houdré, E Giacobino, C. Ciuti, and A. Bramati. Polariton superfluids reveal quantum hydrodynamic solitons. *Science*, 332(6034):1167–1170, 2011.

[9] A Amo, D. Sanvitto, Fabrice Laussy, Dario Ballarini, Elena del Valle, M. Martin, Aristide Lemaître, J Bloch, D. Krizhanovskii, M.S. Skolnick, C Tejedor, and L. Vina. Collective fluid dynamics of a polariton condensate in a semiconductor microcavity. *Nature*, 457:291–5, 02 2009.

[10] Alberto Amo, Jerome Lefrere, Simon Pigeon, Claire Adrados, Cristiano Ciuti, Iacopo Carusotto, Romuald Houdre, Elisabeth Giacobino, and Alberto Bramati. Superfluidity of polaritons in semiconductor microcavities. *Nature Physics*, 5, 09 2009.

[11] B. P. Anderson, P. C. Haljan, C. A. Regal, D. L. Feder, L. A. Collins, C. W. Clark, and E. A. Cornell. Watching dark solitons decay into vortex rings in a bose-einstein condensate. *Phys. Rev. Lett.*, 86:2926–2929, Apr 2001.

[12] M H Anderson, J R Ensher, and M R Matthews. Observation of bose-einstein condensation in a dilute atomic vapor. *Science*, 269(5221), 7 1995.

[13] N. W. Ashcroft and N. D. Mermin. *Solid State Physics*. Holt-Saunders, 1976.

[14] Gurgen Ashotovich Askar'yan. The self-focusing effect. *Soviet Physics Uspekhi*, 16(5):680, 1974.

[15] Marc Aßmann, Jean-Sebastian Tempel, Franziska Veit, Manfred Bayer, Arash Rahimi-Iman, Andreas Löffler, Sven Höfling, Stephan Reitzenstein, Lukas Worschech, and Alfred Forchel. From polariton condensates to highly photonic quantum degenerate states of bosonic matter. *Proceedings of the National Academy of Sciences*, 108(5):1804–1809, 2011.

[16] A. Baas, J. Ph. Karr, H. Eleuch, and E. Giacobino. Optical bistability in semiconductor microcavities. *Phys. Rev. A*, 69:023809, Feb 2004.

[17] A. Baas, J.-Ph. Karr, M. Romanelli, A. Bramati, and E. Giacobino. Quantum degeneracy of microcavity polaritons. *Phys. Rev. Lett.*, 96:176401, May 2006.

[18] D. Ballarini, D. Sanvitto, A. Amo, L. Viña, M. Wouters, I. Carusotto, A. Lemaitre, and J. Bloch. Observation of long-lived polariton states in semiconductor microcavities across the parametric threshold. *Phys. Rev. Lett.*, 102:056402, Feb 2009.

[19] Dario Ballarini, David A. Caputo, G. Dagvadorj, R T Juggins, Milena De Giorgi, Lorenzo Dominici, Ken W. West, Loren N. Pfeiffer, Giuseppe Gigli, Marzena H. Szymańska, and Daniele Sanvitto. Directional goldstone waves in polariton condensates close to equilibrium. *Nature Communications*, 11, 2020.

[20] Carlos Barceló, Stefano Liberati, and Matt Visser. Analogue gravity. *Living reviews in relativity*, 14(1):1–159, 2011.

[21] Charles-Edouard Bardyn, Torsten Karzig, Gil Refael, and Timothy C. H. Liew. Chiral bogoliubov excitations in nonlinear bosonic systems. *Phys. Rev. B*, 93:020502, Jan 2016.

[22] J. J. Baumberg, P. G. Savvidis, R. M. Stevenson, A. I. Tartakovskii, M. S. Skolnick, D. M. Whittaker, and J. S. Roberts. Parametric oscillation in a vertical microcavity: A polariton condensate or micro-optical parametric oscillation. *Phys. Rev. B*, 62:R16247–R16250, Dec 2000.

[23] Jacqueline Bloch, Iacopo Carusotto, and Michiel Wouters. Spontaneous coherence in spatially extended photonic systems: Non-equilibrium bose-einstein condensation. 2021.

[24] N N Bogoliubov. Problems of dynamic theory in statistical physics; problemy dinamicheskoi teorii v statisticheskoi fiziki. 1 1946.

[25] Lugiato L. A. Bonifacio, R. Mean field model for absorptive and dispersive bistability with inhomogeneous broadening. *Lettere al Nuovo Cimento*, 21(15), 1978.

[26] Bose. Plancks gesetz und lichtquantenhypothese. *Zeitschrift für Physik*, 26:178–181.

[27] Walter R. Bosenberg, Alexander Drobshoff, Jason I. Alexander, Lawrence E. Myers, and Robert L. Byer. 93% pump depletion, 3.5-w continuous-wave, singly resonant optical parametric oscillator. *Opt. Lett.*, 21(17):1336–1338, Sep 1996.

[28] T Boulier, M Bamba, A Amo, Claire Adrados, A Lemaitre, E Galopin, I Sagnes, J Bloch, C Ciuti, E Giacobino, et al. Polariton-generated intensity squeezing in semiconductor micropillars. *Nature communications*, 5(1):1–7, 2014.

[29] T. Boulier, E. Cancellieri, N. D. Sangouard, Q. Glorieux, A. V. Kavokin, D. M. Whittaker, E. Giacobino, and A. Bramati. Injection of orbital angular momentum and storage of quantized vortices in polariton superfluids. *Phys. Rev. Lett.*, 116:116402, Mar 2016.

[30] T Boulier, H Terças, DD Solnyshkov, Q Glorieux, E Giacobino, G Malpuech, and A Bramati. Vortex chain in a resonantly pumped polariton superfluid. *Scientific reports*, 5(1):1–5, 2015.

[31] Dirk Bouwmeester, Jian-Wei Pan, Klaus Mattle, Manfred Eibl, Harald Weinfurter, and Anton Zeilinger. Experimental quantum teleportation. *Nature*, 390:575–579, 1997.

[32] Joachim Brand and William P. Reinhardt. Solitonic vortices and the fundamental modes of the "snake instability": Possibility of observation in the gaseous bose-einstein condensate. *Phys. Rev. A*, 65:043612, Apr 2002.

[33] Samuel L. Braunstein and H. J. Kimble. Teleportation of continuous quantum variables. *Phys. Rev. Lett.*, 80:869–872, Jan 1998.

[34] Heinz-Peter Breuer and Francesco Petruccione. *The Theory of Open Quantum Systems*. Oxford University Press, 01 2007.

[35] Tim Byrnes, Na Kim, and Yoshihisa Yamamoto. Erratum: Exciton-polariton condensates. *Nature Physics*, 10, 11 2014.

[36] Filippo Caruso, Andrea Crespi, Anna Gabriella Ciriolo, Fabio Sciarrino, and Roberto Osellame. Fast escape of a quantum walker from an integrated photonic maze. *Nature Comm.*, 7, JUN 2016.

[37] Iacopo Carusotto and Cristiano Ciuti. Quantum fluids of light. *Rev. Mod. Phys.*, 85:299–366, Feb 2013.

[38] Guillaume Cassabois. *Relaxation de coherence dans des heterostructures de semiconducteurs*. 1999.

[39] A. Chabchoub, O. Kimmoun, H. Branger, N. Hoffmann, D. Proment, M. Onorato, and N. Akhmediev. Experimental observation of dark solitons on the surface of water. *Phys. Rev. Lett.*, 110:124101, Mar 2013.

[40] Rick Chartrand. Numerical differentiation of noisy, nonsmooth data. *ISRN Applied Mathematics*, 2011:1–11, May 2011.

[41] Ming Chen, Mincho A. Tsankov, Jon M. Nash, and Carl E. Patton. Microwave magnetic-envelope dark solitons in yttrium iron garnet thin films. *Phys. Rev. Lett.*, 70:1707–1710, Mar 1993.

[42] C. Ciuti, P. Schwendimann, B. Deveaud, and A. Quattropani. Theory of the angle-resonant polariton amplifier. *Phys. Rev. B*, 62:R4825–R4828, Aug 2000.

[43] C Ciuti, P Schwendimann, and A Quattropani. Theory of polariton parametric interactions in semiconductor microcavities. *Semiconductor Science and Technology*, 18(10):S279–S293, sep 2003.

[44] Cristiano Ciuti and Iacopo Carusotto. Quantum fluid effects and parametric instabilities in microcavities. *physica status solidi (b)*, 242:2224–2245, 2005. 25 figures, 16 pages long.

[45] F. Claude, M. J. Jacquet, R. Usciati, I. Carusotto, E. Giacobino, A. Bramati, and Q. Glorieux. High-resolution coherent probe spectroscopy of a polariton quantum fluid. *Phys. Rev. Lett.*, 129:103601, Aug 2022.

[46] Ferdinand Claude, Sergei V. Koniakhin, Anne Maître, Simon Pigeon, Giovanni Lerario, Daniil D. Stupin, Quentin Glorieux, Elisabeth Giacobino, Dmitry Solnyshkov, Guillaume Malpuech, and Alberto Bramati. Taming the snake instabilities in a polariton superfluid. *Optica*, 7(12):1660–1665, Dec 2020.

[47] Monique Combescot, Odile Betbeder-Matibet, and François Dubin. The many-body physics of composite bosons. *Physics Reports*, 463(5):215–320, 2008.

[48] K. B. Davis, M. O. Mewes, M. R. Andrews, N. J. van Druten, D. S. Durfee, D. M. Kurn, and W. Ketterle. Bose-einstein condensation in a gas of sodium atoms. *Phys. Rev. Lett.*, 75:3969–3973, Nov 1995.

[49] De Broglie, Louis. Recherches sur la théorie des quanta. *Ann. Phys.*, 10(3):22–128, 1925.

[50] V. DeGiorgio and Marlan O. Scully. Analogy between the laser threshold region and a second-order phase transition. *Phys. Rev. A*, 2:1170–1177, Oct 1970.

[51] J. Denschlag, J. E. Simsarian, D. L. Feder, Charles W. Clark, L. A. Collins, J. Cubizolles, L. Deng, E. W. Hagley, K. Helmerson, W. P. Reinhardt, S. L. Rolston, B. I. Schneider, and W. D. Phillips. Generating solitons by phase engineering of a bose-einstein condensate. *Science*, 287(5450):97–101, 2000.

[52] T. D. Doan, Huy Thien Cao, D. B. Tran Thoai, and H. Haug. Condensation kinetics of microcavity polaritons with scattering by phonons and polaritons. *Phys. Rev. B*, 72:085301, Aug 2005.

[53] K. Dunnett, A. Ferrier, A. Zamora, G. Dagvadorj, and M. H. Szymańska. Properties

of the signal mode in the polariton optical parametric oscillator regime. *Phys. Rev. B*, 98:165307, Oct 2018.

[54] PR Eastham. Mode locking and mode competition in a nonequilibrium solid-state condensate. *Physical Review B*, 78(3):035319, 2008.

[55] A. Einstein. *Quantentheorie des einatomigen idealen Gases*, pages 237–244. John Wiley Sons, Ltd, 2005.

[56] Dieter Forster. *Hydrodynamic fluctuations, broken symmetry, and correlation functions*. CRC Press, 2018.

[57] Dmitri Foursa and Philippe Emplit. Investigation of black-gray soliton interaction. *Phys. Rev. Lett.*, 77:4011–4014, Nov 1996.

[58] D J Frantzeskakis. Dark solitons in atomic bose–einstein condensates: from theory to experiments. *Journal of Physics A: Mathematical and Theoretical*, 43(21):213001, may 2010.

[59] Prof. J.C. McLennan F.R.S., H.D. Smith M.A., and J.O. Wilhelm M.A. Xiv. the scattering of light by liquid helium. *The London, Edinburgh, and Dublin Philosophical Magazine and Journal of Science*, 14(89):161–167, 1932.

[60] Michael J Fuerstman, Pascal Deschatelets, Ravi Kane, Alexander Schwartz, Paul JA Kenis, John M Deutch, and George M Whitesides. Solving mazes using microfluidic networks. *Langmuir*, 19(11):4714–4722, 2003.

[61] Luca Giacomelli and Iacopo Carusotto. Understanding superradiant phenomena with synthetic vector potentials in atomic bose-einstein condensates. *Phys. Rev. A*, 103:043309, Apr 2021.

[62] V. Goblot, H. S. Nguyen, I. Carusotto, E. Galopin, A. Lemaître, I. Sagnes, A. Amo, and J. Bloch. Phase-controlled bistability of a dark soliton train in a polariton fluid. *Phys. Rev. Lett.*, 117:217401, Nov 2016.

[63] Jeffrey Goldstone. Field theories with superconductor solutions. *Il Nuovo Cimento (1955-1965)*, 19(1):154–164, 1961.

[64] Pjotrs Grišins, Hai Son Nguyen, Jacqueline Bloch, Alberto Amo, and Iacopo Carusotto. Theoretical study of stimulated and spontaneous hawking effects from an acoustic black hole in a hydrodynamically flowing fluid of light. *Phys. Rev. B*, 94:144518, Oct 2016.

[65] E P Gross. Structure of a quantized vortex in boson systems. *Nuovo Cimento (Italy) Divided into Nuovo Cimento A and Nuovo Cimento B*.

[66] Gilbert Grynberg, Alain Aspect, Claude Fabre, and Claude Cohen-Tannoudji. *Introduction to Quantum Optics: From the Semi-classical Approach to Quantized Light*. Cambridge University Press, 2010.

[67] Hartmut Haug and Stephan W Koch. *Quantum Theory of the Optical and Electronic Properties of Semiconductors*. WORLD SCIENTIFIC, 5th edition, 2009.

[68] Stephen W Hawking. Particle creation by black holes. In *Euclidean quantum gravity*, pages 167–188. World Scientific, 1975.

[69] A. Heidmann, R. J. Horowicz, S. Reynaud, E. Giacobino, C. Fabre, and G. Camy. Observation of quantum noise reduction on twin laser beams. *Phys. Rev. Lett.*, 59:2555–2557, Nov 1987.

[70] Yoshimasa Hidaka and Yuki Minami. Spontaneous symmetry breaking and Nambu–Goldstone modes in open classical and quantum systems. *Progress of Theoretical and Experimental Physics*, 2020(3), 03 2020. 033A01.

[71] F. T. Hioe and Surendra Singh. Correlations, transients, bistability, and phase-transition analogy in two-mode lasers. *Phys. Rev. A*, 24:2050–2074, Oct 1981.

[72] J. J. Hopfield. Theory of the contribution of excitons to the complex dielectric constant of crystals. *Phys. Rev.*, 112:1555–1567, Dec 1958.

[73] Tomoyuki Horikiri, Tim Byrnes, Kenichiro Kusudo, Natsuko Ishida, Yasuhiro Matsuo, Yutaka Shikano, Andreas Löffler, Sven Höfling, Alfred Forchel, and Yoshihisa Yamamoto. Highly excited exciton-polariton condensates. *Phys. Rev. B*, 95:245122, Jun 2017.

[74] Kerson Huang. *Introduction to statistical physics*. Chapman and Hall/CRC, 2009.

[75] A. Imamog¯lu, R. J. Ram, S. Pau, and Y. Yamamoto. Nonequilibrium condensates and lasers without inversion: Exciton-polariton lasers. *Phys. Rev. A*, 53:4250–4253, Jun 1996.

[76] M. J. Jacquet, T. Boulier, F. Claude, A. Maître, E. Cancellieri, C. Adrados, A. Amo, S. Pigeon, Q. Glorieux, A. Bramati, and E. Giacobino. Polariton fluids for analogue gravity physics. *Philosophical Transactions of the Royal Society A: Mathematical, Physical and Engineering Sciences*, 378(2177):20190225, 2020.

[77] Omar Jamadi, Elena Rozas, Grazia Salerno, Marijana Milićević, Tomoki Ozawa, Isabelle Sagnes, Aristide Lemaître, Luc Le Gratiet, Abdelmounaim Harouri, Iacopo Carusotto, et al. Direct observation of photonic landau levels and helical edge states in strained honeycomb lattices. *Light: Science & Applications*, 9(1):1–10, 2020.

[78] J V Jelley. Cerenkov radiation and its applications. *British Journal of Applied Physics*, 6(7):227–232, jul 1955.

[79] J.S.Russel. Report on waves. 1844.

[80] Brian Julsgaard, Jacob Sherson, J Cirac, Jaromír Fiurásek, and E. Polzik. Experimental demonstration of quantum memory for light. *Nature*, 432:482–6, 12 2004.

[81] A. M. Kamchatnov and L. P. Pitaevskii. Stabilization of solitons generated by a supersonic flow of bose-einstein condensate past an obstacle. *Phys. Rev. Lett.*, 100:160402, Apr 2008.

[82] P. Kapitza. Viscosity of Liquid Helium below the λ-Point. , 141(3558):74, January 1938.

[83] Jean-Philippe Karr. *Effets non linéaires et quantiques dans les microcavités semiconductrices*. Theses, Université Pierre et Marie Curie - Paris VI, December 2001.

[84] Jacek Kasprzak, Murielle Richard, S Kundermann, A Baas, P Jeambrun, Jonathan Mark James Keeling, FM Marchetti, MH Szymańska, R André, JL Staehli, et al. Bose–einstein condensation of exciton polaritons. *Nature*, 443(7110):409–414, 2006.

[85] Jonathan Keeling and Natalia G. Berloff. Exciton–polariton condensation. *Contemporary Physics*, 52(2):131–151, 2011.

[86] Yuri S Kivshar and Dmitry E Pelinovsky. Self-focusing and transverse instabilities of solitary waves. *Physics Reports*, 331(4):117–195, 2000.

[87] Jan Klaers, Julian Schmitt, Frank Vewinger, and Martin Weitz. Bose–einstein condensation of photons in an optical microcavity. *Nature*, 468(7323):545–548, 2010.

[88] S Klembt, TH Harder, OA Egorov, K Winkler, R Ge, MA Bandres, M Emmerling, L Worschech, TCH Liew, M Segev, et al. Exciton-polariton topological insulator. *Nature*, 562(7728):552–556, 2018.

[89] Victor I. Klimov. *Semiconductor and Metal Nanocrystals: Synthesis and Electronic and Optical Properties*. 2007.

[90] V. Kohnle, Y. Léger, M. Wouters, M. Richard, M. T. Portella-Oberli, and B. Deveaud. Four-wave mixing excitations in a dissipative polariton quantum fluid. *Phys. Rev. B*, 86:064508, Aug 2012.

[91] V. Kohnle, Y. Léger, M. Wouters, M. Richard, M. T. Portella-Oberli, and B. Deveaud-Plédran. From single particle to superfluid excitations in a dissipative polariton gas. *Phys. Rev. Lett.*, 106:255302, Jun 2011.

[92] S. V. Koniakhin, O. Bleu, D. D. Stupin, S. Pigeon, A. Maitre, F. Claude, G. Lerario, Q. Glorieux, A. Bramati, D. Solnyshkov, and G. Malpuech. Stationary quantum vortex street in a driven-dissipative quantum fluid of light. *Phys. Rev. Lett.*, 123:215301, Nov 2019.

[93] Dr. D. J. Korteweg and Dr. G. de Vries. Xli. on the change of form of long waves advancing in a rectangular canal, and on a new type of long stationary waves. *The London, Edinburgh, and Dublin Philosophical Magazine and Journal of Science*, 39(240):422–443, 1895.

[94] EA Kuznetsov and SK Turitsyn. Instability and collapse of solitons in media with a defocusing nonlinearity. *Zh. Eksp. Teor. Fiz*, 94:129, 1988.

[95] CW Lai, NY Kim, S Utsunomiya, G Roumpos, H Deng, MD Fraser, T Byrnes, P Recher,

N Kumada, T Fujisawa, et al. Coherent zero-state and π-state in an exciton–polariton condensate array. *Nature*, 450(7169):529–532, 2007.

[96] L. Landau. Theory of the superfluidity of helium ii. *Phys. Rev.*, 60:356–358, Aug 1941.

[97] L.D. Landau and E.M. Lifshitz. *Statistical Physics*. Number vol. 5. Elsevier Science, 1980.

[98] Robert V. Lange. Nonrelativistic theorem analogous to the goldstone theorem. *Phys. Rev.*, 146:301–303, Jun 1966.

[99] Fabrice P. Laussy, Ivan A. Shelykh, Guillaume Malpuech, and Alexey Kavokin. Effects of bose-einstein condensation of exciton polaritons in microcavities on the polarization of emitted light. *Phys. Rev. B*, 73:035315, Jan 2006.

[100] Anthony J. Leggett. Bose-einstein condensation in the alkali gases: Some fundamental concepts. *Rev. Mod. Phys.*, 73:307–356, Apr 2001.

[101] G. Lerario, S. V. Koniakhin, A. Maître, D. Solnyshkov, A. Zilio, Q. Glorieux, G. Malpuech, E. Giacobino, S. Pigeon, and A. Bramati. Parallel dark-soliton pair in a bistable two-dimensional exciton-polariton superfluid. *Phys. Rev. Research*, 2:042041, Dec 2020.

[102] Giovanni Lerario, Anne Maître, Rajiv Boddeda, Quentin Glorieux, Elisabeth Giacobino, Simon Pigeon, and Alberto Bramati. Vortex-stream generation and enhanced propagation in a polariton superfluid. *Phys. Rev. Research*, 2:023049, Apr 2020.

[103] Zejian Li, Ferdinand Claude, Thomas Boulier, Elisabeth Giacobino, Quentin Glorieux, Alberto Bramati, and Cristiano Ciuti. Dissipative phase transition with driving-controlled spatial dimension and diffusive boundary conditions. *Phys. Rev. Lett.*, 128:093601, Feb 2022.

[104] T. C. H. Liew, A. V. Kavokin, and I. A. Shelykh. Optical circuits based on polariton neurons in semiconductor microcavities. *Phys. Rev. Lett.*, 101:016402, Jul 2008.

[105] F. London. The λ-Phenomenon of Liquid Helium and the Bose-Einstein Degeneracy. , 141(3571):643–644, April 1938.

[106] Luigi A Lugiato. Ii theory of optical bistability. In *Progress in optics*, volume 21, pages 69–216. Elsevier, 1984.

[107] Andrei I Maimistov. Solitons in nonlinear optics. *Quantum electronics*, 40(9):756, 2010.

[108] Anne Maitre. *Generation, propagation and control of quantized vortices and dark solitons in polariton superfluids*. Theses, Sorbonne Université, November 2020.

[109] Anne Maître, Giovanni Lerario, Adrià Medeiros, Ferdinand Claude, Quentin Glorieux, Elisabeth Giacobino, Simon Pigeon, and Alberto Bramati. Dark-soliton molecules in an exciton-polariton superfluid. *Phys. Rev. X*, 10:041028, Nov 2020.

[110] Guillaume Malpuech, Alexey Kavokin, and Fabrice P Laussy. Polariton bose condensation in microcavities. *physica status solidi (a)*, 195(3):568–578, 2003.

[111] Jean-Michel Ménard, C. Poellmann, Michael Porer, U. Leierseder, Élisabeth Galopin, Aristide Lemaître, Alberto Amo, Jacqueline Bloch, and Rupert Huber. Revealing the dark side of a bright exciton–polariton condensate. *Nature Communications*, 5, 2014.

[112] J. Mertz, T. Debuisschert, A. Heidmann, C. Fabre, and E. Giacobino. Improvements in the observed intensity correlation of optical parametric oscillator twin beams. *Opt. Lett.*, 16(16):1234–1236, Aug 1991.

[113] S Michaelis de Vasconcellos, A Calvar, A Dousse, J Suffczyński, N Dupuis, A Lemaître, I Sagnes, J Bloch, P Voisin, and P Senellart. Spatial, spectral, and polarization properties of coupled micropillar cavities. *Applied Physics Letters*, 99(10):101103, 2011.

[114] Claire Michel, Omar Boughdad, Mathias Albert, Pierre-Élie Larré, and Matthieu Bellec. Superfluid motion and drag-force cancellation in a fluid of light. *Nature communications*, 9(1):1–6, 2018.

[115] M Milićević, G Montambaux, T Ozawa, O Jamadi, B Real, I Sagnes, A Lemaître, L Le Gratiet, A Harouri, J Bloch, et al. Type-iii and tilted dirac cones emerging from flat bands in photonic orbital graphene. *Physical Review X*, 9(3):031010, 2019.

[116] Yuki Minami and Yoshimasa Hidaka. Spontaneous symmetry breaking and nambu-goldstone modes in dissipative systems. *Phys. Rev. E*, 97:012130, Jan 2018.

[117] Yuki Minami, Hiroyoshi Nakano, and Yoshimasa Hidaka. Rainbow nambu-goldstone modes under a shear flow. *Phys. Rev. Lett.*, 126:141601, Apr 2021.

[118] Fabrizio Minganti, Alberto Biella, Nicola Bartolo, and Cristiano Ciuti. Spectral theory of liouvillians for dissipative phase transitions. *Phys. Rev. A*, 98:042118, Oct 2018.

[119] Toshiyuki Nakagaki, Hiroyasu Yamada, and Ágota Tóth. Maze-solving by an amoeboid organism. *Nature*, 407(6803):470–470, 2000.

[120] Masaaki Nakayama, Katsuya Murakami, and DaeGwi Kim. Polariton dispersion relations under condensation in a cubr microcavity. *physica status solidi c*, 13(2-3):81–84, 2016.

[121] Masaaki Nakayama and Masafumi Ueda. Observation of diffusive and dispersive profiles of the nonequilibrium polariton-condensate dispersion relation in a cubr microcavity. *Physical Review B*, 95, 03 2017.

[122] Yoichiro Nambu. Quasi-particles and gauge invariance in the theory of superconductivity. *Phys. Rev.*, 117:648–663, Feb 1960.

[123] Gaël Nardin, Gabriele Grosso, Yoan Léger, Barbara Pięłka, François Morier-Genoud, and Benoît Deveaud-Plédran. Hydrodynamic nucleation of quantized vortex pairs in a polariton quantum fluid. *Nature Physics*, 7(8):635–641, August 2011.

[124] Gaël Nardin, Gabriele Grosso, Yoan Léger, Barbara Pitka, François Morier-Genoud, and Benoît Deveaud-Plédran. Hydrodynamic nucleation of quantized vortex pairs in a polariton quantum fluid. *Nature Physics*, 7(8):635–641, 2011.

[125] H. S. Nguyen, D. Gerace, I. Carusotto, D. Sanvitto, E. Galopin, A. Lemaître, I. Sagnes, J. Bloch, and A. Amo. Acoustic black hole in a stationary hydrodynamic flow of microcavity polaritons. *Phys. Rev. Lett.*, 114:036402, Jan 2015.

[126] H. S. Nguyen, D. Vishnevsky, C. Sturm, D. Tanese, D. Solnyshkov, E. Galopin, A. Lemaître, I. Sagnes, A. Amo, G. Malpuech, and J. Bloch. Realization of a double-barrier resonant tunneling diode for cavity polaritons. *Phys. Rev. Lett.*, 110:236601, Jun 2013.

[127] R Niemczyk and Stanisław Zawiślak. Review of maze solving algorithms for 2d maze and their visualisation. In *Engineer of the XXI Century*, pages 239–252. Springer, 2020.

[128] P. Nozieres and D. Pines. *Theory Of Quantum Liquids*. Advanced Books Classics. Avalon Publishing, 1999.

[129] Sajal Paul, J. B. Roy, and P. K. Basu. Empirical expressions for the alloy composition and temperature dependence of the band gap and intrinsic carrier density in gaxin1xas. *Journal of Applied Physics*, 69(2):827–829, 1991.

[130] V. Pavlov and A. Voronin. *Soviet Automatic Control*, 17:45–51, 1984.

[131] M. Pieczarka, O. Bleu, E. Estrecho, M. Wurdack, M. Steger, D. W. Snoke, K. West, L. N. Pfeiffer, A. G. Truscott, E. A. Ostrovskaya, J. Levinsen, and M. M. Parish. Bogoliubov excitations of a polariton condensate in dynamical equilibrium with an incoherent reservoir. *Phys. Rev. B*, 105:224515, Jun 2022.

[132] Maciej Pieczarka, Eliezer Estrecho, Maryam Boozarjmehr, Olivier Bleu, Mark Steger, Kenneth West, Loren N. Pfeiffer, David W. Snoke, Jesper Levinsen, Meera M. Parish, Andrew G. Truscott, and Elena A. Ostrovskaya. Observation of quantum depletion in a non-equilibrium exciton–polariton condensate. *Nature Communications*, 11(1):429, December 2020.

[133] Maciej Pieczarka, Marcin Syperek, Łukasz Dusanowski, Jan Misiewicz, Fabian Langer, Alfred Forchel, Martin Kamp, Christian Schneider, Sven Höfling, Alexey Kavokin, and Grzegorz Sek. Ghost branch photoluminescence from a polariton fluid under nonresonant excitation. *Phys. Rev. Lett.*, 115:186401, Oct 2015.

[134] S. Pigeon, I. Carusotto, and C. Ciuti. Hydrodynamic nucleation of vortices and solitons in a resonantly excited polariton superfluid. *Phys. Rev. B*, 83:144513, Apr 2011.

[135] Simon Pigeon and Alberto Bramati. Sustained propagation and control of topological excitations in polariton superfluid. *New Journal of Physics*, 19(9):095004, sep 2017.

[136] S. Pirandola, U. L. Andersen, L. Banchi, M. Berta, D. Bunandar, R. Colbeck, D. Englund, T. Gehring, C. Lupo, C. Ottaviani, J. L. Pereira, M. Razavi, J. Shamsul Shaari, M. Tomamichel, V. C. Usenko, G. Vallone, P. Villoresi, and P. Wallden. Advances in quantum cryptography. *Adv. Opt. Photon.*, 12(4):1012–1236, Dec 2020.

[137] Lev P Pitaevskii. Vortex lines in an imperfect bose gas. *Sov. Phys. JETP*, 13(2):451–454, 1961.

[138] L.P. Pitaevskii, L.P. Pítajevskíj, L.P.P. S. Stringari, S. Stringari, and S. Stringari. *Bose-Einstein Condensation*. International Series of Monographs on Physics. Clarendon Press, 2003.

[139] Darwin R Reyes, Moustafa M Ghanem, George M Whitesides, and Andreas Manz. Glow discharge in microfluidic chips for visible analog computing. *Lab on a Chip*, 2(2):113–116, 2002.

[140] I. Ribet, C. Drag, M. Lefebvre, and E. Rosencher. Widely tunable single-frequency pulsed optical parametric oscillator. *Opt. Lett.*, 27(4):255–257, Feb 2002.

[141] G. Rochat, C. Ciuti, V. Savona, C. Piermarocchi, A. Quattropani, and P. Schwendimann. Excitonic bloch equations for a two-dimensional system of interacting excitons. *Phys. Rev. B*, 61:13856–13862, May 2000.

[142] S. R. K. Rodriguez, W. Casteels, F. Storme, N. Carlon Zambon, I. Sagnes, L. Le Gratiet, E. Galopin, A. Lemaître, A. Amo, C. Ciuti, and J. Bloch. Probing a dissipative phase transition via dynamical optical hysteresis. *Phys. Rev. Lett.*, 118:247402, Jun 2017.

[143] Emmanuel Rosencher and Claude Fabre. Oscillation characteristics of continuous-wave optical parametric oscillators: beyond the mean-field approximation. *J. Opt. Soc. Am. B*, 19(5):1107–1116, May 2002.

[144] Rajarshi Roy, R. Short, J. Durnin, and L. Mandel. First-passage-time distributions under the influence of quantum fluctuations in a laser. *Phys. Rev. Lett.*, 45:1486–1490, Nov 1980.

[145] D. Sanvitto, Simon Pigeon, A. Amo, Dario Ballarini, Milena De Giorgi, I. Carusotto, R. Hivet, Ferruccio Pisanello, V. Sala, Paulo Sergio Guimaraes, E. Giacobino, Cristiano Ciuti, and G. Gigli. All-optical control of the quantum flow of a polariton condensate. *Nature Photonics*, 5:610–614, 09 2011.

[146] Vincenzo Savona. Linear optical properties of semiconductor microcavities with embedded quantum wells. In Henri Benisty, Claude Weisbuch, École Polytechnique, Jean-Michel Gérard, Romuald Houdré, and John Rarity, editors, *Lecture Notes in Physics, Berlin Springer Verlag*, volume 531, page 173. 1999.

[147] P. G. Savvidis, J. J. Baumberg, R. M. Stevenson, M. S. Skolnick, D. M. Whittaker, and J. S. Roberts. Angle-resonant stimulated polariton amplifier. *Phys. Rev. Lett.*, 84:1547–1550, Feb 2000.

[148] P. G. Savvidis, C. Ciuti, J. J. Baumberg, D. M. Whittaker, M. S. Skolnick, and J. S. Roberts. Off-branch polaritons and multiple scattering in semiconductor microcavities. *Phys. Rev. B*, 64:075311, Jul 2001.

[149] M. Scheidt, B. Beier, R. Knappe, K.-J. Boller, and R. Wallenstein. Diode-laser-pumped continuous-wave ktp optical parametric oscillator. *J. Opt. Soc. Am. B*, 12(11):2087–2094, Nov 1995.

[150] Bruno Scherrer, Isabelle Ribet, Antoine Godard, Emmanuel Rosencher, and Michel Lefebvre. Dual-cavity doubly resonant optical parametric oscillators: demonstration of pulsed single-mode operation. *J. Opt. Soc. Am. B*, 17(10):1716–1729, Oct 2000.

[151] Ch Schneider, K Winkler, Michael D Fraser, Martin Kamp, Y Yamamoto, EA Ostrovskaya, and Sven Höfling. Exciton-polariton trapping and potential landscape engineering. *Reports on Progress in Physics*, 80(1):016503, 2016.

[152] C. Shannon. Presentation of a maze solving machine. In *Trans. 8th Conf. Cybernetics*, page 169, 1951.

[153] M Sich, DN Krizhanovskii, MS Skolnick, Andriy V Gorbach, Robin Hartley, Dmitry V Skryabin, EA Cerda-Méndez, K Biermann, R Hey, and PV Santos. Observation of bright polariton solitons in a semiconductor microcavity. *Nature photonics*, 6(1):50–55, 2012.

[154] D. D. Solnyshkov, C. Leblanc, S. V. Koniakhin, O. Bleu, and G. Malpuech. Quantum analogue of a kerr black hole and the penrose effect in a bose-einstein condensate. *Phys. Rev. B*, 99:214511, Jun 2019.

[155] R Spano, J Cuadra, G Tosi, C Antón, C A Lingg, D Sanvitto, M D Martín, L Viña, P R Eastham, M van der Poel, and J M Hvam. Coherence properties of exciton polariton OPO condensates in one and two dimensions. *New Journal of Physics*, 14(7):075018, jul 2012.

[156] Oliver Steinbock, Agota Toth, and Kenneth Showalter. Navigating complex labyrinths: optimal paths from chemical waves. *Science*, 267(5199):868–871, 1995.

[157] S. Stellmer, C. Becker, P. Soltan-Panahi, E.-M. Richter, S. Dörscher, M. Baumert, J. Kronjäger, K. Bongs, and K. Sengstock. Collisions of dark solitons in elongated bose-einstein condensates. *Phys. Rev. Lett.*, 101:120406, Sep 2008.

[158] Petr Stepanov, Ivan Amelio, Jean-Guy Rousset, Jacqueline Bloch, Aristide Lemaître, Alberto Amo, Anna Minguzzi, Iacopo Carusotto, and Maxime Richard. Dispersion relation of the collective excitations in a resonantly driven polariton fluid. *Nature Communications*, 10(1):3869, August 2019.

[159] R. M. Stevenson, V. N. Astratov, M. S. Skolnick, D. M. Whittaker, M. Emam-Ismail, A. I. Tartakovskii, P. G. Savvidis, J. J. Baumberg, and J. S. Roberts. Continuous wave

observation of massive polariton redistribution by stimulated scattering in semiconductor microcavities. *Phys. Rev. Lett.*, 85:3680–3683, Oct 2000.

[160] Yongbao Sun, Patrick Wen, Yoseob Yoon, Gangqiang Liu, Mark Steger, Loren N. Pfeiffer, Ken West, David W. Snoke, and Keith A. Nelson. Bose-einstein condensation of long-lifetime polaritons in thermal equilibrium. *Phys. Rev. Lett.*, 118:016602, Jan 2017.

[161] A Szöke, V Daneu, J Goldhar, and NA Kurnit. Bistable optical element and its applications. *Applied Physics Letters*, 15(11):376–379, 1969.

[162] M. H. Szymańska, J. Keeling, and P. B. Littlewood. Nonequilibrium quantum condensation in an incoherently pumped dissipative system. *Phys. Rev. Lett.*, 96:230602, Jun 2006.

[163] F. Tassone and Y. Yamamoto. Exciton-exciton scattering dynamics in a semiconductor microcavity and stimulated scattering into polaritons. *Phys. Rev. B*, 59:10830–10842, Apr 1999.

[164] J. Teja and N. C. Wong. Twin-beam generation in a triply resonant dual-cavity optical parametric oscillator. *Opt. Express*, 2(3):65–71, Feb 1998.

[165] Laszlo Tisza. Transport phenomena in helium ii. *Nature*, 141:913–913, 1938.

[166] Toshio Tsuzuki. Nonlinear waves in the pitaevskii-gross equation. *Journal of Low Temperature Physics*, 4:441–457, 1971.

[167] Luke Tweedy, Peter A. Thomason, Peggy I. Paschke, Kirsty Martin, Laura M. Machesky, Michele Zagnoni, and Robert H. Insall. Seeing around corners: Cells solve mazes and respond at a distance using attractant breakdown. *Science*, 369(6507), 2020.

[168] S. Utsunomiya, L. Tian, G. Roumpos, C. W. Lai, N. Kumada, T. Fujisawa, M. Kuwata-Gonokami, A. Löffler, S. Höfling, A. Forchel, and Y. Yamamoto. Observation of Bogoliubov excitations in exciton-polariton condensates. *Nature Physics*, 4(9):700–705, August 2008.

[169] Filippo Vicentini, Fabrizio Minganti, Riccardo Rota, Giuliano Orso, and Cristiano Ciuti. Critical slowing down in driven-dissipative bose-hubbard lattices. *Phys. Rev. A*, 97:013853, Jan 2018.

[170] M. Vladimirova, S. Cronenberger, D. Scalbert, K. V. Kavokin, A. Miard, A. Lemaître, J. Bloch, D. Solnyshkov, G. Malpuech, and A. V. Kavokin. Polariton-polariton interaction constants in microcavities. *Phys. Rev. B*, 82:075301, Aug 2010.

[171] A. M. Weiner, J. P. Heritage, R. J. Hawkins, R. N. Thurston, E. M. Kirschner, D. E. Leaird, and W. J. Tomlinson. Experimental observation of the fundamental dark soliton in optical fibers. *Phys. Rev. Lett.*, 61:2445–2448, Nov 1988.

[172] C. Weisbuch, M. Nishioka, A. Ishikawa, and Y. Arakawa. Observation of the coupled

exciton-photon mode splitting in a semiconductor quantum microcavity. *Phys. Rev. Lett.*, 69:3314–3317, Dec 1992.

[173] Esther Wertz, Lydie Ferrier, DD Solnyshkov, Robert Johne, Daniele Sanvitto, Aristide Lemaître, Isabelle Sagnes, Roger Grousson, Alexey V Kavokin, Pascale Senellart, et al. Spontaneous formation and optical manipulation of extended polariton condensates. *Nature physics*, 6(11):860–864, 2010.

[174] D. M. Whittaker. Classical treatment of parametric processes in a strong-coupling planar microcavity. *Phys. Rev. B*, 63:193305, Apr 2001.

[175] Gary A. Williams. Vortex-loop phase transitions in liquid helium, cosmic strings, and high- T_c superconductors. *Phys. Rev. Lett.*, 82:1201–1204, Feb 1999.

[176] Michiel Wouters and Iacopo Carusotto. Excitations in a nonequilibrium bose-einstein condensate of exciton polaritons. *Phys. Rev. Lett.*, 99:140402, Oct 2007.

[177] Michiel Wouters and Iacopo Carusotto. Goldstone mode of optical parametric oscillators in planar semiconductor microcavities in the strong-coupling regime. *Phys. Rev. A*, 76:043807, Oct 2007.

[178] P. YU and M. Cardona. *Fundamentals of Semiconductors: Physics and Materials Properties*. Graduate Texts in Physics. Springer Berlin Heidelberg, 2010.

[179] Joanna M. Zajac and Wolfgang Langbein. Parametric scattering of microcavity polaritons into ghost branches. *Phys. Rev. B*, 92:165305, Oct 2015.

[180] V. E. Zakharov and A. M. Rubenchik. Instability of waveguides and solitons in nonlinear media. *Soviet Journal of Experimental and Theoretical Physics*, 38:494, March 1974.

[181] V. E. Zakharov and A. B. Shabat. Interaction between solitons in a stable medium. *Soviet Journal of Experimental and Theoretical Physics*, 37:823, November 1973.